

学位論文

**Deep Long-Period Earthquakes beneath Volcanoes:
Mechanism Analyses and Cooling Magma Model**

(火山型深部長周期地震のメカニズム解析と冷却マグマモデル)

平成 26 年 12 月博士（理学）申請

東京大学大学院理学系研究科

地球惑星科学専攻

麻生 尚文

PhD Thesis

**Deep Long-Period Earthquakes beneath Volcanoes:
Mechanism Analyses and Cooling Magma Model**

Naofumi Aso

**Department of Earth and Planetary Science
Graduate School of Science, the University of Tokyo**

December 2014

Abstract

In the convergence margins like Japan various earthquakes occur. Other than well-known events such as shallow inland earthquakes, interplate earthquakes, and intraslab earthquakes, there are slow earthquakes that relate to slow deformation process. Among them, deep long-period events (DLPs) or low-frequency earthquakes (deep LFEs), which are relatively small earthquakes ($M < 2$) at around 30 km in depth radiating low-frequency seismic waves that are dominant in 2–8 Hz, are best observable seismologically and their seismological study is essentially important to understand the variety of deformation process on the Earth. These events beneath active volcanoes are called volcanic DLPs and those on the plate boundaries are called deep tectonic LFEs. During the last decade, the discipline of deep tectonic LFEs has greatly developed owing to the deployment of the high sensitivity seismograph network “Hi-net” by National Research Institute for Earth Science and Disaster Prevention (NIED) in Japan. On the other hand, volcanic DLPs have been less studied even though they were discovered earlier than deep tectonic LFEs. Especially, the genesis of volcanic DLPs has not been revealed yet along with the difficulty of analyzing noisy signals. In the present study, we first work on the mechanism analyses of volcanic DLPs and then consider a new model for driving force of volcanic DLPs.

Determination of hypocenter distribution and focal mechanisms is essentially important for understanding source process. We therefore work on cluster shapes and source mechanisms at several regions of DLPs in Japan. We obtained fine shape of source clusters in 22 major regions of DLPs in Japan by applying relocation method that improves relative locations among events. Among these regions, 28 clusters were extracted including seven linear clusters and four planar clusters.

Then, we determine source mechanisms at four clusters, where either linear or planar structure is observed. We first develop an inversion method special for volcanic DLPs that have monochromatic waveforms with unclear onsets. We applied this method at four clusters and examined stability tests, but statistically significant results were not observed in most regions. However, compensated linear vector dipole (CLVD) component was not negligible for some events in E. Shimane, where the symmetry axis of the CLVD component is subparallel to the orientation formed by the linear hypocenter distribution. Owing to the development of analyzing much data to extract signal, we have enabled higher level of discussion on mechanisms compared with the previous study on DLPs. The analysis method specialized for DLPs and the statistical perspective of analyzing many events as well as further observations with higher quality would help understanding details of DLPs in the future.

The existence of a driving force such as shear stress or pressure gradient, which is often assumed for shallower LPs, is not necessarily expected at the Moho depth beneath volcanoes. Therefore, I propose the hypothesis that cooling magma produces thermal stress and trigger volcanic

DLPs, taking account of their hypocenter distribution. I evaluate the effect by calculating thermal strains for tabular or cylindrical magma intrusions. The produced deviatoric stress is CLVD-like rather than DC-like and can be a reason for the CLVD components observed for some DLPs. Namely, if the thermal stress acts as a driving force of DLPs, we expect a relationship between cluster shape and focal mechanism. Compared with the results of the first half of this thesis, the non-negligible CLVD component in the direction of the lineation formed by hypocenter distribution in E. Shimane can be explained by the relationship expected from the cooling magma model, although the polarity of CLVD is not well determined. The mathematical formulation and calculation enabled quantitative evaluation of the hypothesis in the present study. The thermal strain rate can be comparable with or larger than the direct effect from plate movements. However, for the realistic range of conditions, the thermal strain rate is much smaller than the stress relaxation rate within the cooling magma so that the elastic accumulation of thermal stress seems difficult. In this theoretical modeling, we considered a new possibility of driving force for DLPs, but the limitation of applicable condition and the lack of clear evidence did not necessarily support the model. Further detail evaluation of the applicability together with considering alternative models is important in modeling DLPs.

As a conclusion of the present study, we estimated cluster shapes of DLPs nationwide by source relocation and some of their focal mechanisms by the source inversions tuned specially for volcanic DLPs. Stability tests pointed out insignificance of the inversion results in most regions, but some events in E. Shimane were revealed to have the non-negligible CLVD components whose symmetry axis is sub-parallel to the lineation formed by hypocenter distribution. Then, we considered a new triggering of the volcanic DLPs first in the world. The qualitative relationships between cluster shape and focal mechanism expected from this model are partly consistent with the observation in E. Shimane, while quantitative discussion based on the theoretical calculation infers it is difficult to consider the elastic accumulation of thermal stress under realistic conditions. Throughout this PhD thesis work, we contributed on understanding volcanic DLPs from both observational and theoretical approaches, which is the highest level of quantitative study on DLPs. Following this pioneer study we expect further understanding of DLPs in the future.

Contents

Abstract	v
Contents	vii
1. Introduction	1
1.1. Slow Earthquakes and Volcanic DLPs	1
1.2. Semi-Volcanic DLPs	3
1.3. Similar Phenomena	6
1.3.1. Shallow Volcanic LPs	6
1.3.2. Deep Tectonic LFEs	7
1.4. Characteristics of Volcanic DLPs	8
1.4.1. Activities	8
1.4.2. Mechanisms	10
1.5. Purpose of This Study	11
2. Mechanism Analyses	13
2.1. Cluster Shapes	13
2.1.1. Waveform Network Cross-Correlation Relocation Method	13
2.1.1.1. Relative Location Correction to Maximize NCC	13
2.1.1.2. Hypocenter Inversion from Relative Location Corrections	14
2.1.2. Data	14
2.1.3. Results	17
2.2. Source Inversion	24
2.2.1. Data	25
2.2.2. Inversion Method	35
2.2.2.1. Estimating Source Function	35
2.2.2.2. Detecting Arrival Times	37
2.2.2.3. Moment Tensor Inversion	40
2.2.2.4. Synthetic Tests of Inversion	41
2.2.3. Results of Inversion	51
2.2.3.1. E. Shimane	51
2.2.3.2. Kirishima	63
2.2.3.3. S. Mt. Iwate	72
2.2.3.4. Yakedake	81
2.2.4. Summary of Inversion Results	91

3. Cooling Magma Model	93
3.1. Model	95
3.2. Method	97
3.2.1. Thermal Calculation	97
3.2.2. Thermal Strain Rates	98
3.3. Results	99
3.3.1. Neglecting Early Stage Deformation	99
3.3.2. Strain Rates	101
3.3.3. Cumulative Strains	104
3.3.4. Strain Orientations	105
3.3.5. Dependency of Shape	107
3.3.6. Connection to Earthquakes	108
3.4. Discussion	108
3.4.1. Consistency and Inconsistency with the Mechanism Analyses	114
3.4.2. Alternative Implications	121
3.4.2.1. Fluid Movements	121
3.4.2.2. Slips on Faults	124
3.4.2.3. Explosion	125
3.4.2.4. Tensile Cracks	126
3.4.2.5. Compressional Cylinder	127
4. Summary	129
Appendices	133
A1. Cluster Shape Estimation	133
A2. Source Type Diagram	135
A2.1. Previous Diagrams	137
A2.2. New Diagram	139
A3. Thermal Calculation for a 1D Cartesian Coordinates	144
A4. Thermal Calculation for a 1D Polar Coordinates	146
A5. Thermal Calculation for a 2D Cylindrical Coordinates	147
A6. Thermal Strain and Thermal Stress	148
A7. Spatial Derivatives of the Analytic Solutions	149
Acknowledgments	151
References	153

1. Introduction

1.1. Slow Earthquakes and Volcanic DLPs

Earthquake seismology has greatly developed in the last century. At the present day, earthquakes are understood as a release process of the accumulated stress mostly originating in the plate tectonics. Especially in the subduction zones at convergence margins like Japan, various types of earthquakes occur. The principal events are the interplate earthquakes with magnitude up to M_w 9 that occur on the plate boundaries shallower than 70 km. Another kind of destructive events are the inland earthquakes with magnitude up to M_w 7 that occur in the crust shallower than 20 km. There are also intraslab earthquakes in the subducting plate below 70 km and outerrise earthquakes in the oceanic plate before subduction.

In contrast with these ordinary earthquakes, a group of slow earthquakes or low-frequency events are newly recognized recently. Deep volcanic long-period events (DLPs) are small earthquakes at depths around 10–60 km that radiate seismic waves of 2–8 Hz in active volcanic regions (Figure 1.1; Figure 1.2). Similar events at shallower depth in the upper crust are called volcanic long-period events (LPs). There are earthquakes that occur near the surface, and radiate longer period signal. They are called very-long-period events (VLPs) and these events are sometimes caused by a collapse of caldera [e.g., Kumagai *et al.*, 2001]. Earthquakes on the plate interface similar to DLPs are called deep tectonic low-frequency earthquakes (LFEs), and their successive occurrence is recognized as deep tectonic tremors. Events on the plate interface that radiate seismic waves of much lower frequency (~ 100 s) are recognized as very-low-frequency events (VLFs). Deep tectonic LFEs, tremors, and VLFs are often simultaneously observed with slow-slip events (SSEs), which are geodetically detectable shear dislocation, and these tectonic slow events are all thought to be slip events on the plate interface. VLFs are also observed at shallower depth around ~ 10 km on the place interface up-dip of hypocenters of regular inter-plate events. Afterslips following major inter-plate events are also slow slip events on plate interface. Among these varieties of slow earthquakes, volcanic DLPs and tectonic LFEs are seismologically best observable and their seismological study is important to understand a variety of deformation process in the Earth. In the hypocenter catalog of Japan Meteorological Agency (JMA), 41,237 events are marked as low-frequency events from June 2000 to October 2014, while 1,994,451 ordinary events are detected in the same period, and 24,597 events are thought to be tectonic LFEs and the other 16,640 are thought to be volcanic DLPs. While the knowledge of tectonic LFEs has greatly developed during the last decade, volcanic DLPs are less understood regardless of earlier discovery than tectonic LFEs. Therefore we try to understand volcanic DLPs.

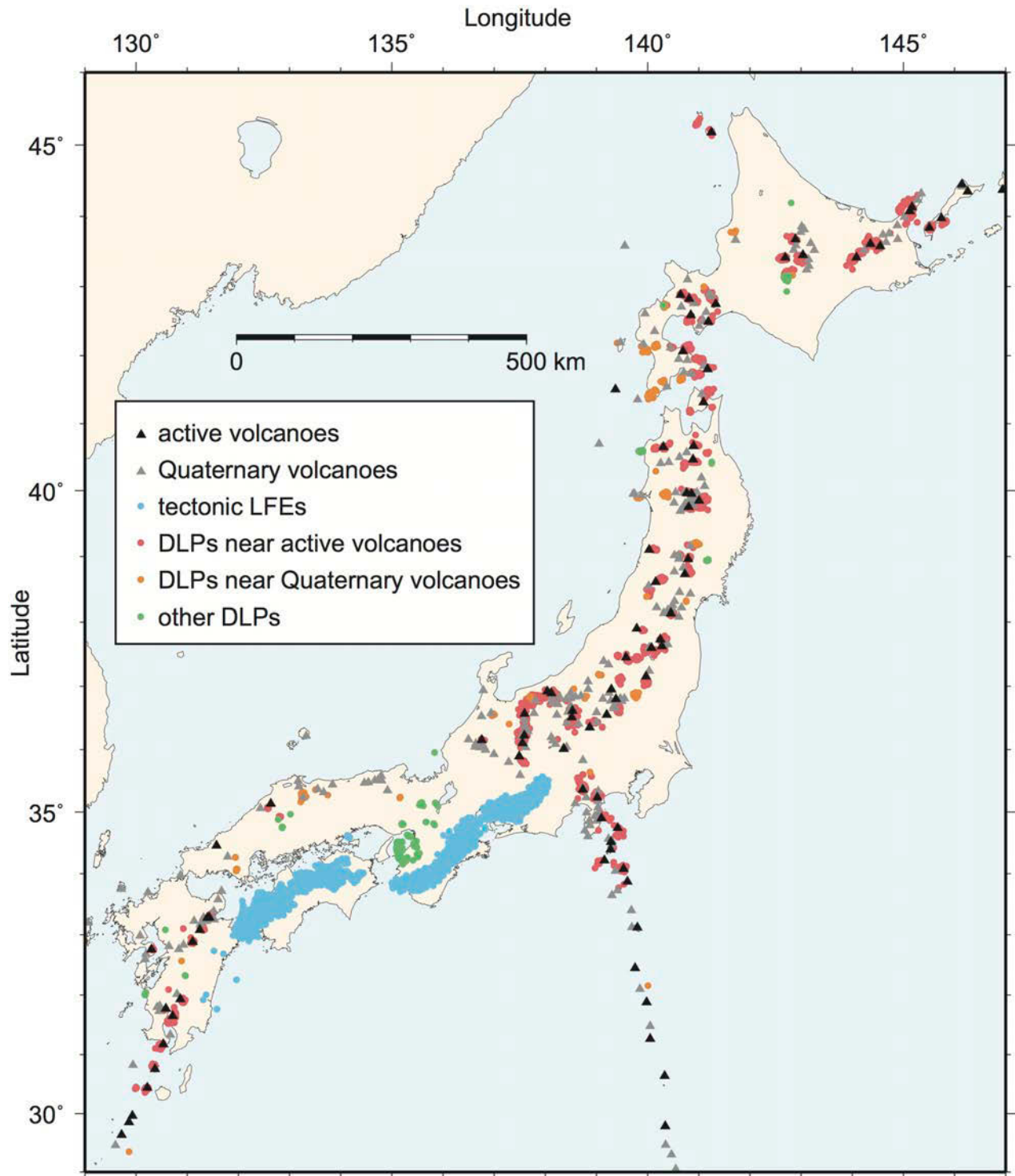


Figure 1.1 Distribution of LFEs, DLPs, and volcanoes in Japan

All low-frequency (long-period) events detected by JMA from June 2000 to October 2014 are plotted. Blue, red, orange, and green dots represent tectonic D-LFEs, DLPs beneath active volcanoes, DLPs beneath Quaternary volcanoes, and other DLPs far from volcanoes. Black and gray triangles show active volcanoes [Japan Meteorological Agency, 2013] and Quaternary volcanoes [Committee for Catalog of Quaternary Volcanoes in Japan, 1999], respectively.

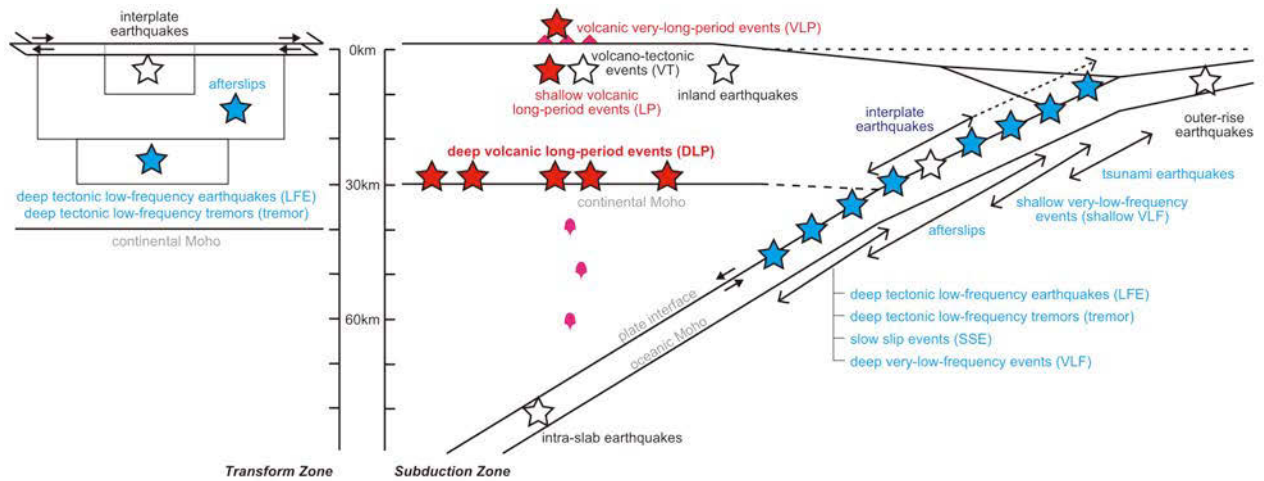


Figure 1.2 Schematic cross-section of transform and subduction zones

Red stars represent slow or low-frequency phenomena in volcanic regions and blue stars represent those near plate interfaces, while white stars represents regular events.

Small earthquakes at depths around 10–60 km that radiate seismic waves of 2–8 Hz in active volcanic regions are called “volcanic deep long-period events” or “volcanic DLPs”. They are also called “DLP events”, “DLPs”, “volcanic deep low-frequency earthquakes”, or “volcanic deep LFEs”. The terminology “volcanic LFEs” is also used for these events to compare with “tectonic LFEs” and it does not generally include shallow LP events unlike its literal meaning. Volcanic DLP events have been discovered worldwide such as in Japan [Hasegawa *et al.*, 1991; Ukawa and Obara, 1993; Hasegawa and Yamamoto, 1994], the Aleutian [Power *et al.*, 1995; Power *et al.*, 2004], Cascadia [Nichols *et al.*, 2011], California [Pitt *et al.*, 2002; Lewicki *et al.*, 2014], Hawaii [Aki and Koyanagi, 1981; Shaw and Chouet, 1991; Okubo and Wolfe, 2008], the Philippines [White, 1996], Iceland [Soosalu *et al.*, 2010], and Antarctica [Lough *et al.*, 2013].

1.2. Semi-Volcanic DLPs

Earthquakes similar to volcanic DLPs but far from active volcanoes are called “semi-volcanic deep long-period events”. These events were recognized since 2000 [Katsumata and Kamaya, 2003; Takahashi and Miyamura, 2009] but at least some of these events are found to be similar to volcanic DLP events recently [Aso *et al.*, 2011, 2013; Vidale *et al.*, 2014], and are called “semi-volcanic”. Some of them occur near dormant Quaternary volcanoes but some do not [Aso *et al.*, 2011, 2013]. The similarity of volcanic and semi-volcanic DLPs infers that they would be related to the phenomena that do not necessarily co-exist with active volcanism on the ground surface.

Since most of the DLP events or deep LFEs away from both active volcanoes and plate boundaries reported to date are located near dormant Quaternary volcanoes, most of these DLPs

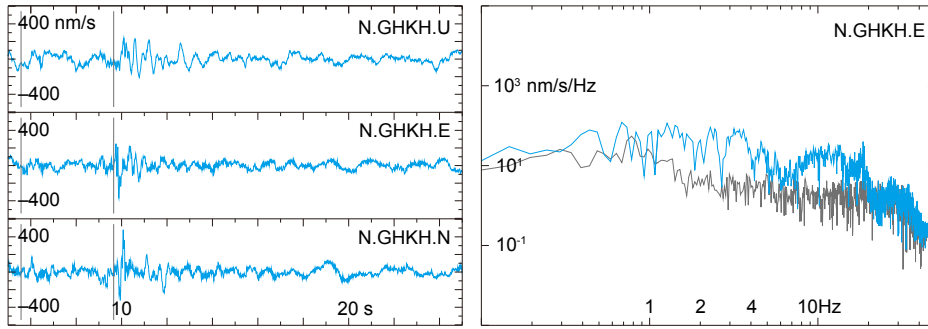
occurring in spotty regions are also thought to be semi-volcanic DLPs while tectonic LFEs occur in belt-like zones.

One example of such events is observed between Shimane and Tottori prefectures (eastern Shimane or western Tottori) [Ohmi and Obara, 2002]. They occur right beneath a Yokota Quaternary volcanic cluster (dormant volcano erupted at 1–2 Ma lastly), although there is no active volcano (erupted within 10,000 year or have vigorous fumarolic activity) within 50 km from their epicenters. Another example of semi-volcanic DLPs is in Osaka Bay in an area located 100 km from the nearest Quaternary volcano [Aso *et al.*, 2011].

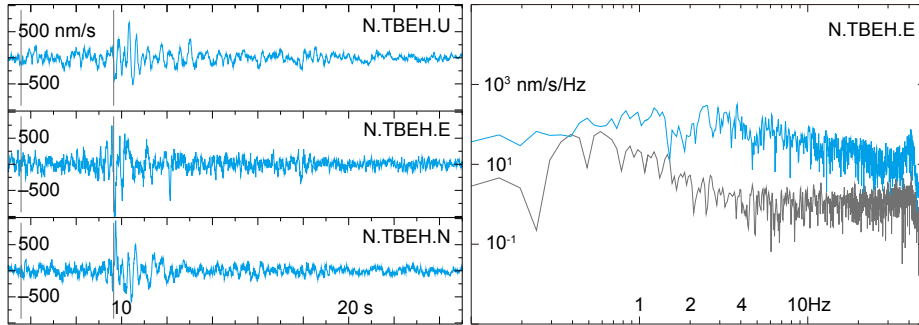
Such semi-volcanic DLPs often occur near the source region of large inland strike-slip earthquakes. DLPs in Osaka Bay are located 10–30 km away from the 50 km-long fault plane of the 1995 Kobe earthquake (M_w 6.8). DLPs in eastern Shimane are located 10 km away from the 20 km-long fault plane of the 2000 western Tottori earthquake (M_w 6.6). The 2008 Iwate-Miyagi Nairiku earthquake (M_w 6.9) also occurred right above DLPs [Ando and Okuyama, 2010]. In addition to these examples, most of large crustal earthquakes in western Japan occurred within 20 km from active volcanoes, Quaternary volcanoes, or semi-volcanic DLPs [Ide *et al.*, 2010]. Key control on these phenomena might be a crustal fluid because volcanoes above volcanic DLPs are located on the top of flow channels of magma and fluids from the mantle, semi-volcanic DLPs may also be related to crustal fluid movements [Sano and Nakajima, 2008; Ohmi and Obara, 2002; Aso *et al.*, 2011], and crustal earthquakes are affected by fluids [e.g., Zhao *et al.*, 1996].

The definition of active volcanoes has not been well established worldwide, although JMA defines them as the volcanoes erupted within 10,000 year or have vigorous fumarolic activity. Therefore, the definition of volcanic DLPs based only on the distance to active volcanoes cannot be rigorous. Because of this ambiguous definition of active volcano, we call both volcanic DLPs and semi-volcanic DLPs constitutively as volcanic DLPs in the present study, based on the current knowledge that both are thought to be similar phenomena.

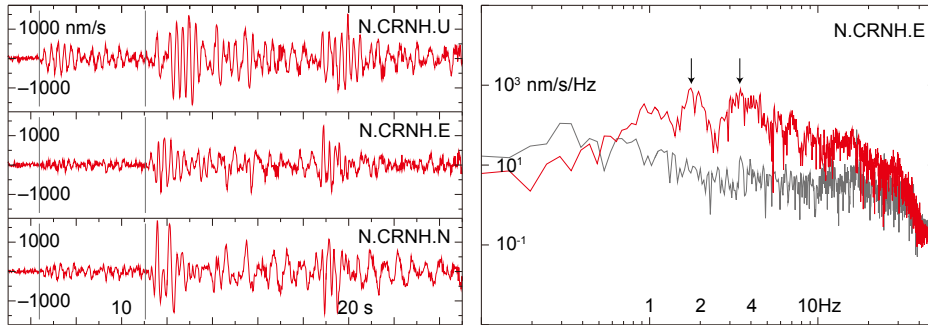
(a) tectonic LFE in N. Kochi



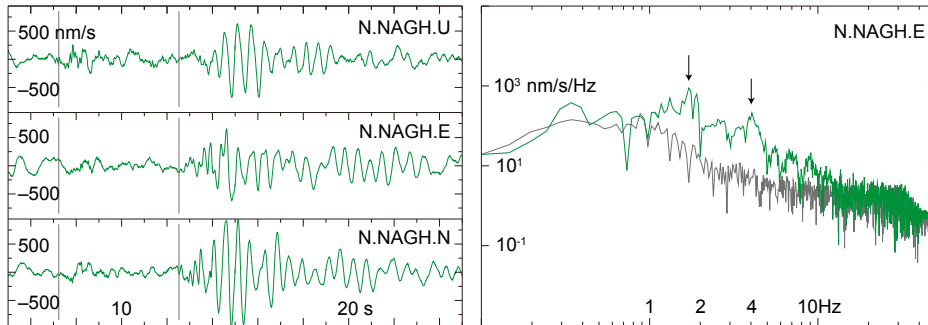
(b) tectonic LFE in C. Ehime



(c) DLP in Sakurajima



(d) DLP in Osaka Bay



(e) DLP in E. Shimane

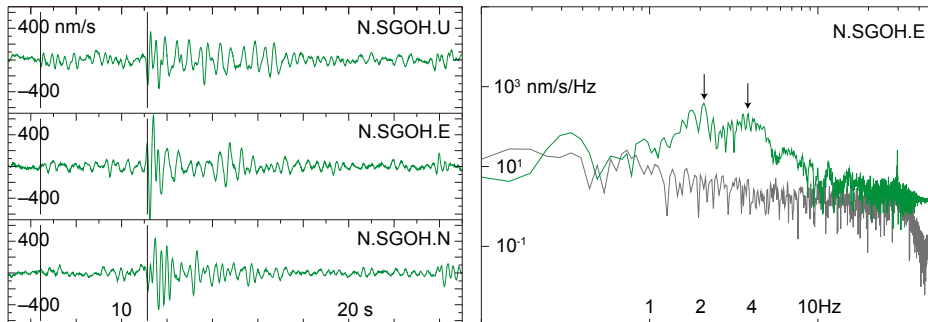


Figure 1.3 Representative waveforms and spectra of LFEs and DLPs

These events have similar magnitudes and were observed at similar hypocentral distances. In each left panel, the three-component velocity waveforms are shown by color lines versus the time elapsed from the event origin time, and vertical gray lines show P- and S-wave arrival times. In each right panel, the power spectral density for the velocity waveform of the east–west component within 10 s starting from the S-wave arrival is shown by a color line, and a gray line shows the background spectrum. Downward arrows mark distinct spectral peaks. (a) The tectonic LFE that occurred in northern Kochi at 03:24:50 on May 11th, 2007 (JST). (b) The tectonic LFE that occurred in central Ehime at 06:36:33 on September 4th, 2008 (JST). (c) The volcanic DLP in Sakurajima that occurred at 12:58:28 on July 24th, 2004 (JST). (d) The volcanic (semi-volcanic) DLP in Osaka Bay that occurred at 14:17:05 on November 9th, 2007 (JST). (e) The volcanic (semi-volcanic) DLP in eastern Shimane that occurred at 12:59:13 on August 21st, 2006 (JST).

1.3. Similar Phenomena

1.3.1. Shallow Volcanic LPs

In volcanic regions, various types of earthquakes shallower than 10 km are known [e.g., *Nishimura and Iguchi, 2006*]. There are not only high-frequency events caused by shear fracture, but also low-frequency events. The continuous events are called tremor. Temporal variation of frequency contents during each tremor episode is also observed [*Kamo et al., 1977; Maryanto et al., 2008*] and some models are developed to explain gradual and/or abrupt changes of frequencies [*Julian, 1994; Neuberg et al., 2000*]. These low-frequency events and tremors are regarded as critically important because they often precede and accompany volcanic eruptions [e.g., *Minakami, 1960; Ishihara and Iguchi, 1989; Chouet et al., 1994; Chouet, 1996; Varley et al., 2010*]. LPs often have slowly decaying coda waves [*Chouet, 2003*]. They often contain considerable non-double-couple component [*Iguchi, 1994; Kumagai et al., 2002; Eyre et al., 2013*]. Among them, most common is compensated linear vector dipole (CLVD). Although single forces are also observed [e.g., *Takeo et al., 1990*], single forces are sometimes attributed to using inappropriate velocity structures [*De Barros et al., 2011*].

Several mechanical models are suggested for them [e.g., *Julian, 1994; Fujita and Ida, 2003*]. These models mostly focus on the low-frequency harmonic seismic radiation. Some LPs would be slow failure process on a fault [*Bean et al., 2014*]. Some focus on a resonant oscillation within a volume filled by a fluid or a gas [e.g., *Nakano et al., 1998; Kumagai and Chouet, 2000*]. *Kumagai and Chouet [2000]* calculated excited modes of resonant oscillation and their decay based on theoretical calculations. Another plausible mechanism is instability of fluid flow within narrow conduits [e.g., *Julian, 1994; Ohminato et al., 1998*]. *Julian [1994]* calculated oscillation excited by a non-linear effect in a coupled system of fluid dynamics and elasticity assuming a constant pressure gradient.

Jellinek and Bercovici [2011] pointed out the effect of bubble on the dynamic fluid movement. As well as regular earthquakes, *Dmitrieva et al.* [2013] suggested low-frequency signals are produced by repeatedly occurring stick-slip events. Although these models for shallow LPs might be applicable to DLPs, spatial separation of LPs and DLPs suggests us to consider another special mechanism for DLPs. Although single forces are attributed to special movements within heterogeneous medium [*Takei and Kumazawa*, 1994] or landslides [*Kawakatsu*, 1989], we consider simple point process for the deep events and only focus on the movements that can be written by a moment tensor.

1.3.2. Deep Tectonic LFEs

After *Nishide et al.* [2000] reported tectonic LFEs using Hi-net later than the discovery of volcanic DLPs, JMA began to detect and locate LFEs as part of their routine monitoring [*Katsumata and Kamaya*, 2003, 2004]. At almost the same time, *Obara* [2002] recognized tectonic tremor occurring for several days, and *Rogers and Dragert* [2003] demonstrated episodic tremor and slip (ETS), which is tremor occurring with simultaneous slow slip on the plate boundary. Although tectonic LFEs and tremors were thought to be different phenomena for several years after their discoveries, tectonic LFEs were demonstrated as a constituent of ETS on the plate boundary [*Shelly et al.*, 2006, 2007a]. They occur with belt-like distribution along the iso-depth contour of 30-40 km on the subducting plate [*Obara*, 2002]. Such tremors or LFEs have been discovered worldwide [*Ide*, 2011] including strike-slip conditions [*Shelly and Hardebeck*, 2010]. The mechanisms of tectonic LFEs are recognized as the double-couple that is consistent to the shear slip on the plate interface [*Ide et al.*, 2007b; *Frank et al.*, 2013]. Remarkable phenomena about activities such as spatial migrations [e.g., *Obara*, 2002] and tidal responses [e.g., *Nakata et al.*, 2008] are also recognized. The migration of tremor is known to be parabolic and is modeled considering ductile stress relaxation process [*Ando et al.*, 2010, 2012]. The variety of periodicity is also reported [*Obara et al.*, 2010; *Idehara et al.*, 2014]. The existence of fluid is thought to be related to the generation of tremor [*Katsumata and Kamaya*, 2003; *Shelly et al.*, 2006]. Not only LFE or episodic tremor and slip, but also many other low-frequency events such as long-term slow slip events [*Hirose et al.*, 1999], shallow very-low-frequency (VLF) earthquakes [*Ishihara*, 2003], and deep VLF earthquakes [*Ito et al.*, 2007] were found recently. Focal mechanisms obtained for VLF signals are also consistent with the slip on the faults [*Ide and Yabe*, 2014]. These phenomena follow a common scaling law [*Ide et al.*, 2007a] and are thought to be common phenomena at different frequency bands. The relations among these low-frequency events and interplate megathrust earthquakes are attracting attention to understand the subduction zones systematically [e.g., *Rubinstein et al.*, 2010; *Obara*, 2011].

Although tectonic LFEs and volcanic DLPs radiate seismic waves at similar frequencies, they are thought to be different physical mechanisms based on systematic analyses of seismicity. We therefore focus on the physical mechanism of volcanic DLPs, which is less understood (Table 1.1).

Table 1.1 Comparison between volcanic DLPs and tectonic D-LFEs

	Volcanic DLPs	Tectonic D-LFEs
Hypocenter	near the Moho beneath volcanoes or far from volcanoes	on the plate boundaries
Waveform	harmonic or monochromatic	unclear spectral peaks
M2 tide triggering	no	yes
Magnitude	G–R law ($b=2$)	distinct upper limit ($M_{\max} \sim 0.5$)
Hypocenter distribution	various	slightly dipping line or plane
Mechanism	non-double-couple components? CLVD?	double-couple mechanism
Driving force	? (this study)	plate tectonics

1.4. Characteristics of Volcanic DLPs

1.4.1. Activities

DLPs are thought to be instantaneous events because their waveforms often include emergent P- and S-wave arrivals. The dominant frequency of the radiated seismic waves is lower than the characteristic frequency of ordinary earthquakes of similar amplitude. Most of the waveforms show monochromatic or harmonic characteristic and their coda waves tend to have long duration. Their dominant frequency range is around 2–8 Hz similar to tectonic LFEs. It is currently in discussion whether the long coda originates in long source duration or near source effect, although the large site effect can be ruled out because similar waveforms are observed at multiple stations regardless of azimuthal angle and also high frequency seismic waves from ordinary earthquakes are also observed at the same stations.

Their depths vary within 10–60 km, but roughly correspond to the depth of Mohorovicic discontinuities (the Moho depth) [Okada and Hasegawa, 2000; Takahashi and Miyamura, 2009] (Figure 1.4). DLPs in E. Shimane is at around 30 km depth and the Moho depth obtained by receiver functions there is around 30 km although it has uncertainties of ~5 km at each station and varies among stations [Ramesh *et al.*, 2005]. Some events are clearly shallower than the Moho. Relatively shallow events are observed beneath Mt. Fuji at depth of 11–16 km [Nakamichi *et al.*, 2004; Ukawa, 2005], where the Moho depth is around 38–40 km [Katsumata, 2010]. There is also shallow cluster in Kirishima of ~10–15 km although there is a deep cluster of ~20–25 km, where the Moho depth is around 34 km [Katsumata, 2010]. One of the major DLP activities in the central Japan is observed at Yakedake and their focal depth is estimated within 10–40 km, while the Moho depth is 36–38 km. The activity in S. Mt. Iwate is around 25–35 km in depth, where the Moho depth is estimated to be

~35 km [Nakajima *et al.*, 2002]. As deep examples, DLPs in Mt. Chokai distribute down to 45 or 50 km deep, where the Moho depth is ~32–33 km [Nakajima *et al.*, 2002]. As shown here, DLPs seem to locate above the Moho in some regions and beneath the Moho in the other regions. However, local estimation of Moho depth has an error of several kilometers, while spatially smoothed estimation is precise within an error around 1 km. Since precise estimation of the Moho depth exactly beneath volcanoes is not currently available, their occurrence near the Moho is more important information as a mean feature rather than discussing regional variety of their depth offset in respect to the Moho depth.

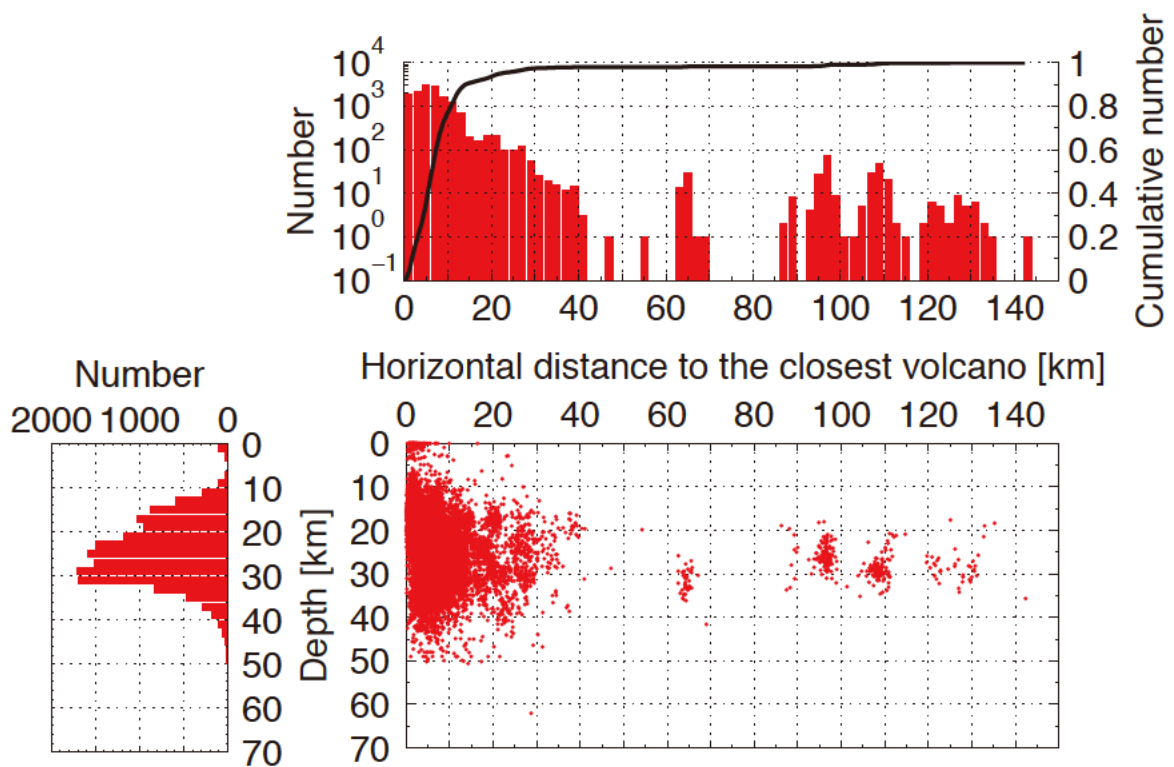


Figure 1.4 Hypocenter distribution of volcanic DLP events in Japan

The spatial distribution of DLPs detected by JMA from June 2000 to March 2013 is shown. (top right) Histogram of volcanic DLP events versus horizontal distance to the closest Quaternary volcano. A black line shows their cumulative number. (bottom right) Depth of volcanic DLP events in Japan versus horizontal distance to the closest Quaternary volcano. (bottom left) Histogram of volcanic DLP events versus depth.

The DLP sequences sometimes occur simultaneously with shallow seismicity of ordinary earthquakes [Hasegawa and Yamamoto, 1994]. Some sequences might be related to the volcanic eruptions because they occur before eruptions [Ukawa and Ohtake, 1987; Matsubara *et al.*, 2004] or

after eruptions [Power *et al.*, 2002]. However, such temporal correlations with other seismic and volcanic activities are not commonly observed. Rather than such evidence, there is no correlation between volcanic activity and DLPs activities [Takahashi and Miyamura, 2009]. Occurrence of DLPs far from active volcanoes also supports the eruption and DLPs are not necessarily directly connected phenomena. In eastern Shimane, within the ten-year record of dense seismogram network, relatively constant seismicity is observed rather than the shallower volcanic events. Although some DLPs might relate eruptions, we regard most DLPs occur without relationship with eruptions.

Table 1.2 DLPs and Volcanoes in Japan

	with DLPs*	without DLPs*	total
Active volcanoes	79 (72%)	31 (28%)	110
Quaternary volcanoes	653 (81%)	157 (19%)	810

*The volcanoes from which there are DLPs within 30 km and the others.

To understand the physical mechanism such as the condition of occurrence, it is important whether they are triggered by external force or not. While tectonic LFEs are modulated by earth tide and ocean tide, tidal modulation is not observed for volcanic DLPs [Aso *et al.*, 2013]. One possible reason might be small amplitude of tidal stress because of distant location from coast, but we infer volcanic DLPs do not occur on mature faults such as plate interfaces so that clear responsibility of tide is not observed.

The magnitude distribution helps understanding background physics. An exponential magnitude distribution (or power distribution for moment) is known for ordinary earthquakes as Gutenberg-Richter scaling law (G-R law) and its exponent b of $P(M) \propto 10^{-bM}$ is known as a b -value. The b -value is small for reverse faults and large for normal faults, and is controlled by stress state [Schorlemmer *et al.*, 2005]. The G-R law with $b \sim 2$ is obtained for volcanic DLPs detected by cross-correlation method with JMA events [Aso *et al.*, 2013]. Their study uses the JMA magnitude for small earthquakes that is proportional to $\log(\text{amp.})/0.85$ [Japan Meteorological Agency, 2003] and is good estimate for small ordinary events [Watanabe, 1971], but the attenuation is thought to be minor in the low-frequency range and it might not mean the exact moment magnitude. The magnitude calculated from the maximum amplitude of velocity waveforms is about $M < 2$.

1.4.2. Mechanisms

There have been several previous works on the mechanisms of volcanic DLP events. These works used variety of methods to extract information of tiny signals from noisy data, such as the pattern of S-wave polarization [Ukawa and Ohtake, 1987], S-wave to P-wave (S/P) amplitude ratios [Ukawa and Ohtake, 1987], S/P spectral ratios [Nakamichi *et al.*, 2003], or waveform inversions [Nishidomi and Takeo, 1996; Okada and Hasegawa, 2000]. As shown in the followings, the moment

tensor solutions are highly various even beneath a single volcano, and it is difficult to statistically discuss the fundamental mechanism from these limited observations. *Ukawa and Ohtake* [1987] obtained a unidirectional single force at Izu-Ooshima, which is recognized as a traction force by a magma flow. *Nishidomi and Takeo* [1996] obtained a strike-slip double-couple mechanism in western Tochigi. *Okada and Hasegawa* [2000] obtained significant non-DC components with swarm-like activities in northwestern Miyagi and inferred rapid fluid movements. *Nakamichi et al.* [2003] obtained non-DC mechanisms and proposed a tensile crack coupled either with a shear crack or with an oblate spheroid magma chamber beneath Iwate volcano. *Ohmi and Obara* [2002] obtained a single-force source mechanism at eastern Shimane (or western Tottori). In the same region, *Aso and Ide* [2014] obtained CLVD mechanism in the NNE direction, which is consistent with the combination of the single force obtained by *Ohmi and Obara* [2002] and its reaction force.

Rheological properties of rocks are expected to be within a ductile regime at these depths because the friction strength, which depends on the effective normal stress and the friction coefficients, is higher than ductile stress, which depends on the temperature and the strain rate [*Shimamoto*, 1986]. The occurrence of brittle failure suggests low effective normal stress, low friction coefficient, low temperature, and/or high strain rates. Another possibility is a failure driven by a rapid movement of magma or crustal fluids related to high pressure gradients.

Although there is no special model suggested for DLP events, several discussions have been done for their physical models. To produce oscillatory nature of waveforms, a flow-induced instability is proposed by *Ukawa and Ohtake* [1987]. The flow instability is also discussed by *Julian* [1994] for shallow LP events as a main focus.

Although volcanic DLP events have been well recognized since the early 1980s, their understanding is not well developed yet and there is little universal knowledge about these events [*Chouet*, 2003; *McNutt*, 2005], probably because of their weak signals and little attention of volcanologists or seismologist rather than shallow volcanic events or the events on plate boundaries.

1.5. Purpose of This Study

These characteristic observations of DLPs give rise to a number of questions. Why do brittle deformations occur? Why are low-frequency harmonic seismic waves radiated? Why do they have non-double-couple components? Why do they distribute far from active volcanoes? Why do they distribute around the Moho? Do DLPs have direct relationship with eruption or inland earthquakes?

To approach the answers to these big questions, we set three practical goals for this thesis. One is providing a scheme that enable objective comparison of the spatial activities of DLPs in different regions, where DLPs have been studied arbitrarily. Another is estimating source mechanisms with confidence from weak signals. The other is considering possible driving force for brittle deformation that produces volcanic DLPs at the specific region around the Moho beneath most of volcanoes.

First, we work on data analyses of DLPs. We objectively compare cluster shapes in 22 regions by applying relocation method and analyze source process at four regions by the inversion procedure developed for their analyses. Then, we consider a new triggering model of DLPs that is consistent with current geophysical and geological knowledge. Since verification process is important in model study, we also try to compare the expectation from the model with the obtained mechanisms.

2. Mechanism Analyses

To understand the physical mechanisms of volcanic DLPs, both source relocation and source mechanism inversion are important. We first estimate cluster shapes in 2.1 and analyze mechanisms in 2.2.

2.1. Cluster Shapes

We relocate the hypocenters of the template events using the network cross-correlation (NCC) relocation method developed by *Ohta and Ide* [2008, 2011], which utilizes the NCC to constrain the relative hypocenter locations. First, we determined the relative location and time of each event pair to maximize the NCC. Then, a linear inversion technique was employed to determine the hypocenters, consistent with the relative locations of all the event pairs.

2.1.1. Waveform Network Cross-Correlation Relocation Method

2.1.1.1. Relative Location Correction to Maximize NCC

Generally, the preliminary time and location such as in the JMA catalog have some determination error. Therefore, the origin time and hypocentral location should be corrected as,

$$t^k \rightarrow t^k + \Delta t^k, \quad \mathbf{x}^k \rightarrow \mathbf{x}^k + \Delta \mathbf{x}^k, \quad (2.1)$$

where Δt^k and $\Delta \mathbf{x}^k$ are “absolute corrections” of time and location of the k -th event, respectively.

Correcting times and locations in (2.1), NCC is represented as

$$\begin{aligned} & \text{NCC}^{kk'} \\ &= \sum_{i=1}^{N_{\text{sta}}} \sum_{j=1}^{N_{\text{comp}}} \sum_{l=1}^{N_{\text{phase}}} w_{ij}^l \text{CC} \left(\mathbb{W}_{ij} \left(t^k + \Delta t^k + \tau_i^l(\mathbf{x}^k + \Delta \mathbf{x}^k) \right), \mathbb{W}_{ij} \left(t^{k'} + \Delta t^{k'} + \tau_i^l(\mathbf{x}^{k'} + \Delta \mathbf{x}^{k'}) \right) \right), \end{aligned} \quad (2.2)$$

where $\tau_i^l(\mathbf{x})$ is the travel time of l -th phase from the source at \mathbf{x} to the i -th station, $\mathbb{W}_{ij}(t)$ is the data vector around time t of j -th component at i -th station, and w_{ij}^l is the weighting factor. Slightly shifting these two windows by $\tau_i^l(\mathbf{x}^k + \Delta \mathbf{x}^k) - \tau_i^l(\mathbf{x}^k) + \Delta t^k$ in time direction,

$$\begin{aligned} \text{NCC}^{kk'} &\cong \sum_{i=1}^{N_{\text{sta}}} \sum_{j=1}^{N_{\text{comp}}} \sum_{l=1}^{N_{\text{phase}}} w_{ij}^l \text{CC} \left(\mathbb{W}_{ij} \left(t^k + \tau_i^l(\mathbf{x}^k) \right), \mathbb{W}_{ij} \left(t^{k'} + \Delta t^{k'} - \Delta t^k + \tau_i^l(\mathbf{x}^{k'} + \Delta \mathbf{x}^{k'}) \right. \right. \\ &\quad \left. \left. + \tau_i^l(\mathbf{x}^k) - \tau_i^l(\mathbf{x}^k + \Delta \mathbf{x}^k) \right) \right). \end{aligned} \quad (2.3)$$

Assuming $\tau_i^l(\mathbf{x}^k) - \tau_i^l(\mathbf{x}^k + \Delta \mathbf{x}^k) \cong \tau_i^l(\mathbf{x}^{k'} + \Delta \mathbf{x}^{k'} - \Delta \mathbf{x}^k) - \tau_i^l(\mathbf{x}^{k'} + \Delta \mathbf{x}^{k'})$,

$$\begin{aligned} & \text{NCC}^{kk'} \\ &\cong \sum_{i=1}^{N_{\text{sta}}} \sum_{j=1}^{N_{\text{comp}}} \sum_{l=1}^{N_{\text{phase}}} w_{ij}^l \text{CC} \left(\mathbb{W}_{ij} \left(t^k + \tau_i^l(\mathbf{x}^k) \right), \mathbb{W}_{ij} \left(t^{k'} + \Delta t^{k'} - \Delta t^k + \tau_i^l(\mathbf{x}^{k'} + \Delta \mathbf{x}^{k'} - \Delta \mathbf{x}^k) \right) \right) \end{aligned}$$

$$\begin{aligned}
&= \sum_{i=1}^{N_{\text{sta}}} \sum_{j=1}^{N_{\text{comp}}} \sum_{l=1}^{N_{\text{phase}}} w_{ij}^l \text{CC} \left(\mathbb{W}_{ij} \left(t^k + \tau_i^l(\mathbb{X}^k) \right), \mathbb{W}_{ij} \left(t^{k'} + \Delta t^{kk'} + \tau_i^l(\mathbb{X}^{k'} + \Delta \mathbb{X}^{kk'}) \right) \right) \\
&\quad \equiv \text{NCC}^{kk'}(\Delta t^{kk'}, \Delta \mathbb{X}^{kk'}), \tag{2.4}
\end{aligned}$$

where $\Delta t^{kk'} = \Delta t^{k'} - \Delta t^k$ and $\Delta \mathbb{X}^{kk'} = \Delta \mathbb{X}^{k'} - \Delta \mathbb{X}^k$ are “relative correction” of time and location of the k' -th event relative to the k -th event, respectively. Therefore, $\text{NCC}^{kk'}(\Delta t^{kk'}, \Delta \mathbb{X}^{kk'})$ in (2.4) is a function of relative corrections. By maximizing NCC in this formulation, relative corrections of time and location can be obtained for each event pair.

2.1.1.2. Hypocenter Inversion from Relative Location Corrections

The relative corrections of time and location ($\Delta t^{kk'}$ and $\Delta \mathbb{X}^{kk'}$), which are obtained as shown in 2.1.1.1, are functions of the absolute corrections of time and location (Δt^k and $\Delta \mathbb{X}^k$). Here, the number of independent data parameters, $\Delta t^{kk'}$ and $\Delta \mathbb{X}^{kk'}$, is $4(N_{\text{event}} - 1)$ and the number of independent unknown parameters, Δt^k and $\Delta \mathbb{X}^k$, is $4N_{\text{event}}$, where N_{event} is the number of events. Since the data parameters are less than the unknown parameters, adopting the constraint on the deviation from the initial estimation error given by JMA for each event, absolute corrections were solved from relative corrections by linear inversion technique.

2.1.2. Data

We focus on major activities of DLPs in Japan, where tens of events are already detected by JMA. For this purpose, we analyze DLPs from April 2002 to March 2014 in 22 major regions as shown in Figure 2.1 and listed in Table 2.1.

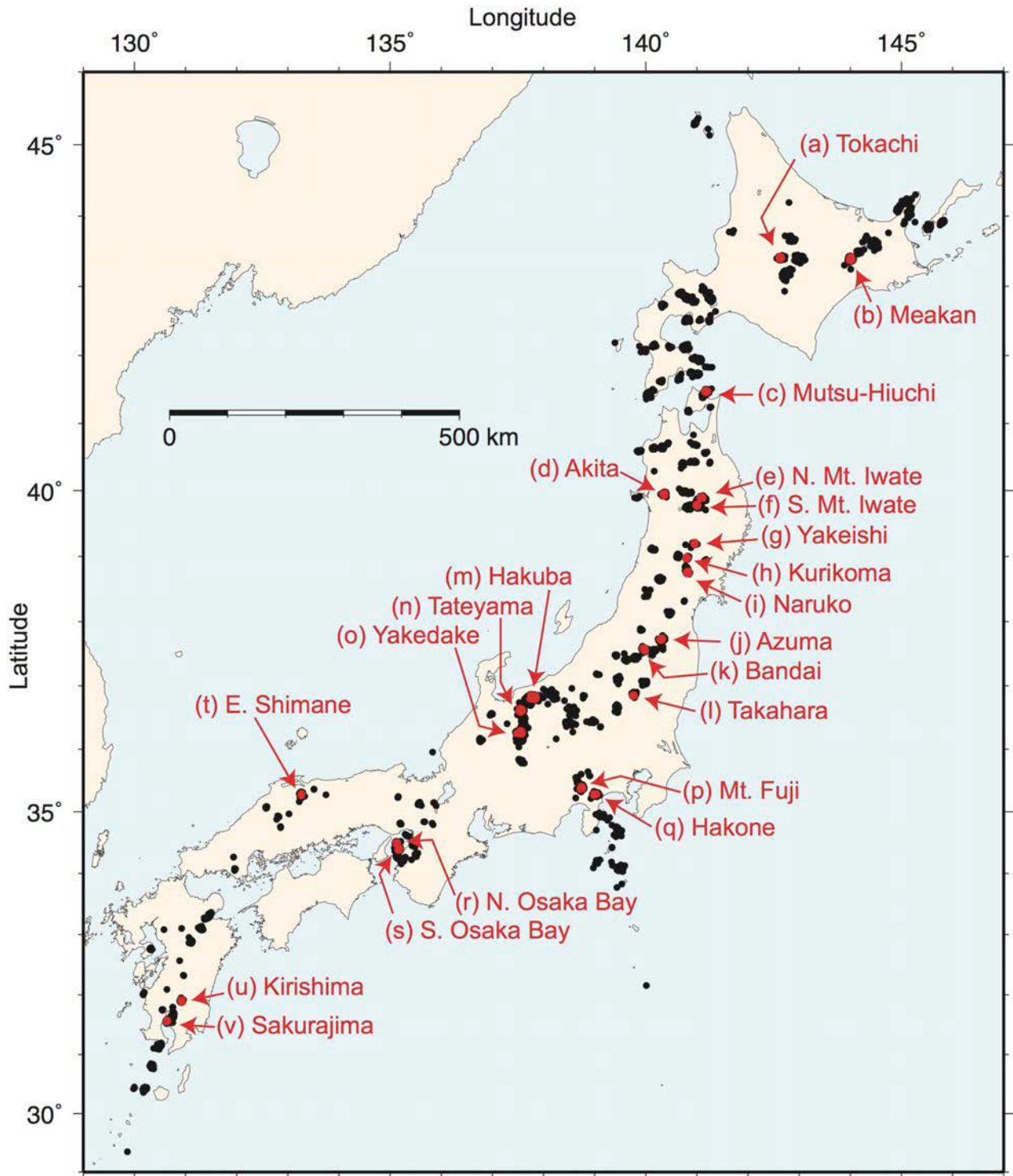


Figure 2.1 Analyzed regions for cluster shapes

Black dots represents all DLPs detected by JMA from June 2000 to October 2014. Red dots are events in analyzed regions for cluster shape estimation.

Table 2.1 Analyzed regions for cluster shapes

	Region	Latitude [°]	Longitude [°]	Depth [km]	M_{\min}	N_{ev}	Length ($4r_1$)	r_2 / r_1	r_3 / r_2	type	θ [°]	ϕ [°]
a1	Tokachi	43.4127	142.6268	29.76	0.6	12	1.14	0.17	0.62	l	-156	66
a2	Tokachi	43.4035	142.6325	27.76	0.6	20	1.02	0.59	0.51	s		
b	Meakan	43.3900	144.0152	23.53	1.0	55	1.61	0.65	0.35	p	-124	29
c	Mutsu-Hiuchi	41.4819	141.1731	18.09	0.8	41	3.34	0.80	0.68	s		
d	Akita	39.9514	140.3552	31.54	0.0	55	0.96	0.59	0.71	s		
e	N. Mt. Iwate	39.8969	141.0923	33.98	0.0	84	0.85	0.57	0.69	s		
f	S. Mt. Iwate	39.7800	141.0015	32.01	0.6	80	1.32	0.47	0.83	l	-123	1
g	Yakiishi	39.1935	140.9584	32.08	-	57	1.31	0.30	0.46	l	-124	59
h	Kurikoma	38.9759	140.7990	19.21	-	73	1.68	0.73	0.54	s		
i	Naruko	38.7614	140.8192	23.71	0.8	60	1.93	0.59	0.62	s		
j	Azuma	37.7278	140.2980	27.28	0.6	75	0.54	0.59	0.74	s		
k1	Bandai	37.5816	139.9727	24.55	0.0	21	0.82	0.87	0.35	p	-156	16
k2	Bandai	37.5778	139.9604	27.67	0.0	25	0.56	0.78	0.77	s		
k3	Bandai	37.5633	139.9798	31.81	0.0	42	1.62	0.59	0.73	s		
l	Takahara	36.8478	139.7620	28.10	0.0	80	0.49	0.53	0.79	s		
m	Hakuba	36.8134	137.7986	38.49	0.0	85	0.77	0.84	0.66	s		
n1	Tateyama	36.6189	137.5500	30.19	0.5	20	1.01	0.61	0.89	s		
n2	Tateyama	36.6222	137.5607	32.06	0.5	18	2.18	0.51	0.57	s		
n3	Tateyama	36.6204	137.5536	34.16	0.5	15	0.83	0.54	0.64	s		
o	Yakedake	36.2601	137.5483	22.81	0.4	47	0.74	0.60	0.42	p	172	7
p	Mt. Fuji	35.3846	138.7439	15.53	0.9	69	3.30	0.75	0.71	s		
q	Hakone	35.2787	139.0115	22.50	0.5	58	0.87	0.60	0.45	p	-54	16
r1	N. Osaka Bay	34.4944	135.1228	25.52	0.4	24	0.44	0.28	0.86	l	-165	88
r2	N. Osaka Bay	34.4970	135.1322	25.44	0.4	22	0.46	0.45	0.60	l	-91	80
s	S. Osaka Bay	34.3931	135.1702	29.56	-	37	0.31	0.75	0.63	s		
t	E. Shimane	35.2676	133.2654	30.36	1.2	41	1.42	0.23	0.88	l	23	37
u	Kirishima	31.9060	130.9239	22.63	0.3	86	2.37	0.32	0.76	l	-20	75
v	Sakurajima	31.5671	130.6384	27.36	0.7	56	0.87	0.54	0.67	s		

The lengths r_1 , r_2 , and r_3 are the radii of estimated oblique spherical cluster shape in three principal axis directions. θ and ϕ are the azimuth and dip of the principal symmetry axis of the cluster, respectively, which is the lineation direction for linear clusters and the plane-normal direction for planar clusters.

Magnitude threshold is also shown in Table 2.1. To systematically relocate events at all regions without arbitrary choice of data, we use nationwide borehole seismogram network Hi-net, which is deployed relatively homogeneously using same seismogram. We used closest 30–40 Hi-net stations in each region. As a velocity structure, we adopted JMA 1D structure as shown in Figure 2.2 to keep consistency with the travel time calculation by JMA. Although the JMA assumes S-wave velocity as independent value with P-wave velocity, we used $v_s = v_p / \sqrt{3}$, but the difference is slight. The relocation of relative location is less sensitive to the shallower structure rather than that of absolute location.

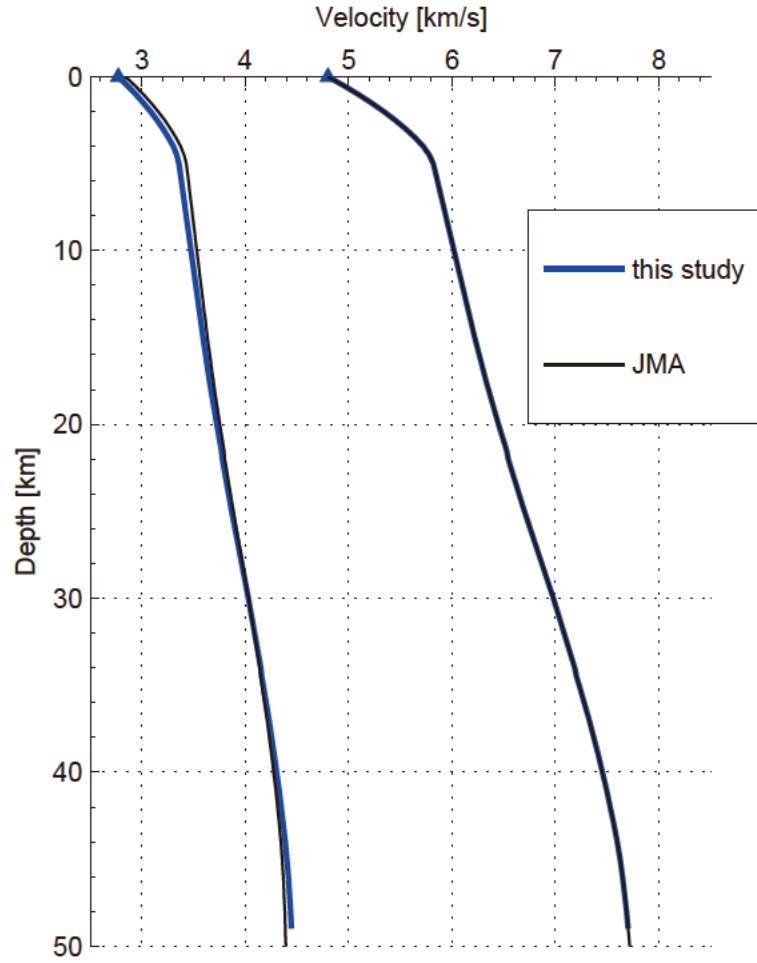


Figure 2.2 Velocity structure used in this study

P- and S-wave velocities are shown. Blue lines represent the structure used in the present study and black lines represent the structure used by JMA. The velocities at the surface in this study are also indicated as blue triangles.

2.1.3. Results

Obtained cluster of relocated hypocenters is shown in Figure 2.3. Multiple clusters were found in Tokachi, Bnadai, Tateyama, and N. Osaka Bay, and we extracted 28 clusters among 22 regions. In most regions cluster shapes up to several kilometers are determined with uncertainties of most events less than 500m except Mutsu-Hiuchi, where the coverage of stations is not good.

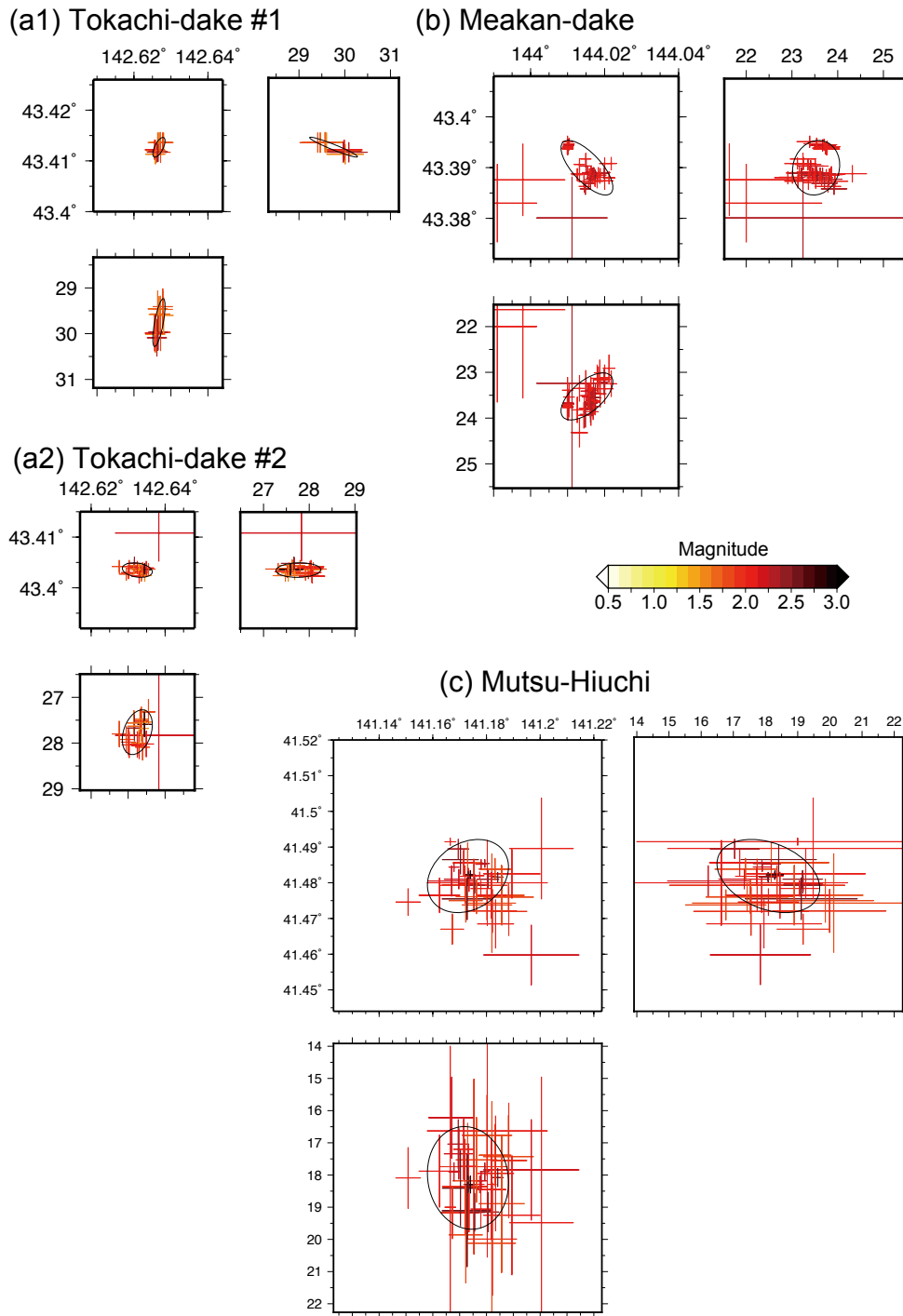


Figure 2.3 Relocated hypocenters in 28 major clusters of volcanic DLPs

Relocated hypocenters in each cluster are shown in a map view and in latitudinal and longitudinal cross sections. Color dots represent relocated DLPs (the color indicates the magnitude), and color lines represent their estimation errors. Black lines represent the determined cluster shape. The spatial scale is common except for (c). (a1) Tokachi-dake #1 (a2) Tokachi-dake #2 (b) Meakan-dake (c) Mutsu-Hiuchi

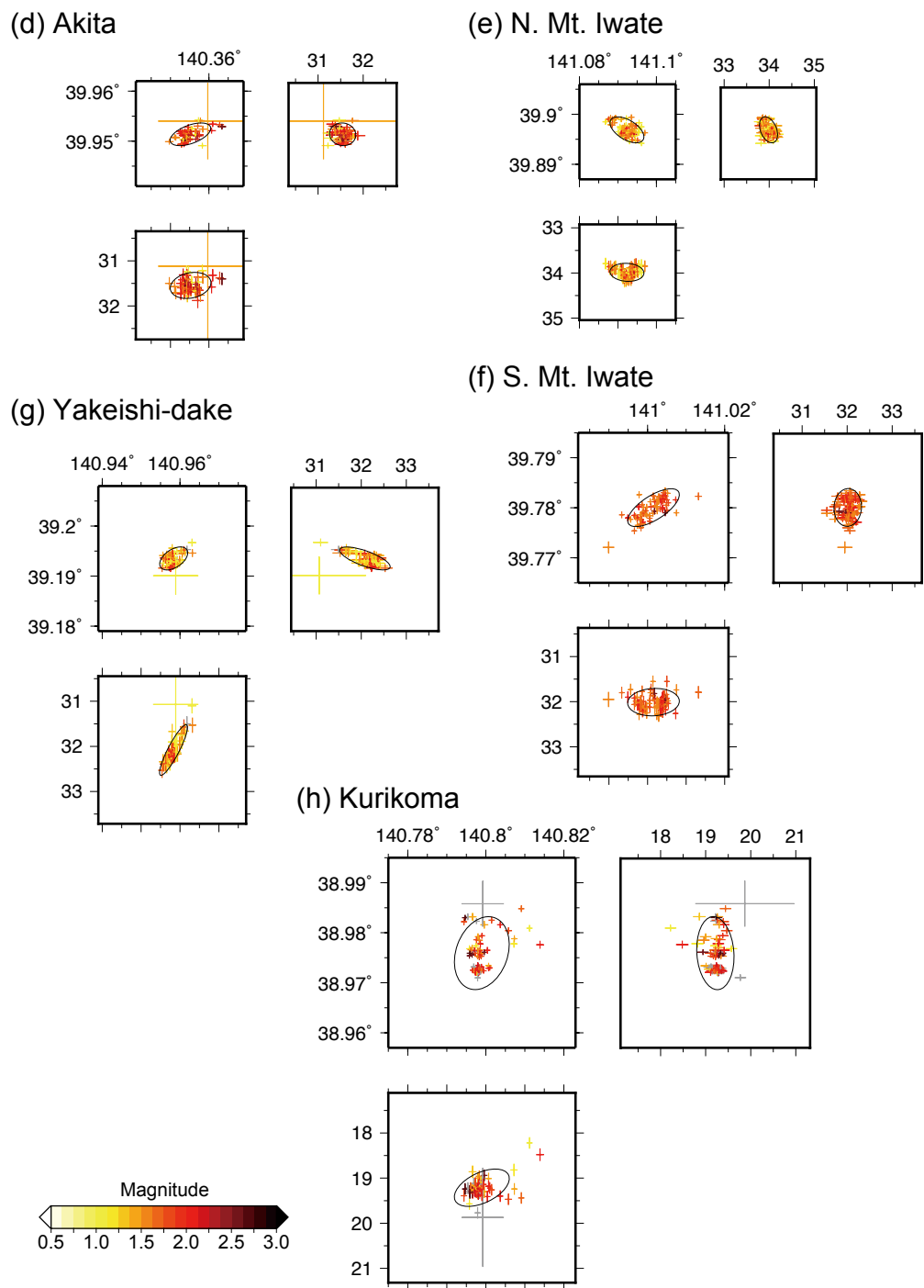


Figure 2.3 Relocated hypocenters in 28 major clusters of volcanic DLPs (continued)

(d) Akita (e) N. Mt. Iwate (f) S. Mt. Iwate (g) Yakeishi-dake (h) Kurikoma

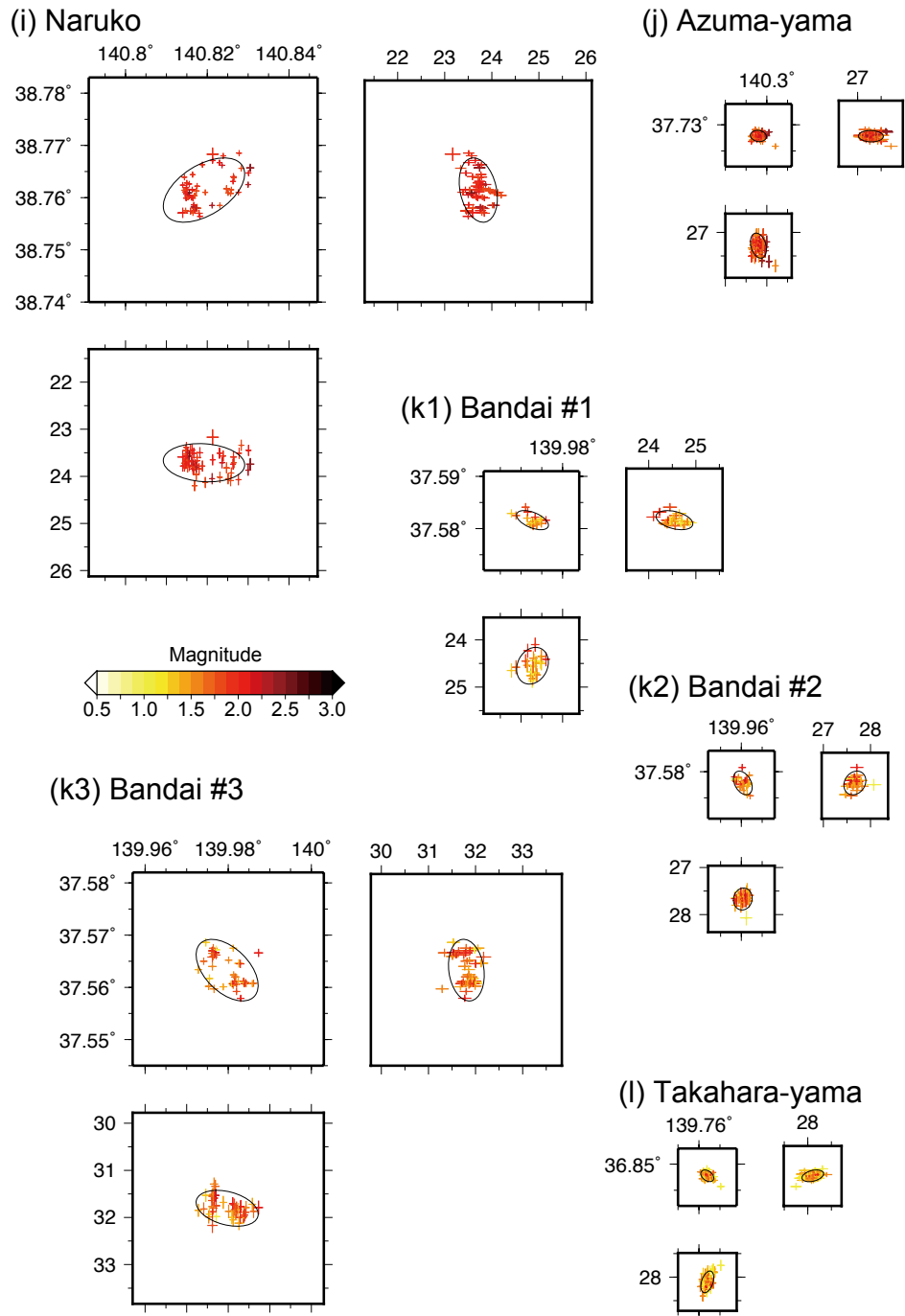


Figure 2.3 Relocated hypocenters in 28 major clusters of volcanic DLPs (continued)

(i) Naruko (j) Azuma-yama (k1) Bandai #1 (k2) Bandai #2 (k3) Bandai #3 (l) Takahara-yama

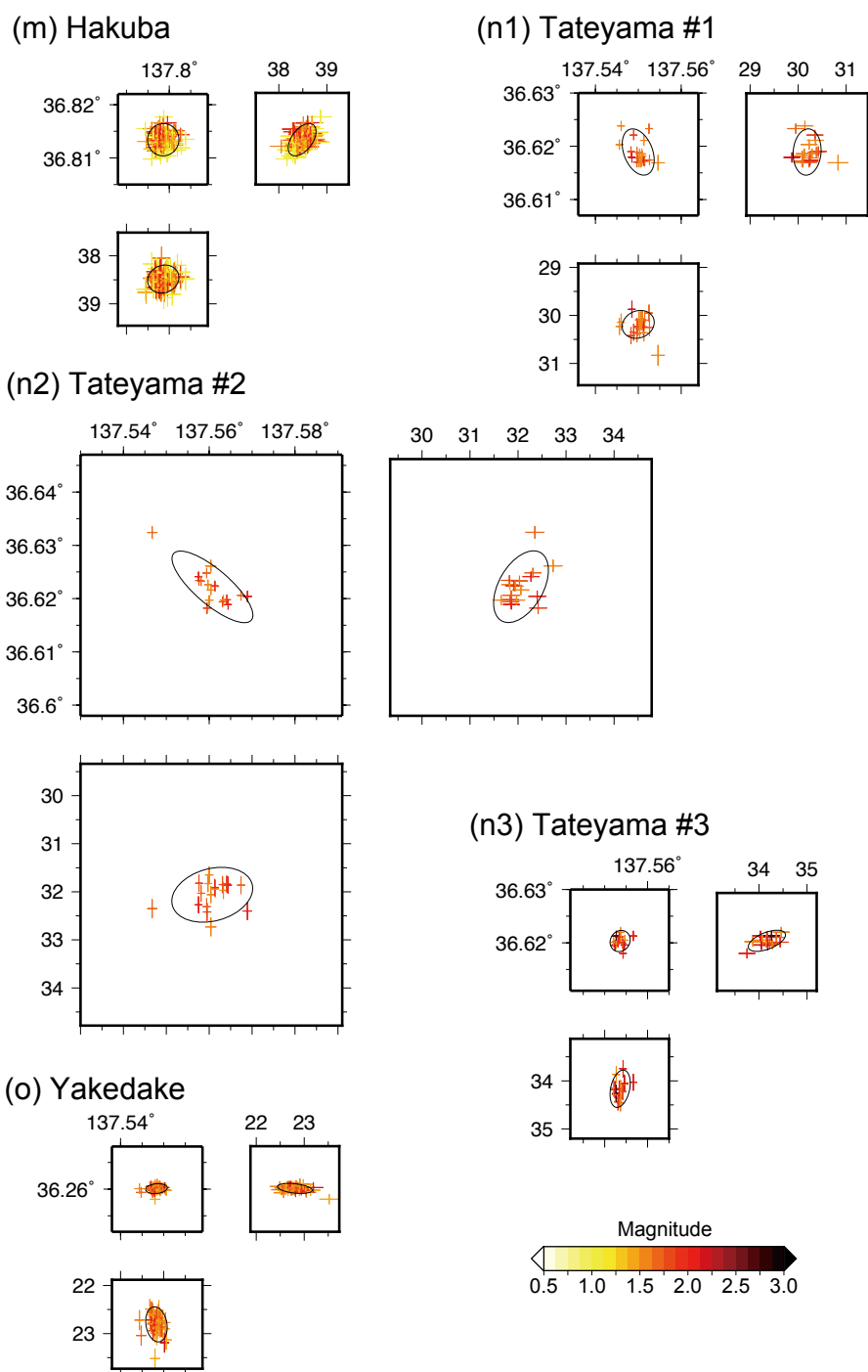
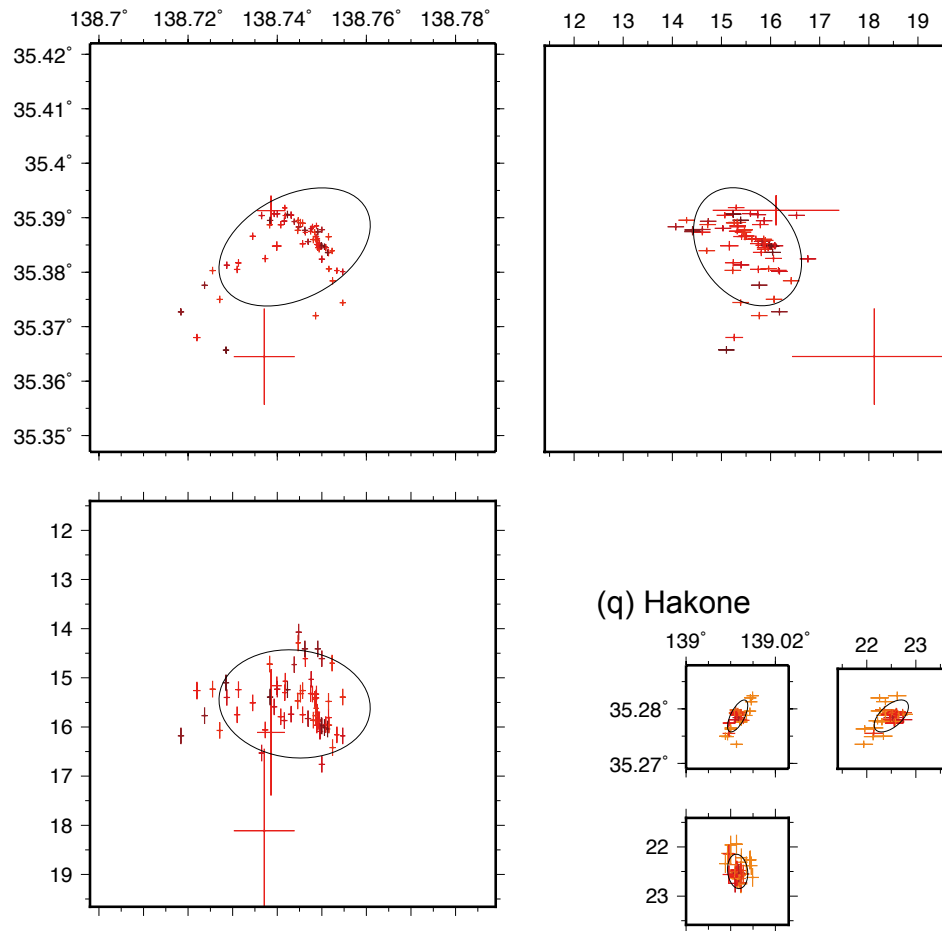


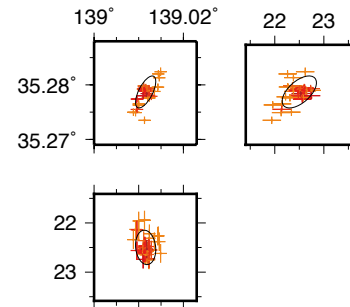
Figure 2.3 Relocated hypocenters in 28 major clusters of volcanic DLPs (continued)

(m) Hakuba (n1) Tateyama #1 (n2) Tateyama #2 (n3) Tateyama #3 (o) Yakedake

(p) Mt. Fuji

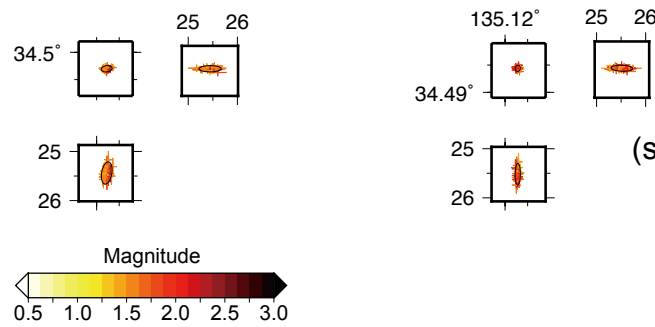


(q) Hakone



(r1) N. Osaka Bay #1

(r2) N. Osaka Bay #2



(s) S. Osaka Bay

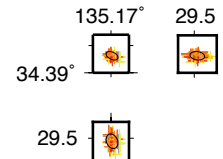


Figure 2.3 Relocated hypocenters in 28 major clusters of volcanic DLPs (continued)

(p) Mt. Fuji (q) Hakone (r1) N. Osaka Bay #1 (r2) N. Osaka Bay #2 (s) S. Osaka Bay

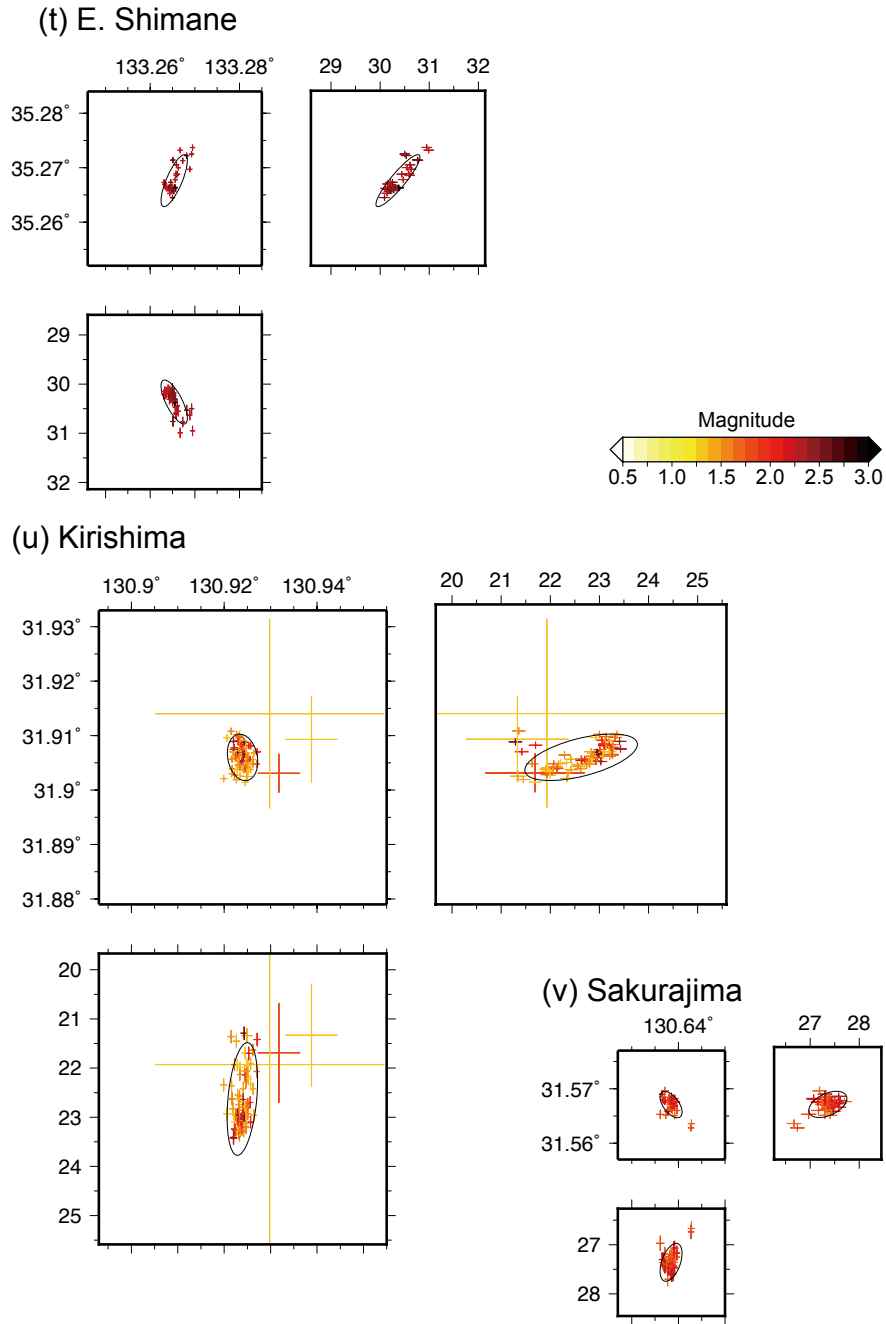


Figure 2.3 Relocated hypocenters in 28 major clusters of volcanic DLPs (continued)

(t) E. Shimane (u) Kirishima (v) Sakura-jima

For each cluster we estimated spherical shape (Figure 2.3) by least square method (Appendix A2 and Figure 2.4). Parameters for the relocated cluster shape are also shown in Table 2.1. Classification of the shape whether linear, planar, or spherical is based on the ratios of diameters of

spheroid (Figure 2.4). Among 28 clusters, clear lineation was found in Tokachi cluster #1, S. Mt. Iwate, Yakeishi, N. Osaka Bay clusters #1 and #2, E. Shimane, and Kirishima. Planar structure was found in Meakan, Bandai cluster #1, Yakedake, and Hakone. Surprisingly, there were less planar clusters than linear clusters although magma intrusion is often regarded as planar. Especially clear lineation was found in E. Shimane and Kirishima. To compare with previous work, we also focus on the DLPs in S. Mt. Iwate, where *Nakamichi et al.* [2003] obtained various focal mechanisms. As a planar cluster we focus on Yakedake. We therefore conduct source inversion in these four regions.

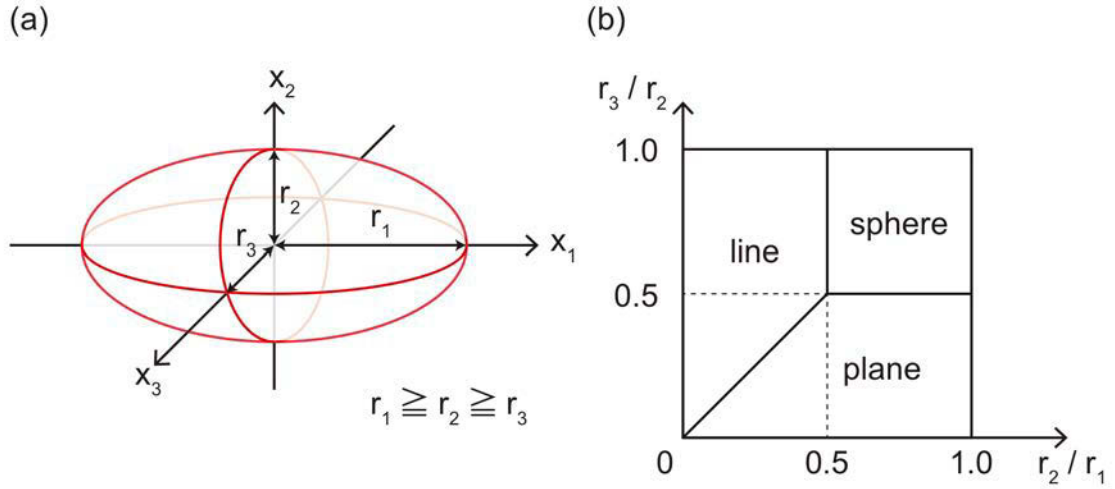


Figure 2.4 Cluster shape recognition

(a) Schematics of cluster shape approximated by an oblique sphere. (b) Categorization of cluster shape using the ratios among radii in three principal axes.

2.2. Source Inversion

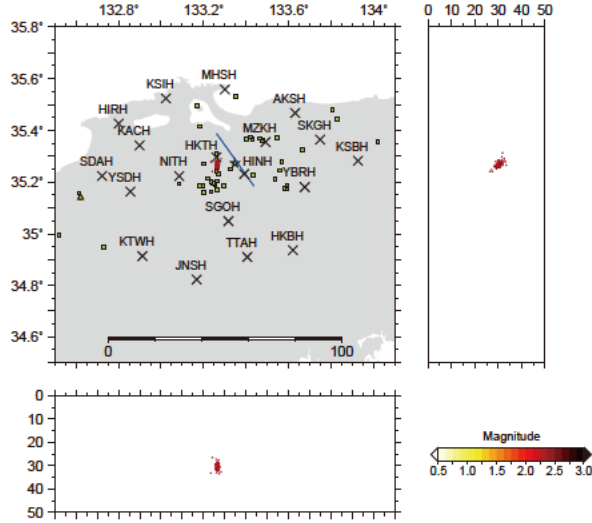
We estimate source process of DLP events in E. Shimane, Kirishima, S. Mt. Iwate, and Yakedake where cluster shape is clearly found to be linear or planar. DLPs in E. Shimane is located beneath the 50 km-wide Yokota Quaternary volcanic cluster and is also close to the fault plane of the 2000 western Tottori earthquake. Kirishima located at the south Kyushu region is one of the most active volcanoes in Japan and a major eruption occurred in January 2011 at the summit Shinmoe-dake. These events locate within several kilometers from the summit. Mt. Iwate in the Tohoku region is also regarded as an active volcano by JMA but we only observe fumarolic gasses there currently. The DLPs we focus on are the events located 10 km south of the summit of Mt. Iwate. Yakedake in the central Japan is an active volcano that recorded many phreatic explosions in the last century and the fumarolic activity is currently still high. The DLPs are within 10 km from the summit of Yakedake.

2.2.1. Data

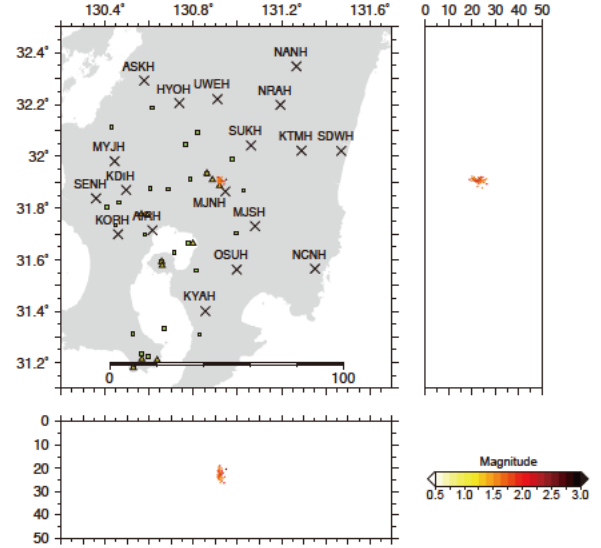
We analyze DLP events already detected by JMA during the 12.5-year period from June 2002 to October 2014. Since larger events generally have high S/N waveforms, we only analyze events with JMA magnitude $M_{\text{JMA}} \geq 1.2$ in E. Shimane, $M_{\text{JMA}} \geq 0.5$ in Kirishima, $M_{\text{JMA}} \geq 0.8$ in S. Mt. Iwate, and $M_{\text{JMA}} \geq 0.6$ in Yakedake. The events at S. Mt. Iwate are the largest cluster “DLFA” in *Nakamichi et al.* [2003].

Before working on inversions, we again applied source relocation of the same algorithm as before but using the event sets for the source inversions. We call this process as the second relocation to compare with the first relocation in 22 regions. The only differences are event set and data source. We used only continuous record in the first relocation but we use both event record and continuous record in the second relocation. This enables analyses during a longer time period, so we increased the magnitude threshold. Station maps for the second relocation is shown in Figure 2.5. Similar shapes are reproduced (Figure 2.6) except for a slight difference of depth variation in S. Mt. Iwate. In S. Mt. Iwate, the ratios of r_3/r_2 and r_2/r_1 got closer values and this cluster might be planar rather than linear. We therefore consider both possibilities in the discussion part. We use this result of the second relocation to compare with the obtained source mechanisms.

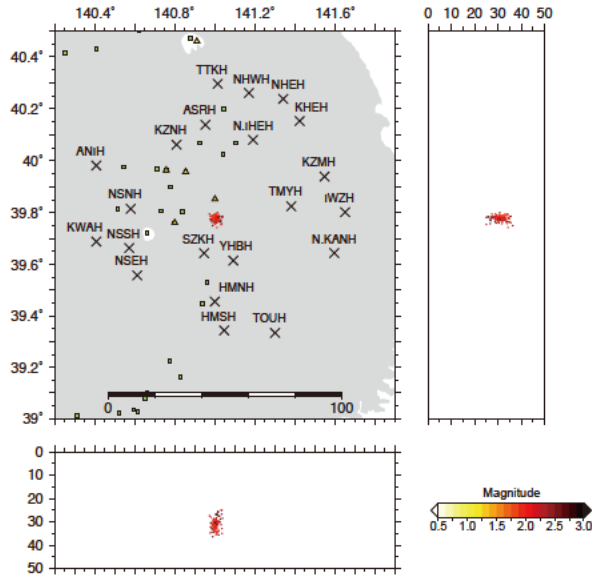
(a) E. Shimane



(b) Kirishima



(c) S. Mt. Iwate



(d) Yakedake

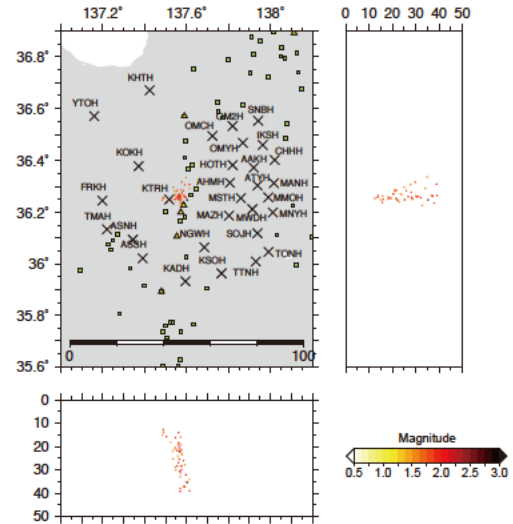


Figure 2.5 Station distribution for second relocation of volcanic DLPs

Stations used in relocation are shown by crosses with station names. Original hypocenter of JMA is shown by dots, whose color is coded by magnitude. Green squares and red triangles show Quaternary volcanoes [Committee for Catalog of Quaternary Volcanoes in Japan, 1999] and active volcanoes, respectively. (a) E. Shimane. The estimated extent of source area of the 2000 western Tottori earthquake [Fukuyama et al., 2003] is shown by a blue line with the hypocenter shown by a star. (b) Kirishima. (c) S. Mt. Iwate. (d) Yakedake.

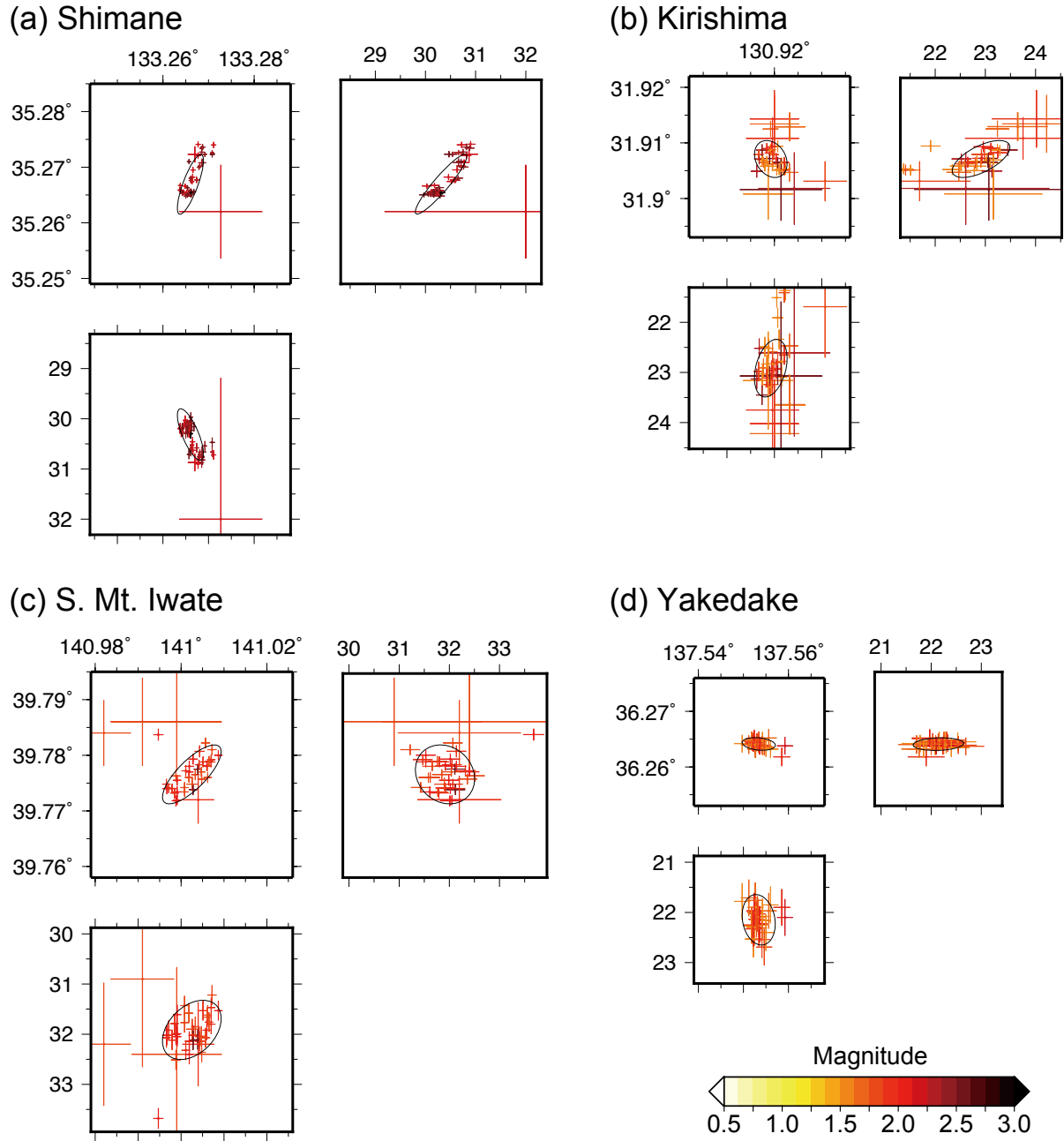


Figure 2.6 Results of second relocation of volcanic DLPs

Relocated hypocenters in each cluster are shown by dots, whose color is coded by magnitude, in a map view and in latitudinal and longitudinal cross sections. Color lines represent their estimation errors. Red lines represent the determined cluster shape. (a) E. Shimane. (b) Kirishima. (c) S. Mt. Iwate. (d) Yakedake.

To systematically analyze events at all regions without arbitrary choice of data, we use nationwide borehole seismogram network Hi-net, which is deployed relatively homogeneously using the same seismometers. We used three-component velocity seismograms at a sampling rate of 100 Hz

at the closest eight stations from the epicenter of a DLP in each region (Figure 2.7). We analyzed all events recorded by at least five stations. The analyzed events that satisfy these criteria are listed in Table 2.2–Table 2.5.

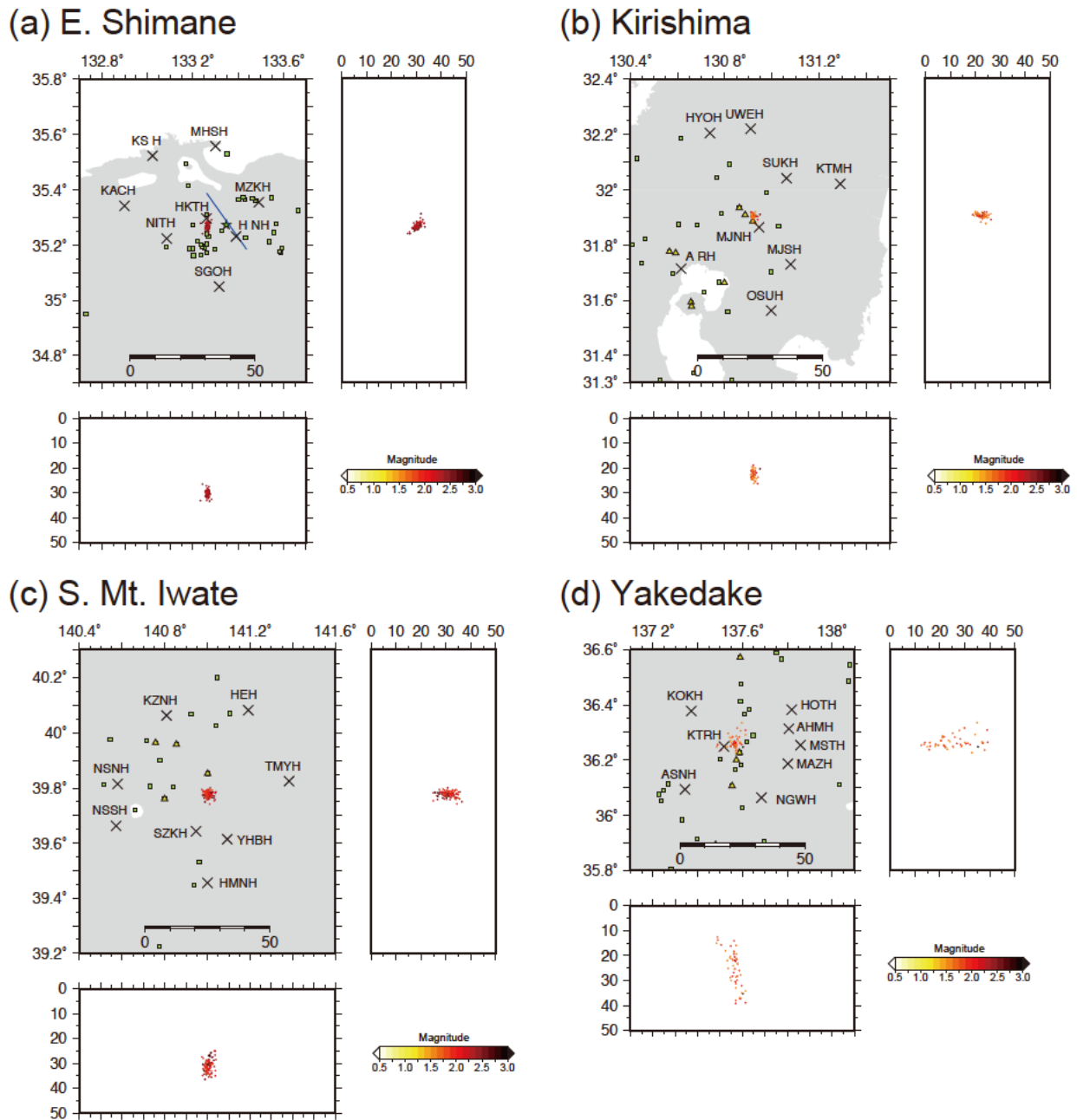


Figure 2.7 Station maps for source inversion

Spatial distribution of the DLPs and the Hi-net stations used in the source inversion process are shown in a map view and in latitudinal and longitudinal cross-sections. All DLPs occurred from June 2000 to October 2014 are plotted by color dots, whose color represents magnitude. Crosses show Hi-net stations used in the present study. Green squares and red triangles show Quaternary volcanoes [Committee for Catalog of Quaternary Volcanoes in Japan, 1999]

and active volcanoes, respectively. (a) E. Shimane. The estimated extent of source area of the 2000 western Tottori earthquake [*Fukuyama et al.*, 2003] is shown by a blue line with the hypocenter shown by a star. (b) Kirishima. (c) S. Mt. Iwate. (d) Yakedake.

Table 2.2 Analyzed events for source mechanisms in E. Shimane

Event ID	Year	Month	Day	Hour	Min	Sec	M _{JMA}	VR
#01	2002	7	19	3	40	36.97	1.3	33.3
#02	2002	7	19	3	40	45.47	1.6	13.5
#03	2002	8	29	23	56	31.14	1.2	12.7
#04	2003	4	22	12	15	58.36	1.4	14.3
#05	2003	4	22	12	16	27.19	1.4	5.8
#06	2003	4	22	14	1	18.75	1.4	11.0
#07	2003	4	22	14	34	43.96	1.2	3.5
#08	2003	4	22	19	25	40.39	1.2	5.5
#09	2003	4	23	3	9	50.59	1.2	23.0
#10	2003	12	24	11	54	46.26	1.2	14.8
#11	2004	7	17	10	46	2.32	1.3	20.4
#12	2005	3	27	5	27	55.99	1.4	4.3
#13	2005	3	27	7	5	59.73	1.2	12.2
#14	2005	4	23	15	46	52.27	1.4	17.0
#15	2005	4	23	15	46	58.58	1.2	3.6
#16	2005	4	23	15	47	2.50	1.2	9.3
#17	2005	7	25	6	19	12.04	1.4	16.7
#18	2005	9	4	1	46	53.66	1.3	7.3
#19	2005	9	4	1	49	14.98	1.2	16.6
#20	2006	1	24	9	28	15.51	1.2	8.7
#21	2006	1	24	9	28	20.52	1.2	6.2
#22	2006	1	24	9	29	9.38	1.3	3.6
#23	2006	4	13	7	51	25.16	1.6	5.7
#24	2006	5	17	3	6	5.81	2.1	21.5
#25	2006	5	17	5	16	16.11	1.2	11.4
#26	2006	8	8	12	19	14.84	1.5	15.2
#27	2006	8	20	6	11	4.97	1.4	4.6
#28	2006	8	20	6	11	29.39	1.4	6.2
#29	2006	8	21	12	45	13.83	1.4	26.0
#30	2006	8	21	12	46	25.00	1.5	11.5
#31	2007	1	3	8	47	57.66	1.2	2.4
#32	2007	3	11	1	46	40.85	1.5	8.4
#33	2007	4	8	14	50	7.12	1.2	15.9
#34	2007	4	9	9	9	6.01	1.6	19.4
#35	2007	4	9	9	9	31.93	1.6	7.4
#36	2007	7	2	14	11	6.62	1.2	10.8
#37	2007	7	2	14	27	55.85	1.2	1.5
#38	2008	2	24	8	37	9.46	1.3	1.0
#39	2008	3	11	12	56	43.42	1.2	8.1
#40	2008	8	28	16	23	52.71	1.3	7.4
#41	2008	9	8	5	29	33.05	1.5	15.8
#42	2008	9	8	5	29	39.70	1.4	5.9
#43	2008	12	26	11	31	41.48	1.2	2.6
#44	2009	3	11	3	47	25.50	1.4	32.4
#45	2009	3	13	8	16	47.68	1.2	3.8
#46	2009	3	29	10	5	40.03	1.5	8.6
#47	2009	5	20	1	29	44.80	1.3	10.1
#48	2010	9	19	5	7	17.04	1.4	23.7
#49	2011	4	10	14	1	33.48	1.3	29.8
#50	2011	11	1	23	33	40.32	1.2	10.8
#51	2013	2	4	19	34	41.73	1.3	4.0

Table 2.3 Analyzed events for source mechanisms in Kirishima

Event ID	Year	Month	Day	Hour	Min	Sec	M _{JMA}	VR
#01	2003	3	4	7	55	51.02	0.8	8.4
#02	2003	10	24	20	9	4.52	0.5	6.1
#03	2004	7	12	21	6	8.88	0.8	3.1
#04	2004	7	12	21	6	41.08	1.5	15.2
#05	2004	7	12	21	6	58.17	1.1	7.1
#06	2004	7	12	21	9	20.54	1.3	2.4
#07	2004	7	12	21	10	11.58	1.6	16.1
#08	2004	7	12	21	11	11.14	1.0	5.4
#09	2004	7	14	4	16	48.79	0.7	11.9
#10	2004	10	14	12	54	47.67	0.5	0.8
#11	2005	1	11	2	14	58.36	0.6	5.2
#12	2005	1	11	2	18	7.55	0.5	2.9
#13	2005	1	11	2	18	19.27	1.1	3.3
#14	2005	7	1	23	57	21.87	0.7	6.5
#15	2005	9	13	18	39	58.56	0.8	8.0
#16	2007	3	29	4	34	17.98	0.6	1.3
#17	2007	3	29	4	35	3.36	1.5	30.8
#18	2007	3	29	4	41	30.72	0.9	14.1
#19	2007	3	29	4	41	46.35	1.3	2.2
#20	2008	5	20	7	27	51.78	1.0	26.2
#21	2008	5	20	7	32	51.30	0.9	8.1
#22	2010	2	10	6	28	22.30	0.5	0.1
#23	2010	8	2	6	11	17.07	1.3	12.5
#24	2010	8	5	11	27	0.98	0.6	2.7
#25	2010	8	7	21	56	26.40	0.6	0.9
#26	2010	8	14	20	5	11.17	0.7	1.2
#27	2010	12	27	7	39	4.14	1.4	15.0
#28	2011	4	26	18	28	22.12	0.9	10.9
#29	2011	6	3	22	0	33.08	0.5	6.2
#30	2011	6	3	22	0	49.77	0.6	13.7
#31	2011	6	4	15	11	8.25	0.7	5.7
#32	2011	9	9	14	42	45.01	0.8	2.2
#33	2011	9	9	14	43	40.19	0.9	3.6
#34	2011	10	2	15	5	46.23	0.8	7.2
#35	2011	10	2	15	8	56.04	0.5	8.6
#36	2011	11	1	22	46	58.66	0.7	3.0
#37	2011	11	7	19	25	39.20	0.5	4.3
#38	2012	3	23	15	8	25.70	0.5	3.1
#39	2012	3	23	15	9	25.08	0.8	4.9
#40	2012	5	23	19	56	12.43	0.9	7.6
#41	2012	11	7	14	14	0.75	0.6	3.8
#42	2012	12	19	10	23	1.75	0.5	2.0
#43	2013	1	28	16	13	44.97	0.6	1.0
#44	2013	1	28	16	16	13.25	0.6	0.2
#45	2013	2	17	7	49	46.97	0.7	7.7
#46	2013	9	23	6	5	5.08	0.6	5.4
#47	2013	10	13	23	52	38.96	0.5	4.1
#48	2014	3	9	0	7	42.51	0.5	2.8

Table 2.4 Analyzed events for source mechanisms in S. Mt. Iwate

Event ID	Year	Month	Day	Hour	Min	Sec	M _{JMA}	VR
#01	2002	6	28	4	45	27.32	1.0	18.6
#02	2002	6	28	4	45	53.91	1.1	8.2
#03	2002	11	2	20	41	54.45	0.8	2.5
#04	2002	11	18	12	40	43.79	0.8	3.2
#05	2003	7	24	3	10	38.87	0.9	1.8
#06	2004	2	28	18	1	36.59	0.8	9.8
#07	2004	4	19	23	26	47.67	1.0	22.9
#08	2004	5	3	7	21	25.32	0.9	15.8
#09	2004	12	12	5	48	55.54	0.8	3.1
#10	2005	2	2	23	20	53.68	0.9	1.7
#11	2005	2	22	0	14	36.95	1.5	3.9
#12	2005	2	22	6	6	25.92	1.5	12.4
#13	2005	4	11	6	56	57.67	0.9	1.3
#14	2005	5	10	15	52	20.97	0.9	2.3
#15	2005	9	14	5	47	29.57	0.9	1.8
#16	2006	6	2	13	51	33.09	0.8	2.9
#17	2006	6	8	3	24	40.34	0.8	1.0
#18	2006	6	8	16	43	11.16	0.8	3.9
#19	2006	6	13	6	13	17.30	0.8	2.1
#20	2007	1	8	13	53	29.11	1.1	18.3
#21	2007	7	16	4	40	31.47	1.0	3.0
#22	2007	9	5	3	57	42.81	0.8	33.2
#23	2007	12	10	7	26	59.72	1.0	7.5
#24	2008	3	9	12	7	54.34	0.8	7.2
#25	2008	4	25	2	24	29.25	1.1	8.2
#26	2008	6	5	21	35	33.32	1.0	5.2
#27	2009	3	9	12	3	53.48	0.8	13.3
#28	2009	12	5	14	4	19.82	0.9	2.9
#29	2010	6	4	16	25	3.23	0.8	1.1
#30	2010	9	1	12	45	24.05	0.9	2.3
#31	2010	9	10	6	30	33.07	0.8	19.9
#32	2010	11	29	0	18	41.04	0.9	3.8
#33	2011	1	4	19	6	1.85	0.9	9.5
#34	2011	1	17	2	44	50.74	1.0	0.6
#35	2011	6	25	20	51	52.70	1.0	3.2
#36	2011	10	29	2	4	48.44	0.9	4.5
#37	2011	12	24	19	49	50.50	0.8	13.1
#38	2012	10	1	7	33	4.33	1.0	0.9
#39	2013	11	13	20	28	38.12	0.8	15.3
#40	2013	11	19	23	53	27.41	0.9	12.6
#41	2014	4	28	13	0	38.65	0.9	4.1

Table 2.5 Analyzed events for source mechanisms in Yakedake

Event ID	Year	Month	Day	Hour	Min	Sec	M _{JMA}	VR
#01	2004	2	12	14	1	22.36	0.7	17.5
#02	2004	4	6	2	7	31.53	0.6	19.4
#03	2004	4	10	14	49	40.29	0.7	40.7
#04	2004	4	21	17	23	56.61	0.6	7.8
#05	2004	5	13	10	40	29.78	0.7	24.6
#06	2004	5	13	10	42	17.99	1.0	16.4
#07	2004	9	7	5	36	50.83	0.8	5.0
#08	2004	12	16	18	49	18.93	0.8	3.7
#09	2004	12	16	22	13	23.49	0.6	27.0
#10	2004	12	16	22	14	20.85	0.6	10.3
#11	2004	12	16	23	7	34.33	0.8	23.3
#12	2004	12	16	23	8	28.93	0.8	21.4
#13	2004	12	16	23	11	12.19	0.6	18.2
#14	2004	12	31	18	56	39.07	0.6	17.7
#15	2005	1	19	0	2	36.95	0.6	21.1
#16	2005	1	19	0	33	19.24	0.6	19.2
#17	2005	1	19	2	6	56.90	0.6	10.3
#18	2005	1	31	6	44	12.00	0.8	20.5
#19	2005	2	5	20	5	2.11	0.7	9.7
#20	2005	2	14	18	38	49.53	0.9	6.7
#21	2006	3	18	23	3	50.15	0.6	32.2
#22	2006	12	17	20	46	20.41	0.7	0.6
#23	2007	9	13	1	37	32.65	1.0	1.6
#24	2009	3	10	22	6	3.86	0.6	17.8
#25	2009	3	10	22	9	26.30	0.7	8.9
#26	2009	3	10	22	9	35.03	0.7	25.2
#27	2009	5	20	17	4	56.45	0.6	1.5
#28	2009	8	15	12	9	33.16	0.6	1.4
#29	2011	8	3	9	27	16.66	1.0	1.6
#30	2011	10	31	18	22	59.86	0.9	2.3
#31	2011	11	12	6	33	14.84	0.7	8.1
#32	2012	4	4	23	42	5.04	1.0	6.3
#33	2013	12	6	9	50	44.13	1.0	5.5
#34	2013	12	20	12	9	28.64	1.2	15.6
#35	2014	5	6	7	3	17.00	0.9	9.4

For the calculation of theoretical waveforms and travel times, we adopted the horizontally layered structure of P-wave velocity used by JMA as shown in Figure 2.2, which is identical to the structure used in relocation. Although the JMA assumes S-wave velocity as independent value with P-wave velocity, we used $v_s = v_p/\sqrt{3}$ because we assume the orthogonality of P- and S-waves. These two cases are not so different (Figure 2.8). We set the density of each layer following the relationship of *Brocher* [2005] such as

$$\rho = 1.6612v_p - 0.4721v_p^2 + 0.0671v_p^3 - 0.0043v_p^4 + 0.000106v_p^5, \quad (2.5)$$

where density is ρ [g/cm³] and P-wave velocity is v_p [km/s]. For P-wave quality factor Q_p and S-wave quality factor Q_s , we used simple assumption of

$$Q_P = (v_P - 3.00) \times 200 \quad (2.6)$$

$$Q_S = (v_P - 3.00) \times 100. \quad (2.7)$$

This structure has no systematic difference with the structure used by the local Tottori observatory operated by Kyoto University [Horikawa *et al.*, 2001; Pulido and Dalguer, 2009] (Figure 2.8).

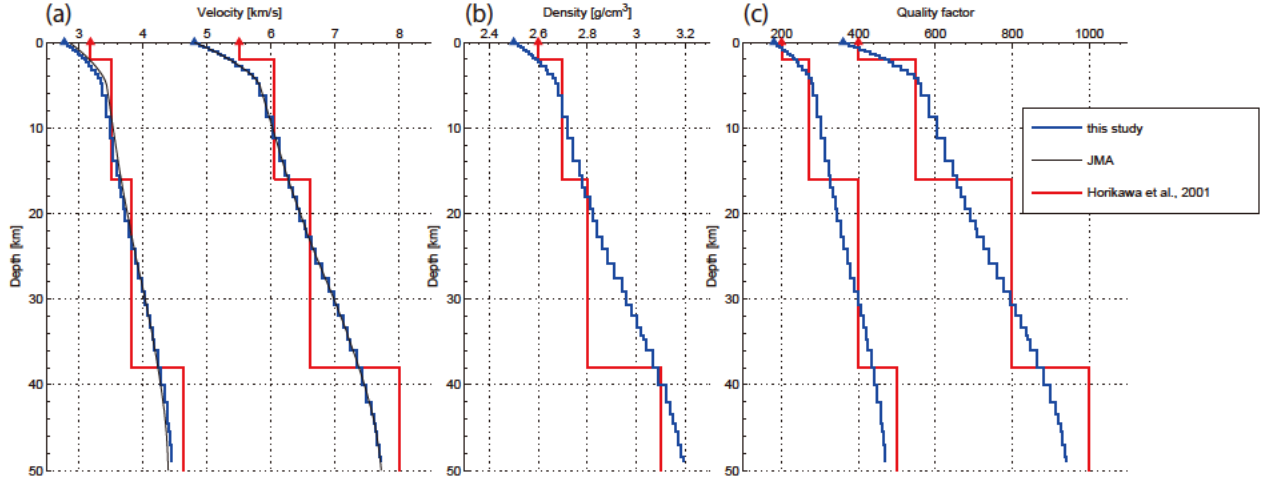


Figure 2.8 Structure for calculating Green's function

The seismic structure of velocity, density, and quality factor that was used in the present study for calculating Green's function. Blue lines represent the structure used in the present study, black lines represent the structure used by JMA, and red lines represents the structure used at the local Tottori Observatory, Kyoto Univ. [Horikawa *et al.*, 2001]. The values at the surface in this study are also shown as triangles. (a) P- and S-wave velocities. (b) Density. (c) P- and S-wave quality factors.

Although it is difficult to reproduce observed waveform from such simplified structure completely, the monochromatic waveforms allow us to neglect frequency dependent response and the waveforms of ~ 2 Hz are mainly sensitive to the structure at several kilometers. Considering an angular wavenumber of ~ 3 rad/km and a travel distance of ~ 30 km, the effect of scattering starts to contaminate the waveform produced assuming ray theoretical approximation [Aki and Richards, 1980]. Therefore, we have to care about the validity of using simple structure. Since the analysis of similar spectral range with similar hypocentral distance have been done successfully for tectonic LFEs, scattering effect does not necessarily spoil all information in time domain and we expect similar applicability for volcanic DLPs too. Practically, we try to extract source mechanism from the early phases of the waveforms with less scattering effects using Green function considering attenuation effects. In the future, considering the scattering effect quantitatively as a 3-D problem would help us to extract further information correctly.

The theoretical Green function in the horizontally layered structure with inelastic attenuation [Ide and Takeo, 1997] is calculated by the method that Takeo [1985] developed by introducing complex velocities to reflection-transmission matrices [Kennet and Kerry, 1979] and the discrete wavenumber integration method [Bouchon, 1981]. The wavenumber domain of integration was between $1/300 \text{ km}^{-1}$ and $999/300 \text{ km}^{-1}$.

2.2.2. Inversion Method

We estimate source process at a point source. We basically need to estimate moment tensor at each time step during the source duration, and therefore the number of model parameters tends to be large because we need to estimate 6 parameters for each moment tensor at each time step. Since we now only have limited available stations, it is difficult to solve such large number of model parameters stably from small number of data. Aso and Ide [2014] assumed that moment tensor has a common orientation at every time step and only their amplitude changes during the source duration within negative to positive values. This technique greatly reduces the number of model parameters and this assumption is acceptable for such small event with short duration. However, its inversion problem is non-linear and they combined grid search for the constant moment tensor orientation and linear inversion for the scalar source function, which results in long calculation time. Another difficulty in the previous method is that results highly depend on the picked arrivals because of their harmonic waveforms, but the detection of arrivals is not easy because of unclear onsets especially for S-waves. It is also difficult to read the polarities at the onset, maximum moment rate, or final moment because the source function starts gradually and oscillates harmonically.

To overcome these difficulties, we try to estimate the source function at first in the present study. Once the source function is obtained, inversion is reduced to a simple linear problem to determine six parameters of the moment tensor. If each calculation can be done quickly, it is also possible to run multiple inversions using alternative sets of arrival times. Since the temporal discretization of the source function is as high as original seismograph, it might be also possible to resolve the polarity of initial fracture even if the source is oscillating.

2.2.2.1. Estimating Source Function

First, we stack all waveforms at every station in every direction for phases of P- and S-waves to obtain source function. The similarity of all these velocity waveforms is supported from observed data (Figure 2.9) and is also expected from the theory of Green's function as $u(t) \propto \ddot{M}(t - \tau)$ neglecting scattering effects [Aki and Richards, 2002].

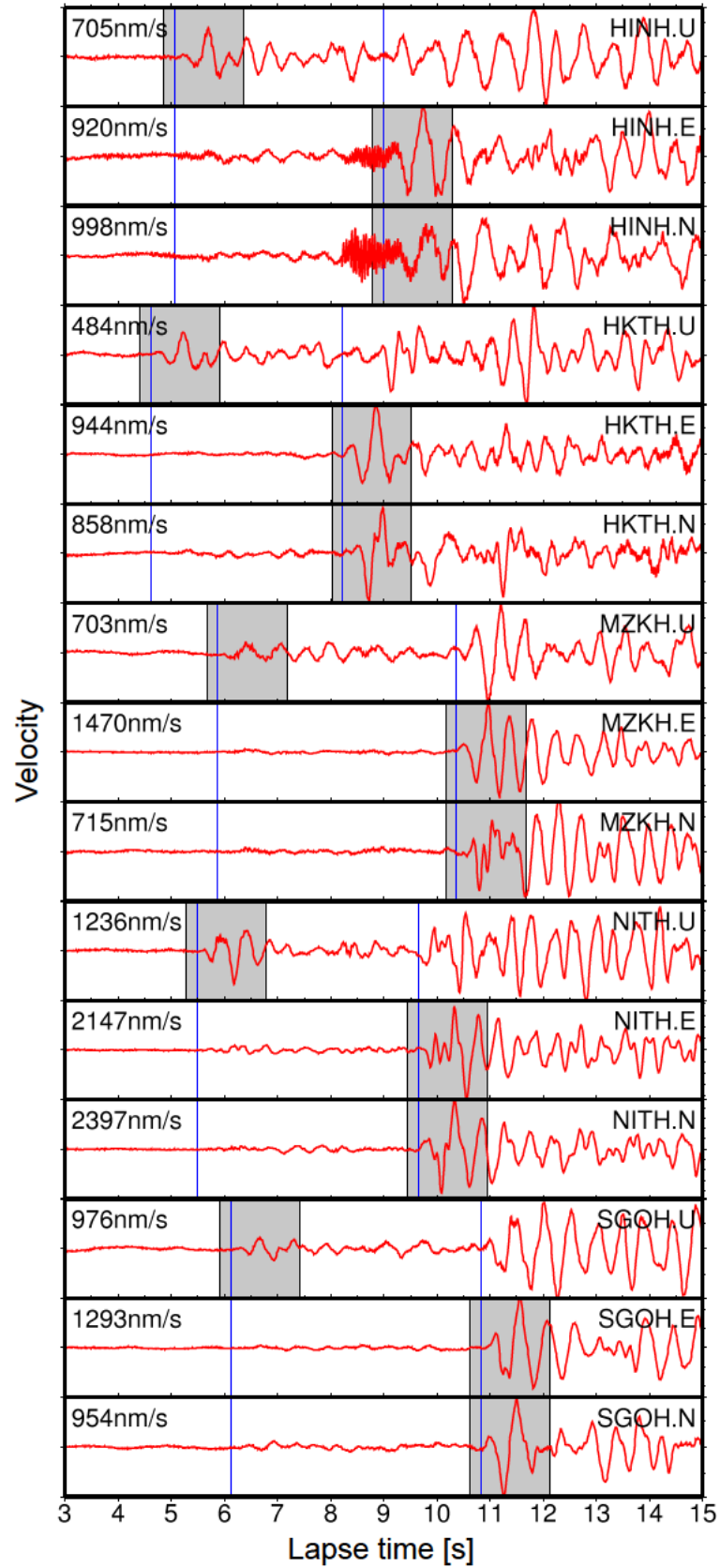


Figure 2.9 Representative waveforms in E. Shimane

The representative velocity waveforms of the DLP #01 in E. Shimane that occurred at 03:40:36 on July 19th, 2002 (JST) are shown versus the time elapsed from the event origin

time. Vertical black lines show P- and S-wave arrivals and the windows used for the best solution are shown by gray shades. About 8 seconds after the event, another event (#02) can be seen.

We first calculate 1.5-s stacked waveforms for every possible master waveform (stations, three components, and phases of P and S). For fixed arrivals, the staking with the master of j -th channel is expressed as:

$$\mathbb{v}_j = \sum_i^{nch} \langle \mathbb{w}_i | \mathbb{w}_j \rangle \times \mathbb{w}_i, \quad (2.8)$$

where $\langle \rangle$ represents cross correlation. The weight of cross correlation corrects waveforms to have common polarity and also gives higher priorities on more similar events. We allow arrival time difference of target events as:

$$\mathbb{v}_j = \sum_i^{nch} \langle \mathbb{w}_i(t_{ij}^{ccmax}) | \mathbb{w}_j \rangle \times \mathbb{w}_i(t_{ij}^{ccmax}), \quad (2.9)$$

where

$$\max_t \langle \mathbb{w}_i(t) | \mathbb{w}_j \rangle = \langle \mathbb{w}_i(t_{ij}^{ccmax}) | \mathbb{w}_j \rangle. \quad (2.10)$$

We also allow arrival time difference of master event as:

$$\mathbb{v}_j = \max_{\tau} \left[\sum_i^{nch} \langle \mathbb{w}_i(t_{ij}^{ccmax}(\tau)) | \mathbb{w}_j(\tau) \rangle \times \mathbb{w}_i(t_{ij}^{ccmax}(\tau)) \right], \quad (2.11)$$

so that

$$\max_t \langle \mathbb{w}_i(t) | \mathbb{w}_j(\tau) \rangle = \langle \mathbb{w}_i(t_{ij}^{ccmax}(\tau)) | \mathbb{w}_j(\tau) \rangle. \quad (2.12)$$

In the present study, we find the maximum within $-0.25 \leq \tau [s] \leq 0.25$.

Then, we find an onset t_{j0} within each stacked waveform to maximize

$$amp_j(t_0) = \int_{t_0}^{t_0+1.0} [v_j(t)]^2 dt / \int_{t_0-0.5}^{t_0} [v_j(t)]^2 dt \xrightarrow[t_0 \rightarrow t_{j0}]{} max. \quad (2.13)$$

Among obtained stacked waveform for every master, we use the waveform $v_{jbest}(t_{jbest0})$ that have sharp onset so that

$$amp_j(t_{j0}) \xrightarrow[j \rightarrow jbest]{} max. \quad (2.14)$$

We adopt this waveform is the common shape of signal at every channel and assume this is a source acceleration function $\ddot{M}(t)$.

2.2.2.2. Detecting Arrival Times

Then, we obtain arrival times by fitting the stacked waveform to each channel (Figure 2.10). To quantify the fitness of the stacked waveform and waveforms of three components at i -th station for k -th phase (P or S), we use a root mean square of cross-correlation weighted by amplitudes:

$$R_{ik}(t) = \sqrt{\frac{\sum_{j=1}^3 (|\mathbb{W}_{ijk}(t)| \langle \mathbb{V} | \mathbb{W}_{ijk}(t) \rangle)^2}{\sum_{j=1}^3 |\mathbb{W}_{ijk}(t)|^2}}. \quad (2.15)$$

Although one may use an summation of absolute value such as

$$R_{ik}(t_k) = \sum_{i=U,E,N} |\langle \mathbb{V} | \mathbb{W}_{ijk}(t_k) \rangle|, \quad (2.16)$$

this is not a rotation invariant value and therefore we use (2.15) as a fitness function. By maximizing this value, onset can be determined for each station and phase. However, we add one more constraint that maximizes orthogonality of P- and S-waves:

$$T_i(t_P, t_S) = 1 - \left\langle \left(\begin{array}{c} \langle \mathbb{V} | \mathbb{W}_{iUP}(t_P) \rangle \\ \langle \mathbb{V} | \mathbb{W}_{iEP}(t_P) \rangle \\ \langle \mathbb{V} | \mathbb{W}_{iNP}(t_P) \rangle \end{array} \right) \middle| \left(\begin{array}{c} \langle \mathbb{V} | \mathbb{W}_{iUS}(t_S) \rangle \\ \langle \mathbb{V} | \mathbb{W}_{iES}(t_S) \rangle \\ \langle \mathbb{V} | \mathbb{W}_{iNS}(t_S) \rangle \end{array} \right) \right\rangle. \quad (2.17)$$

This orthogonality is not satisfied for reflected waves from the free surface. Such effect might be considerable for observed waveforms, but it is difficult to produce synthetic waveforms perfectly considering the effect of the free surface or heterogeneity. However, detecting P-waves is not as difficult as detecting S-waves because there is no preceding phase before P. Once the direct P-wave is correctly read, we therefore expect the direct S-wave can be extracted by searching for the motion perpendicular to the direct P-wave.

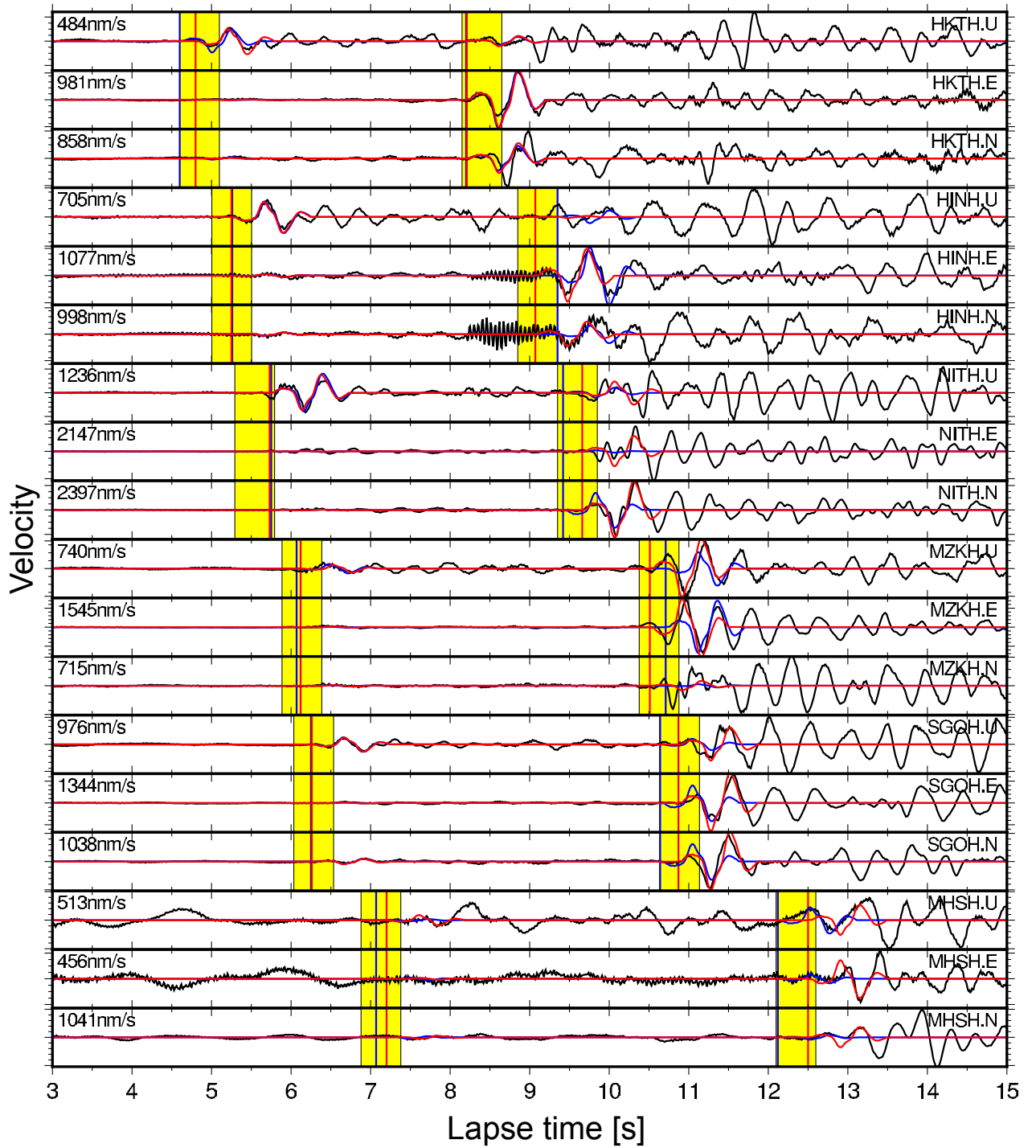


Figure 2.10 Stacked waveform and waveform fitting

Example of waveform fitting by the stacked waveform is shown for the representative event #01 in E. Shimane that occurred at 03:40:36 on July 19th, 2002 (JST). Black lines are the original waveform without any filtering and red and blue lines represent the first and second candidates of waveform fitting, respectively. Arrival times corresponding to the fits are also shown by vertical lines. Yellow time windows represent the time period searched for the best fittings.

Using the fitness functions and the orthogonality function after normalizing them to have a mean value of zero and a standard deviation of 1, we determine P- and S-arrivals simultaneously to maximize the summation of them:

$$E_i(t_P, t_S) = \tilde{R}_{iP}(t_P) + \tilde{R}_{iS}(t_S) + \tilde{T}_i(t_P, t_S) \rightarrow \max. \quad (2.18)$$

In the present study, we use either the first best set of P- and S-arrivals or the second best set in the inversion process. Among local maximums of the evaluate function $E_i(t_P, t_S)$, we first use the first largest case of $E_{i1} = E_i(t_{P1}, t_{S1})$. We also try to use the second largest case of $E_{i2} = E_i(t_{P2}, t_{S2})$ if the evaluate function is large $E_{i2} > 1.5$.

2.2.2.3. Moment Tensor Inversion

Using the source acceleration function obtained by stacking and arrival times obtained by fitting, we estimate the moment tensor. Although single forces are often assumed for earthquakes in volcanic regions [Kawakatsu, 1989; Ohminato *et al.*, 2006], we do not consider single forces because reaction force also radiates seismic waves at such depth. For each seismogram, we extracted a 1.2-second time window beginning 0.2 seconds before the arrival of either P-wave in a vertical component or S-wave in a horizontal component (Figure 2.9). We carry out multiple trials of inversions using either the first candidate set of arrivals or the second candidate at each station where the second candidate is available. Since we use eight stations, maximum trial number of linear inversions is $2^8=256$, which costs acceptable calculation time. Among these trials, we select the trial that gives the largest variance reduction (VR) as the final solution for the event.

While obtained source function can take both negative and positive values, we extract the initial source process at the first pulse of moment rate function that exceeds 10% of the maximum moment rate as a typical mechanism of the event (Figure 2.11).

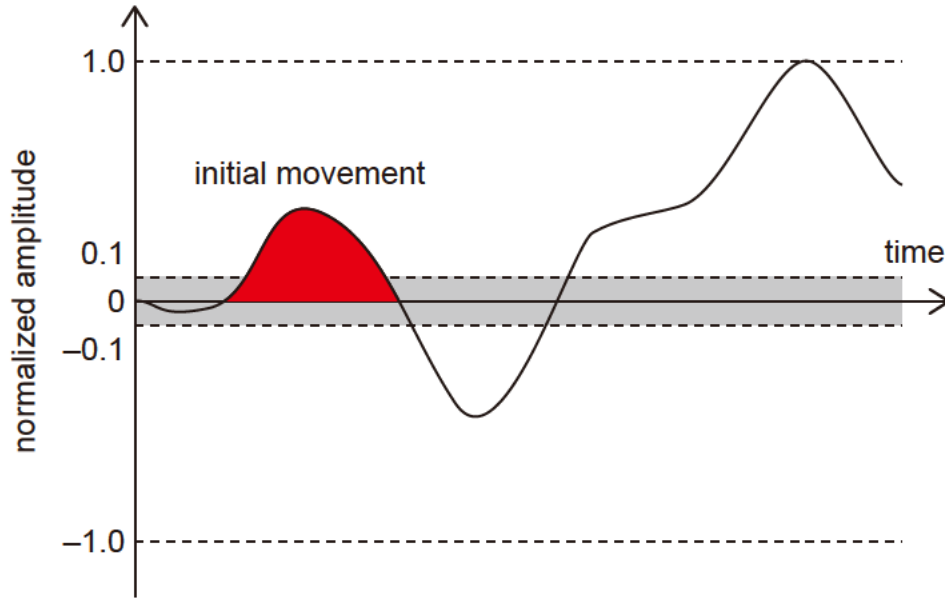


Figure 2.11 Recognition of the initial movement

Schematics to show the recognition process of the initial movements from the obtained source function. After normalization by the maximum absolute value, the first peak that exceeds amplitude of 0.1 is considered to be the initial movement.

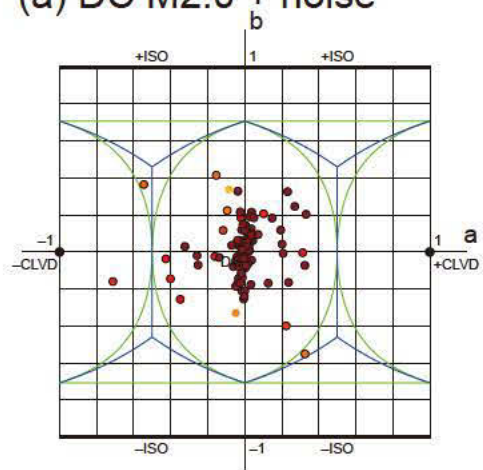
2.2.2.4. Synthetic Tests of Inversion

To confirm that this procedure of inversion can resolve the actual moment tensor, we carry out a synthetic test. Assuming double-couple events, we determine their source mechanisms from their synthetic waveforms that are composed by the theoretical seismogram and background noise. We use the station set in E. Shimane (Figure 2.7a) and the source location is assumed to be same as the event #01 in E. Shimane. The source function is identical to that determined by the following inversion for the event and the moment tensor is assumed to be the double-couple whose P-, N-, and T-axes are in NE-SW, vertical, and NW-SE directions, respectively. The structure to produce the synthetic waveforms is identical to that for inversion. For each of M2.0, M1.8, and M1.6 events, we produce synthetic waveforms composed by the theoretical waveform and background noise. As the background noise, we used the real seismograms that correspond to the 100 imaginary source origin times at every minutes during 00:00:00–01:39:00 on August 1st, 2004 (JST). As the seasonal variation of seismic noise is reported [e.g., *Stehly et al.*, 2006], it might be better to use noise from different seasons, but we use this period as one of the realistic noise in the present study for simplicity.

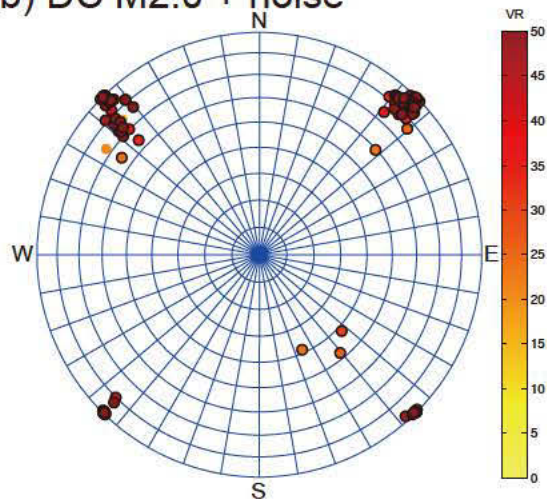
The results are shown in Figure 2.12. To visualize the source type, we used a new source type diagram developed in the Appendix A2. Even for M2.0 events, the artificial isotropic parts appeared while deviatoric parts are relatively well determined (Figure 2.12a). For this case, 70 events out of 100

had an isotropic component larger than the estimation error (1σ) of the linear inversion, which means they are recognized with a considerable isotropic component in the context of linear inversion. However, the estimation error is a square root of the corresponding diagonal component of model covariance matrix assuming all independent data follow unique normal distribution and the validity of using this estimate is arguable. Moreover, this isotropic component is rather artificial regarding that the actual signal is double-couple. To explain this apparent inconsistency, we need to consider the cause of errors.

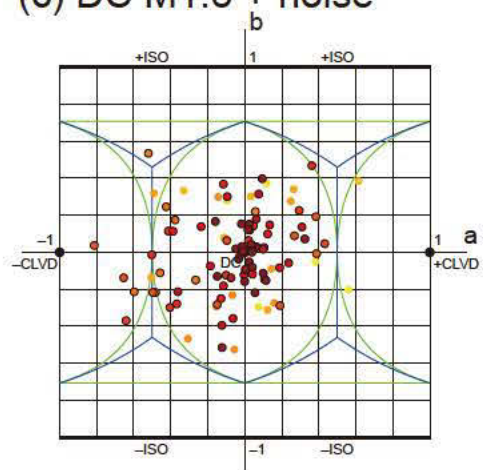
(a) DC M2.0 + noise



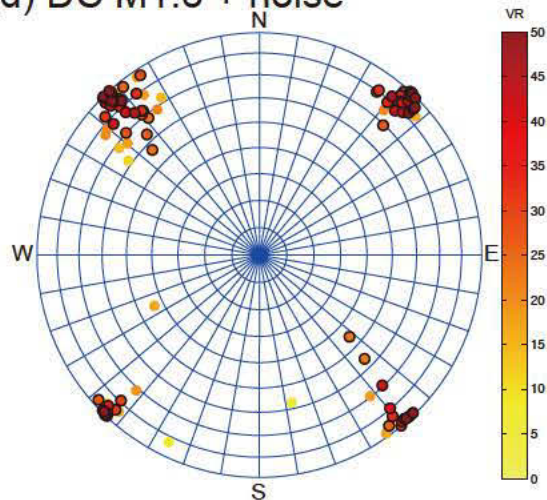
(b) DC M2.0 + noise



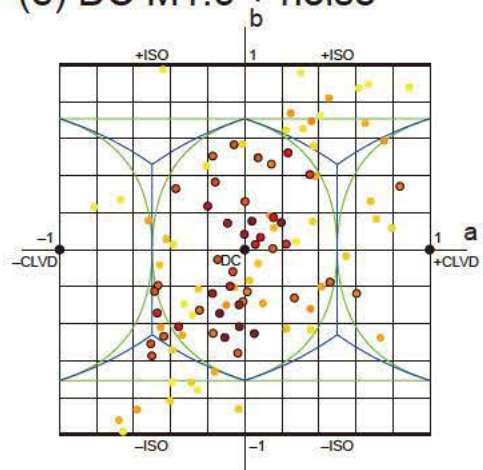
(c) DC M1.8 + noise



(d) DC M1.8 + noise



(e) DC M1.6 + noise



(f) DC M1.6 + noise

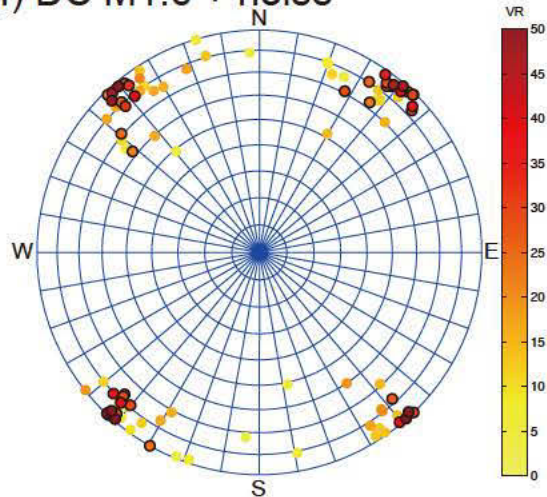


Figure 2.12 Synthetic test for DC events

The results of 100 synthetic double-couple (DC) events in E. Shimane that have seismic waveforms composed by a theoretical waveform and background noise are shown. Colors represent VR values. Solutions with $VR > 20\%$ are marked with thick outlines. (a) Synthetic M2.0 events on the source-type diagram newly developed in Appendix A2. The solid green lines are the area where double-couple (DC), compensated linear vector dipole (CLVD), and isotropic deformation (ISO) dominate. We refer to the source type as being dominated by one component when that component is larger than the other two combined. (b) The major symmetry axis of synthetic M2.0 events in the lower hemisphere. (c) Synthetic M1.8 events on the source-type diagram. (d) Major symmetry axis of synthetic M1.8 events on the polar plot. (e) Synthetic M1.6 events on the source-type diagram. (f) Major symmetry axis of synthetic M1.6 events on the polar plot.

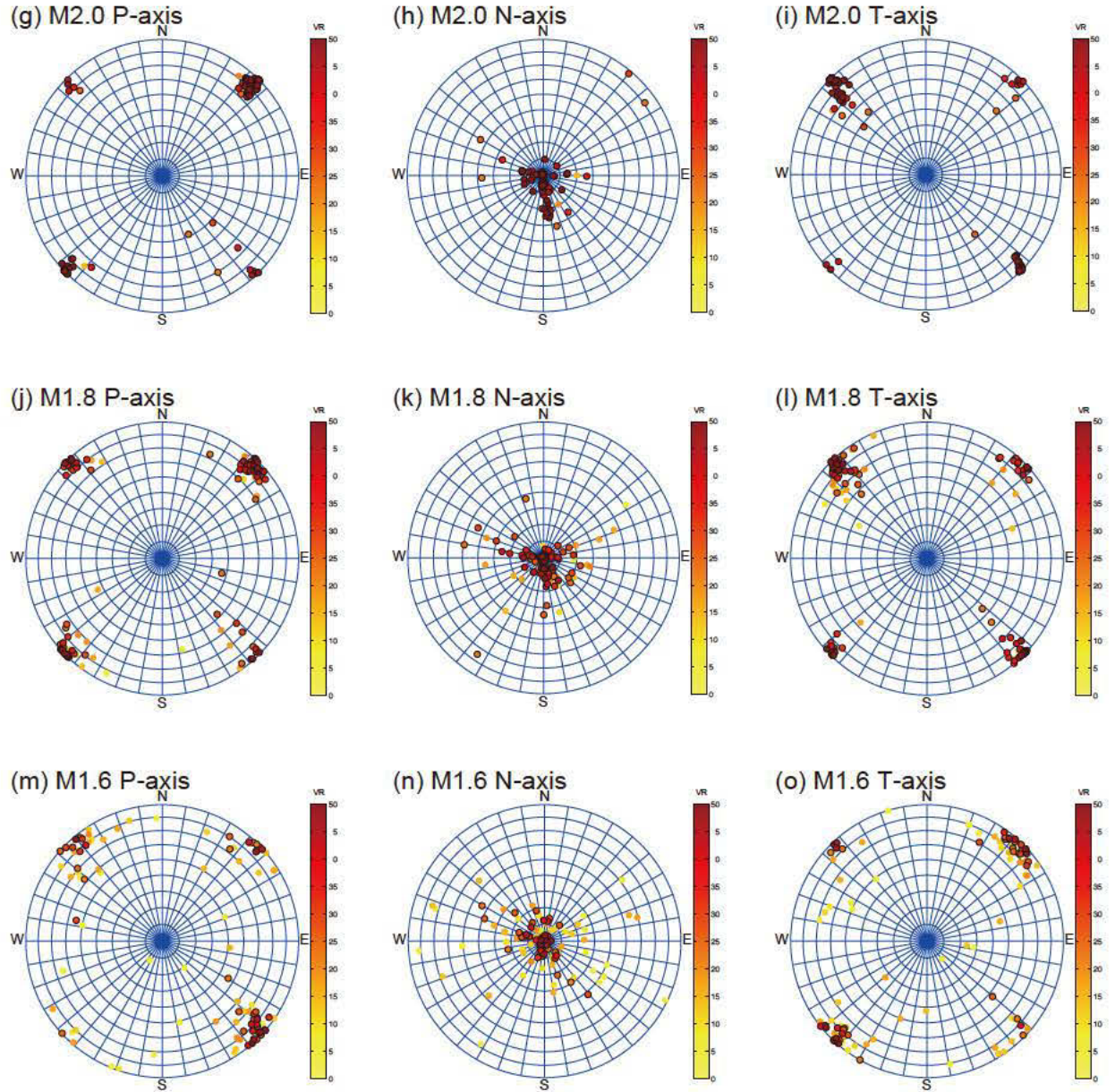


Figure 2.12 Synthetic test for DC events (continued)

(g) P-axis of the synthetic M2.0 DC events. (h) N-axis of the synthetic M2.0 DC events. (i) T-axis of the synthetic M2.0 DC events. (j) P-axis of the synthetic M1.8 DC events. (k) N-axis of the synthetic M1.8 DC events. (l) T-axis of the synthetic M1.8 DC events. (m) P-axis of the synthetic M1.6 DC events. (n) N-axis of the synthetic M1.6 DC events. (o) T-axis of the synthetic M1.6 DC events.

First, the estimation error of the linear inversion is important information, because it tells which parameter is easy to determine based on the synthetic waveforms corresponding to each parameter. For this case, the estimation error of isotropic component is 2.5–3.5 times larger than each double

couple component in the unit of scalar moment. This is basically because isotropic component appear only in P-wave while deviatoric components appear both in P- and S-waves and the P-wave amplitude is also smaller than the S-wave amplitude.

Even though the theoretical estimation error explained above is important, the linear inversion assumes all data are independent and follow unique normal distribution. The distribution of actual data is not so simple and also there are uncertainties in the model assumed for producing synthetic waveform. To consider all of these effects, empirical error estimation by analyzing numerous data using variety of synthetic waveforms under various assumptions is more important. In this case, the variety of isotropic component in Figure 2.12a comes from the data distribution because included background noise tends to produce high isotropic components as shown in Figure 2.18c and d. Owing to these multiple reasons, deviatoric components are determined better than isotropic components and the isotropic components are not reliable any more. Hence we focus more on deviatoric parts in the present study.

The effect of noise is larger in the cases of M1.8 or M1.6 because of small amplitudes of signal, but it is notable that most of the events with $VR > 20\%$ (96 out of 98 for M2.0, 73 out of 79 for M1.8, and 40 out of 44 for M1.6) are still within the DC-like range (Figure 2.12a, c and e). This means analyzing lots of events and looking at distribution of higher-VR events are important.

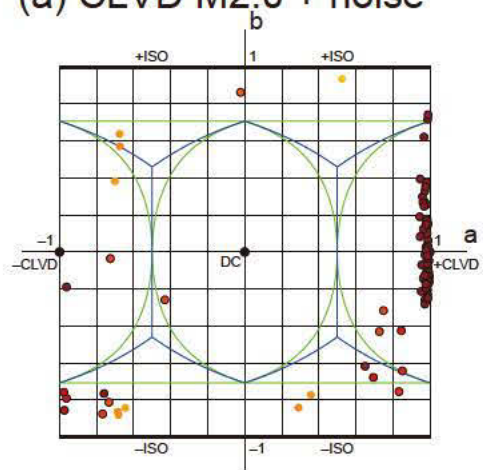
Another important characteristic of noise is its effect on the principal axes (Figure 2.12b, d, and f). Although noise fluctuates the symmetry axis (or principal axis) direction, it is still stably obtained in the NE-SW or NW-SE direction and no systematic inclination was observed, which again support the importance of analyzing lots of events. The stability of principal axes is also verified looking at the P, N, and T-axes (Figure 2.12g–o). For M2.0 events, P axis in NE and T axis in NW is correctly obtained for many cases, but completely opposite mechanism are also obtained. This bias is more strongly observed for smaller M1.8 or M1.6 events. This is because half-cycle skipping occurred at the recognition process of onset mechanism (Figure 2.11). The source function we used has different polarity between the onset mechanism and the maximum mechanism (Figure 2.14) but worse S/N results in inaccurate recognition of the onset mechanism at the maximum mechanism. This test result implies it is still difficult to discuss on the polarity of the focal mechanism in this inversion procedure. However, N-axis is stably obtained near vertically and each of P and T axes is in the NE-SW or NW-SE direction (typically $<10\text{--}20^\circ$), which means the orientation of deviatoric component is reproduced well except polarity information.

We also worked on the same test for CLVD mechanism assuming the +CLVD events whose symmetry axis in the N-S direction (Figure 2.13). We again confirm that the deviatoric component is determined better than the isotropic component and the isotropic component is not reliable. The orientation of major symmetry axis is stably obtained as in the N-S direction. The most notable thing in this test is that the obtained mechanism for smaller signal tends to be –CLVD although the input

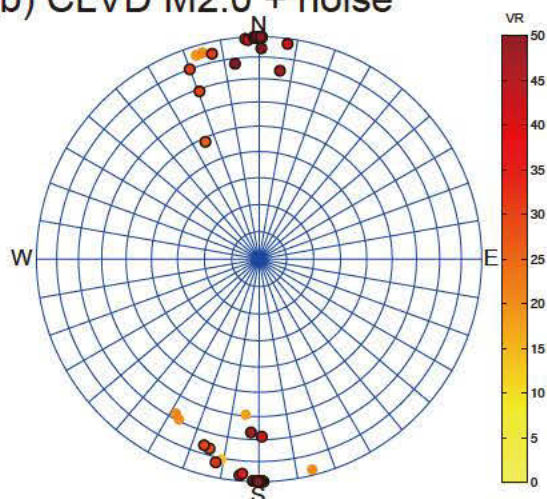
mechanism is +CLVD (Figure 2.13c and Figure 2.13e). This is because half-cycle skipping occurred at the recognition process of onset mechanism as well as the DC cases and the polarity is difficult to discuss in this inversion procedure. Because of this bias, the major symmetry axis corresponds to the P-axis for +CLVD-like M2.0 events but it corresponds to the T-axis for the –CLVD-like M1.6 events (Figure 2.13g–o). From the distribution of P, N, and T-axes, the other two axes different from the major symmetry axis are obtained nearly homogeneously within the plane perpendicular to the major symmetry axis.

Although it is difficult to discuss on isotropic component or the polarity of focal mechanism, the clear difference between Figure 2.12 and Figure 2.13 tells that deviatoric component can be resolved by focusing on the events with $VR > 20\%$. The orientations of principal axes are also stably obtained. Considering these test results, we focus on deviatoric components from the source type diagram and the orientation of major symmetry axis from the polar plot in the present study. The synthetic tests applied in E. Shimane are not necessarily applicable to other regions with different station distributions, but the index of VR is useful to quantify how well the data is explained by the synthetics and the threshold of $VR > 20\%$ looks acceptable to extract more reliable solutions, so we use $VR > 20\%$ as a criteria to extract information of real signal from large amount of data in any regions.

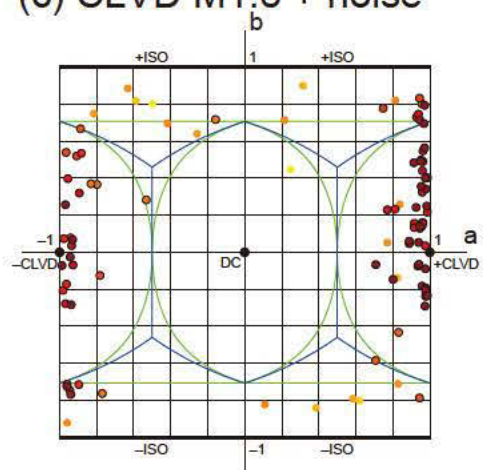
(a) CLVD M2.0 + noise



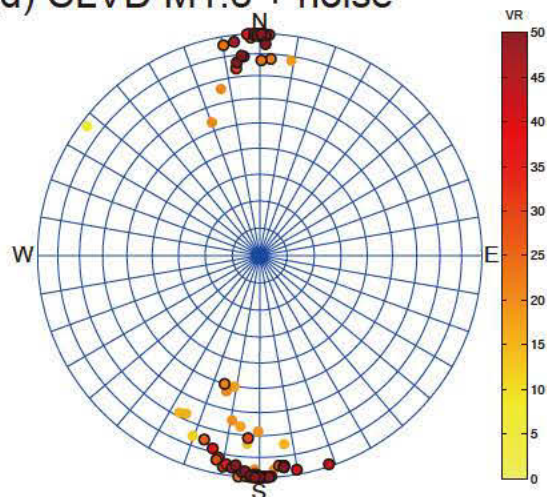
(b) CLVD M2.0 + noise



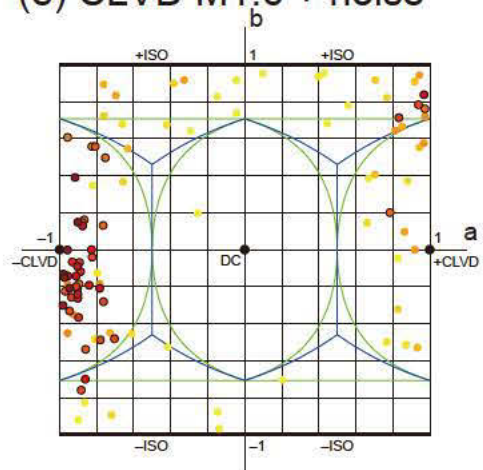
(c) CLVD M1.8 + noise



(d) CLVD M1.8 + noise



(e) CLVD M1.6 + noise



(f) CLVD M1.6 + noise

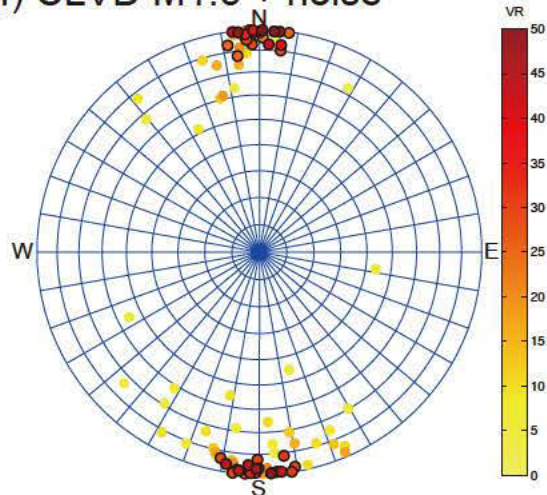


Figure 2.13 Synthetic test for CLVD events

The results of 100 synthetic CLVD events in E. Shimane that have seismic waveforms composed by a theoretical waveform and background noise are shown. Colors represent VR values. Solutions with $VR > 20\%$ are marked with thick outlines. (a) Synthetic M2.0 events on the source-type diagram newly developed in Appendix A2. The solid green lines are the area where double-couple (DC), compensated linear vector dipole (CLVD), and isotropic deformation (ISO) dominate. We refer to the source type as being dominated by one component when that component is larger than the other two combined. (b) The major symmetry axis of synthetic M2.0 events in the lower hemisphere. (c) Synthetic M1.8 events on the source-type diagram. (d) Major symmetry axis of synthetic M1.8 events on the polar plot. (e) Synthetic M1.6 events on the source-type diagram. (f) Major symmetry axis of synthetic M1.6 events on the polar plot.

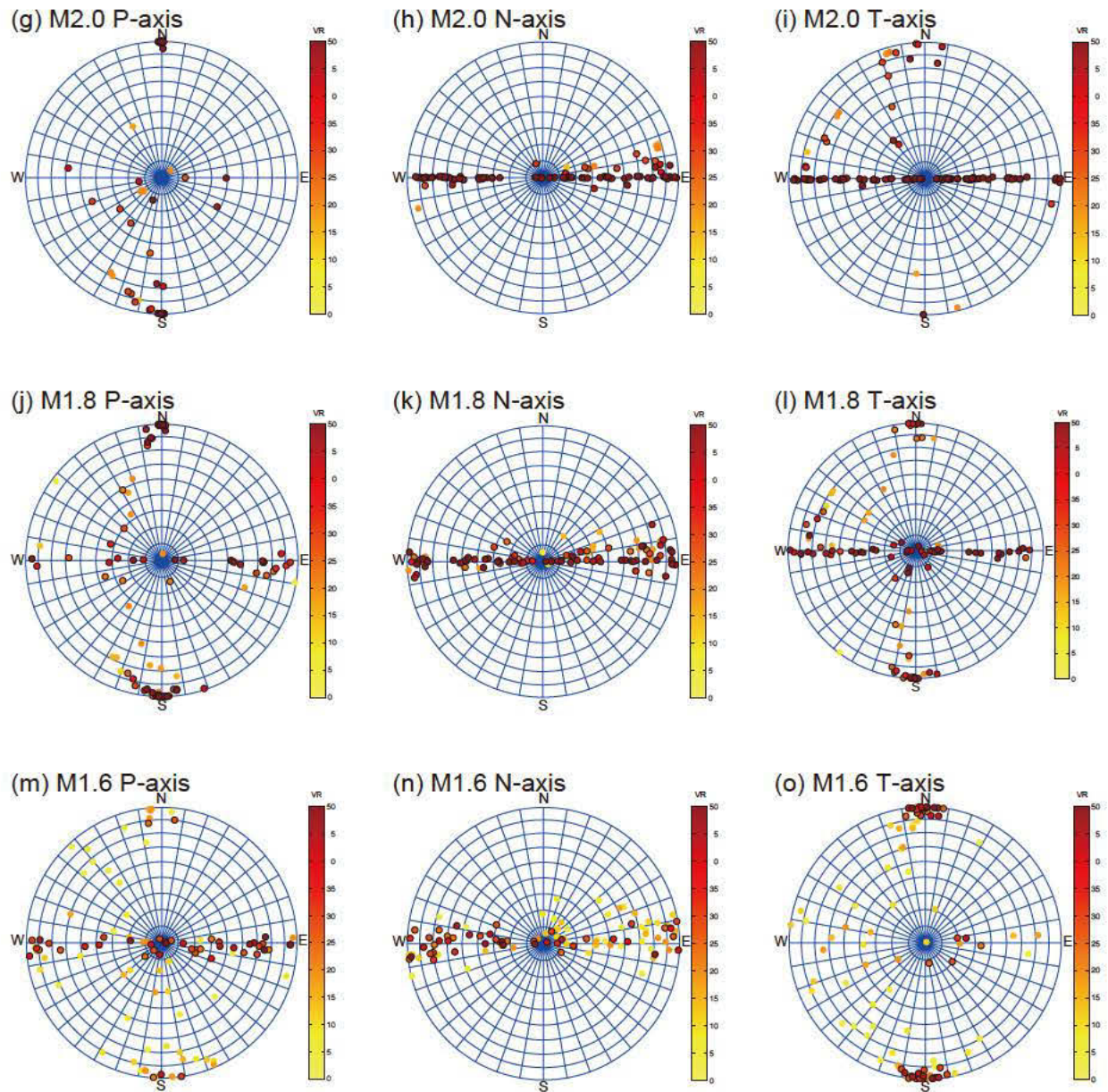


Figure 2.13 Synthetic test for CLVD events(continued)

(g) P-axis of the synthetic M2.0 CLVD events. (h) N-axis of the synthetic M2.0 CLVD events. (i) T-axis of the synthetic M2.0 CLVD events. (j) P-axis of the synthetic M1.8 CLVD events. (k) N-axis of the synthetic M1.8 CLVD events. (l) T-axis of the synthetic M1.8 CLVD events. (m) P-axis of the synthetic M1.6 CLVD events. (n) N-axis of the synthetic M1.6 CLVD events. (o) T-axis of the synthetic M1.6 CLVD events.

2.2.3. Results of Inversion

2.2.3.1. E. Shimane

In eastern Shimane, we obtained similar results of *Aso and Ide* [2014] and verified their results using slightly different inversion procedures. For each event, a scalar source function and a focal mechanism are obtained. Figure 2.14 shows an example. For most events, oscillating source functions between positive and negative values with a dominant frequency of ~ 2 Hz are obtained, which is different from ordinary earthquakes. For this event, the solution is obtained with VR of 33.3% (Figure 2.15).

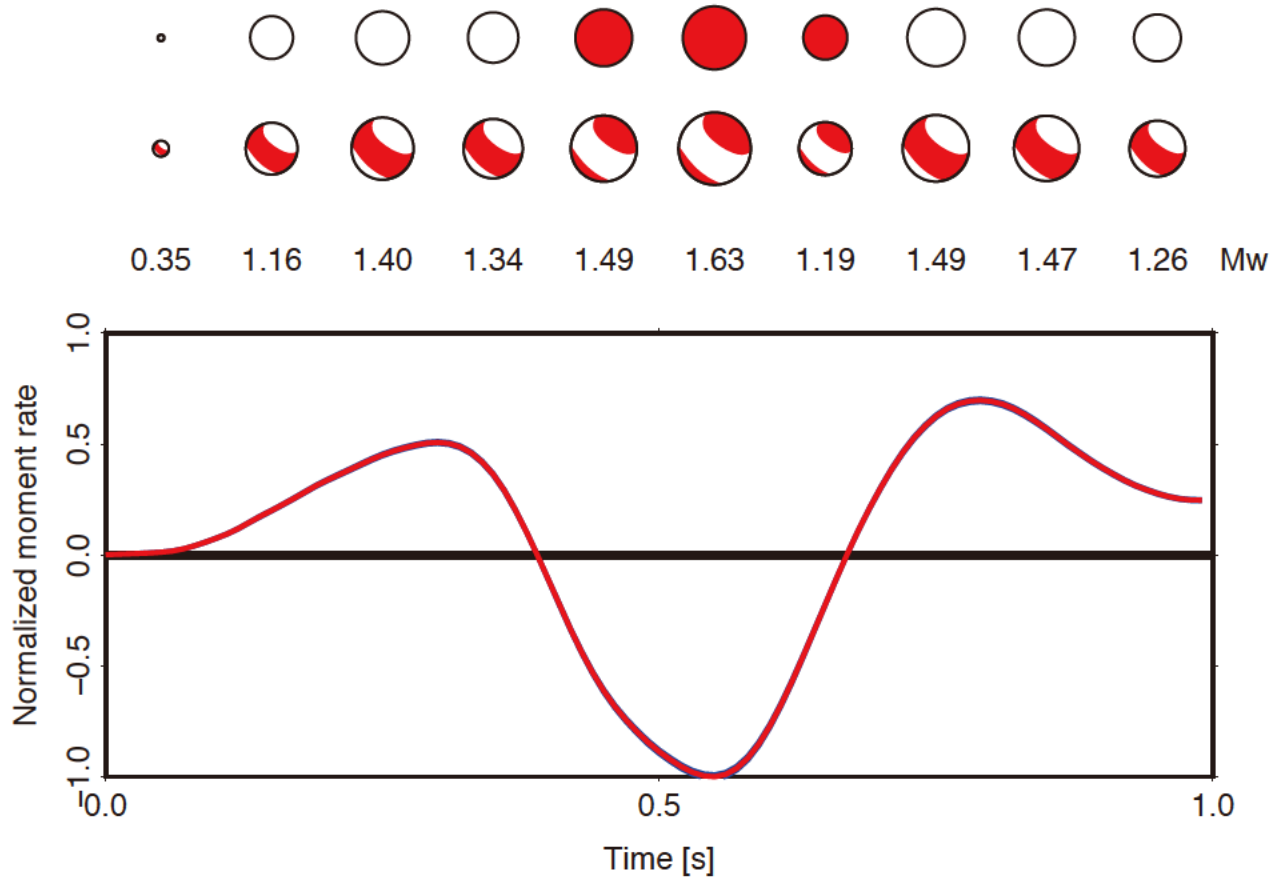


Figure 2.14 Source mechanism for the representative event in E. Shimane

Obtained source process of the representative DLP #01 in E. Shimane that occurred at 03:40:36 on July 19th, 2002 (JST). The moment tensor at each time step is shown separately as isotropic and deviatoric components. The size of each beach ball plot corresponds to the moment magnitude of each isotropic or deviatoric component. The moment magnitude of the full moment tensor is also given. In the bottom panel, the red line is the moment rate normalized by the maximum absolute value and the blue lines represent the range of within estimation errors.

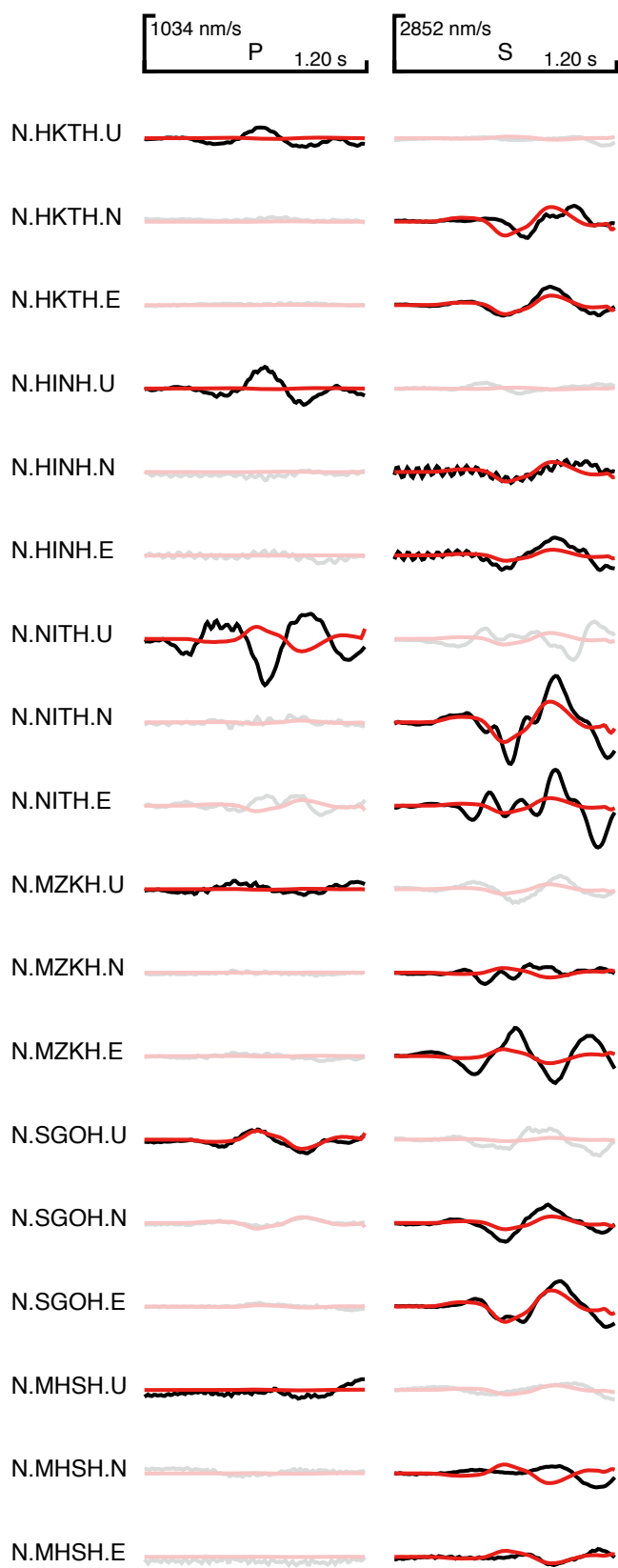


Figure 2.15 Waveform fitness for the representative event in E. Shimane

Comparison of observed and synthetic waveforms. Three-component waveforms around P and S wave arrival times at six stations for the event #01 in E. Shimane. Each waveform is 1.2 s long starting from 0.2 s before the arrival time. Black and red lines indicate the observed and synthetic waveforms, respectively. The amplitude is normalized for each P or S wave. We used the windows around P wave arrivals for vertical components and around S wave arrivals for horizontal components for the inversion. The time windows not used are shaded.

For all 53 events, the temporal distribution of the onset mechanism is shown in Figure 2.16. No temporal change of mechanism is observed. We find some events have CLVD component in the NNE direction, but this characteristic is discussed quantitatively later. The spatial distribution is shown in Figure 2.17. Although there is no systematic spatial variation of the mechanism, the dominant orientation of the CLVD component is subparallel to the direction of the source distribution (x_1 direction). Some events seem to be large magnitude with small VR value, which are artificial results of analyzing noisy data. Since noise have a characteristic period around several seconds, analyzing noise results in the source function that does not oscillate between positive and negative values but have one-sided shape. This tends to produce large moment release during the onset phase, which is equal to the window length of 1.2 s, although such noisy signal cannot be explained by synthetics well and results in smaller VR.

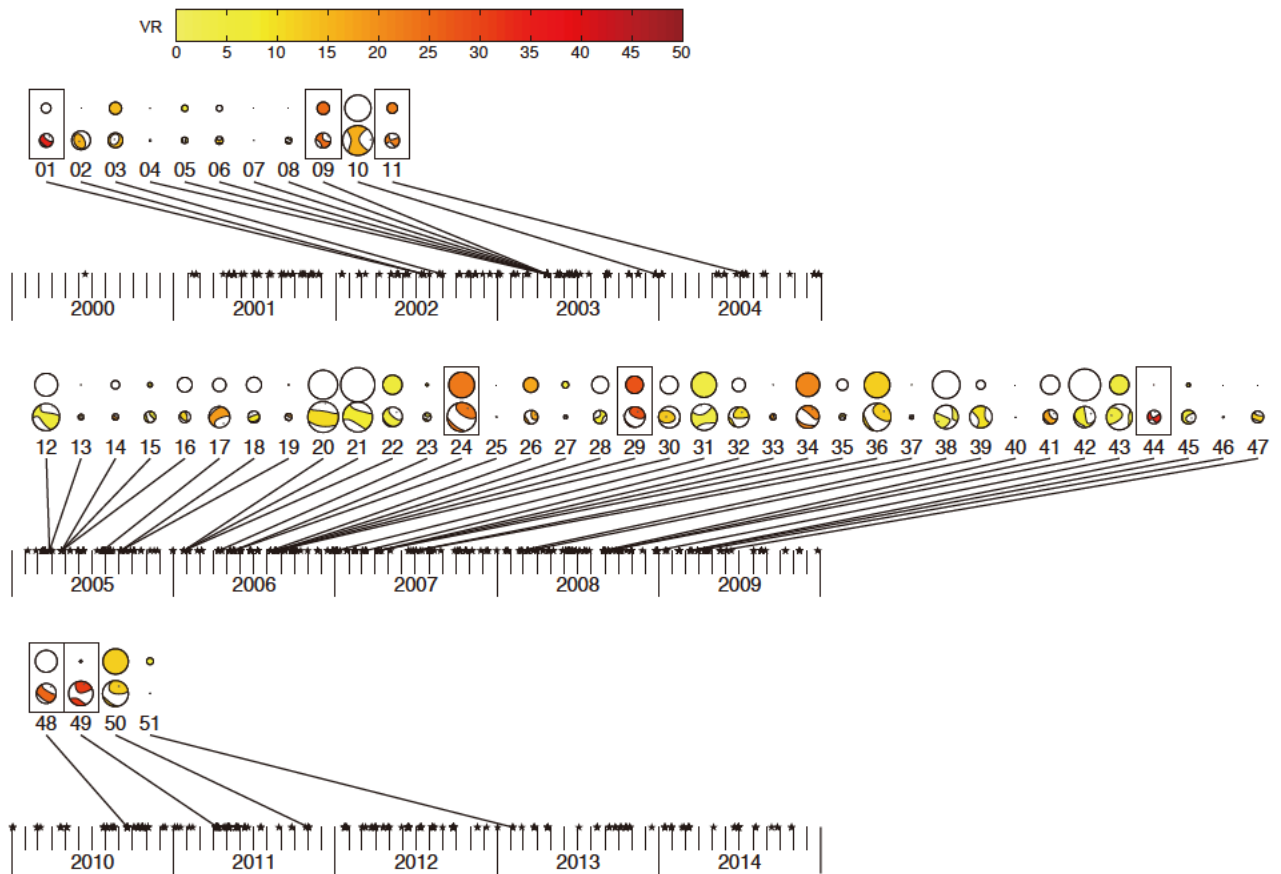


Figure 2.16 Temporal mechanism distribution in E. Shimane

Temporal distribution of DLP mechanisms in E. Shimane. Moment tensors for all 51 events plotted on a time axis. Each moment tensor is shown separately as beach ball plots of the isotropic and deviatoric components. The size of each beach ball plot corresponds to the moment magnitude of each isotropic or deviatoric component, and the color represents the VR value of each event. The major symmetry axis is shown by a small dot in each deviatoric beach ball. Solutions with VR > 20% are marked with thick outlines. Black stars on the time axis represent the total activity of DLPs in E. Shimane as determined by the JMA from June 2000 to October 2014. The event identification is also annotated on the figure.

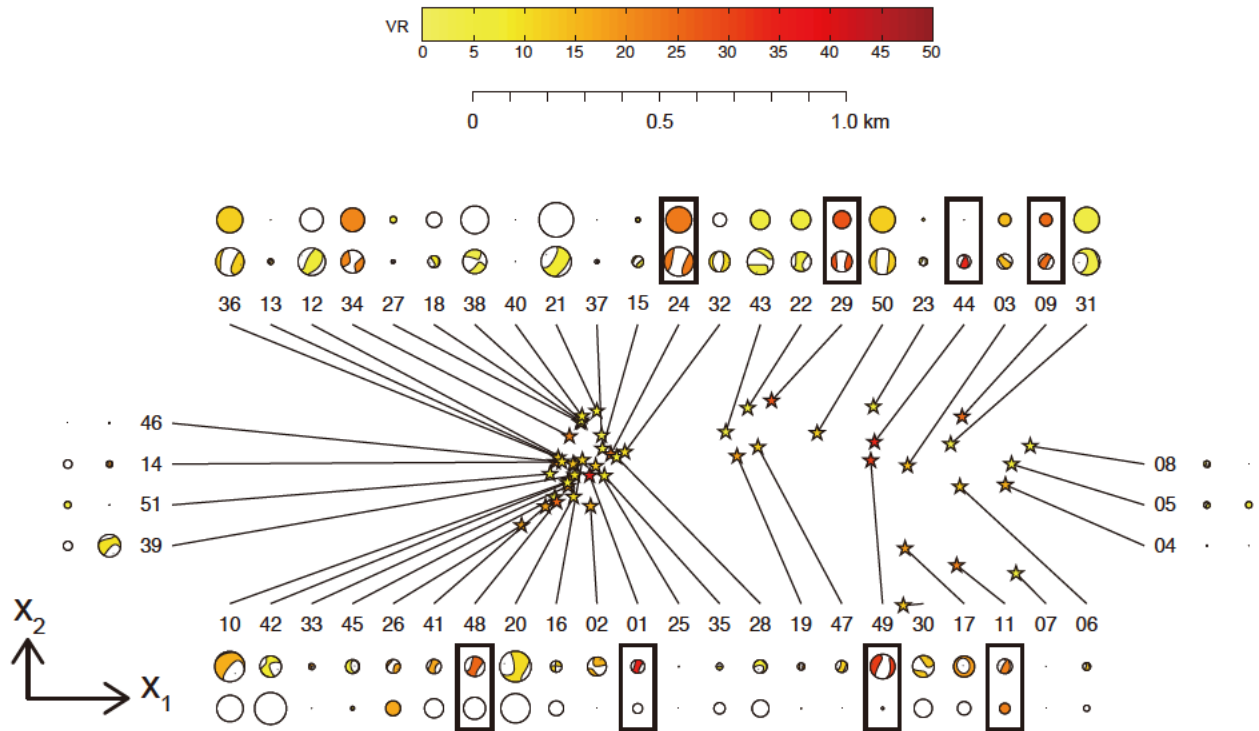


Figure 2.17 Spatial mechanism distribution in E. Shimane

Spatial distribution of DLP mechanisms in E. Shimane. Moment tensors for all 51 events shown in the x_1 - x_2 plane. Colored stars represent the location and each moment tensor is shown separately as beach ball plots of isotropic and deviatoric components, with their size corresponding to the moment magnitude of each isotropic or deviatoric component. The major symmetry axis is shown by a small dot in each deviatoric beach ball. The colors of the stars and beach ball plots represent the VR value. Solutions with $VR > 20\%$ are marked with thick outlines. The event identification is also annotated on the figure.

The distribution of source type is not so clear evidence of CLVD because some events are more like double-couple rather than CLVD and there is no complete CLVD event, but it is interesting that some events are not like double-couple and closer to CLVD (Figure 2.18). To visualize the source type, we developed a new source type diagram in Appendix A2 and we use the diagram together with the traditional source type diagram developed by *Hudson et al.* [1989]. Although it is difficult to make statistical discussions only from the eight events, statistical p-value for two CLVD-like events out of eight, which is the probability that same or larger number of CLVD-like events are expected to appear from the noise analyses, is estimated to be $1 - \text{binocdf}(2-1, 8, 1/100) = 0.0027$ considering only one event out of 100 was CLVD-like in the analysis of background noise, while $\text{binocdf}(x, N, p)$ is a binominal cumulative density function at x with a probability p for each of N trials. The orientation of the major symmetry axis is clearer (Figure 2.19). The orientation of the CLVD component is subparallel to the lineation formed by the hypocenter distribution (green star in Figure 2.19a). Such orientation is not come from station distribution or too simple structure because this is not observed for the analysis of

background noise data (Figure 2.19b). Such dependency of station set or structure is discussed in the following. We also looked at the distribution of P, N, and T-axes but clearer concentration is observed for the distribution of the major symmetry axis (Figure 2.20).

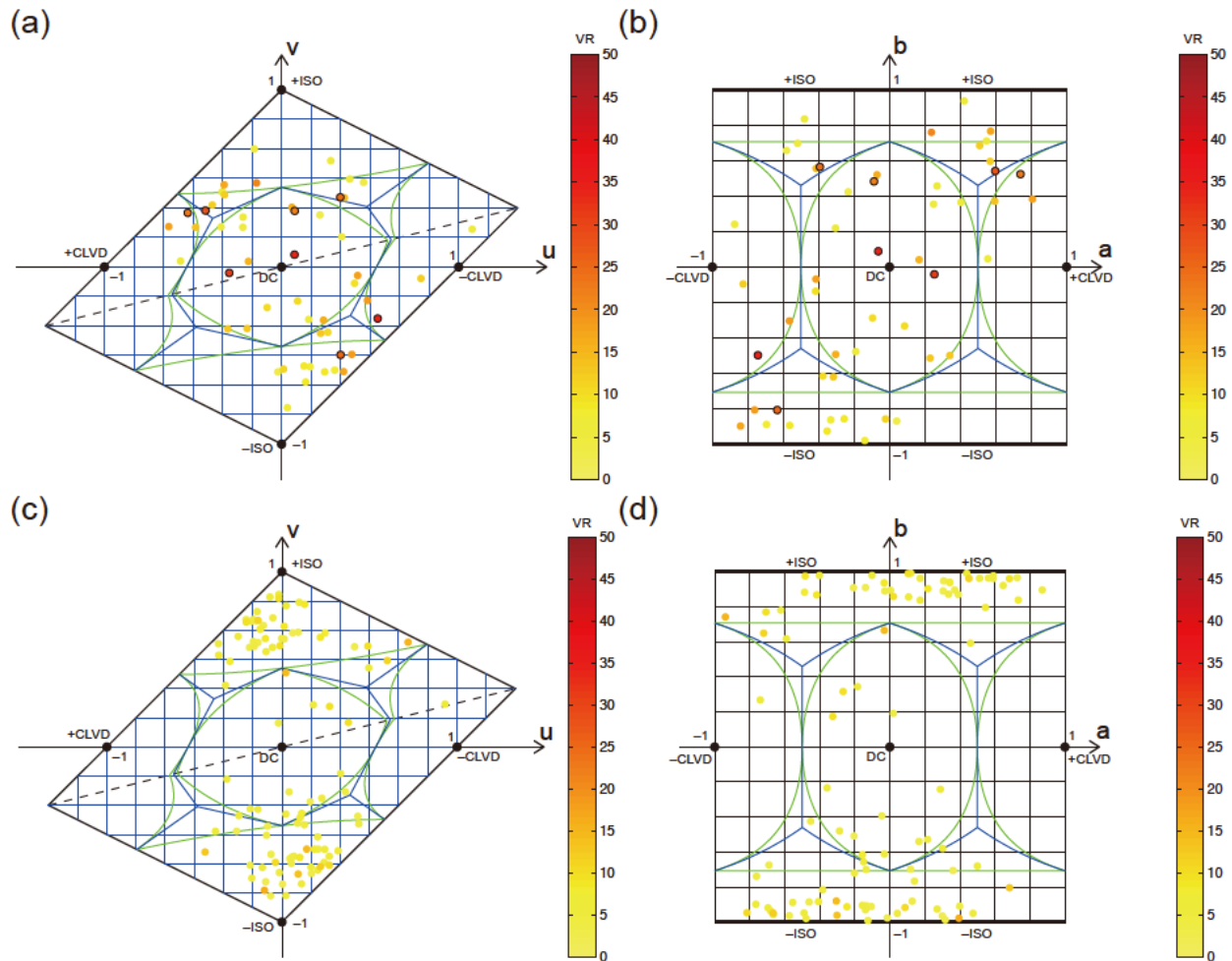
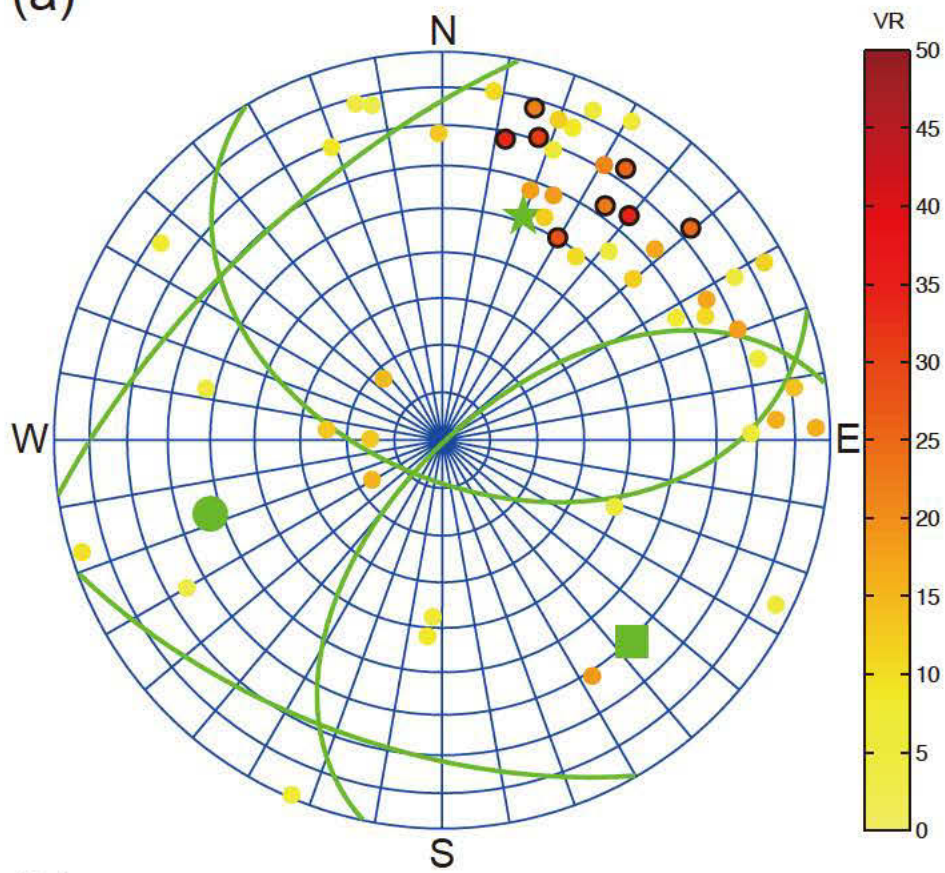


Figure 2.18 Source type distribution in E. Shimane

Source-type diagram of 51 DLPs in E. Shimane and the result of analyzing 100 imaginary events composed by background noise are shown in separate panels. Each result is shown in the traditional diagram and in the newly developed diagram. Colors represent VR values. Solutions with $VR > 20\%$ are marked with thick outlines. The solid green lines are the area where double-couple (DC), compensated linear vector dipole (CLVD), and isotropic deformation (ISO) dominate. We refer to the source type as being dominated by one component when that component is larger than the other two combined. (a) DLPs in E. Shimane in the traditional diagram. (b) DLPs in E. Shimane in the new diagram. (c) Background distribution in the traditional diagram. (d) Background distribution in the new diagram.

(a)



(b)

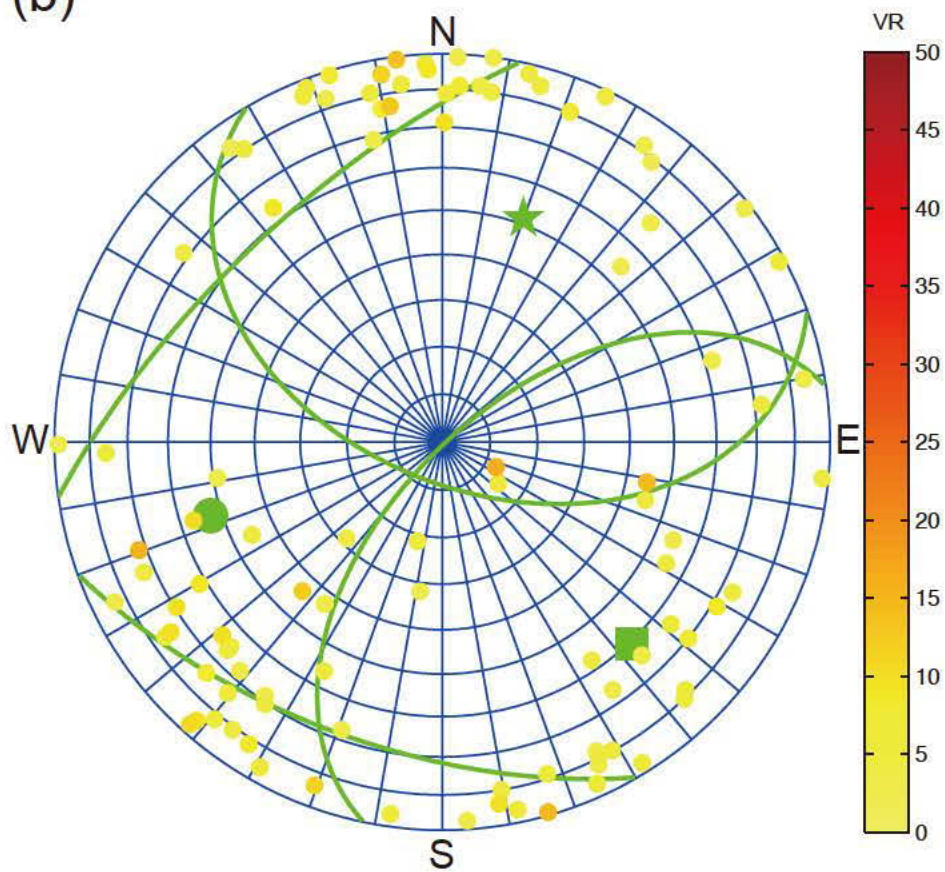


Figure 2.19 Symmetry axis distribution in E. Shimane

Polar plot of 51 DLPs in E. Shimane and the result of analyzing 100 imaginary events composed by background noise are shown in separate panels. The principal symmetry axis is plotted in the lower hemisphere. Colors represent VR values. Solutions with VR>20% are marked with thick outlines. The Green star, circle, and square mark the directions of x_1 , x_2 , and x_3 , respectively. The green lines represent the locations at 30° tilted from the x_1 or x_3 , which is used to evaluate whether each point is close to the axis or not. (a) DLPs in E. Shimane. (b) Background distribution.

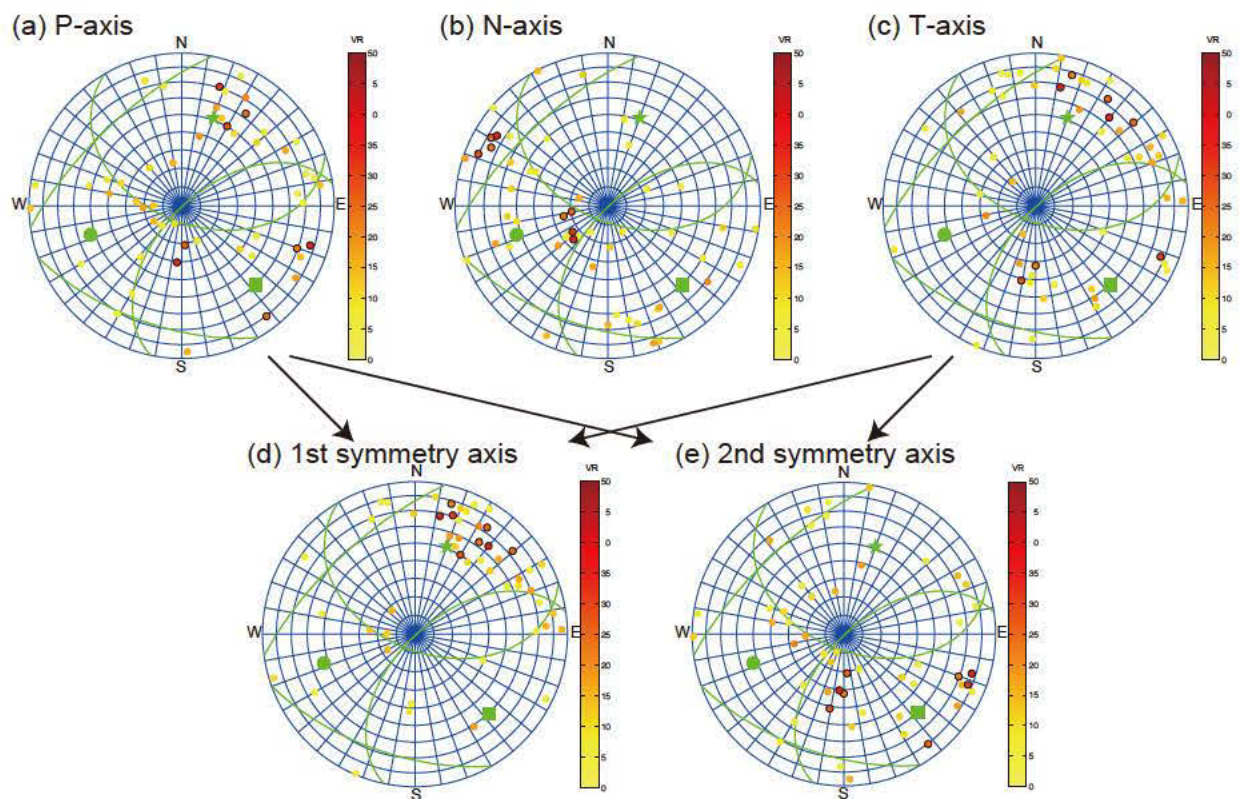


Figure 2.20 Principal axes and symmetry axes in E. Shimane

Polar plot of 51 DLPs in E. Shimane in the lower hemisphere. Colors represent VR values. Solutions with VR>20% are marked with thick outlines. The Green star, circle, and square mark the directions of x_1 , x_2 , and x_3 , respectively. The green lines represent the locations at 30° tilted from the x_1 or x_3 , which is used to evaluate whether each point is close to the axis or not. Either P-axis or T-axis is each of the 1st and 2nd major symmetry axes. (a) P-axis. (b) N-axis. (c) T-axis. (d) 1st major symmetry axis same as Figure 2.19a. (e) 2nd major symmetry axis.

We have already discussed on the synthetic test in 2.2.2.4, but the dependency of results on source location, structure, or station set is not yet examined well. Here we verify these effects.

Figure 2.21 shows results assuming different location at $\pm 0.01^\circ$ in latitudinal or longitudinal direction or ± 1 km in depth together with the original result. These results are stably obtained in the context of source type and principal symmetry axis. This agreement is not surprising because the strongest effect of the differential location appear on the synthetic arrival times but they are used not directly but indirectly by searching actual arrivals around the synthetic arrivals automatically. It is notable that such effect of differential location is effectively removed in this analysis method.

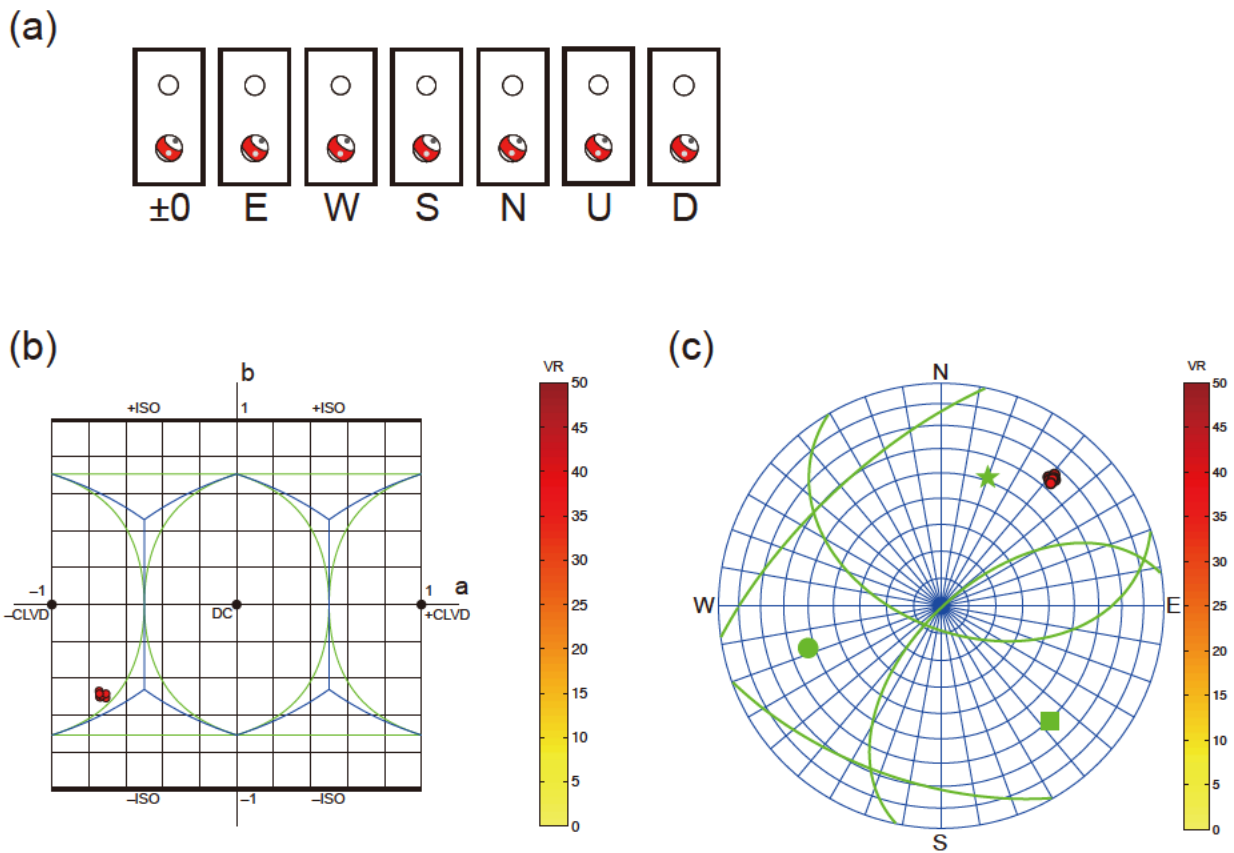


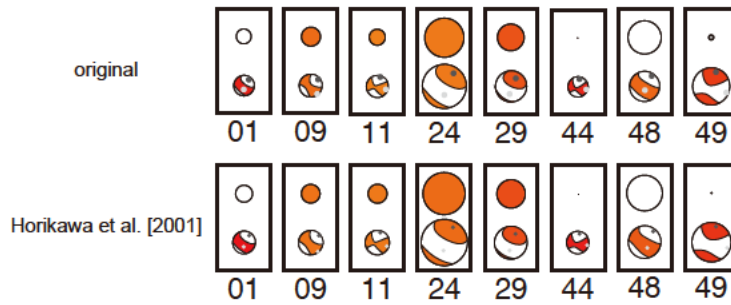
Figure 2.21 Hypocenter dependency test in E. Shimane

Results of the event #01 in E. Shimane assuming different hypocenter locations are shown. Assumed different locations are shifted $\pm 0.01^\circ$ in latitudinal or longitudinal direction or ± 1 km in depth from the original location. The original result is also shown together with the fluctuated results. Colors represent VR values. (a) Beach-ball plot. (a) Source-type diagram newly developed in the Appendix A2. The solid green lines are the area where double-couple (DC), compensated linear vector dipole (CLVD), and isotropic deformation (ISO) dominate. We refer to the source type as being dominated by one component when that component is

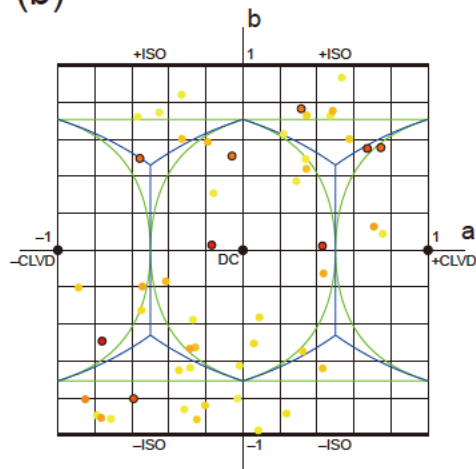
larger than the other two combined. (c) Polar plot of the principal symmetry axis in the lower hemisphere. The green star, circle, and square mark the directions of x_1 , x_2 , and x_3 , respectively. The green lines represent the locations at 30° tilted from the x_1 or x_3 , which is used to evaluate whether each point is close to the axis or not.

The inversion results may possibly depend on assumed structures. Indeed, if the exact heterogeneous structure was available, it should be possible to calculate perfect theoretical waveforms using the complex “real” structure. However, such structure is not available currently and poorly defined 3-D structures may yield results that are as inaccurate as those using a 1-D structure. Therefore, we used a simple structure in this study and here we discuss the dependency of results on the assumed structure. For this purpose, we solved the same problem with the velocity structure used in *Horikawa et al.* [2001] (Figure 2.8). No significant difference with the original results (compare with Figure 2.18 and Figure 2.19) is observed in terms of the non-negligible CLVD component for some events and the orientation of major symmetry axis in the NNE direction.

(a)



(b)



(c)

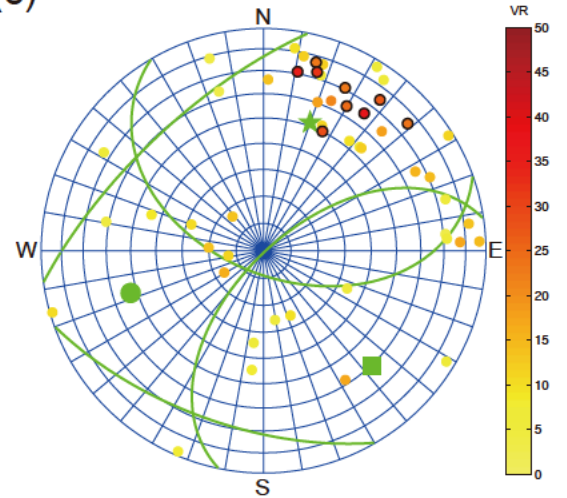


Figure 2.22 Structure dependency test in E. Shimane

Results of the events in E. Shimane using the structure of *Horikawa et al.* [2001] are shown. Colors represent VR values. Solutions with $VR > 20\%$ are marked with thick outlines. (a) Beach-ball plot. (b) Source-type diagram newly developed in the Appendix A2. The solid green lines are the area where double-couple (DC), compensated linear vector dipole (CLVD), and isotropic deformation (ISO) dominate. We refer to the source type as being dominated by one component when that component is larger than the other two combined. (c) Polar plot of the principal symmetry axis in the lower hemisphere. The green star, circle, and square mark the directions of x_1 , x_2 , and x_3 , respectively. The green lines represent the locations at 30° tilted from the x_1 or x_3 , which is used to evaluate whether each point is close to the axis or not.

The systematic effect of the structure is verified to be little in the previous test, but we also consider the local structural effects, which may distort the results. To survey this dependency, we conducted a jackknife test in which each one station was not used in each trial. Figure 2.23 compares the isotropic and deviatoric components of the onset mechanism for the original and jackknifed solutions for eight events that obtained $VR > 20\%$ in the original analysis. The basic nature of $-CLVD$ component in NNE–NE direction is commonly observed from their beach-ball plot for the event #01 (Figure 2.23a). From the source-type diagram, the mechanism looks different from DC although it is not a complete $-CLVD$ event. Fair conclusion would be that the event #01 is marginal event between DC and CLVD but is clearly different from regular DC events. The major symmetry axis of the event #01 was obtained to be between $\sim N$ and $\sim E$ directions. Since jackknife test results tend to vary drastically and it is difficult to discuss on the statistical distribution from the limited number of results, sophisticated bootstrap tests would be important for further examination of error estimates. As a result of the jackknife test for all eight events, some events fall into the DC-like region but we note there are marginal mechanisms between DC and CLVD. Such events are difficult to be explained by pure DC events and contain the non-negligible CLVD component. The CLVD component might be key to understand their physics. The major symmetry axis for the eight events is still concentrated between $\sim N$ and $\sim E$ directions and supports the CLVD component is in the direction around NNE.

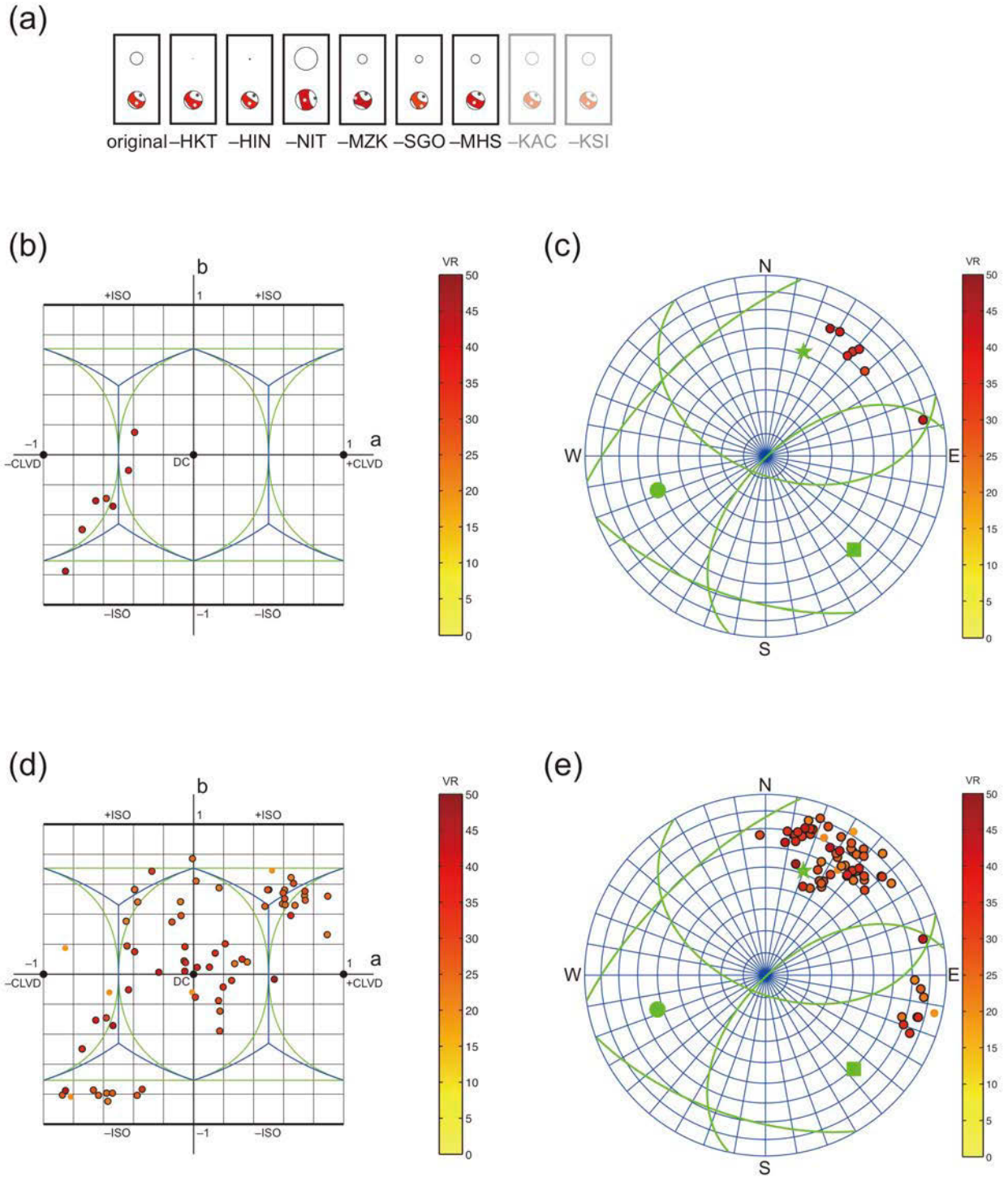


Figure 2.23 Jackknife test in E. Shimane

Results of the events in E. Shimane using station sets that excluded each one of the original station set are shown. Colors represent VR values. Solutions with $VR > 20\%$ are marked with thick outlines. (a) Beach-ball plot for the event #01. (b) Source-type diagram for the event #01. This diagram is newly developed in the Appendix A2. The solid green lines are the area where double-couple (DC), compensated linear vector dipole (CLVD), and isotropic deformation (ISO) dominate. We refer to the source type as being dominated by one component when that

component is larger than the other two combined. (c) Polar plot of the principal symmetry axis in the lower hemisphere for the event #01. The green star, circle, and square mark the directions of x_1 , x_2 , and x_3 , respectively. The green lines represent the locations at 30° tilted from the x_1 or x_3 , which is used to evaluate whether each point is close to the axis or not. (d) Source-type diagram for the events that obtained $VR > 20\%$ in the original analysis. (e) Polar plot of the principal symmetry axis for the events that obtained $VR > 20\%$ in the original analysis.

The obtained mechanism for DLPs in E. Shimane tends to have the NNE-CLVD component although they are not perfect CLVD events. The polarity whether +CLVD or -CLVD is not well determined. This CLVD component is consistent with the combination of the single force obtained by *Ohmi and Obara* [2002] and its reaction force. In this region, the western Tottori earthquake occurred on October 6th, 2000 (JST), and DLPs are observed both before and after the mainshock [*Ohmi et al.*, 2002]. Although no clear causal relationships are observed between the mainshock and DLPs, DLP sequence in April 2003 are reported to be swarm-like rather than that before the mainshock [*Ohmi et al.*, 2004]. Interpreting this as static triggering, the favorable polarity of the CLVD component would be positive, considering the symmetry axis is close to the T-axis of the mainshock.

2.2.3.2. Kirishima

The result for a representative event #17 ($M_{JMA}=1.5$) that occurred at 04:35:03.36 on March 29th, 2007 (JST), which gives the largest VR value, is shown in Figure 2.24. Nearly vertical CLVD component is observed with an oscillating time function, which makes difficult to determine the polarity of the CLVD. The fitness between synthetic and observed waveforms is good for this event (Figure 2.25). Temporal and spatial distributions of all events are shown in Figure 2.26 and Figure 2.27, respectively. There is a temporal variation in seismicity, which range from two events in 2006 to 31 events in 2011. The seismicity is basically low and it is difficult to discuss the temporal variation with a high reliability. The relationship between the DLP activity and the eruption in January 2011 is not so obvious, which is discussed later in 3.4.1. Since only two events were determined with variance reduction larger than 20% (#17 and #20), it is difficult to discuss the tendency of source types (Figure 2.28) or directions (Figure 2.29) statistically. The CLVD component of the event #17 is sub-parallel to the orientation formed by the source distribution (Figure 2.6b). The event #20 might be a DC event if we look at the deviatoric part. However, these events are isotropic-like events and the validity of discussing the residual deviatoric part is suspicious.

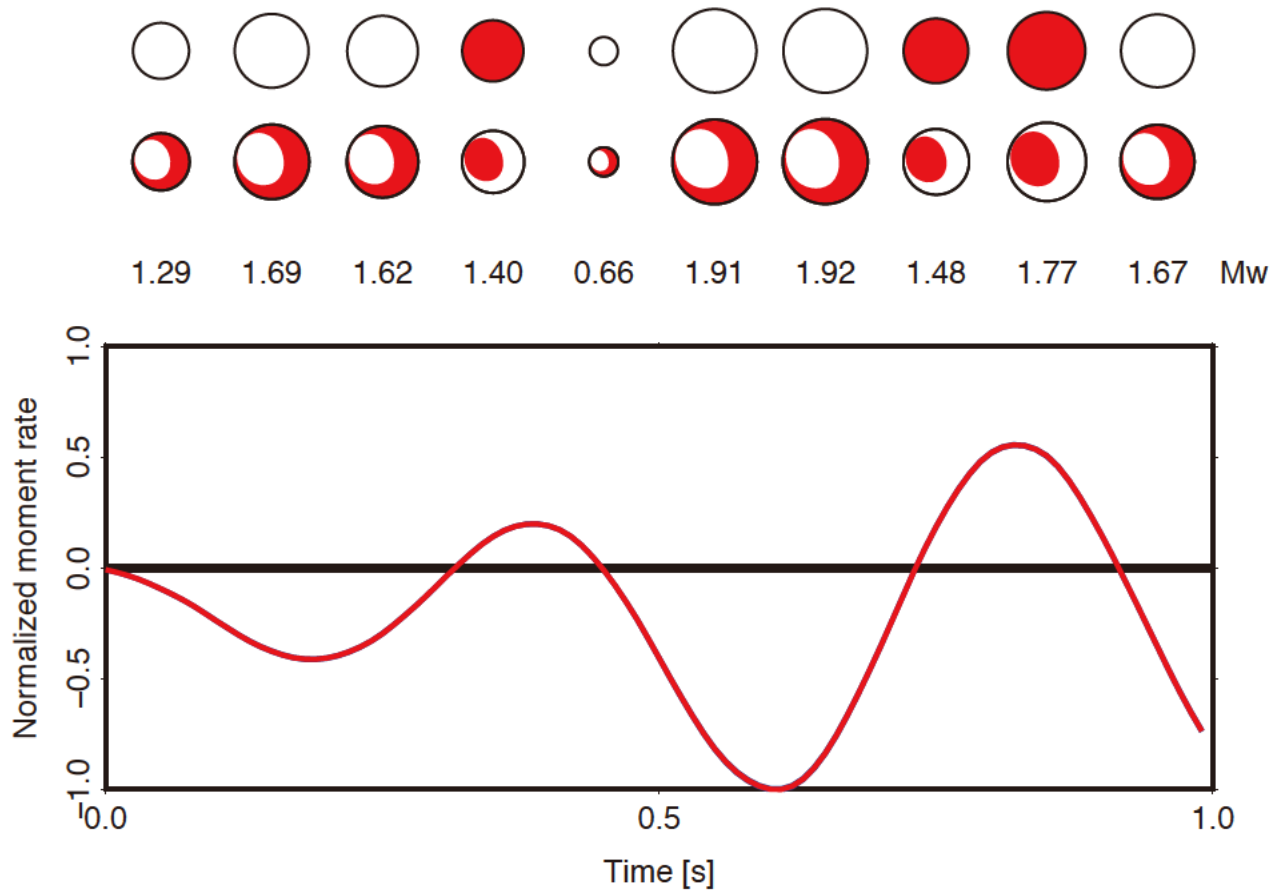


Figure 2.24 Source mechanism for the representative event in Kirishima

Obtained source process of the representative DLP #17 in Kirishima that occurred at 4:35:3.36 on March 29th, 2007 (JST). The legends are same as in Figure 2.14.

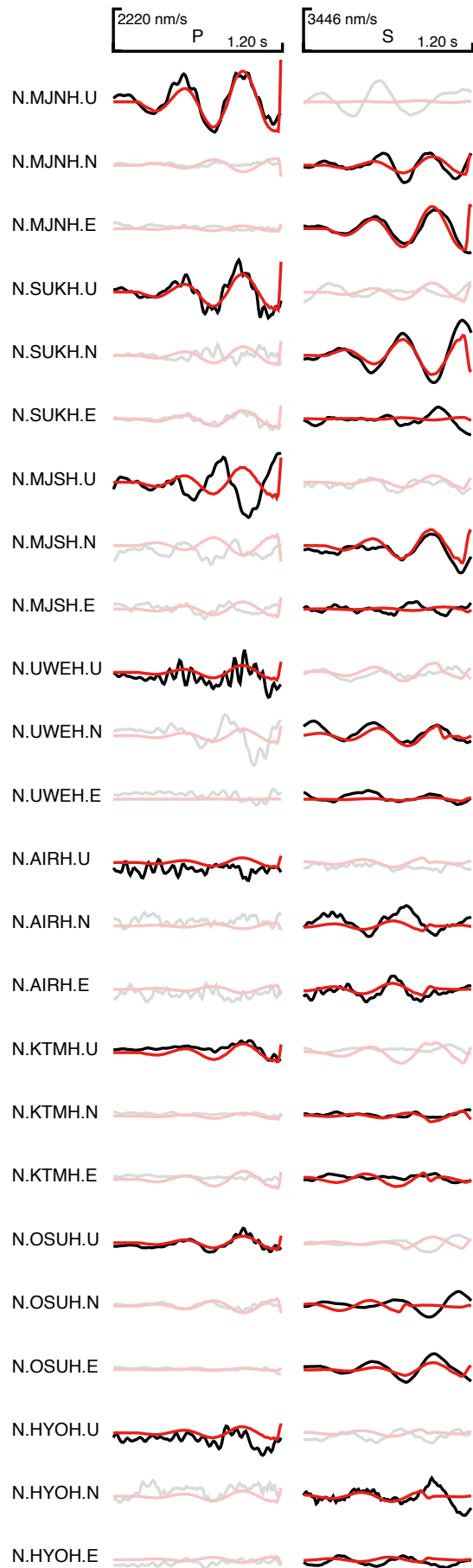


Figure 2.25 Waveform fitness for the representative event in Kirishima

Comparison of observed and synthetic waveforms. Three-component waveforms around P and S wave arrival times at eight stations for the event #17 in Kirishima. The legends are same as in Figure 2.15.

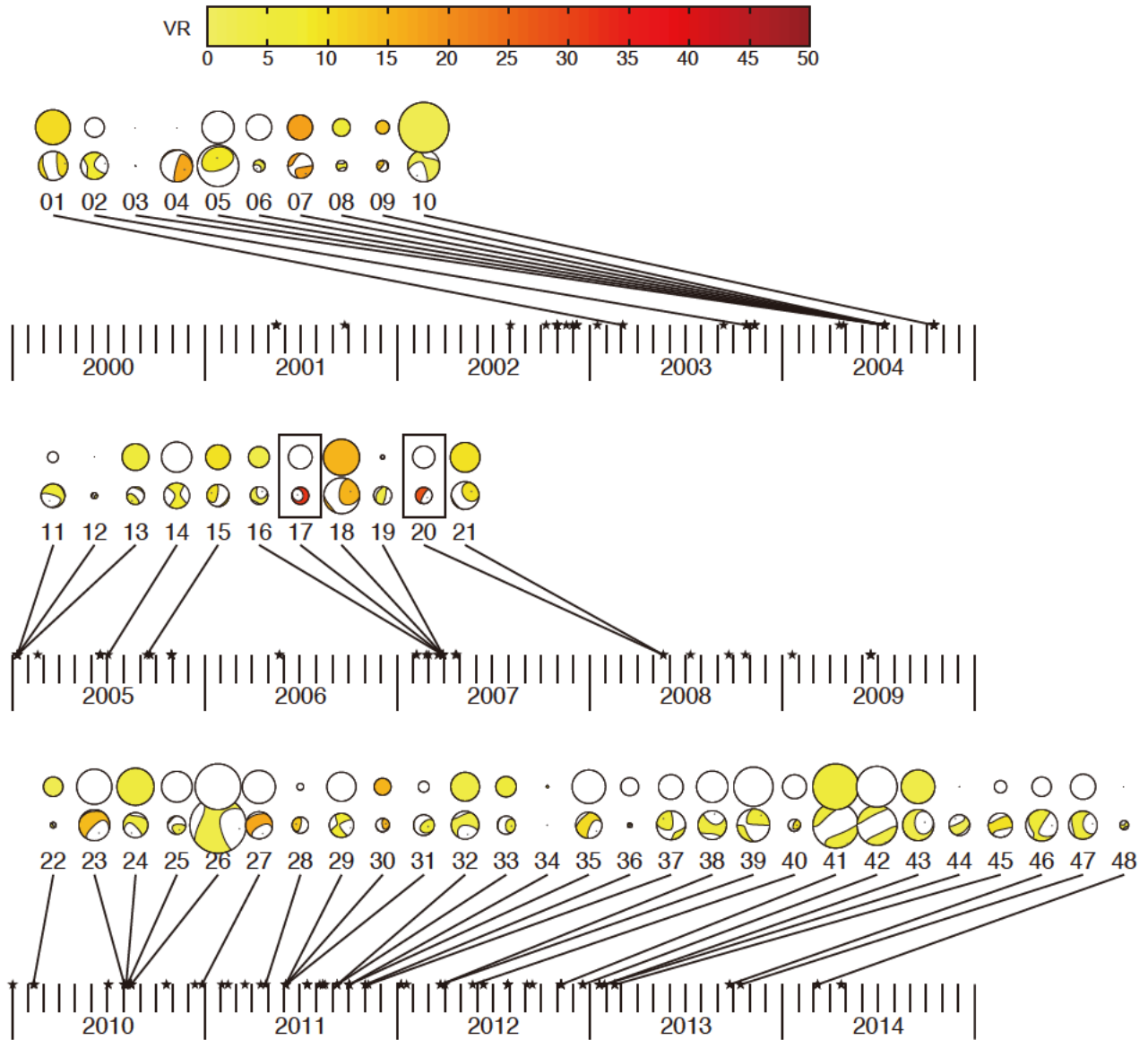


Figure 2.26 Temporal mechanism distribution in Kirishima

Temporal distribution of DLP mechanisms in Kirishima. Moment tensors for all 48 events plotted on a time axis. The legends are same as in Figure 2.16.

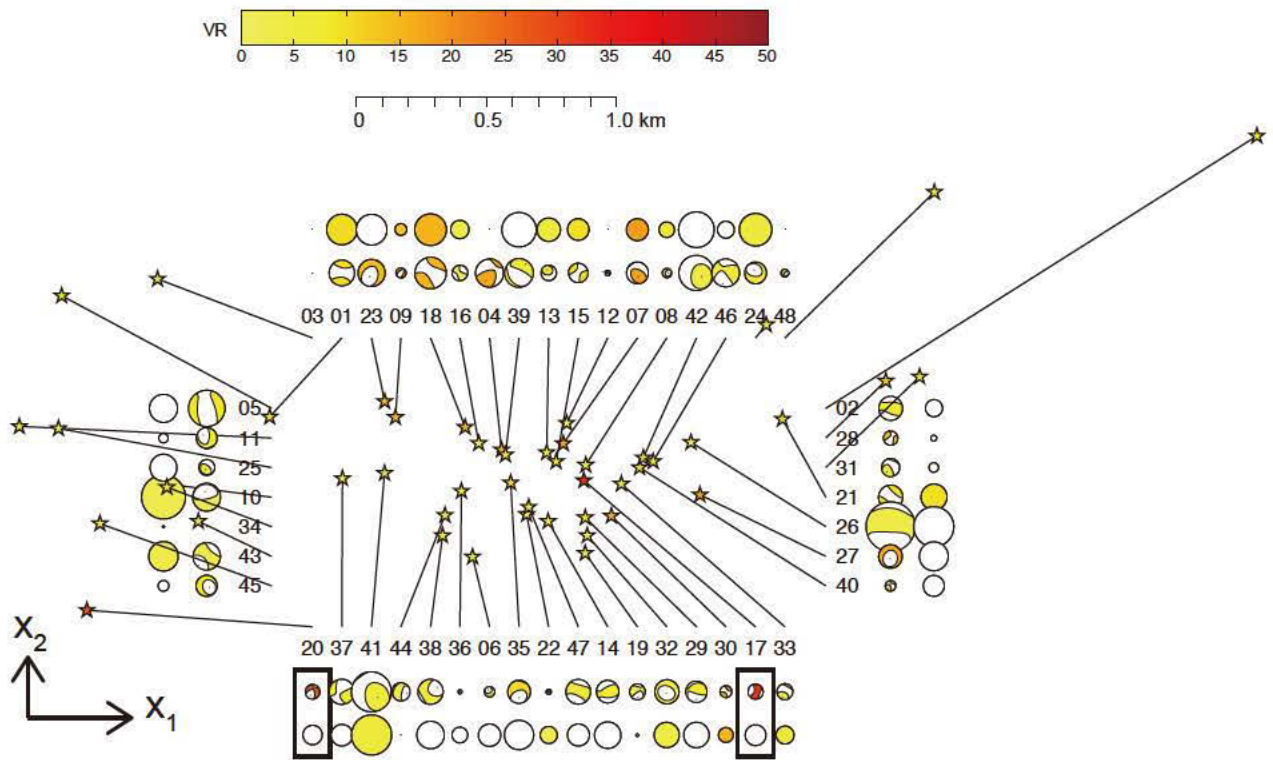


Figure 2.27 Spatial mechanism distribution in Kirishima

Spatial distribution of DLP mechanisms in Kirishima. Moment tensors for all 48 events shown in the x_1 - x_2 plane. The legends are same as in Figure 2.17.

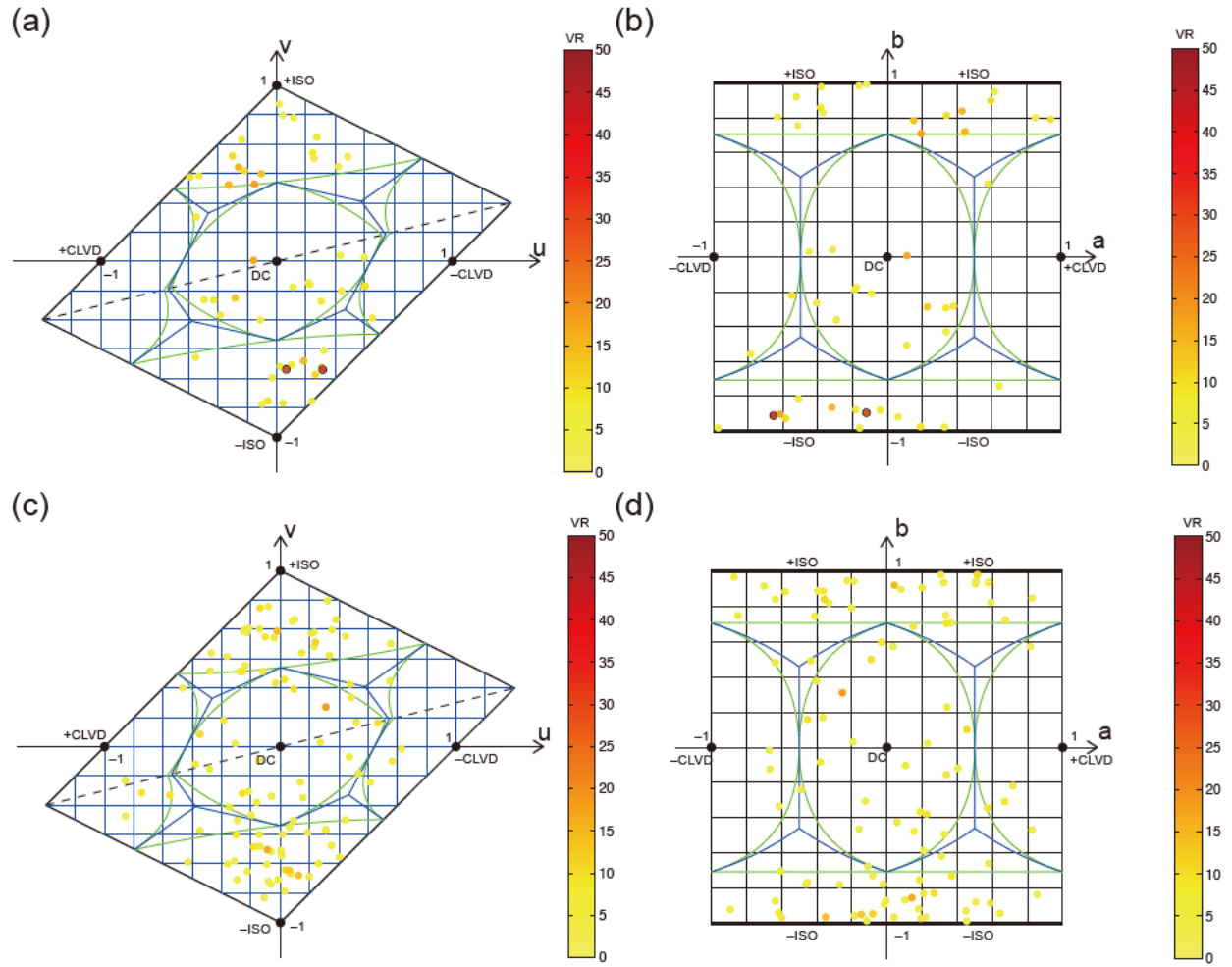
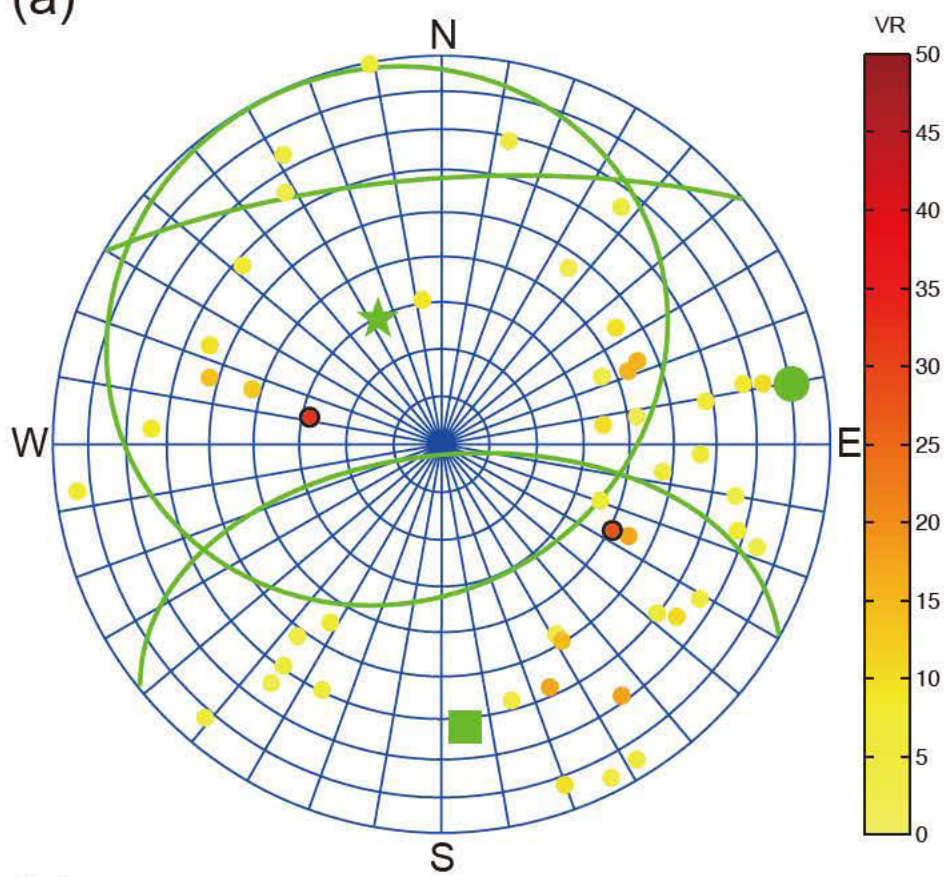


Figure 2.28 Source type distribution in Kirishima

Source-type diagram of 48 DLPs in Kirishima and the result of analyzing 100 imaginary events composed by background noise are shown in separate panels. Each result is shown in the traditional diagram and in the newly developed diagram. The legends are same as in Figure 2.18. (a) DLPs in Kirishima in the traditional diagram. (b) DLPs in Kirishima in the new diagram. (c) Background distribution in the traditional diagram. (d) Background distribution in the new diagram.

(a)



(b)

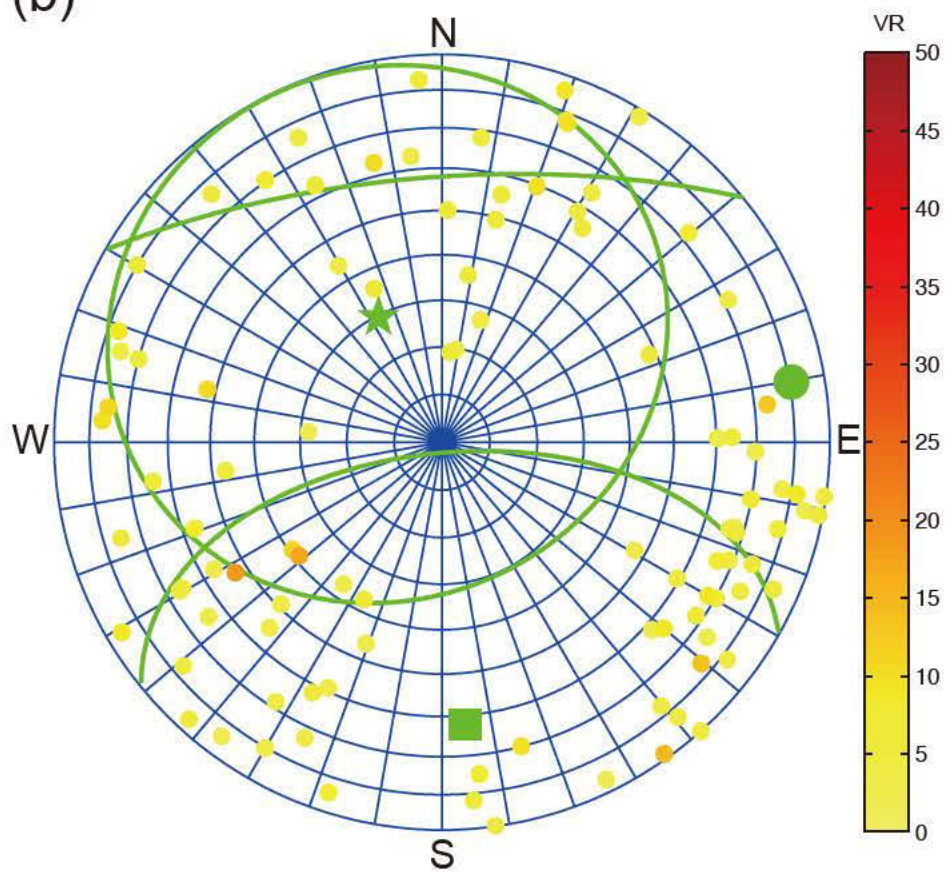


Figure 2.29 Symmetry axis distribution in Kirishima

Polar plot of 48 DLPs in Kirishima and the result of analyzing 100 imaginary events composed by background noise are shown in separate panels. The legends are same as in Figure 2.19.

(a) DLPs in Kirishima. (b) Background distribution.

We look for the dependency of the assumed velocity structure. The result with the velocity model of *Horikawa et al.* [2001] is shown in Figure 2.30. The structure is a reference structure near E. Shimane and might not be appropriate here, but it can be used to find the dependency of results on structures. Although the result of the event #20 does not change a lot, the result of the event #17 looks different from the original and its VR value became worse as 18.60%.

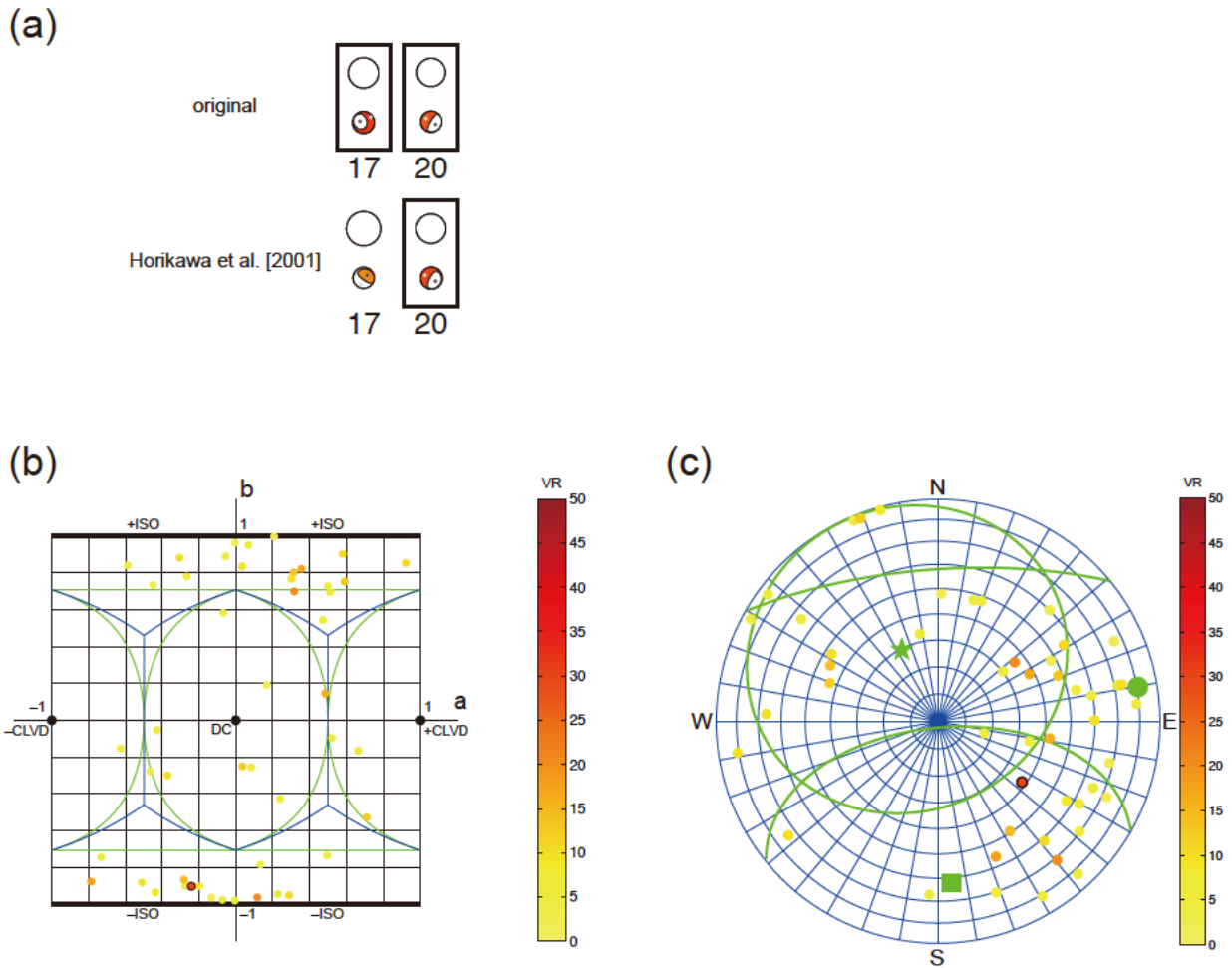
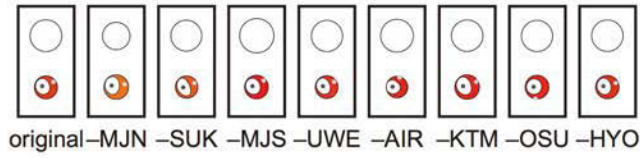


Figure 2.30 Structure dependency test in Kirishima

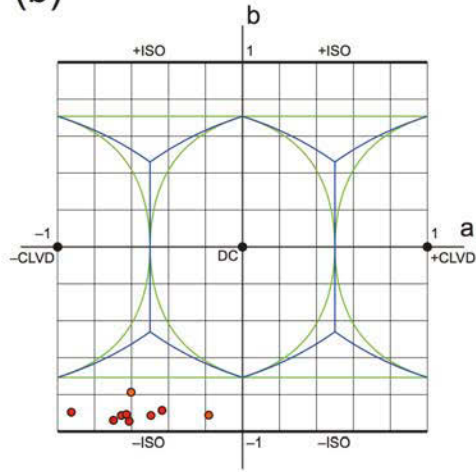
Results of the events in Kirishima using the structure of *Horikawa et al.* [2001] are shown. The legends are same as in Figure 2.22. (a) Beach-ball plot. (b) Source-type diagram newly developed in the Appendix A2. (c) Polar plot of the principal symmetry axis in the lower hemisphere.

The dependency on the station set is examined in Figure 2.31. For the events #17 and #20, isotropic component dominates the mechanism but the isotropic component cannot be resolved well in the present study.

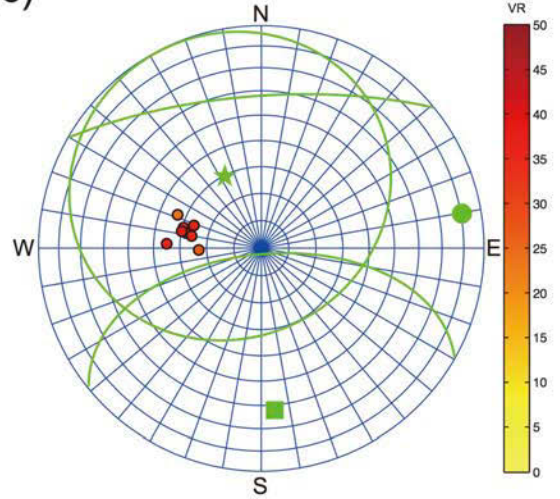
(a)



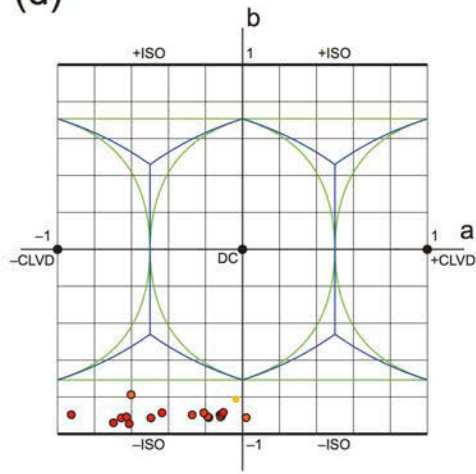
(b)



(c)



(d)



(e)

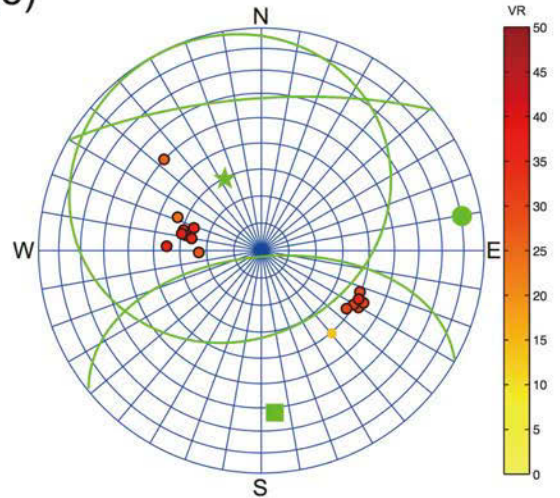


Figure 2.31 Jackknife test in Kirishima

Results of the events in Kirishima using station sets that excluded each one of the original station set are shown. The legends are same as in Figure 2.23. (a) Beach-ball plot for the event #17. (b) Source-type diagram for the event #17. This diagram is newly developed in the Appendix A2. (c) Polar plot of the principal symmetry axis in the lower hemisphere for the event #17. (d) Source-type diagram for the events that obtained $VR > 20\%$ in the original analysis. (e) Polar plot of the principal symmetry axis for the events that obtained $VR > 20\%$ in the original analysis.

Considering the obtained mechanisms for two major events are isotropic-like, which is often produced by analyzing noise, we cannot conclude any statistically significant statement on the obtained mechanism in Kirishima.

2.2.3.3. S. Mt. Iwate

The obtained source mechanism of the representative event #22 that occurred at 3:57:42.81 on September 5th, 2007 (JST) is shown in Figure 2.32. The moment tensor is close to a double-couple. Synthetic waveforms explain basic nature of the observed waveform near the source (Figure 2.33), but the VR value exceeds 20% only for two events (Table 2.4). Temporal and spatial distributions of all events are shown in Figure 2.34 and Figure 2.35, respectively. Relatively constant seismicity is observed in this region. We cannot discuss overall characteristics of the obtained mechanisms from these limited observations (Figure 2.28 and Figure 2.37). These events might have various mechanisms in real as obtained by *Nakamichi et al.* [2003]. Statistical discussion on mechanism distribution is difficult but at least the event #22 that recorded the highest VR is close to DC. For DC events, focusing only on the major symmetry axis (Figure 2.37) is not appropriate way and we discuss on the orientation of the nodal planes after stability tests. Another event with $VR > 20\%$ is the event #07, but it is isotropic-like so we do not further discuss on the event.

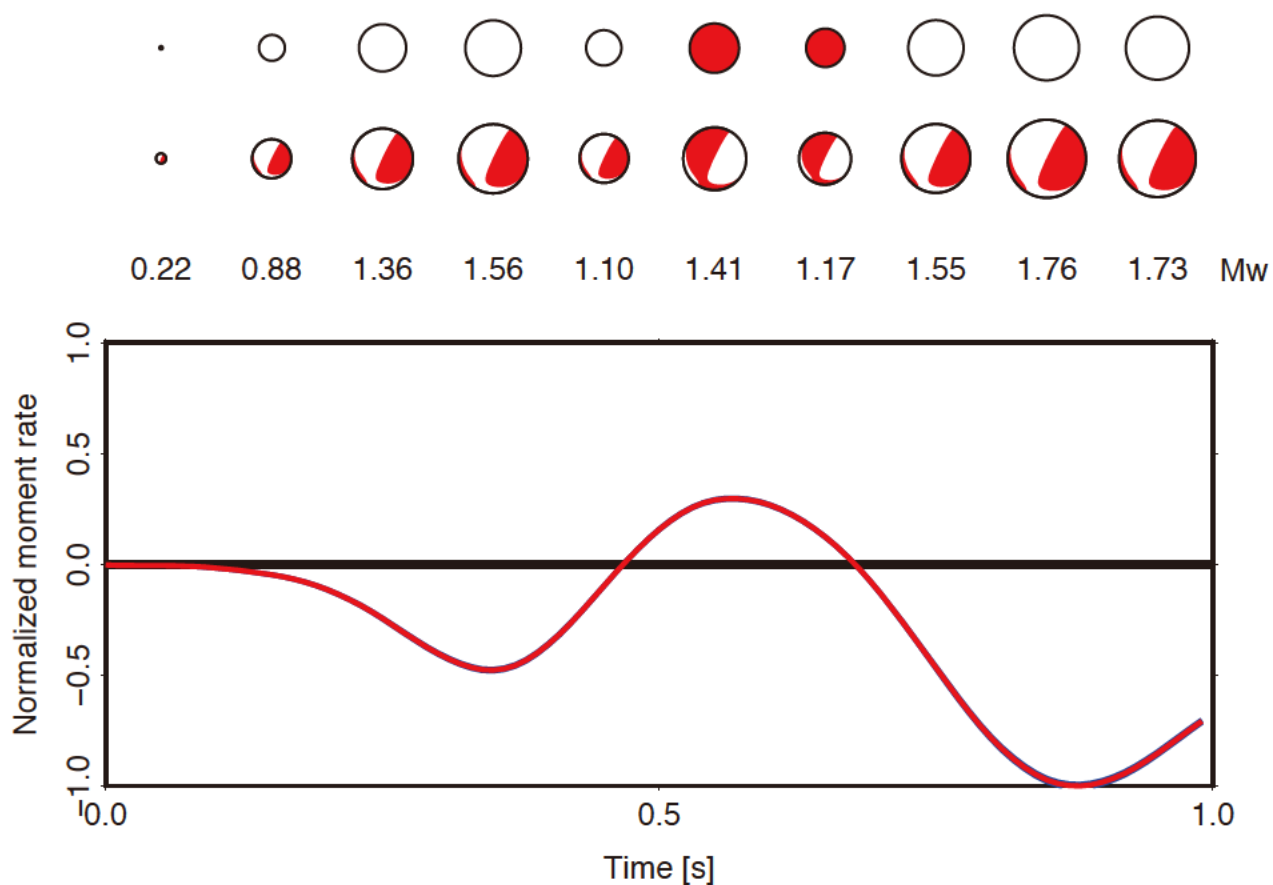


Figure 2.32 Source mechanism for the representative event in S. Mt. Iwate

Obtained source process of the representative DLP #22 in S. Mt. Iwate that occurred at 3:57:42.81 on September 5th, 2007 (JST). The legends are same as in Figure 2.14.

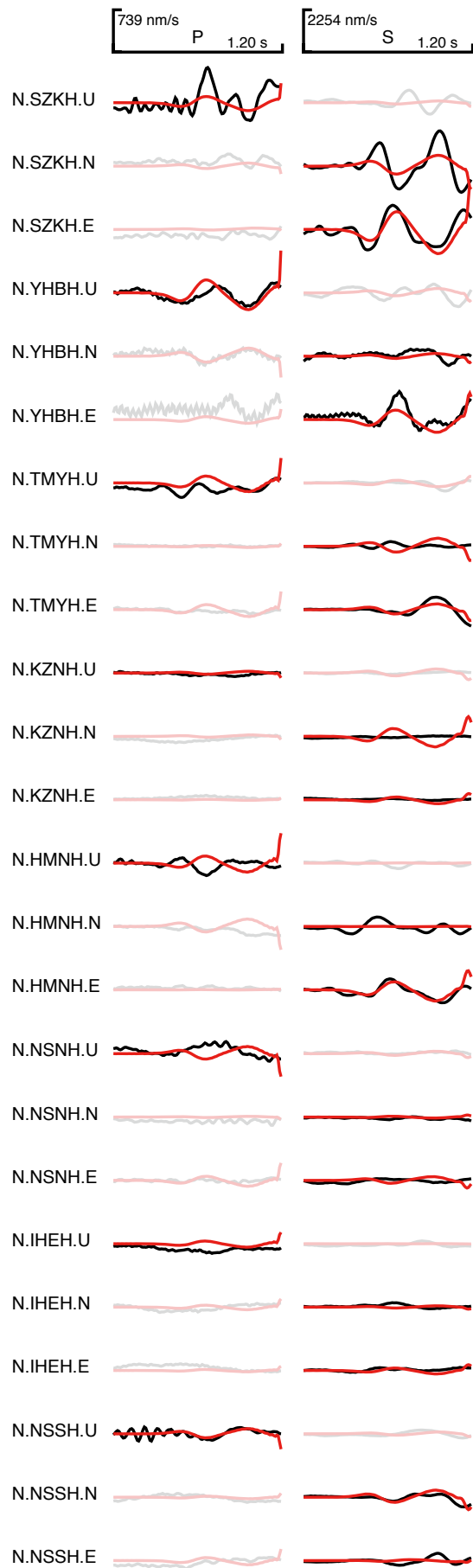


Figure 2.33 Waveform fitness for the representative event in S. Mt. Iwate

Comparison of observed and synthetic waveforms. Three-component waveforms around P and S wave arrival times at eight stations for the event #22 in S. Mt. Iwate. The legends are same as in Figure 2.15.

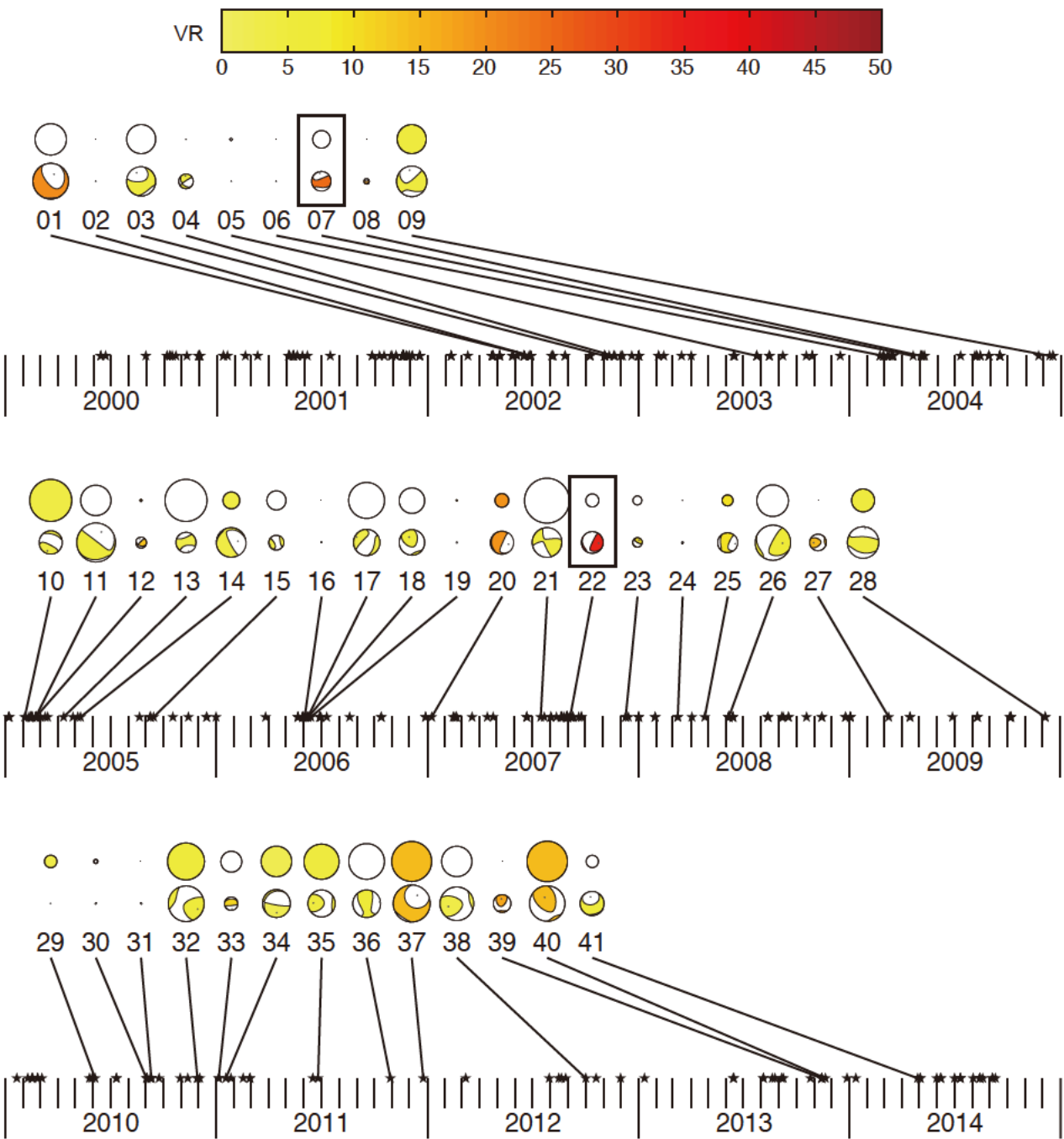


Figure 2.34 Temporal mechanism distribution in S. Mt. Iwate

Temporal distribution of DLP mechanisms in S. Mt Iwate. Moment tensors for all 41 events plotted on a time axis. The legends are same as in Figure 2.16.

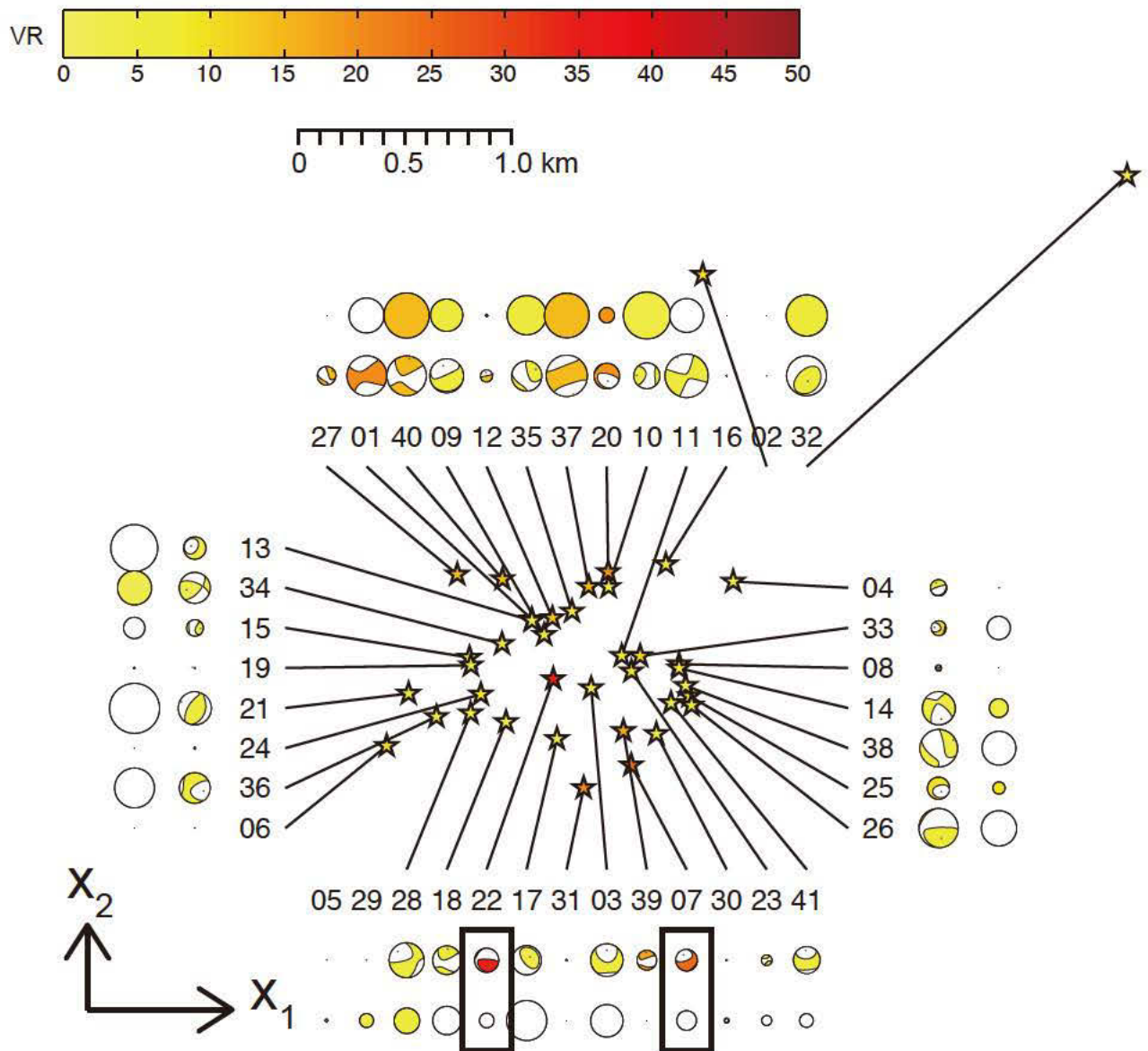


Figure 2.35 Spatial mechanism distribution in S. Mt. Iwate

Spatial distribution of DLP mechanisms in S. Mt. Iwate. Moment tensors for all 41 events shown in the x_1 - x_2 plane. The legends are same as in Figure 2.17. The location of the event outside the plot area is not shown but its mechanism is shown.

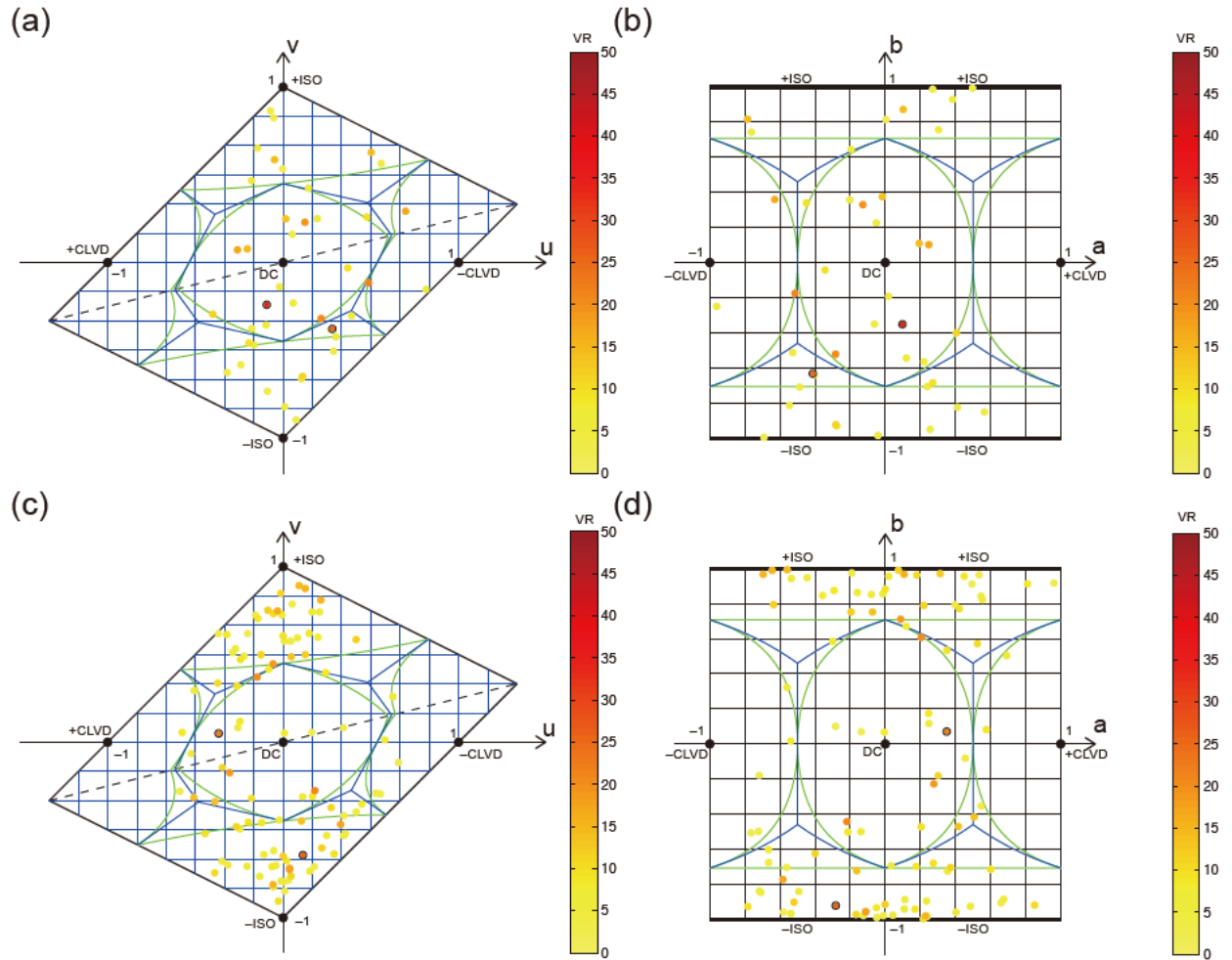
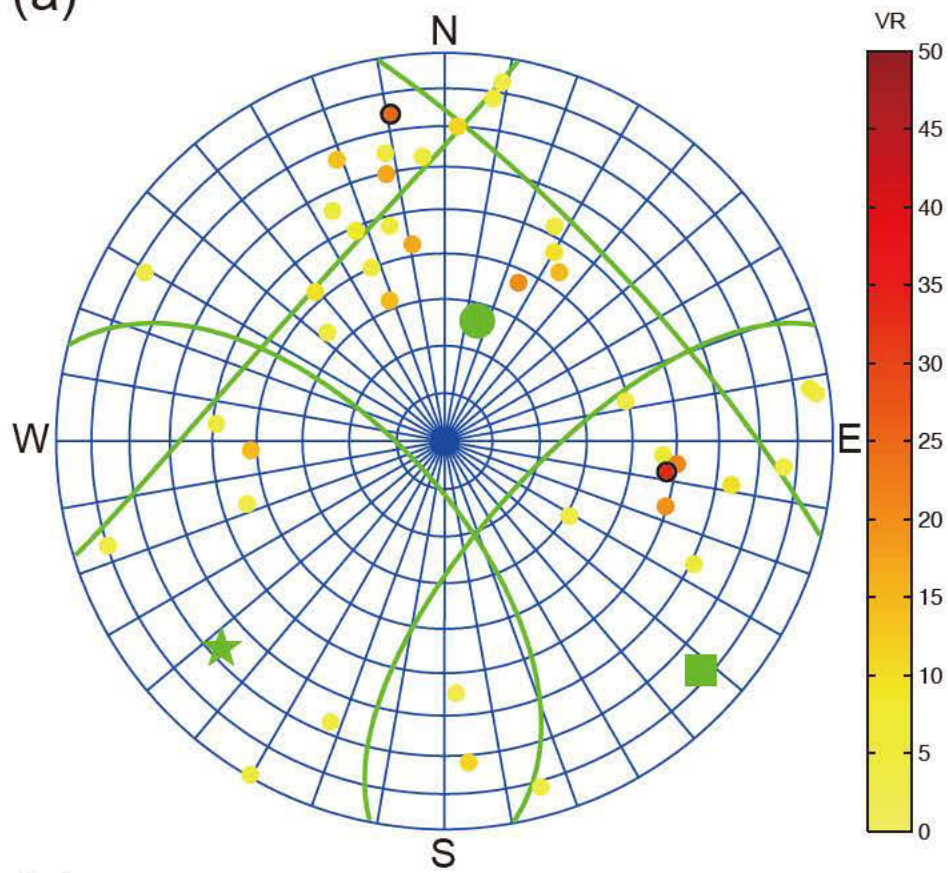


Figure 2.36 Source type distribution in S. Mt. Iwate

Source-type diagram of 41 DLPs in S. Mt. Iwate and the result of analyzing 100 imaginary events composed by background noise are shown in separate panels. The legends are same as in Figure 2.18. (a) DLPs in S. Mt. Iwate in the traditional diagram. (b) DLPs in S. Mt. Iwate in the new diagram. (c) Background distribution in the traditional diagram. (d) Background distribution in the new diagram.

(a)



(b)

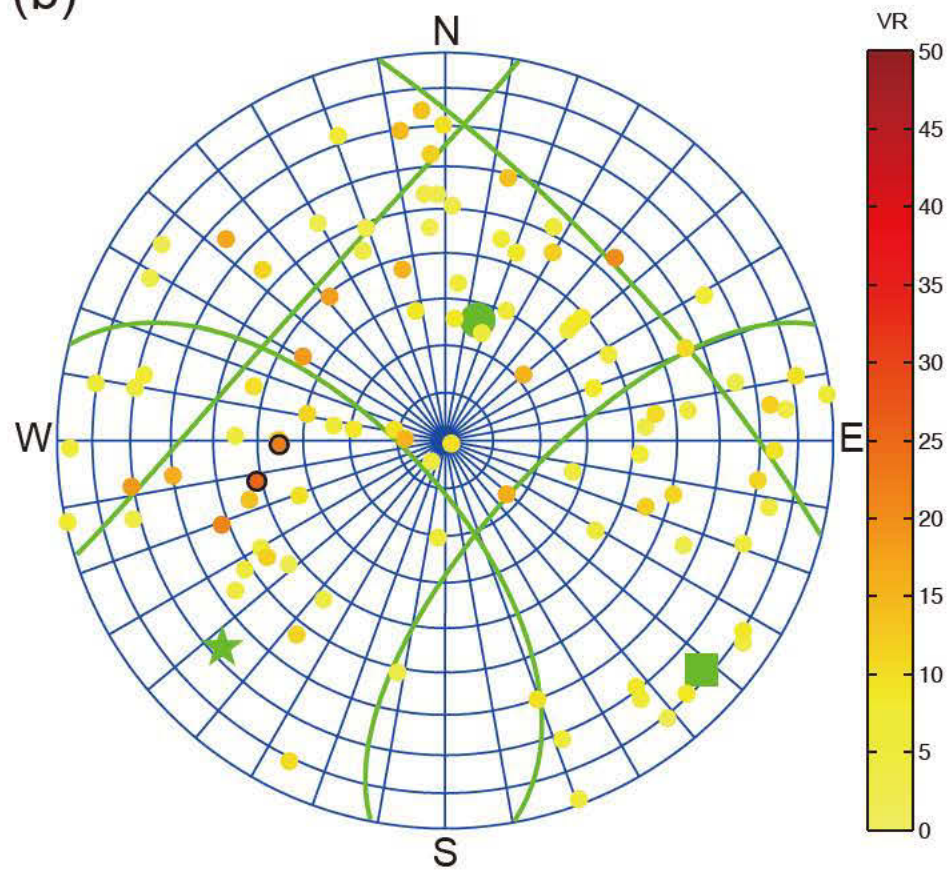


Figure 2.37 Symmetry axis distribution in S. Mt. Iwate

Polar plot of 41 DLPs in S. Mt. Iwate and the result of analyzing 100 imaginary events composed by background noise are shown in separate panels. The principal symmetry axis is plotted in the lower hemisphere. The legends are same as in Figure 2.19. (a) DLPs in S. Mt. Iwate. (b) Background distribution.

The analysis using the structure of *Horikawa et al.* [2001] is shown in Figure 2.38. The event #22 is obtained as DC again and the variance reduction is $VR=31.32\%$, which is still high. Although the major symmetry axis looks different from the original result, it is not appropriate to discuss only on the major symmetry axis for DC-like events and their beach ball plot implied the obtained mechanism is similarly reproduced.

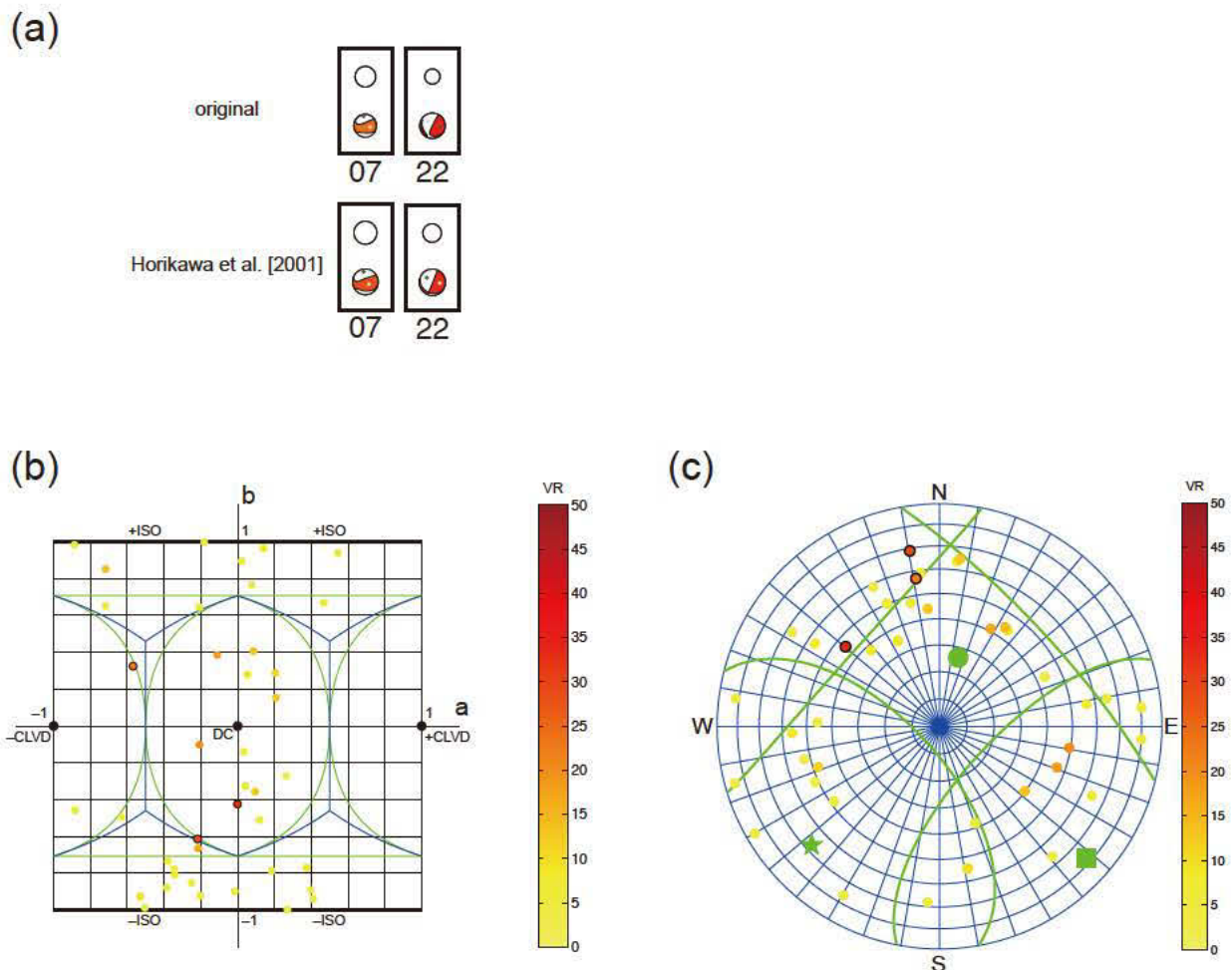


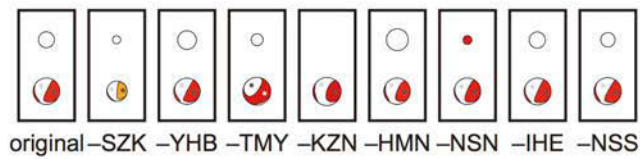
Figure 2.38 Structure dependency test in S. Mt. Iwate

Results of the events in S. Mt. Iwate using the structure of *Horikawa et al.* [2001] are shown. The legends are same as in Figure 2.22. (a) Beach-ball plot. (b) Source-type diagram newly

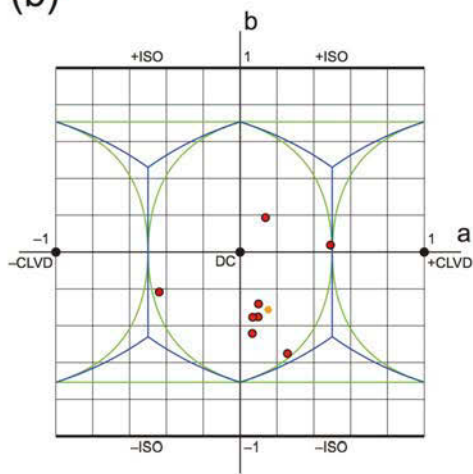
developed in the Appendix A2. (c) Polar plot of the principal symmetry axis in the lower hemisphere.

The jackknife test result is shown in Figure 2.39. The event #22 is stably obtained as DC-like event. Separated distribution of the major symmetry axis (Figure 2.39b) are observed because both P- and T-axes are possible to be regarded as the symmetry axis.

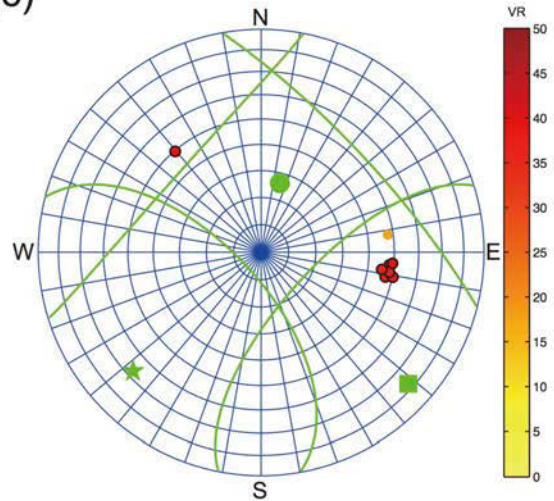
(a)



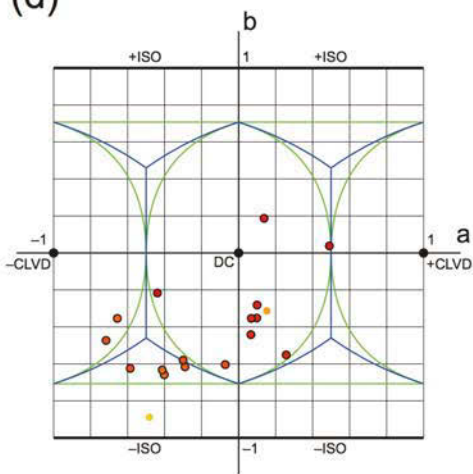
(b)



(c)



(d)



(e)

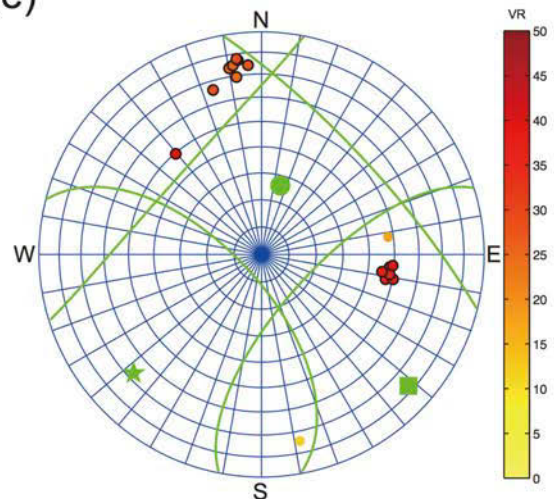


Figure 2.39 Jackknife test in S. Mt. Iwate

Results of the events in S. Mt. Iwate using station sets that excluded each one of the original station set are shown. The legends are same as in Figure 2.23. (a) Beach-ball plot for the event #22. (b) Source-type diagram for the event #22. This diagram is newly developed in the Appendix A2. (c) Polar plot of the principal symmetry axis in the lower hemisphere for the event #22. (d) Source-type diagram for the events that obtained $VR > 20\%$ in the original analysis. (e) Polar plot of the principal symmetry axis for the events that obtained $VR > 20\%$ in the original analysis.

Although it is not sure with confidence whether planar or linear in this cluster, the most reliable event #22 is DC-like and we compare the plausible planar structure with the nodal plane of the DC component. If we consider the source distribution as planar, the plane-normal direction (x_3) of the cluster is consistent with the vertical nodal plane whose strike is in NNE, so we interpret the event #22 is vertical slip on the vertical fault. This focal mechanism seems to be similar to the event “DLFA-1” analyzed in *Nakamichi et al.* [2003].

2.2.3.4. Yakedake

The source mechanism is relatively well determined in Yakedake in the context of VR values. For the representative event #03 that occurred at 14:49:40.29 on April 10th, 2004 (JST), we obtained CLVD-like mechanism with an oscillating time function (Figure 2.40) with a VR value of 40.7% (Figure 2.41; Table 2.5).

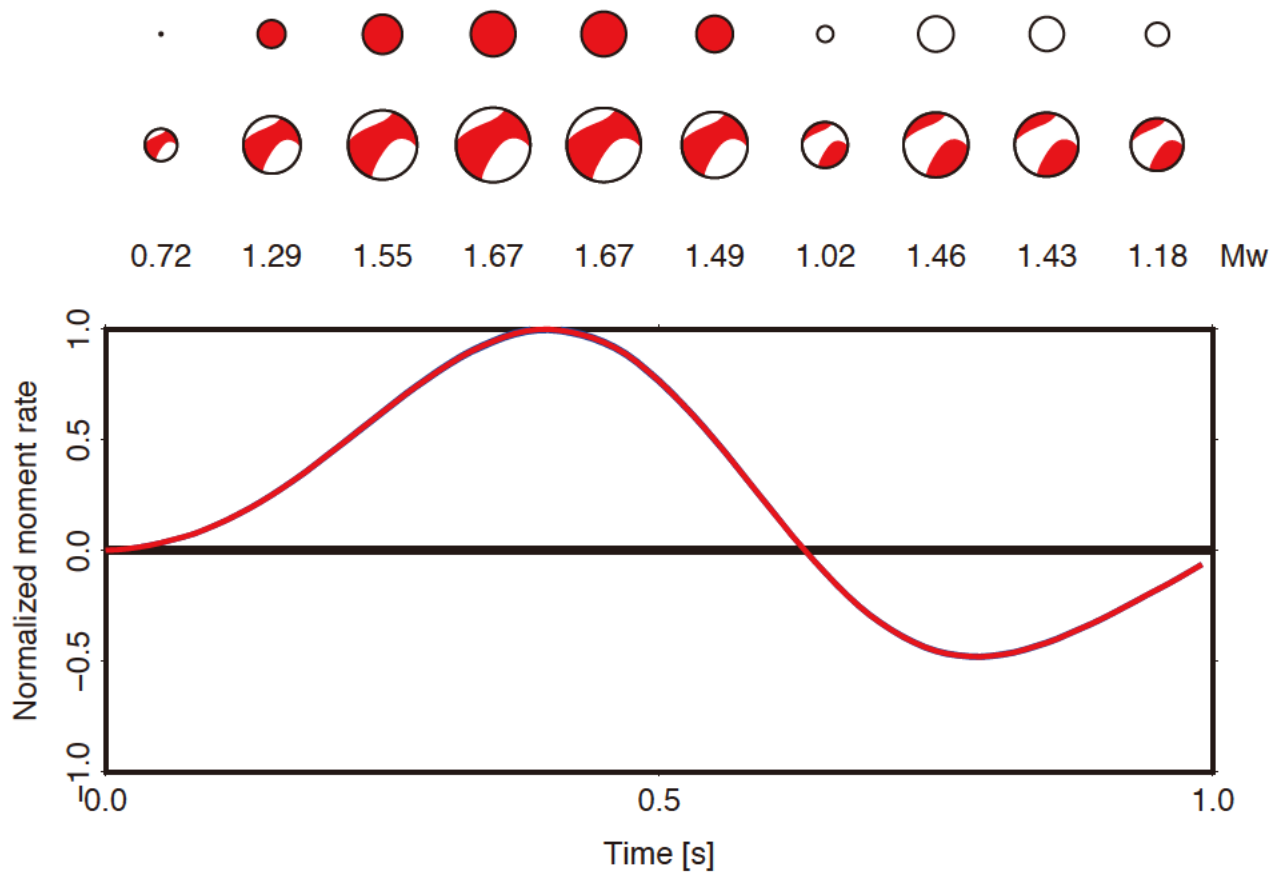


Figure 2.40 Source mechanism for the representative event in Yakedake

Obtained source process of the representative DLP #03 in Yakedake that occurred at 14:49:40.29 on April 10th, 2004 (JST). The legends are same as in Figure 2.14.

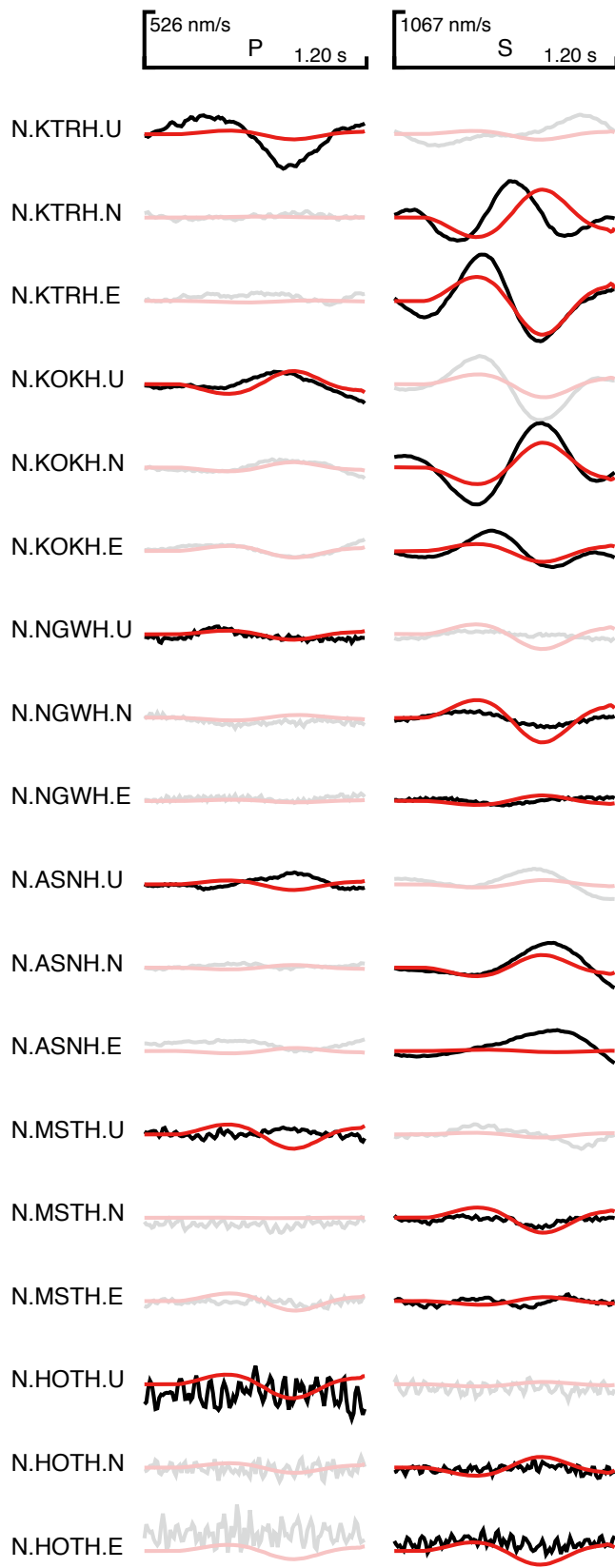


Figure 2.41 Waveform fitness for the representative event in Yakedake

Comparison of observed and synthetic waveforms. Three-component waveforms around P and S wave arrival times at six stations for the event #03 in Yakedake. The legends are same as in Figure 2.15.

Temporal distribution of all events is shown in Figure 2.42. Source mechanisms are obtained with high VR values for many events (nine events with $VR > 20\%$). The DLP activity is not continuously but episodically. For example, 227 events were detected in 2004, while only 12 events were detected in 2006 and also in 2012. Although it is difficult to find temporal variation of mechanism, some major events seem to have similar characteristics. For example, #03 and #26 have similar major symmetry axis in the SE direction. The events #05 and #09 looks similar DC events. Spatial distributions of all events are shown in Figure 2.43. There is no clear relationship between characteristic orientation of source mechanism and that of source distribution (Figure 2.43). Although two DC-like events and two CLVD-like events were obtained among nine events with $VR > 20\%$, (Figure 2.44), three of them were marginal events between CLVD and the other components, which is clearly different from pure DC events (#03, #21, and #26). Although it is difficult to make statistical discussions only from the nine events, the p-value for two CLVD-like events out of nine is estimated to be $1 - \text{binocdf}(2-1, 9, 6/100) = 0.0978$ considering only six events out of 100 was CLVD-like in the analysis of background noise. The direction of the CLVD component of #03 and #26 is closer to the x_3 direction rather than x_1 or x_2 directions, while that of #21 is closer to the x_2 direction (Figure 2.45). Since the event #21 locates slightly away from the events #03 and #26, there might be some mechanism difference.

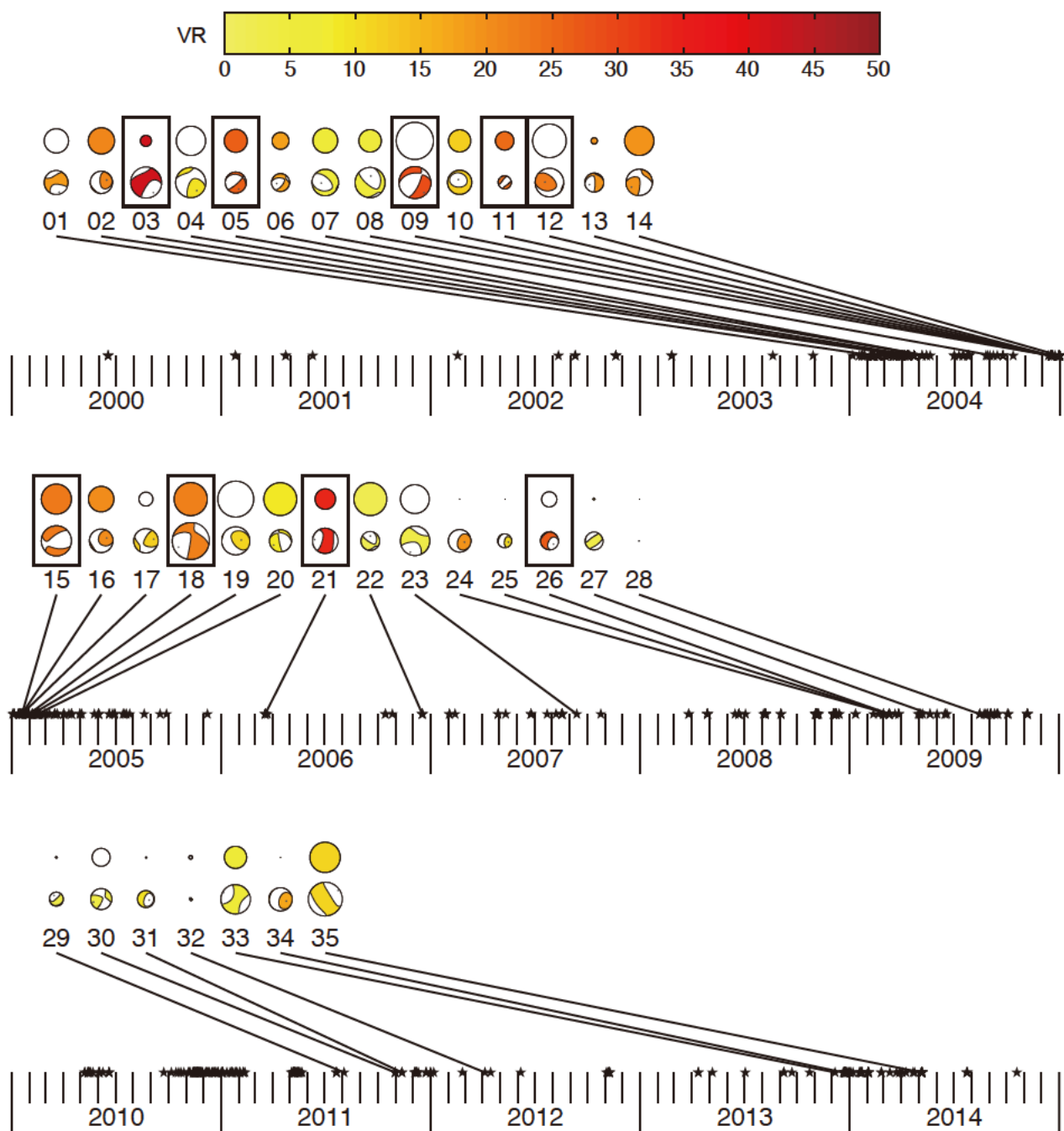


Figure 2.42 Temporal mechanism distribution in Yakedake

Temporal distribution of DLP mechanisms in Yakedake. Moment tensors for all 35 events plotted on a time axis. The legends are same as in Figure 2.16.

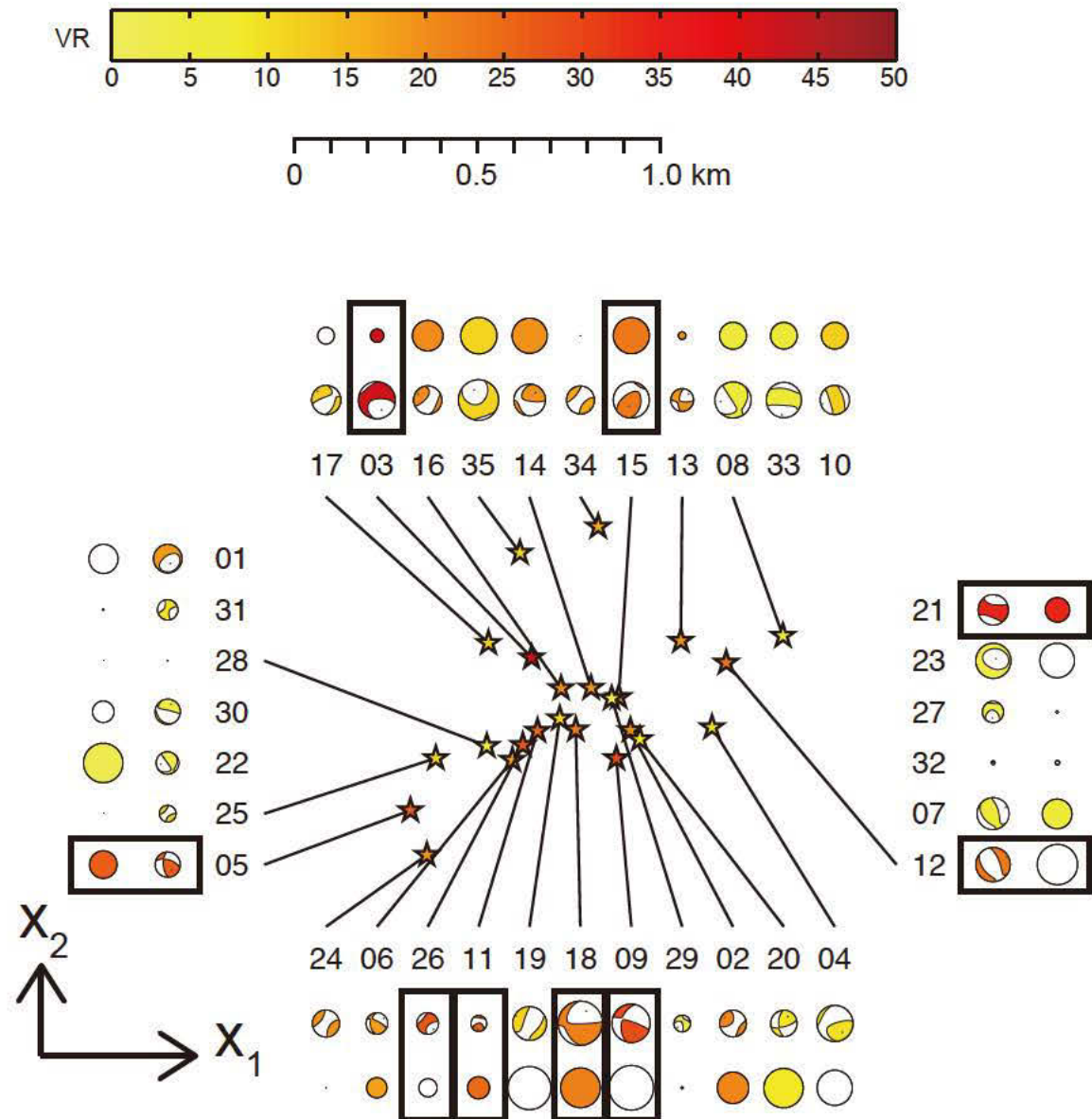


Figure 2.43 Spatial mechanism distribution in Yakedake

Spatial distribution of DLP mechanisms in Yakedake. Moment tensors for all 35 events shown in the x_1 - x_2 plane. The legends are same as in Figure 2.17. The location of the event outside the plot area is not shown but its mechanism is shown.

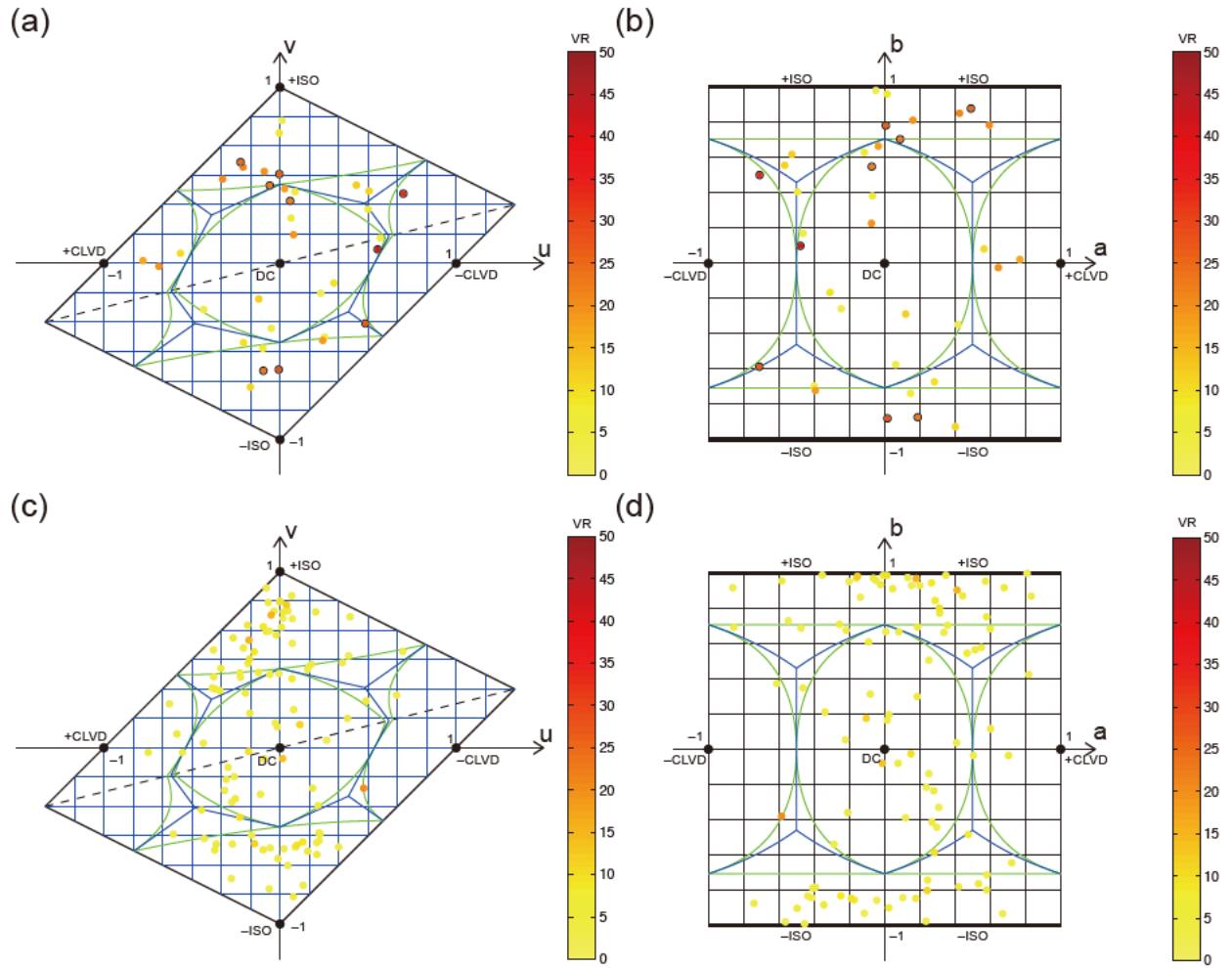
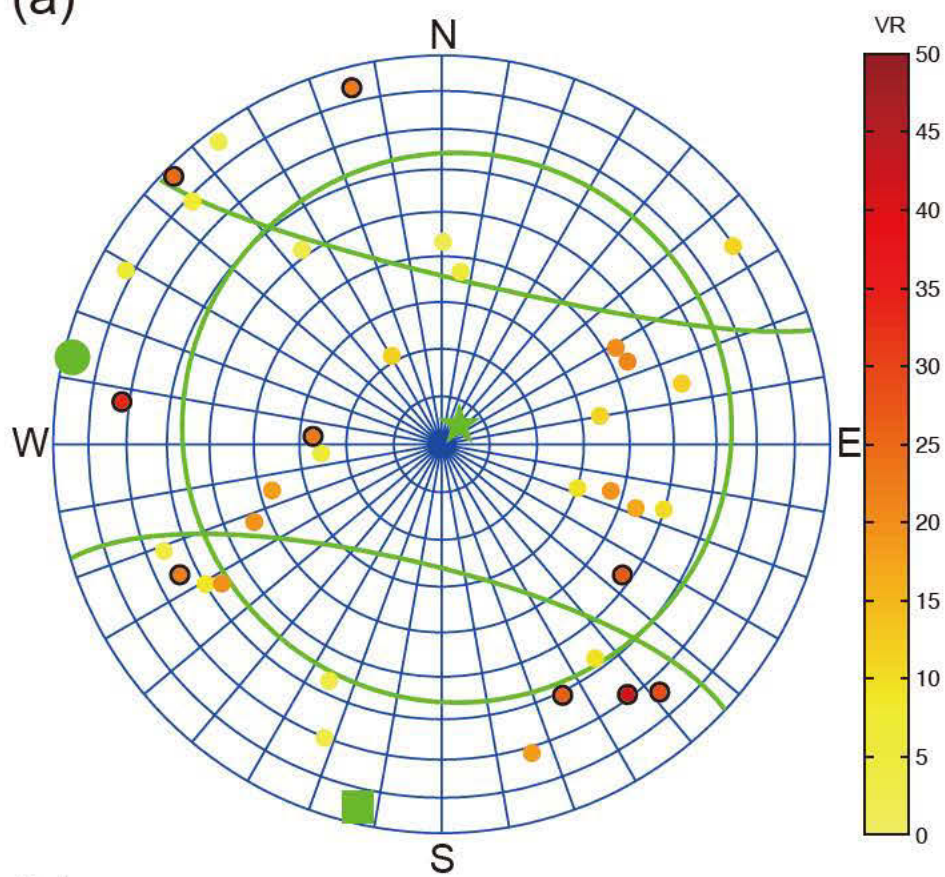


Figure 2.44 Source type distribution in Yakedake

Source-type diagram of 35 DLPs in Yakedake and the result of analyzing 100 imaginary events composed by background noise are shown in separate panels. The legends are same as in Figure 2.18. (a) DLPs in Yakedake in the traditional diagram. (b) DLPs in Yakedake in the new diagram. (c) Background distribution in the traditional diagram. (d) Background distribution in the new diagram.

(a)



(b)

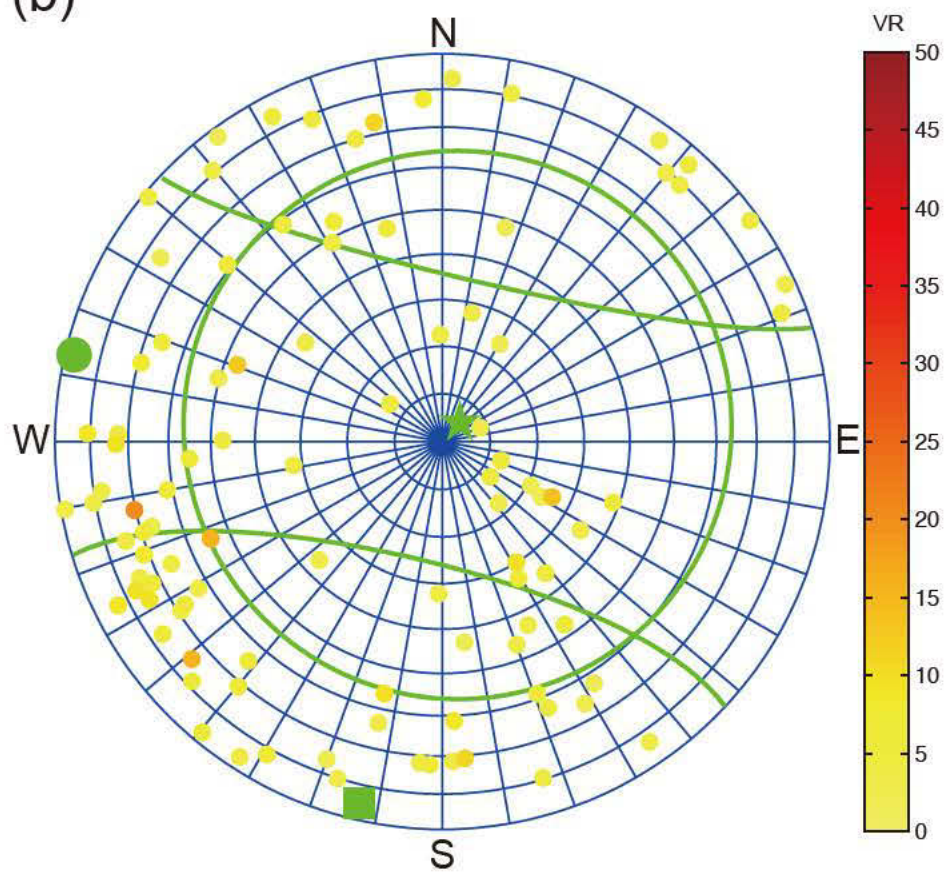


Figure 2.45 Symmetry axis distribution in Yakedake

Polar plot of 35 DLPs in Yakedake and the result of analyzing 100 imaginary events composed by background noise are shown in separate panels. The legends are same as in Figure 2.19. (a) DLPs in Yakedake. (b) Background distribution.

Basic shape of focal mechanism does not change when we use the velocity structure of *Horikawa et al.* [2001] (Figure 2.46). The station set also does not affect the result much (Figure 2.47).

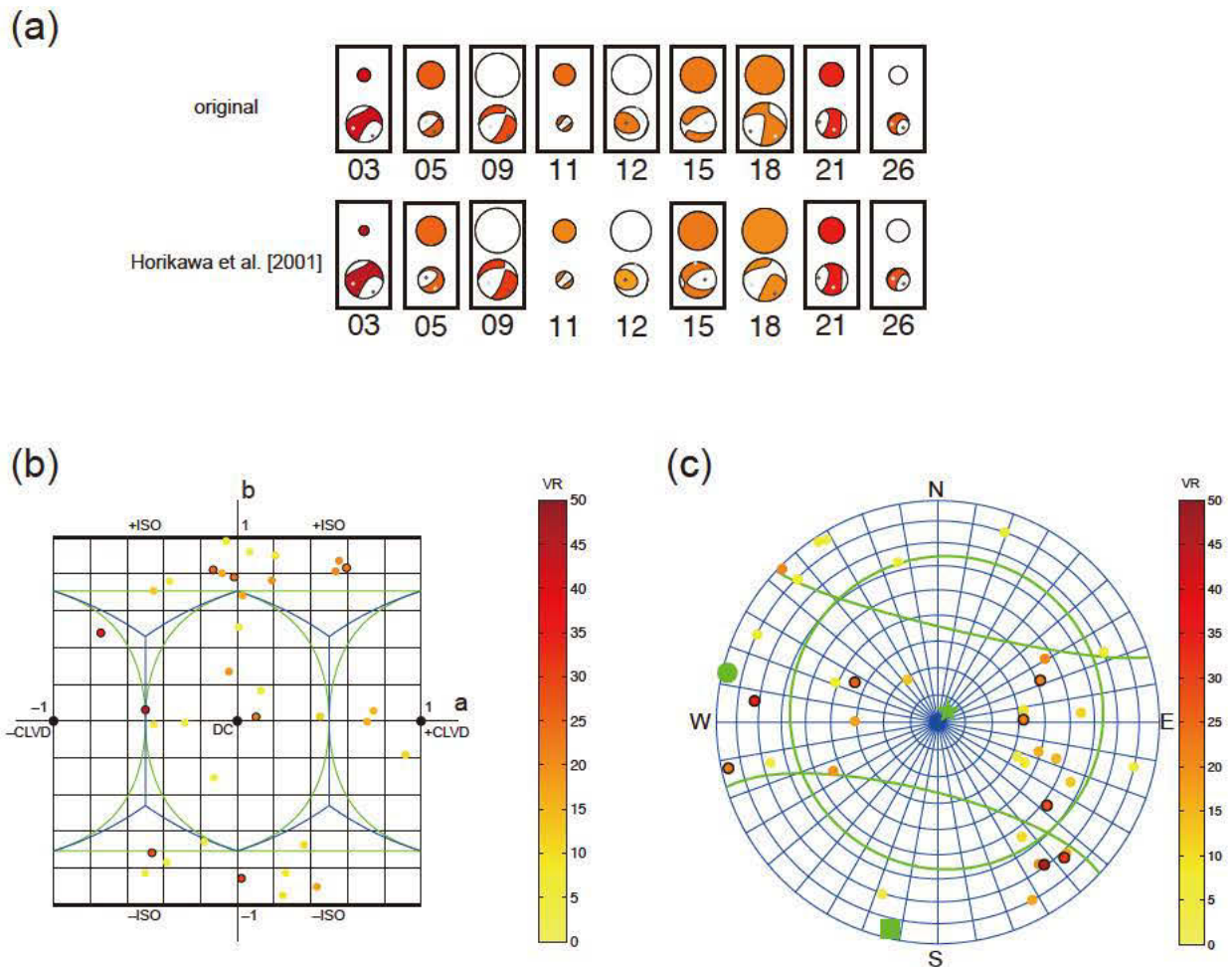


Figure 2.46 Structure dependency test in Yakedake

Results of the events in Yakedake using the structure of *Horikawa et al.* [2001] are shown. The legends are same as in Figure 2.22. (a) Beach-ball plot. (b) Source-type diagram newly developed in the Appendix A2. (c) Polar plot of the principal symmetry axis in the lower hemisphere.

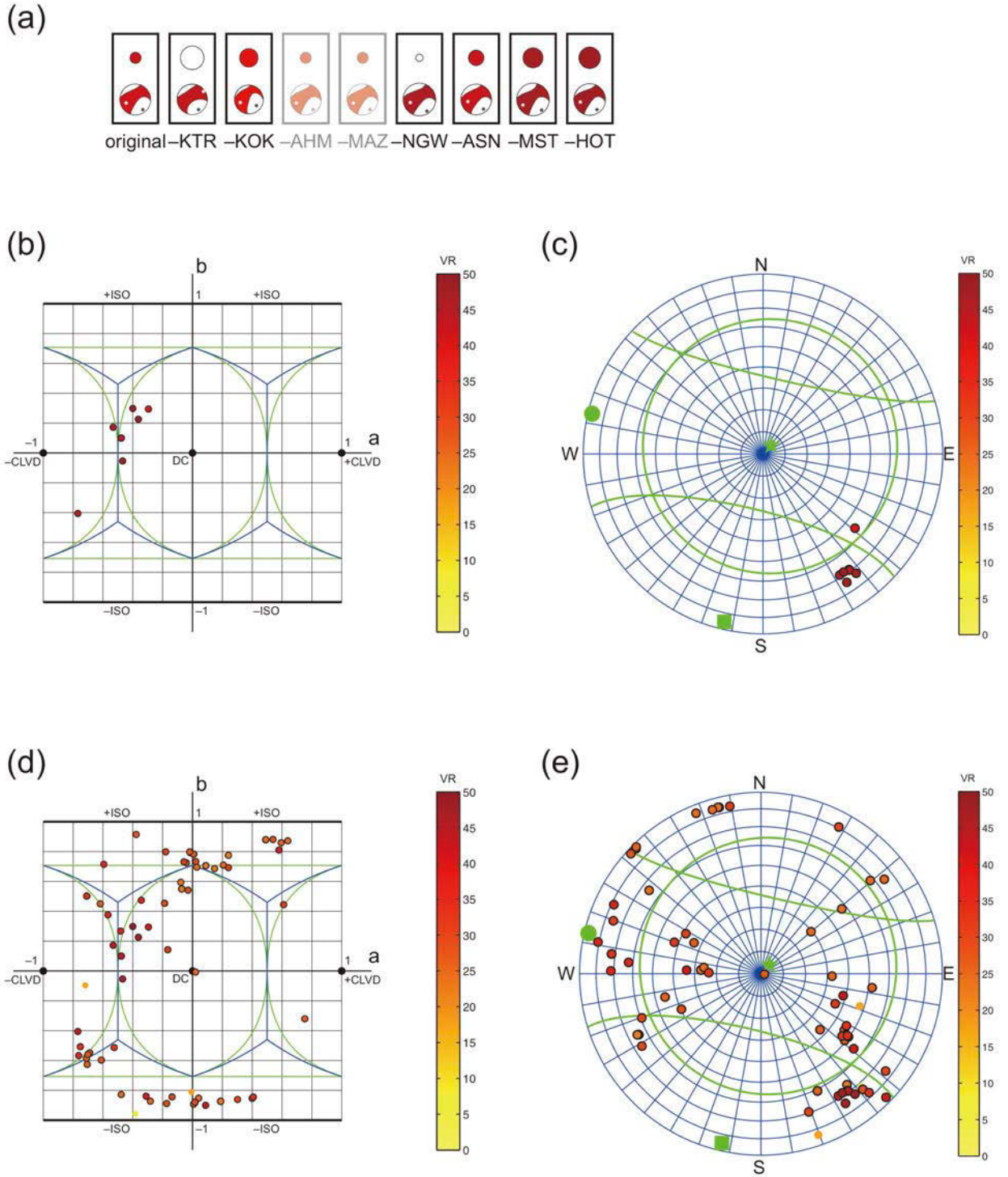


Figure 2.47 Jackknife test in Yakedake

Results of the events in Yakedake using station sets that excluded each one of the original station set are shown. The legends are same as in Figure 2.23. (a) Beach-ball plot for the event #03. (b) Source-type diagram for the event #03. This diagram is newly developed in the Appendix A2. (c) Polar plot of the principal symmetry axis in the lower hemisphere for the event #03. (d) Source-type diagram for the events that obtained VR > 20% in the original

analysis. (e) Polar plot of the principal symmetry axis for the events that obtained $VR > 20\%$ in the original analysis.

In Yakedake, non-double-couple events were observed and some events have the CLVD component whose symmetry axis is between $\sim x_2$ and $\sim x_3$ directions (Figure 2.45). The difficulty in interpretation is the different orientation of the CLVD component between SE (#03 and #26) and W (#21) but each of them are perpendicular to the x_1 direction. In addition to the variety of major symmetry axis orientation, the x_2 and x_3 directions are also less constrained. For the x_3 direction, we obtained $\sim S10W$ direction for the second relocation (Figure 2.6), but the first relocation obtained $\sim S10E$ direction (Figure 2.3o; Table 2.1) and there is $\sim 20^\circ$ difference. However, even considering this variability, the symmetry axis of the CLVD component is more like perpendicular to the x_1 direction, which is different with the sub-parallel relationship in E. Shimane. This difference might be related to the difference of cluster shape among them (linear in E. Shimane and planar in Yakedake) but we do not have any clear explanations. Although the polarity of CLVD has important information, it is difficult to determine systematic characteristics of polarity of the CLVD whether positive or negative and more optimal recognition of polarity by a campaign observation would be important to determine the polarity.

2.2.4. Summary of Inversion Results

We applied sophisticated analysis procedure in four major regions of DLPs in Japan. Following several stability tests, statistically significant results were not obtained for most events. However, the CLVD component is not negligible for some events in E. Shimane and its symmetry axis is sub-parallel to the orientation formed by the hypocenter distribution. The non-negligible CLVD component was also observed for some events in Yakedake but the orientation of the CLVD component is not well interpreted. The representative event in S. Mt. Iwate would be a double-couple event.

We focus on modeling DLPs in the next chapter. Since the observational results obtained here are limited and dependent on region, we do not use them as an important constraint of modeling but we compare them with the model expectations.

3. Cooling Magma Model

Despite the unique observational constraints on volcanic DLP events, there are few studies on their physical mechanisms. For similar but shallower volcanic long-period events, there have been some studies on physical models such as a resonant oscillation [e.g., *Julian*, 1994; *Kumagai and Chouet*, 2000; *Jellinek and Bercovici*, 2011; *Dmitrieva et al.*, 2013], but the majority of this work focuses on the oscillatory nature of seismic waves rather than the initiation mechanism. Although the modeling of oscillatory nature or low-frequency characteristic is one important approach to understand DLPs, these mechanisms typically require an initiation mechanism such as pressure gradients or stress concentrations, which have not been discussed much in the literature. Here, we focus on the latter problem of the generation of initial failure. One reasonable mechanism capable of producing such initial forcing, which has been largely ignored so far, is the effect of thermal stresses. Although there is an alternative idea such as stress concentrations on a fault, events on a regular fault would have planar distribution unlike linear distribution observed for DLPs in some regions and therefore this mechanism cannot be applied at least in some clusters. Fluid flow would be another possible candidate because it is consistent with the linear hypocenter distribution, but we infer high pressure gradients are less likely to be kept at the Moho depths rather than in the shallower crust because the pressures at the depth are thought to be almost uniform because of the high lithostatic pressure of ~ 100 GPa. Although we do not rule out the possibility of fluid flow related to active volcanism, volcanic DLPs distribute toward far from active volcanoes and we do not necessarily focus only on active volcanisms. We therefore consider the thermal stresses driven by cooling body of magmas. Cracks attributed to diffusional process are also studied in the applied physics field [*Otsuki*, 2005; *Ooshida*, 2008].

To address the question of whether thermal processes in volcanic regions can produce stresses consistent with observed volcanic DLP events, we perform calculations of the thermodynamical stresses within a few simple geometries and their effects on brittle failure.

Such brittle failures caused by thermal stresses are geologically observed for shallower depths. The most widely observable is a columnar joints [*Aydin and DeGraff*, 1988] (Figure 3.1). The joint faces of columnar joints are the cavity produced by thermal contraction and density change during solidification. The observed shapes of joints are various and there are columnar joints that are produced by cooling on curved surface such as cylinder [*Spry*, 1962]. The direction of each joint is known to be parallel to that of heat flow. Such cracks produced by cooling process are also observed at wider scale of ~ 8 km in Diamond Joe Stock, Western Arizona, USA [*Gerla*, 1988]. The major rock type of this example is granite produced at the depth ~ 2 km. As observed in plutonic rocks, such cracks can be produced at a certain depth from the ground surface. We therefore suppose such crack

produced in cooling process can exist at the depth around the Moho and estimate the effect quantitatively.

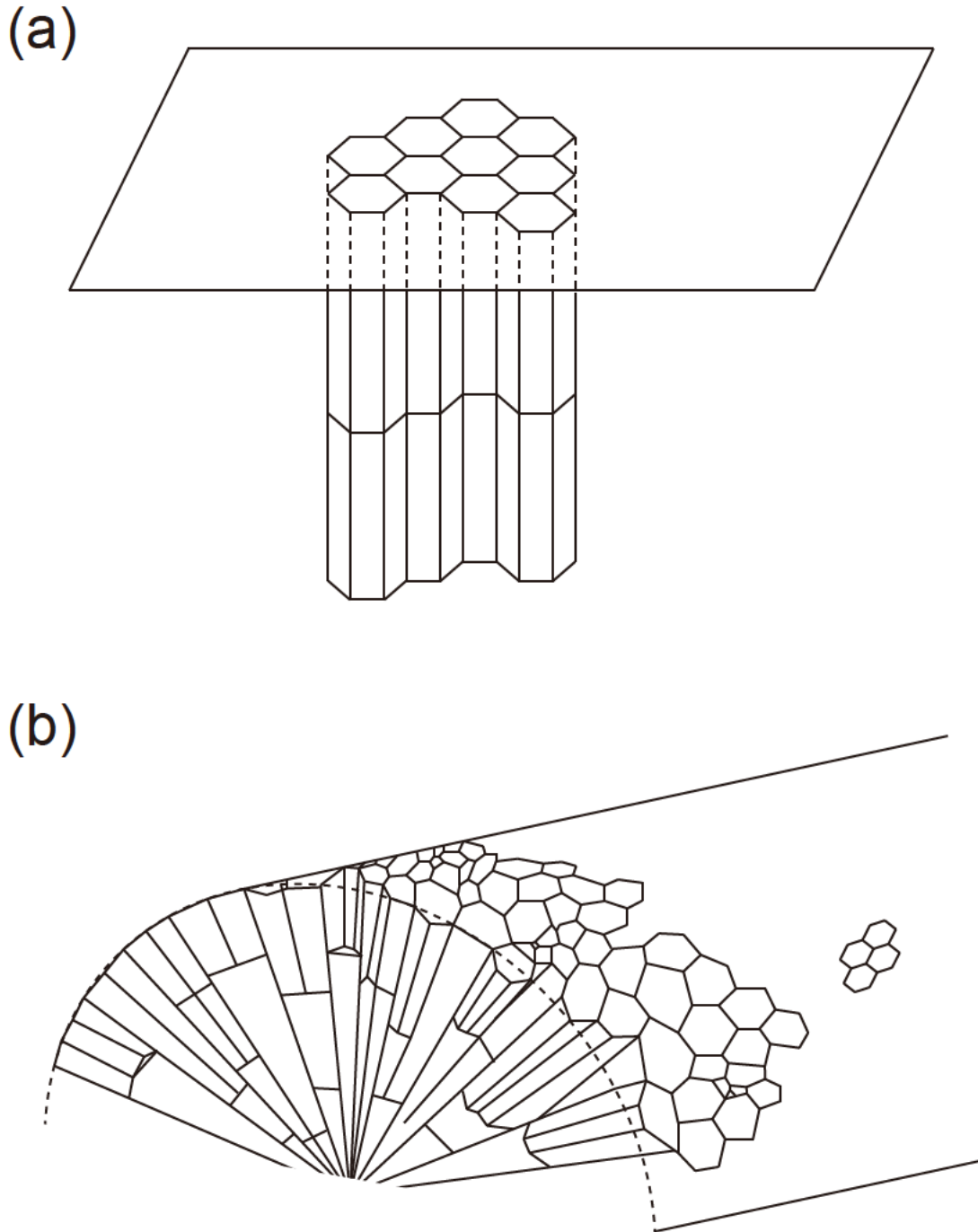


Figure 3.1 Schematic of columnar joints and cylindrical joints

(a) Columnar joints. (b) Cylindrical joints.

To further motivate our focus on thermal stresses, we consider the spatial distribution of volcanic DLP events. As shown in Figure 1.4, most volcanic DLP events occur at depths near the

Moho (crust-mantle boundary), and relatively localized to volcanic regions. The localization alone suggests that tectonic forces do not cause these events since tectonic strain would be widespread within the upper plate. On the other hand, since the Moho is a geological discontinuity where the vertical gradient of density is high, it is possible that ascending magma diapirs tend to stagnate there (Figure 3.2). A stagnant magma body would melt nearby rock just after intrusion and would subsequently cool. This cooling process occurs gradually, and probably controls the in-situ thermodynamical process for a long time. Therefore, we suggest that cooling magma may play an important role in volcanic DLP event occurrence. Thermal contraction of cooling magma can potentially produce large strain rates and, in the present study, we therefore estimate the thermal strain rates caused by cooling magma near the Moho beneath volcanoes. Then, we verify whether the thermal strain rates can cause brittle failure or not, and discuss their connection to the subsequent larger deformations with CLVD mechanisms and low-frequency radiation characteristic of volcanic DLP events. This cooling magma concept is a new idea for the driving force of volcanic DLP events. We note that this model itself does not explain the low-frequency or harmonic characteristics of the seismic waveforms, but is an important candidate for their driving force.

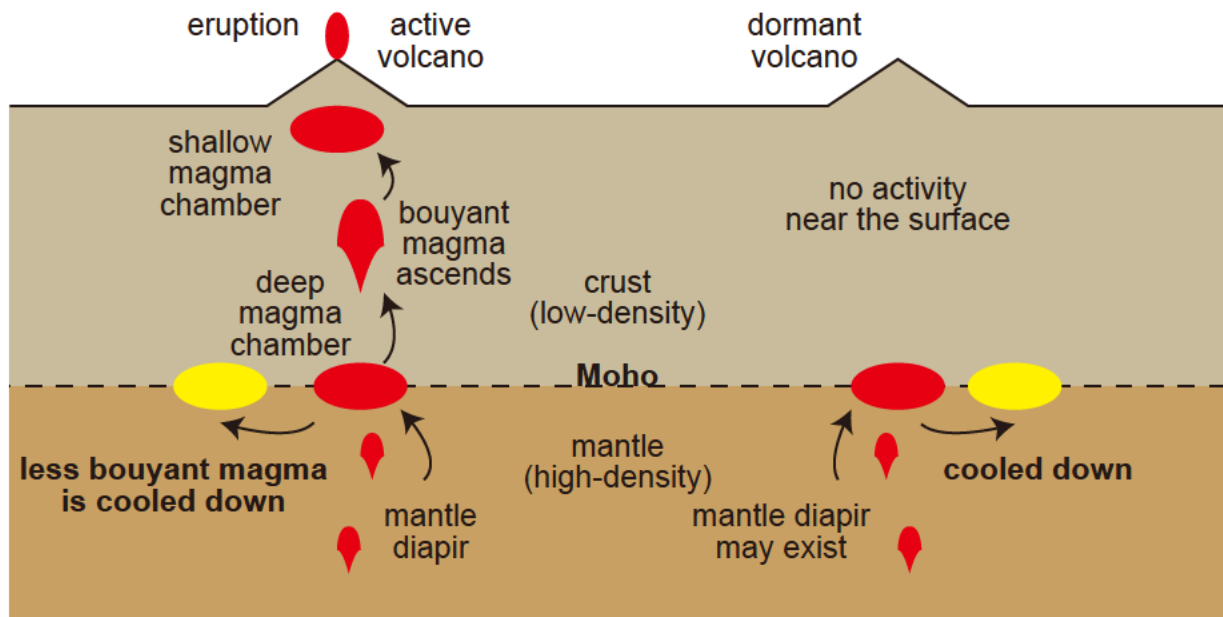


Figure 3.2 Schematic of magma ascending and cooling

Schematic of magma ascending and cooling for an (left) active volcano scenario and a (right) dormant volcano.

3.1. Model

To model the cooling process of emplaced magma, we set an initial thermal distribution within the intruded magma. We assume simple shapes of magmas because small-scale fluctuations are

expected to decay quickly. Although geological study reports planar intrusions at shallow depths, the molten magma region may become pipe-like shape during the cooling process even for a planar intrusion because of more or less heterogeneity. Typical shapes of magmas are spherical, tabular, and cylindrical, which correspond to three-, two-, and one-dimensional intrusions, but all of them are approximately expressed by finite-length cylinders with various aspect ratios. Therefore, we assume tabular and cylindrical magmas as end-members of magma shapes (Figure 3.3a and Figure 3.3b). In section 3.3.5, we also comment on the results for finite-length cylinders with varying aspect ratios (Figure 3.3c).

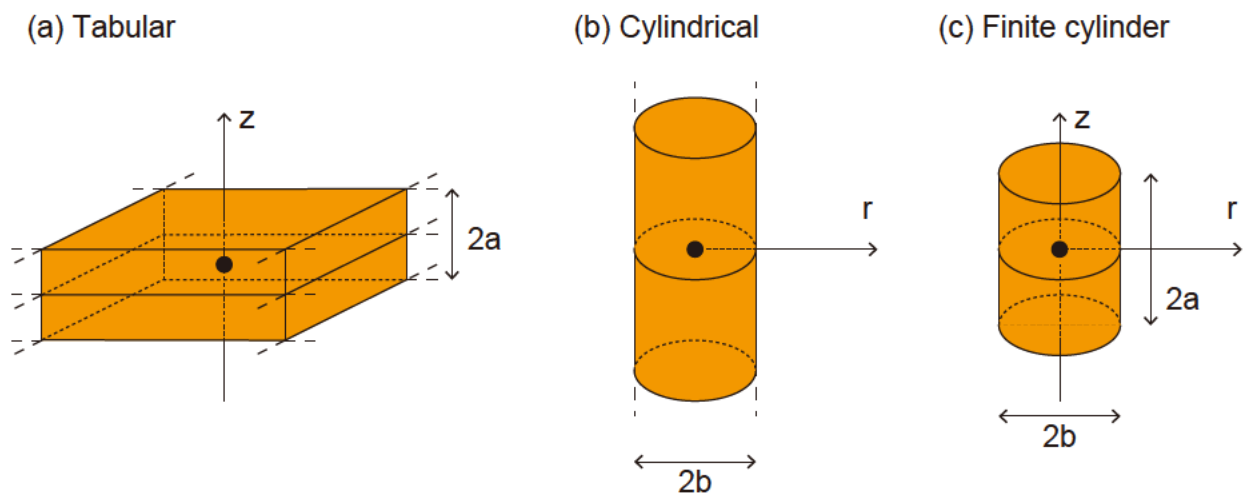


Figure 3.3 Assumed shapes of intruded magma.

The model regions of intruded magma are either (a) tabular, (b) cylindrical and infinitely long, or (c) a finite cylinder.

Before providing our calculation, we first comment on the length scales and timescales of interest. Since many volcanic DLP sequences have continuous seismicity over ten-year long records as explained in the introduction, we focus on phenomena whose timescale is longer than ten years. Since volcanic activity changes over thousands of years, we focus on timescales of 10–1000 years or 3×10^8 – 3×10^{10} seconds. For a typical thermal diffusivity ($10^{-6} \text{ m}^2/\text{s}$), the thermal diffusion length scale is 20–200 meters over the times considered, although it depends on shape, and is consistent with the width of magma that is inferred from each small cluster of volcanic DLP events reported by *Aso et al.* [2013].

We assume an initial thermal perturbation of 400°C uniformly throughout the intruded magma. This assumption is appropriate for a near-liquidus body (950–1250°C [Wyllie, 1977]) that intrudes into host rock at close to Moho depths (600–800°C [Yoshioka and Murakami, 2007]). We do not consider the effect of volatiles because the effect of volatiles is difficult to treat in a simple model and also has

large unknowns. For other model parameters, we assume a Poissonian elastic body ($\lambda = \mu$), a thermal diffusivity of $\alpha_0 \sim 10^{-6} \text{ m}^2 \text{ s}^{-1}$, and a thermal expansion coefficient of $\kappa_0 \sim 10^{-5} \text{ K}^{-1}$ [Eppelbaum *et al.*, 2014]. To include the effect of partial melting, we assume a density change of $\delta\kappa = 1\%/600\text{K} = 1.66 \times 10^{-5} \text{ K}^{-1}$ so that $\kappa = \kappa_0 + \delta\kappa = 2.66 \times 10^{-5} \text{ K}^{-1}$, and assume a latent heat release of $\delta c = 400 \text{ kJ kg}^{-1}/600\text{K} = 0.66 \times 10^3 \text{ J kg}^{-1} \text{ K}^{-1}$ so that the specific heat ($c_0 = 10^3 \text{ J kg}^{-1} \text{ K}^{-1}$) increases by δc and $\alpha = \alpha_0 c_0 / (c_0 + \delta c) = 0.6\alpha_0 = 6 \times 10^{-7} \text{ m}^2 \text{ s}^{-1}$. Although complicated metamorphism might occur, here we adopt a constant rate of partial melting to obtain typical values under homogeneous conditions. We use these rough estimates for an order estimate in the present study.

3.2. Method

In order to achieve our final goal of calculating strain rates throughout the cooling volume, we first calculate the thermal evolution, which can be obtained analytically for the simple geometries assumed. Once the thermal evolution is known, we then calculate the thermal strains. In this section, we separately explain the calculation methods of thermal evolution and thermal strain rates.

3.2.1. Thermal Calculation

We first calculate the thermal evolution, by solving thermal diffusion equations. We expect convection to be insignificant because Rayleigh numbers can be estimated to be much smaller than the critical Rayleigh number. The Rayleigh number is estimated to be $\rho g \kappa \Delta T L^3 / \eta \alpha \sim (3 \times 10^3) \times 9.8 \times (2 \times 10^{-5}) \times 400 \times 100^3 / 10^{18} / (6 \times 10^{-7}) \sim 4 \times 10^{-4}$, for density of $\rho = 3 \times 10^3 \text{ kg/m}^3$, gravitational acceleration of $g = 9.8$, typical length-scale of $L = 100 \text{ m}$, and viscosity of $\eta = 10^{18}$, and is smaller than the critical Rayleigh number of $\sim 10^3$ even considering the variability of viscosity as pointed out later. Detailed derivations are shown in the Appendices 0–A5. For a tabular intrusion, we set an initial condition of $T = \Delta T$ within $|z| \leq a$ and $T = 0$ outside this range. Since the thermal evolution for a thermal perturbation that is expressed as a step function is given by an error function, a plane-symmetric solution is obtained by a combination of error functions as

$$T = \frac{\Delta T}{2} \left[\text{erf}\left(\frac{z^* + a^*}{2\sqrt{t^*}}\right) - \text{erf}\left(\frac{z^* - a^*}{2\sqrt{t^*}}\right) \right] \equiv \Delta T \cdot T_z^*(t^*, z^*), \quad (3.1)$$

where $\text{erf}(x)$ is the error function and non-dimensional variables are defined as $T^* \equiv T/\Delta T$, $z^* \equiv z/\sqrt{\alpha t_c}$, $a^* \equiv a/\sqrt{\alpha t_c}$, and $t^* \equiv t/t_c$ with a characteristic timescale of t_c .

For a cylindrical intrusion, we set an initial condition of $T = \Delta T$ within $r \leq b$ and $T = 0$ outside. Since thermal diffusion in polar coordinates is generally given by a combination of Bessel functions, after Hankel inverse transforming the initial condition, the solution is obtained by a combination of exponential functions about t and Bessel functions about r as

$$T = \Delta T \int_0^\infty J_1(q) \exp\left(-\frac{t^*}{b^{*2}} q^2\right) J_0\left(\frac{r^*}{b^*} q\right) dq \equiv \Delta T \cdot T_r^*(t^*, r^*), \quad (3.2)$$

where $J_n(x)$ is the n -th order Bessel function and the non-dimensional variables are $r^* \equiv r/\sqrt{\alpha t_c}$ and $b^* \equiv b/\sqrt{\alpha t_c}$.

For a finite-length cylindrical intrusion, separation of variables leads to the solution for an initial condition of $T = \Delta T$ within the region $|z| \leq a$ and $r \leq b$ and $T = 0$ outside as

$$T = \Delta T \cdot T_z^*(t^*, z^*) \cdot T_r^*(t^*, r^*) = \Delta T \cdot T_{zr}^*(t^*, z^*, r^*), \quad (3.3)$$

using the solutions (1) and (2) for tabular and cylindrical magmas, respectively, as described above.

We define our characteristic thermal diffusion timescale t_c as the time that it takes for the central temperature perturbation to decrease by half of its original value. This choice of t_c results in $T_z^*(1, 0) = T_r^*(1, 0) = 0.5$, and normalized diffusion length scales of $a^* = 0.95$ and $b^* = 1.66$. For a realistic value of $t_c = 100$ years, the half-width of the tabular intrusion is $a = 41$ m and the radius of the cylinder is $b = 74$ m.

3.2.2. Thermal Strain Rates

Thermal strain is produced by a combination of thermal contraction and elasticity. For the case where temperature is driven only by thermal diffusion within a material of homogeneous parameters of elastic constants (λ and μ), volumetric thermal expansion coefficient (κ), and thermal diffusivity (α), and assuming an adiabatic boundary conditions with no normal displacement, the velocity (v_i) is given as [Timoshenko and Goodier, 1970]

$$v_i = \frac{3\lambda + 2\mu}{\lambda + 2\mu} \frac{\alpha \kappa}{3} \frac{\partial T}{\partial x_i}. \quad (3.4)$$

A detailed derivation is summarized in Appendix 0, but the basic reason for this structure is that strain rates are proportional to the time rate of change of temperature and this time rate of change can be related to spatial temperature gradients through the diffusion equation.

With the thermal evolution obtained in the previous sub-section, we calculate the strain rate in cylindrical coordinates as

$$\begin{aligned} \begin{pmatrix} \dot{\epsilon}_{rr} & \dot{\epsilon}_{r\theta} & \dot{\epsilon}_{rz} \\ \dot{\epsilon}_{\theta r} & \dot{\epsilon}_{\theta\theta} & \dot{\epsilon}_{\theta z} \\ \dot{\epsilon}_{zr} & \dot{\epsilon}_{z\theta} & \dot{\epsilon}_{zz} \end{pmatrix} &= \left(\frac{3\lambda + 2\mu}{\lambda + 2\mu} \frac{\kappa \Delta T}{3t_c} \right) \begin{pmatrix} \frac{\partial^2 T^*}{\partial r^{*2}} & 0 & \frac{\partial^2 T^*}{\partial r^* \partial z^*} \\ 0 & \frac{1}{r^*} \frac{\partial T^*}{\partial r^*} & 0 \\ \frac{\partial^2 T^*}{\partial r^* \partial z^*} & 0 & \frac{\partial^2 T^*}{\partial z^{*2}} \end{pmatrix} \\ &\equiv \left(\frac{3\lambda + 2\mu}{\lambda + 2\mu} \frac{\kappa \Delta T}{3t_c} \right) \begin{pmatrix} \dot{\epsilon}_{rr}^* & \dot{\epsilon}_{r\theta}^* & \dot{\epsilon}_{rz}^* \\ \dot{\epsilon}_{r\theta}^* & \dot{\epsilon}_{\theta\theta}^* & \dot{\epsilon}_{\theta z}^* \\ \dot{\epsilon}_{rz}^* & \dot{\epsilon}_{\theta z}^* & \dot{\epsilon}_{zz}^* \end{pmatrix}, \end{aligned} \quad (3.5)$$

where $\dot{\epsilon}_{ij}^*$ is a normalized strain rate. Using its eigenvalues $\dot{\epsilon}_1^* \geq \dot{\epsilon}_2^* \geq \dot{\epsilon}_3^*$, we define the differential strain rate as

$$\dot{\epsilon}_{dif}^* \equiv \frac{\dot{\epsilon}_1^* - \dot{\epsilon}_3^*}{2}. \quad (3.6)$$

This value can be used as the intensity of the shear strain rate that we are focusing on, because it is maximum shear strain rate on micro-cracks in various directions. High $\dot{\epsilon}_{dif}^*$ is essential for brittle failure because low strain rates result in ductile relaxation rather than accumulation of elastic strain. In addition, cumulative strains are also important to verify whether shear stresses would be brought above the frictional strength or not. Therefore, we focus on strain rates and cumulative strains in sections 3.3.2 and 3.3.3 respectively. In section 3.3.1, we first examine the thermal evolution model and define the time span of interest.

Isotropic strain can also have an important role in brittle failure because it decreases the effective normal stress on any micro-cracks. For isotropic strain, one must account for an apparent strain accompanied by density change because it does not produce elastic stress by itself. For example, although cooling material within free space contracts and thermal strain appears, this process is accommodated by shortening intermolecular distances, and no elastic stress is produced. This apparent strain is given by

$$\epsilon_{app}^* \equiv \frac{\kappa}{3} \delta T / \left(\frac{3\lambda + 2\mu}{\lambda + 2\mu} \frac{\kappa \Delta T}{3} \right) = \frac{\lambda + 2\mu}{3\lambda + 2\mu} \delta T^*, \quad (3.7)$$

where $\delta T = T - T_0$ and $\delta T^* = \delta T / \Delta T$ are the temperature change and its normalized value. Therefore the effective isotropic strain is given by

$$\epsilon_{iso}^* \equiv \frac{1}{3} \sum_i \int \dot{\epsilon}_{ii}^* dt^* - \epsilon_{app}^* = \frac{\delta T^*}{3} - \frac{\lambda + 2\mu}{3\lambda + 2\mu} \delta T^* = \frac{-4\mu}{3(3\lambda + 2\mu)} \delta T^*. \quad (3.8)$$

3.3. Results

3.3.1. Neglecting Early Stage Deformation

The spatio-temporal distribution of deviatoric strain rates for a tabular intrusion is shown in Figure 3.4a, and the corresponding result for a cylindrical intrusion is shown in Figure 3.5a. Since deviatoric part is more stably observed rather than isotropic part as discussed in 2.2.2.4, we mainly focus on deviatoric part of the produced strain or stress. In this context, CLVD is identical to the LVD or crack mechanism. Leaving aside the detail physical deformation process, we focus mainly on the deviatoric component, which is potentially comparable with observations. As shown by both the radii of the beach balls and the contours, the strain rates observed for $t^* < 1.0$ are substantially larger than strain rates at times $t^* > 1.0$, because of the high thermal gradients at early times. However, the temperatures at these times are also close to the liquidus so that we expect significant ductile flow instead of accumulation of elastic strain. Here, we assume complete relaxation of stresses for $T^* > 0.5$ and no ductile deformation for $T^* < 0.5$. Therefore, we focus only on thermal strain rates at times $t^* > 1.0$. Neglecting the deformation in early stages also allows us to consider more complex shapes than the simple tabular or cylindrical ones described above. In particular, small amounts of

surface roughness can be neglected because thermal perturbations associated with these short length scales are expected to decay within $t^* < 1.0$. About the ductile relaxation in a longer timescale, we add detail discussion in 3.3.2.

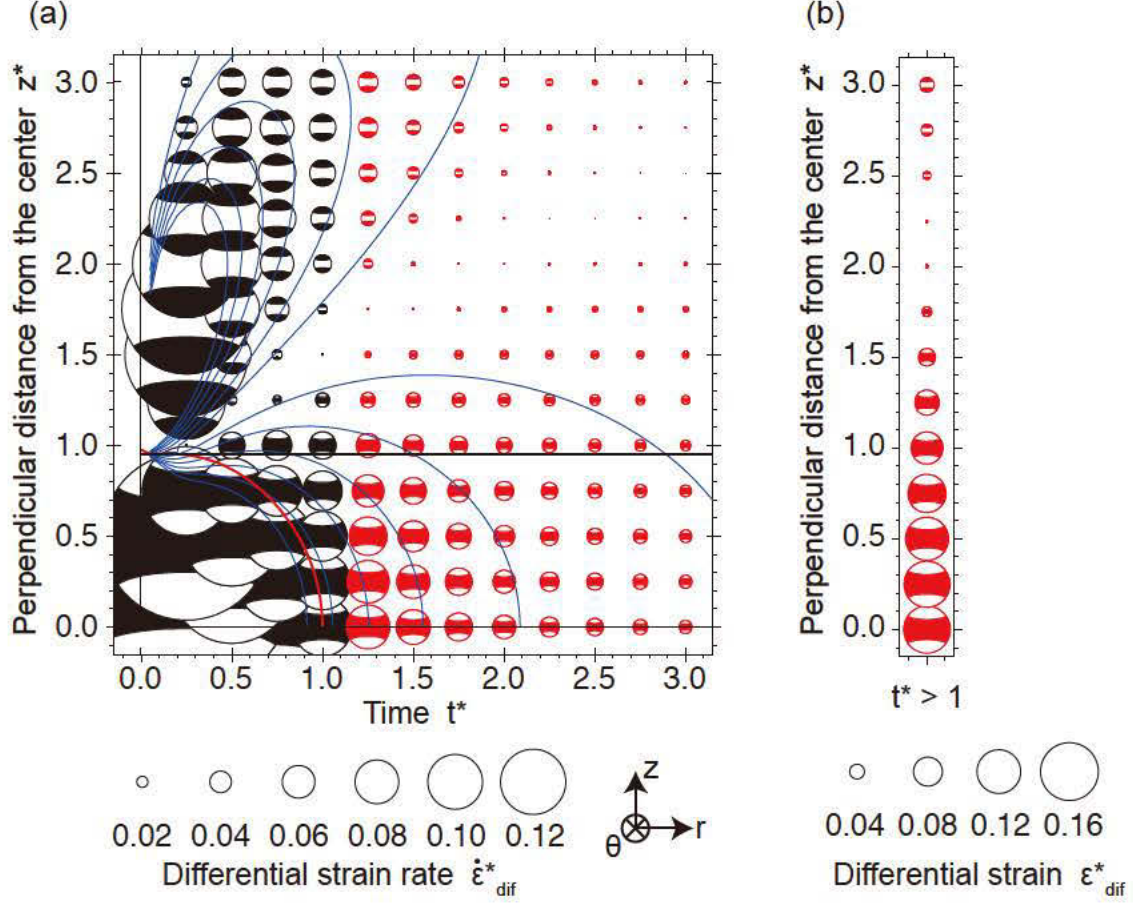


Figure 3.4 Thermal strain rates and strains for a tabular intrusion

a) Thermal strain rates and (b) cumulative thermal strains for $t^* > 1$ caused by a tabular intrusion. The spatiotemporal distribution of deviatoric strain rates are shown in Figure 3.4a. Time is normalized by t_c , which is the time that it takes for the central temperature perturbation to decrease by half of its original value, and the perpendicular distance from the center is normalized by $\sqrt{\alpha t_c}$. The half width of the tabular region is $a^* = 0.95$. At each grid point, deviatoric strain rates are depicted by a beach ball whose diameter corresponds to the differential strain rate shown in the legend below. Thermal strain rates are normalized by $(3\lambda + 2\mu)\kappa\Delta T/3(\lambda + 2\mu)t_c$. Blue contours correspond to the differential strain rates of $\dot{\epsilon}_1^* \dot{\epsilon}_3^* = 0.02, 0.04, 0.06, 0.08, 0.10, \text{ and } 0.12$. A red contour corresponds to the points where $T^* = 0.5$. Cumulative thermal strains for $t^* > 1$ are shown in Figure 3.4b. Thermal strains are normalized by $(3\lambda + 2\mu)\kappa\Delta T/(3\lambda + 2\mu)$.

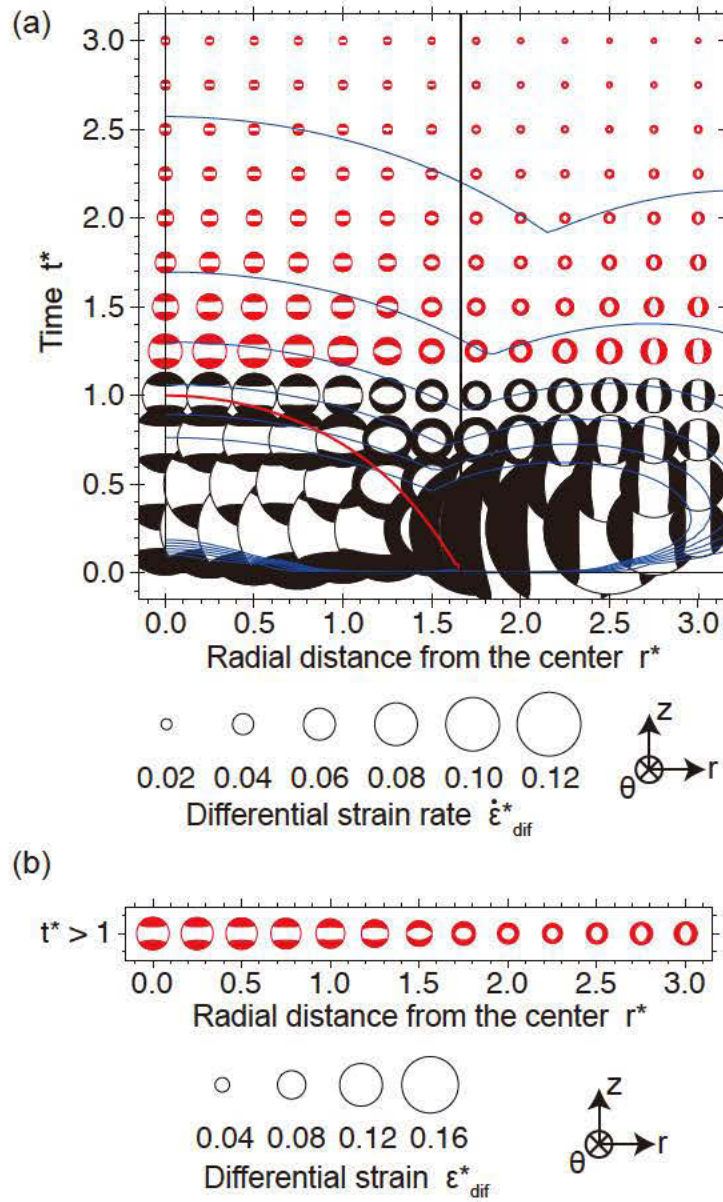


Figure 3.5 Thermal strain rates and strains for a cylindrical intrusion.

(a) Thermal strain rates and (b) cumulative thermal strains of $t^* > 1$ caused by a cylindrical intrusion. Strain rates plotted as in Figure 3.4a with radial distance from the center axis normalized by $\sqrt{\alpha t_c}$ are shown in Figure 3.5a. The radius of the cylindrical region is $b^* = 1.66$. Cumulative thermal strains for $t^* > 1$ plotted as in Figure 3.4b are shown in Figure 3.5b.

3.3.2. Strain Rates

For a tabular intrusion, the differential thermal strain rate within the intruded region ($z^* < a^* = 0.95$) at times $1 < t^* < 2$ is larger than $\dot{\epsilon}_{dif}^* \sim 0.04$ (Figure 3.4a), which corresponds to $\dot{\epsilon}_{dif} \sim 5 \times$

10^{-14} s^{-1} for $t_c = 100$ years because the normalization factor for strain rates is $\frac{3\lambda+2\mu}{\lambda+2\mu} \frac{\kappa\Delta T}{3t_c} = 1.3 \times 10^{-12} \text{ s}^{-1}$. Although the assumption of a Poissonian material might not be realistic for rocks at near liquidus temperatures, the differential strains are proportional to $\frac{3\lambda+2\mu}{\lambda+2\mu}$ and are therefore insensitive to the Poisson's ratio (results can vary only by a factor of two). This strain rate becomes larger for smaller scale of intrusions but continues only for shorter period and becomes smaller for larger scale of intrusions that lasts for longer period.

The ductile relaxation timescale depends on a viscosity. The melt fraction and H_2O fraction have important roles in controlling the viscosity of solidifying melts. The opposite process of gradual melting and gradual solidification might be hysteresis and not necessarily follow the same path. Therefore, we review the condition for solidifying melt, which is close to our case, in stead of the estimation of viscosity for gradual melting [e.g., *Takei and Holtzman*, 2009]. The decrease of melt fraction related to the decrease of temperature is not linear and more solidification occurs in the earlier stage. Considering basalts with 2–4 wt% of H_2O [*Schmincke*, 2004], melt fraction at 1.2 GPa and 800°C is 5–10% [*Annen et al.*, 2006]. The remaining melt composition is SiO_2 -rich Rhyolitic and it would be saturated with water because of the concentration of water in a liquid phase. The water content would be more than 10 wt% [*Burnham*, 1994] and the viscosity is below $10^4 \text{ Pa}\cdot\text{s}$ [*Shaw*, 1972; *Sparkes et al.*, 1994]. The viscosity would increase by an order of up to 10 at 90% solidification [*Costa et al.*, 2009; *Mader et al.*, 2013] and might reach $10^{14} \text{ Pa}\cdot\text{s}$. However, the relaxation time scale is estimated to be $\tau = 2 \times 10^3 \text{ s}$ for a rigidity of $5 \times 10^{10} \text{ Pa}$ and a viscosity of $10^{14} \text{ Pa}\cdot\text{s}$, and brittle failure is thought to occur for strain rates larger than $0.01/\tau = 5 \times 10^{-6} / \text{s}$ [*Webb and Dingwell*, 1990], which is much larger than the estimated thermal strain rate. The occurrence of elastic accumulation of thermal stress is therefore unlikely for the conditions known to be realistic to date.

However, the condition for brittle failure of $0.01/\tau$ has not been examined well. The effect of heterogeneity on viscosity or the viscosity of complicated composite is much less understood. Within the range of uncertainties in the current knowledge, the possibility of the elastic accumulation of thermal stress is not necessarily ruled out. Considering conditions for the applicability of the cooling magma model is important to understand the physics of DLPs in the future together with considering alternative models.

Another possible condition is the failure of the body rock outside but in the vicinity of the intruded magma. An average viscosity around the upper mantle and lower crust is estimated to be $10^{19} - 10^{21} \text{ Pa}$ from post-seismic deformation or glacial rebound [*Burgmann and Drasen*, 2008]. Several study estimates lower viscosity down to 10^{18} Pa [e.g., *Ohzono et al.*, 2012]. The existence of partial melt of 3–20% may reduce the viscosity by an order or two orders of magnitude [*Burgmann and Drasen*, 2008]. The maximum relaxation strain rate gets smaller for lower viscosity and the

relaxation is more difficult for higher viscosity. For a viscosity of 10^{21} Pa·s, brittle failure is thought to occur for strain rates larger than 5×10^{-13} /s, which is an order larger than our estimated strain rates for $t_c = 100$ years. Although the produced strain is not accumulated elastically in this specific case too, actual viscosity may have heterogeneity and the scale of intrusion also may vary, which might result in accumulation of thermal stress.

As a result of this quantitative analysis, the thermal stress is difficult to accumulate elastically under the condition known to be plausible today. However, it can be accumulated elastically under some special conditions (Figure 3.6). Accounting the upper limit of viscosity, the spatial scale has to be smaller than 10–100 m for the elastic accumulation of thermal stress, which is roughly consistent with that largest DLPs are $\sim M_{JMA}2$, although the JMA magnitude does not necessarily mean moment magnitude.

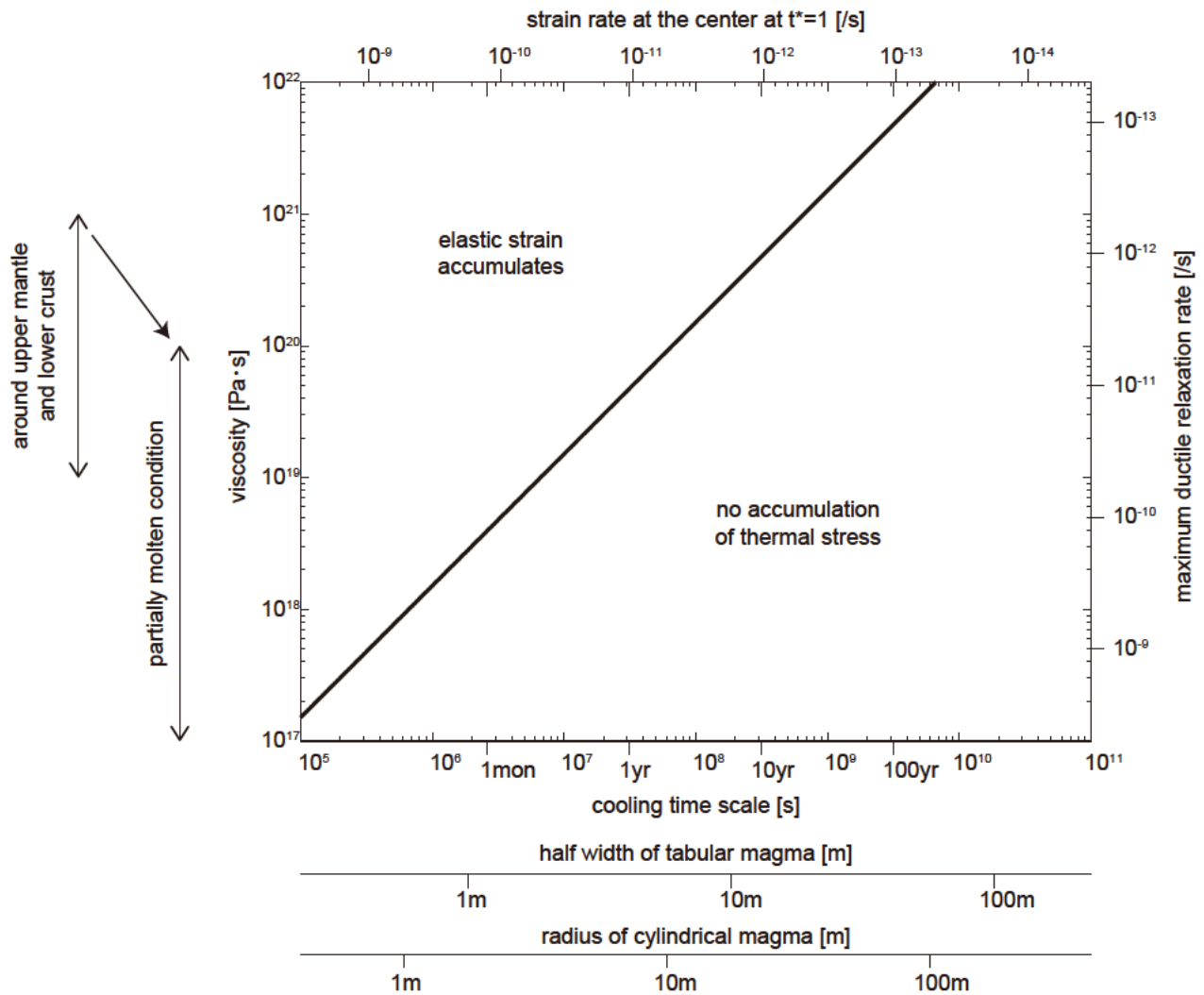


Figure 3.6 Dependency of viscosity and scale on the thermal stress accumulation

Dependency of material viscosity and scale or intruded body on the effect of the thermal stress accumulation is shown in a phase diagram. The bottom horizontal axis is the cooling

time scale and their corresponding spatial scale is shown for a tabular magma and cylindrical magma assuming $\alpha = 6 \times 10^{-7} \text{ m}^2 \text{ s}^{-1}$, respectively. The thermal strain rate corresponding to the cooling time scale is shown in the upper horizontal axis assuming $\kappa = 1.86 \times 10^{-5} \text{ K}^{-1}$, $\Delta T = 400 \text{ K}$, and a Poissonian material $\mu = \lambda$. In the left vertical axis of viscosity, the range estimated from previous studies are shown together with the range supposed for partially-molten condition. The maximum ductile relaxation rate corresponding to the viscosity is shown in the right vertical axis assuming a rigidity of $5 \times 10^{10} \text{ Pa}$. The thermal strain is elastically accumulated when the thermal strain rate is larger than the ductile relaxation. The variability of thermal expansion rate κ and the thermal diffusivity α might vary within an order of magnitude. The increase of κ by an order corresponds to the rightward shift of the line by an order and the increase of α by an order corresponds to the leftward shift of the horizontal axis of spatial scale by an order of 0.5 (or the rightward shift of the main figure by an order).

To calculate the potential effect of thermal strain, we consider the case that all of the thermal strain is accumulated elastically at $t^* > 1$ in the following story. We note that the estimated value of thermal strain rate can be equal to or larger than the strain rates driven by tectonic loading, which is estimated to be $\sim 10^{-14} \text{ s}^{-1}$ within the upper plate of thickness of 60 km, assuming that the plate convergence rate is $\sim 5 \text{ cm/year}$ and half of the tectonic strain is released by earthquakes at the plate interface, and therefore thermal strains might be able to affect the local stress-strain state. For a cylindrical intrusion, we obtain similar amplitudes of differential strain rates within the intruded region ($r^* < b^* = 1.66$) at times $1 < t^* < 2$ (Figure 3.5a).

3.3.3. Cumulative Strains

For brittle failure, the stress caused by accumulated elastic strain has to reach the frictional strength. Therefore, cumulative strains are as important as strain rates. Here, we estimate the cumulative strain and corresponding stress. Cumulative strain over $t^* > 1.0$ is shown in Figure 3.4b and Figure 3.5b for the tabular and cylindrical intrusions, respectively. As shown by both the radii of the beach balls and the contours, the cumulative strain within the intruded magma is larger than $\epsilon_{dif}^* \sim 0.1$, which corresponds to $\epsilon_{dif} \sim 4 \times 10^{-4}$ because the normalization factor for strains is

$$\frac{3\lambda + 2\mu}{\lambda + 2\mu} \frac{\kappa \Delta T}{3} = 4 \times 10^{-3}, \text{ for both the tabular and cylindrical intrusions.}$$

Corresponding differential stresses are $\sim 12 \text{ MPa}$ for a shear modulus of $\mu \sim 30 \text{ GPa}$, and are comparable to the stress drops of

many ordinary earthquakes. Differential strains are smaller in the exterior of the intruded magma than in the interior.

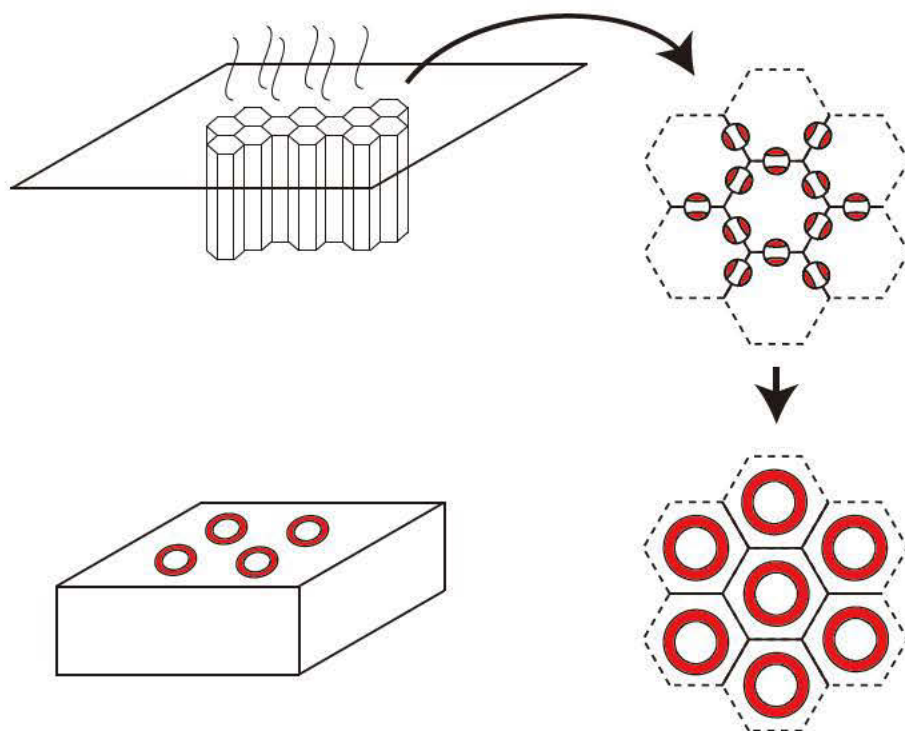
It is also of interest to note that despite thermal contraction within the intruded region, the isotropic strain in this region is large and extensional ($\epsilon_{iso}^*/\epsilon_{dif}^* \sim 0.5$) because the contraction is not enough to accommodate the elastic strains produced. Since we focus on the expected initial shear fracture, it is important to consider the Coulomb failure conditions, which account for both normal and shear stresses. This additional isotropic extensional stress brings faults closer to Coulomb failure. In fact, we estimate that these isotropic stresses are as important as shear stresses in reaching the Coulomb threshold.

3.3.4. Strain Orientations

The orientations of the strain rates for a tabular intrusion are shown in Figure 3.4a with standard beach ball focal mechanism plots. Here, we define the direction of the CLVD axis as the symmetry axis direction, and the polarity of the CLVD as the polarity of the eigenvalue of the deviatoric moment tensor in that direction. Strain rates within the intruded region for the tabular intrusion are negative CLVD in the z direction, because material contracts but it cannot have displacements in the r and θ directions. On the other hand, strain rates within the intruded region for a cylindrical intrusion is positive CLVD (Figure 3.5a) in the z direction because material contracts but it cannot have displacement in the z direction. The polarity of the CLVD is a notable difference between the tabular and cylindrical intrusions. These same patterns of orientation can also be found for cumulative strain (Figure 3.4b and Figure 3.5b).

These orientations can be qualitatively understood from the analogy to the formulation of columnar joints. Considering each crack is represented by a single CLVD, each joint of columnar joints made by tabular intrusion is CLVD whose symmetry axis is various but perpendicular to the normal vector of tabular surface. Combination of such CLVDs will be expressed by a CLVD whose symmetry axis is perpendicular to the tabular surface (Figure 3.7a). The surface of cylindrical intrusion is considered to be tabular intrusions in various directions (Figure 3.7b). Since CLVD is produced at each direction of surface, their combination will be +CLVD in the direction of cylinder axis.

(a)



(b)

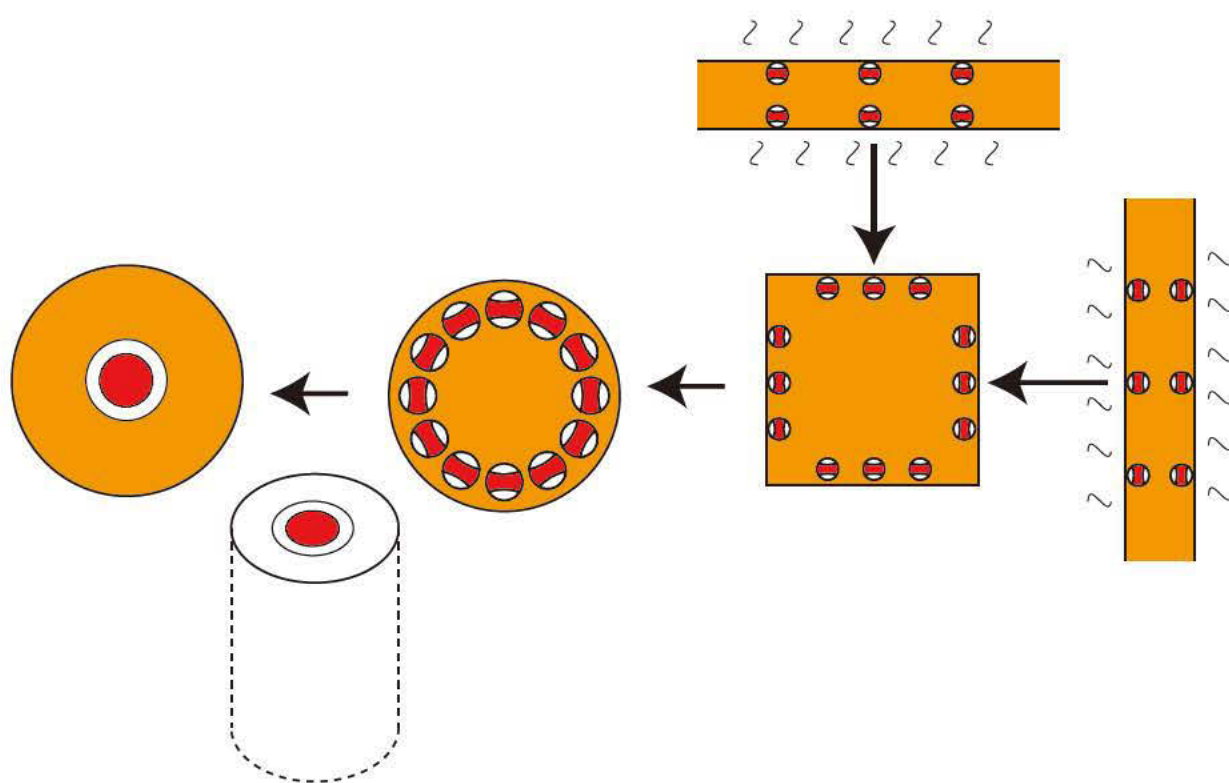


Figure 3.7 Columnar joints and tabular or columnar intrusions

(a) Qualitative mechanism of produced strain for tabular intrusion by a combination of cracks in columnar joints. (b) Qualitative mechanism of produced strain for columnar intrusion by a combination of mechanisms for tabular joints.

3.3.5. Dependency of Shape

We calculated thermal strain rates for tabular and cylindrical magmas, but these shapes are end-members of a finite-length cylinder. To assess the dependency of shape on the thermal strain, we calculated thermal strain for finite cylinders with varying aspect ratios (Figure 3.8), and compared them with the results for the two simple shapes already analyzed (Figure 3.4b and Figure 3.5b). The results for an aspect ratio smaller than 0.2 ($a/b < 0.2$) are close to the results for a tabular intrusion and those for $a/b > 5$ are close to the results for a cylindrical intrusion. We also find that equidimensional intrusions (for which $a/b \sim 1$) do not produce large deviatoric strain rates or cumulative strains.

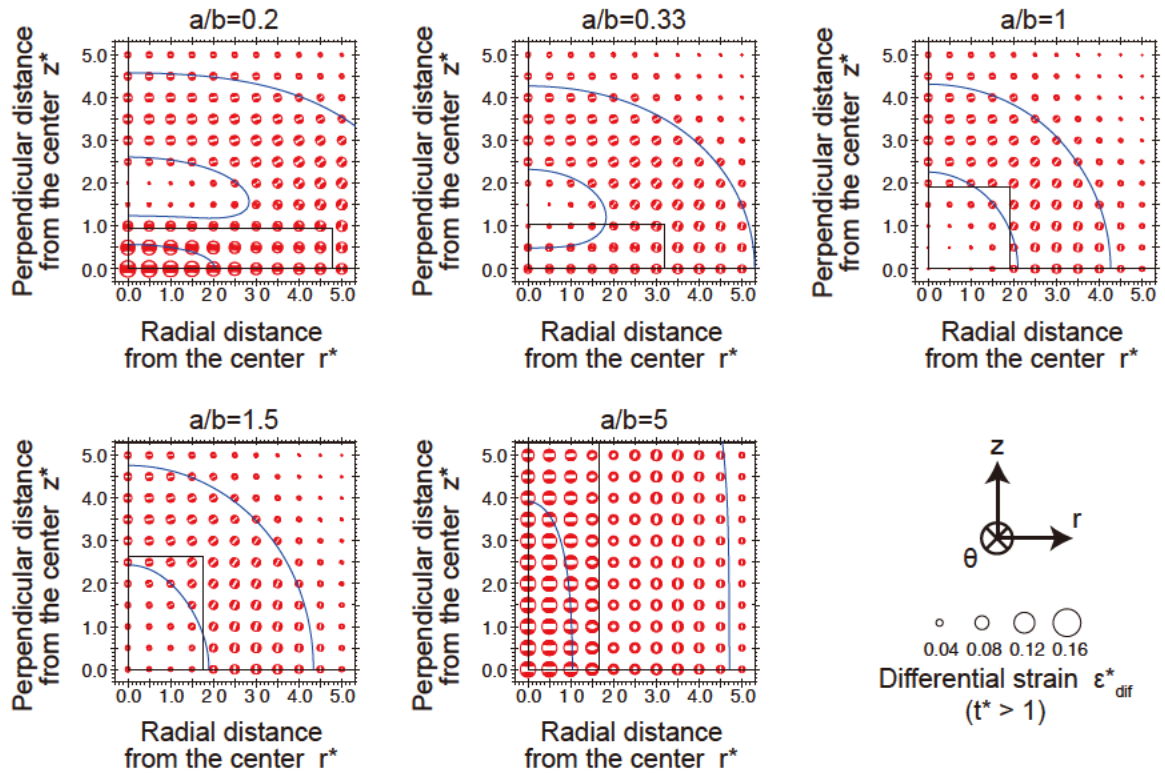


Figure 3.8 Thermal strains for finite-length cylindrical intrusions

Cumulative thermal strains of $t^* > 1$ are shown for different aspect ratios ($a/b = a^*/b^*$) of finite-length cylinders. Time is normalized by t_c , as before. Black lines represent the intruded regions. In each panel, the vertical axis is the perpendicular distance from the center, and the

horizontal axis is the radial distance from the center axis. Distances are normalized by $\sqrt{\alpha t_c}$. Blue contours correspond to differential strains of $\dot{\varepsilon}_1^* - \dot{\varepsilon}_3^* = 0.04, 0.08$.

3.3.6. Connection to Earthquakes

We expect earthquake focal mechanisms to share the same characteristic orientations as those of the calculated strains. Even if an initial fracture were double couple, a combination of simultaneous double couple events on faults in various directions that are all consistent with the CLVD-type strain would result in a CLVD mechanism that is similar to the orientation of the thermal strain. Similar observations of CLVD mechanisms composed of multiple double couple events are also known in shallow volcanic regions [Ekstrom, 1994]. Such large deformation could excite a resonance within the intruded region, which could explain the monochromatic or harmonic waveforms often observed for volcanic DLP events. In this manner, the initial shear crack would grow into a finite faulting and a resonant oscillation, being affected by the CLVD-type thermal strain. While we do not explicitly model the resonant excitation, the thermally driven process discussed here potentially explains both the CLVD mechanisms and harmonic seismic waveforms, which are the most distinct characteristics observed for volcanic DLP events.

We stress once again that our model itself does not explain the low-frequency or harmonic characteristics of the observed waveforms of volcanic DLP events. These characteristics could come from resonant oscillations or guided waves following the original deformation but their mechanism is difficult to constrain at this stage. To explain the oscillatory nature by these models, it is important to know the nature of actual material that determine frequency and impedances of the oscillation. However, in all cases, a driving force is essential for such subsequent phenomena and our model proposes a new possibility for this driving force, although the applicable condition would be very limited.

3.4. Discussion

The thermal strain rates obtained are of the order of $10^{-14} - 10^{-13} \text{ s}^{-1}$ for $t_c = 100$ years, and they do not necessarily contribute to accumulation of elastic strains under realistic conditions. However, such stress might be effective under some special conditions and this value can be equal to or larger than the strains from tectonic loading, which are estimated as $\sim 10^{-14} \text{ s}^{-1}$, which means that the strain field within the intruded magma might be controlled by thermal strain and is dependent on the shape of the magma. Therefore, nearby clusters do not necessarily have similar orientations depending on each cluster shape. This could be one of the reasons why various focal mechanisms are observed even in relatively narrow volcanic regions [Nakamichi *et al.*, 2003].

Even within each cluster, a variety of focal mechanisms can be obtained as long as they collectively yield cumulative deformation that is identical to the produced strain by the magma cooling process. For example, each event might be double-couple, but combination of them will be CLVD such as *Ekstrom* [1994] (Figure 3.9). Furthermore, we expect the mechanism of larger events is closer to the expected stress orientation because they have longer source duration and larger extent of deformation so that the combination of various styles of deformations affected by the local stress would be obtained. Hence, even if the specific orientation obtained from the cooling magma model is not observed for most events, we expect this can be observed for cumulative deformation of all events or for each of larger events if the thermal stress controls local stress field effectively.

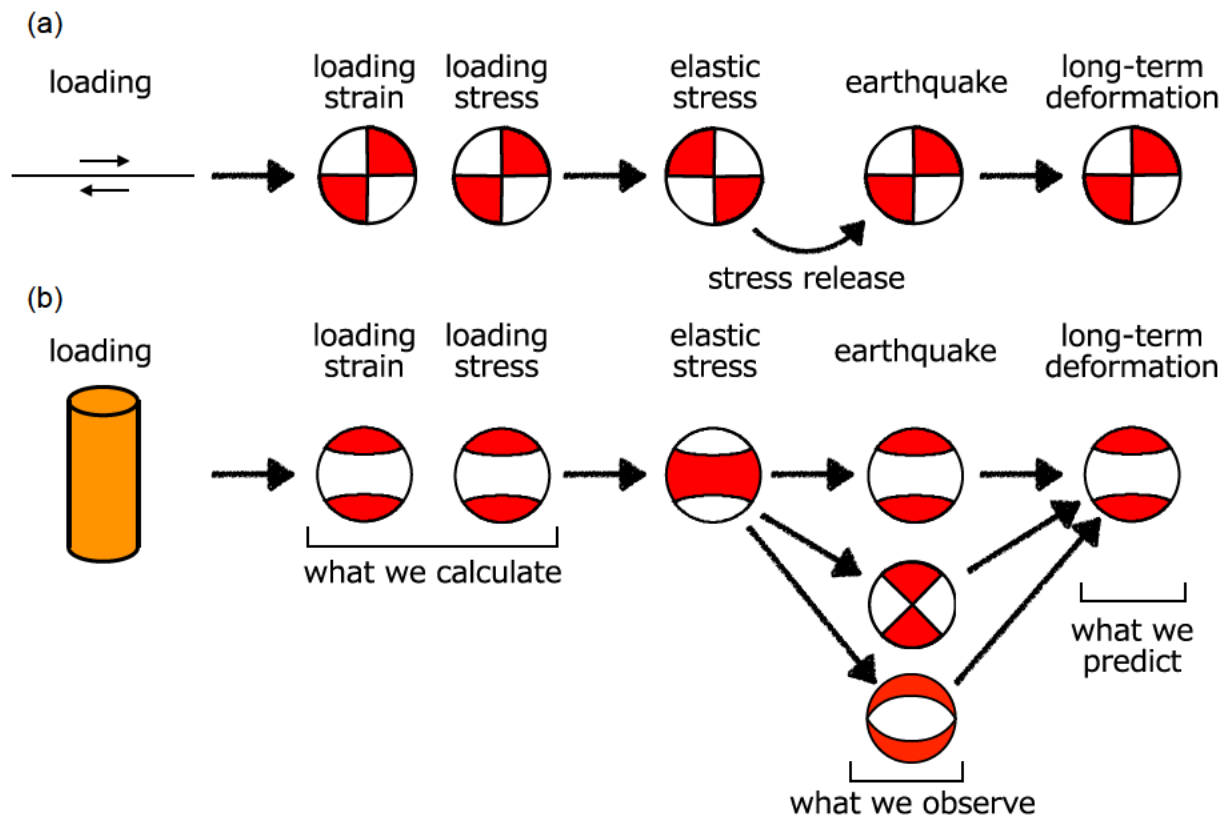


Figure 3.9 Strains and focal mechanisms

Schematic illustration of the relationship between the produced strains and focal mechanisms.

The crack growth within contracting body attributed to diffusional process is also studied in the applied physics field. Especially, experimental study of desiccation process is well studied. Cracking is easy to occur for smaller particles, larger rigidity, or less heterogeneous material [*Kitsunozaki*, 2013].

Crack propagation speed increases with larger stress rate or less viscous material [Kitsunozaki, 2009, 2010]. Effect of external loading on crack pattern is also reported [Nakahara and Matsuo, 2005; Ooshida, 2008]. Similar experimental study is also applied to explain joint generation in geophysics [Muller, 1998a, 1998b; Goehring and Morris, 2005; Toramaru and Matsumoto, 2004]. Although it is difficult to compare these studies with the present study quantitatively, it is important to consider what is the difference between these experimental studies and our theoretical study. In the present study, we focus on tensor value and it is important difference whether CLVD or DC, while experimental studies focus mainly only on opening cracks. The effect from free surface is much more important in these experimental study, while we assume deformations within an elastic body.

A direct approach to solve the condition of crack growth within elastic body would be numerical simulation but the 3-D simulation of the crack growth process considering the thermal stress is a very heavy problem that can become a large scientific topic. We would rather want to discuss on the question how CLVD events occur under the CLVD stress from a much simpler theoretical approach. We consider tabular joints within a tabular cooling magma and discuss how many cracks around a joint have to open as a single event to produce –CLVD mechanism consistent with the CLVD stress. The joint is assumed to be a complete hexagonal cylinder (Figure 3.10).

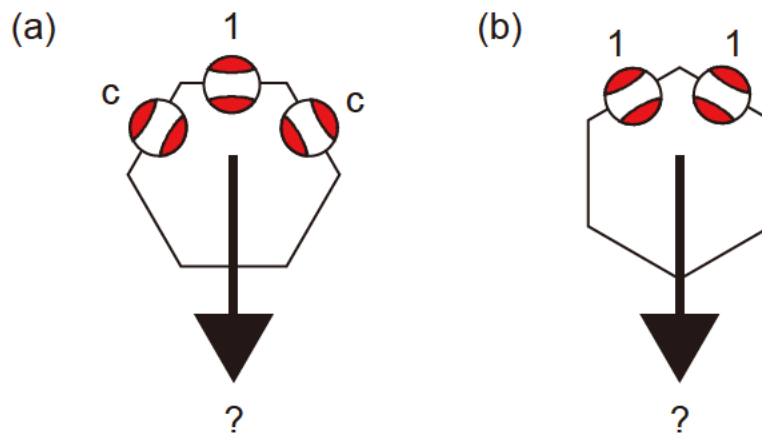


Figure 3.10 Combination of open cracks around a hexagonal joint

Schematic illustration of the combination of open cracks around a hexagonal joint. (a) The case of three opening cracks. (b) The case of two opening cracks.

At first, we show that whether –CLVD mechanism appear when three neighboring sides opened (Figure 3.10a). Deviatoric part of the opening at one side is expressed as a +CLVD such as

$$\begin{bmatrix} 2 & 0 & 0 \\ 0 & -1 & 0 \\ 0 & 0 & -1 \end{bmatrix}. \quad (3.9)$$

Those of neighboring sides are expressed as its rotated tensor by $\pm 60^\circ$ as

$$\begin{aligned} & \begin{bmatrix} -1/2 & \pm\sqrt{3}/2 & 0 \\ \mp\sqrt{3}/2 & 1/2 & 0 \\ 0 & 0 & 1 \end{bmatrix} \begin{bmatrix} 2 & 0 & 0 \\ 0 & -1 & 0 \\ 0 & 0 & -1 \end{bmatrix} \begin{bmatrix} -1/2 & \mp\sqrt{3}/2 & 0 \\ \pm\sqrt{3}/2 & 1/2 & 0 \\ 0 & 0 & 1 \end{bmatrix} \\ &= \begin{bmatrix} -1/4 & \mp 3\sqrt{3}/4 & 0 \\ \mp 3\sqrt{3}/4 & 5/4 & 0 \\ 0 & 0 & -1 \end{bmatrix}. \end{aligned} \quad (3.10)$$

If the three sides open equally, their combination is +CLVD such as

$$\begin{aligned} & \begin{bmatrix} -1/4 & 3\sqrt{3}/4 & 0 \\ 3\sqrt{3}/4 & 5/4 & 0 \\ 0 & 0 & -1 \end{bmatrix} + \begin{bmatrix} 2 & 0 & 0 \\ 0 & -1 & 0 \\ 0 & 0 & -1 \end{bmatrix} + \begin{bmatrix} -1/4 & -3\sqrt{3}/4 & 0 \\ -3\sqrt{3}/4 & 5/4 & 0 \\ 0 & 0 & -1 \end{bmatrix} \\ &= \frac{3}{2} \begin{bmatrix} 1 & 0 & 0 \\ 0 & 1 & 0 \\ 0 & 0 & -2 \end{bmatrix}. \end{aligned} \quad (3.11)$$

This is not surprising result considering symmetry or the problem, but we further evaluate incompleteness of opening in the neighboring. If the opening in the neighboring side is incomplete, the combination becomes

$$\begin{aligned} & c \begin{bmatrix} -1/4 & 3\sqrt{3}/4 & 0 \\ 3\sqrt{3}/4 & 5/4 & 0 \\ 0 & 0 & -1 \end{bmatrix} + \begin{bmatrix} 2 & 0 & 0 \\ 0 & -1 & 0 \\ 0 & 0 & -1 \end{bmatrix} + c \begin{bmatrix} -1/4 & -3\sqrt{3}/4 & 0 \\ -3\sqrt{3}/4 & 5/4 & 0 \\ 0 & 0 & -1 \end{bmatrix} \\ &= \begin{bmatrix} 2 - c/2 & 0 & 0 \\ 0 & -1 + 5c/2 & 0 \\ 0 & 0 & -1 - 2c \end{bmatrix}, \end{aligned} \quad (3.12)$$

where c is the ratio of opening amplitude of the neighboring side compared with the main side. For the range of our interest $0 < c < 1$, diagonal components are already ordered from larger to smaller value as $2 - c/2 > -1 + 5c/2 > -1 - 2c$. Using (A2.7), the deviatoric component is evaluated as:

$$\begin{aligned} a &= \frac{6}{\pi} \sin^{-1} \left(\frac{\lambda_1 - 2\lambda_2 + \lambda_3}{2\sqrt{\lambda_1^2 + \lambda_2^2 + \lambda_3^2 - \lambda_1\lambda_2 - \lambda_2\lambda_3 - \lambda_1\lambda_3}} \right) \\ &= \frac{6}{\pi} \sin^{-1} \left(\frac{3 - 15c/2}{3\sqrt{7c^2 - 2c + 4}} \right). \end{aligned} \quad (3.13)$$

Therefore, the combination mechanism is +CLVD at $c = 0$, DC at $c = 0.4$, and -CLVD at $c = 1$ (Table 3.1). The condition for -CLVD-like mechanism is $c > (-2 + 6\sqrt{3})/13 = 0.64$, which means the mechanism looks like -CLVD that is consistent with the thermal stress when the opening in the neighboring sides exceed 65% of the opening at the main side.

Table 3.1 Focal mechanism produced by three open cracks around a hexagonal joint

c	a	Focal mechanism
0	1	+CLVD
		+CLVD-like
0.1962	0.5	+CLVD
		DC-like
0.4000	0	DC
		DC-like
0.6456	-0.5	-CLVD&DC
		-CLVD-like
1	-1	-CLVD

Then we consider the case when only two neighboring sides are opened simultaneously (Figure 3.10b). Each opening can be expressed as:

$$\begin{aligned} & \begin{bmatrix} -\sqrt{3}/2 & \pm 1/2 & 0 \\ \mp 1/2 & \sqrt{3}/2 & 0 \\ 0 & 0 & 1 \end{bmatrix} \begin{bmatrix} 2 & 0 & 0 \\ 0 & -1 & 0 \\ 0 & 0 & -1 \end{bmatrix} \begin{bmatrix} -\sqrt{3}/2 & \mp 1/2 & 0 \\ \pm 1/2 & \sqrt{3}/2 & 0 \\ 0 & 0 & 1 \end{bmatrix} \\ &= \begin{bmatrix} 5/4 & \mp 3\sqrt{3}/4 & 0 \\ \mp 3\sqrt{3}/4 & -1/4 & 0 \\ 0 & 0 & -1 \end{bmatrix} \end{aligned} \quad (3.14)$$

and their combination is

$$\begin{bmatrix} 5/4 & 3\sqrt{3}/4 & 0 \\ 3\sqrt{3}/4 & -1/4 & 0 \\ 0 & 0 & -1 \end{bmatrix} + \begin{bmatrix} 5/4 & -3\sqrt{3}/4 & 0 \\ -3\sqrt{3}/4 & -1/4 & 0 \\ 0 & 0 & -1 \end{bmatrix} = \begin{bmatrix} 5/2 & 0 & 0 \\ 0 & -1/2 & 0 \\ 0 & 0 & -2 \end{bmatrix}. \quad (3.15)$$

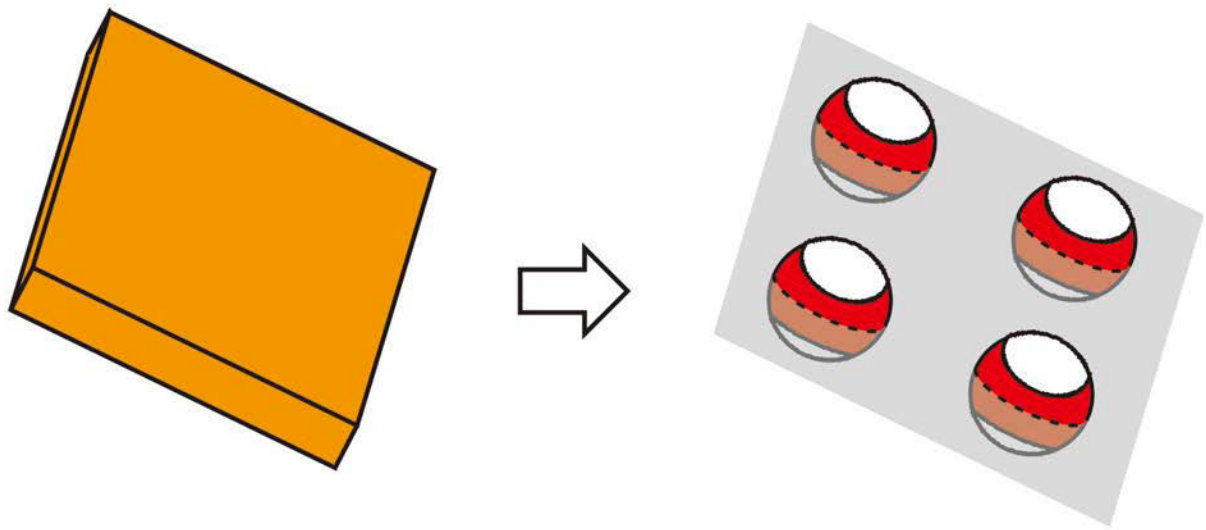
Using (A2.7), the factor a that explain deviatoric component is

$$a = \frac{6}{\pi} \sin^{-1} \left(\frac{\lambda_1 - 2\lambda_2 + \lambda_3}{2\sqrt{\lambda_1^2 + \lambda_2^2 + \lambda_3^2 - \lambda_1\lambda_2 - \lambda_2\lambda_3 - \lambda_1\lambda_3}} \right) = 0.3631 \quad (3.16)$$

and the mechanism is located within the DC-like region of $-0.5 < a < 0.5$. Therefore the expected CLVD mechanism cannot be seen when only two sections are opened as a single event.

For the models of thermal strain for the tabular and cylindrical intrusions, we obtained a relationship between the shape of intruded magma and the orientation of thermal strain. Assuming that DLP events are distributed within the intruded region and that the focal mechanism orientations are similar to that of thermal strain rates, the focal mechanism is expected to correlate with the particular shape of the cluster. DLP events in a linear cluster would have a positive CLVD mechanism, whose direction is parallel to the orientation of cluster, and DLP events in a planar cluster would have a negative CLVD mechanism, whose direction is perpendicular to the plane of the cluster (Figure 3.11). *Aso and Ide* [2014] constrained CLVD mechanisms in the NNE direction for volcanic DLP events within a NNE linear cluster, and this is consistent with our cylindrical model, although it is difficult to determine whether those mechanisms are closer to positive CLVD or negative CLVD because their source is oscillatory and signals at low frequencies were often buried by noise.

(a) Tabular



(b) Cylindrical

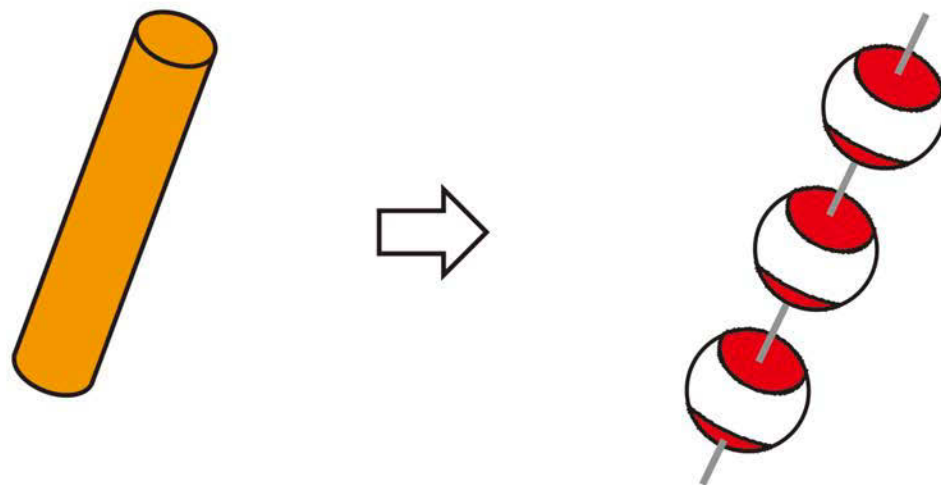


Figure 3.11 Expected source distribution and focal mechanisms.

Schematic illustration of the relationship between the source distribution and focal mechanisms expected from this model for (a) a tabular intrusion and (b) a cylindrical intrusion.

Since our model itself does not explicitly explain the low-frequency or harmonic characteristics of volcanic DLP events, our model may also be applicable to high-frequency events such as volcano-tectonic events, which are thought to be regular events in volcanic regions. Such high-frequency events sometimes co-exist with DLP events [Shelly and Hill, 2011] and they may have similar initiation processes. Another possible application of our model could be to shallower events, although the appearance of fluids or volatiles and the resultant convectonal heat flow make it unlikely that the

simple assumptions made here are appropriate for the shallow crust. The absence of DLP events in the middle crust might be due to the difficulty of having large thermal gradients there.

The process of cooling magma considered here would be a part of a crustal evolution process discussed by *Annen et al.* [2006]. Although it is currently difficult to relate specific aspects of crustal evolution with our cooling magma model, we expect the cooling magma to correspond to the crystallization of mantle-derived basalt or basaltic andesite in the deep crust. If this is correct, the size and shape of these magmas could be inferred from seismological observations with our model, and it may be possible in future work to eventually compare them with geological outcrops and geochemical measurements or to use them to infer the location where andesite emplacements are taking place.

3.4.1. Consistency and Inconsistency with the Mechanism Analyses

Since we worked on source inversions in the first half of this thesis, we infer whether the mechanism expected from the cooling magma model is observed or not. While theoretical model of cooling magma expects source type of CLVD, its symmetry axis parallel to the characteristic orientation of cluster shape, and specific polarities, some of these characteristics are resolved by source inversions. Some events in E. Shimane have the CLVD component whose symmetry axis is parallel to the linear structure formed by the hypocenter distribution, and this is consistent with the cylindrical cooling magma, although polarities are not well determined and we cannot discuss it.

E. Shimane is close to the dormant volcanic cluster that erupted at 1–2 Ma lastly and there is no surface magma activity, but the magma activity near the Moho are not necessarily connected with that on the surface. For example, since magma movements in the deep crust is thought to be permeable flow of $\sim 10^{-2}$ m/year [*Koyaguchi*, 2008], magma starts upwelling near the Moho earlier than 1 My before an eruption. Moreover, not all magmas moving upwards near the Moho reach to the surface. Therefore, magma activity near the Moho is not necessarily connected with the current volcanic activity such as eruptions and such magma near the Moho would distribute more broadly than expected from the distribution of active volcanoes.

Mantle diapir movements are controlled by viscous resistance and the upwelling velocity is estimated as $U \sim \Delta \rho g r^2 / \eta \sim 10^{-15}$ m/s for a density contrast of $\Delta \rho \sim 300$ kg/m³, acceleration of gravity of $g \sim 10$ m/s², radius of $r \sim 50$ m, and the viscosity of $\eta \sim 10^{22}$ Pa·s [*Koyaguchi*, 2008]. Although the incoming speed to the Moho is slower than the outgoing speed from the Moho, magma tends to stagnate near the Moho because of the buoyancy. This implies upwelling magma from the Moho is more discontinuous and spontaneous than supply of mantle diapir and therefore the Moho plays as a temporally container of magma that sometimes act as a magma reservoir but sometimes act as an emplacement of pluton in a solidifying process.

Although it is difficult to rule out the effect of active movement of magma in volcanic regions, some magma is under cooling process even beneath active volcanoes. Moreover, the emplacement of

plutonic rock is a major factor of crustal evolution and would occur universally, and we focus on the cooling process of such inactive magmas (Figure 3.12). In Kirishima, where high activity of eruptions are observed recently, there is no clear evidence of relationship between eruption and DLP activity or geodetic movements and DLP activity while eruption, geodetic movement, and shallower events' activity have temporal relationship (Figure 3.13 and Figure 3.14).

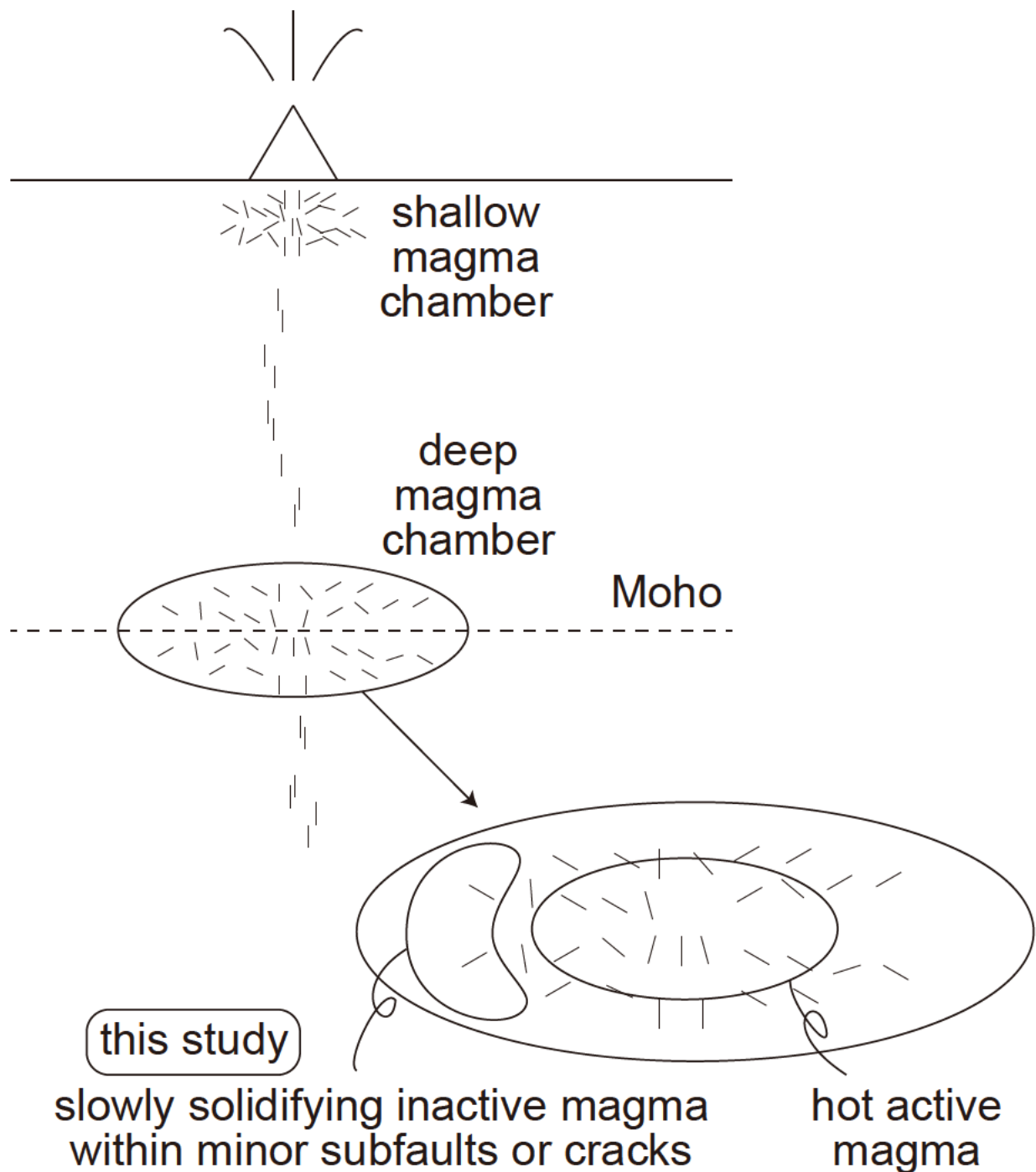


Figure 3.12 Focused process in the context of volcanic system

Even beneath active volcanoes there would be slowly solidifying inactive magma within minor subfaults or cracks. Our target is the cooling process of such “minor” activity in the context of active volcanism, but it would have an important role in DLP occurrence.

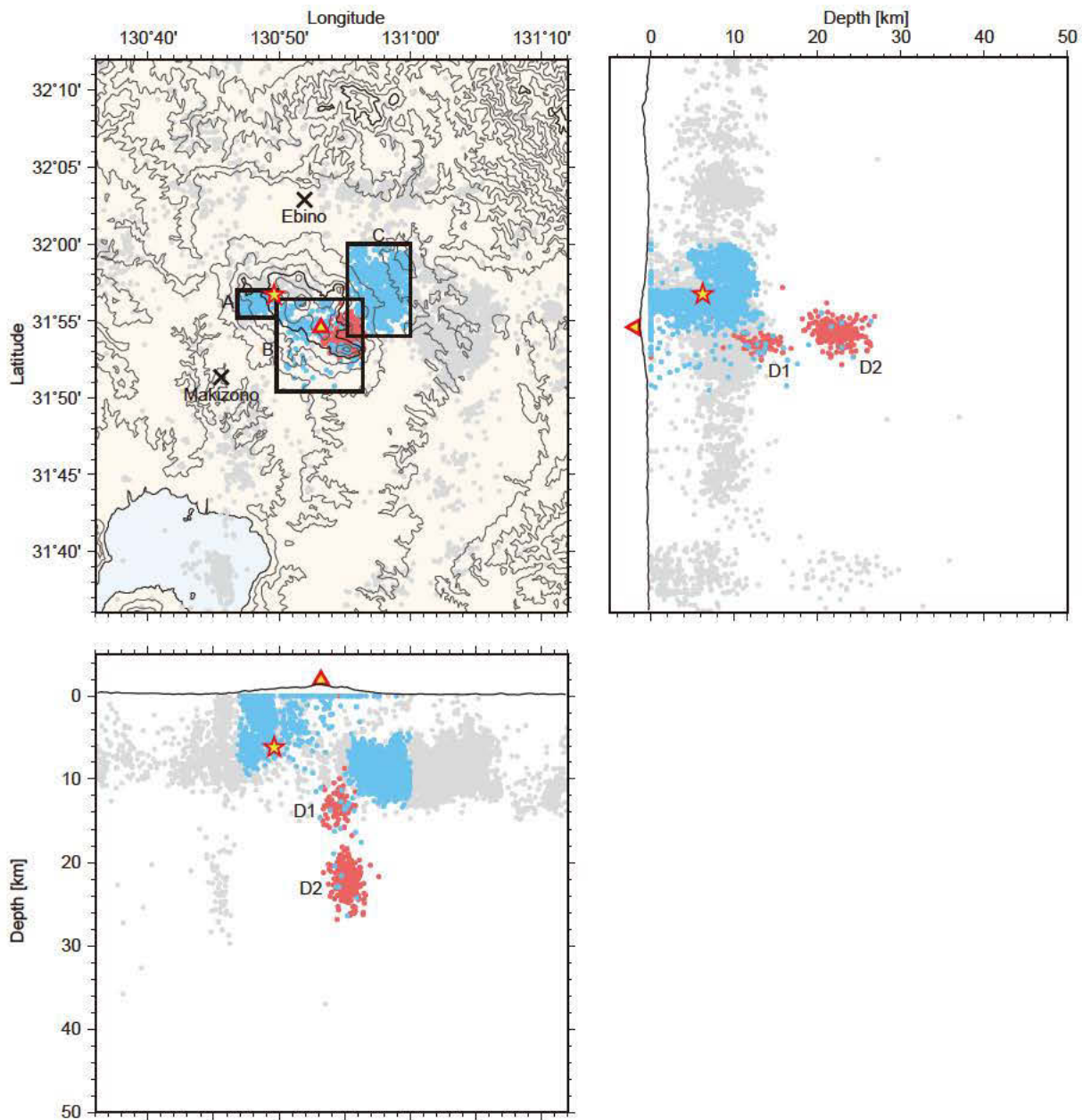


Figure 3.13 Spatial relationship in Kirishima

Earthquake distribution in Kirishima is shown in map view and in latitudinal and longitudinal cross-sections. All events detected by JMA from January 1998 to October 2014 are shown. DLP events are shown by red dots. Blue dots represent regular earthquakes in three sub-regions as indicated by rectangles. The other regular events are shown in gray. Triangle represents the summit of the Shinmoe-dake. Crosses show two GPS stations. Star represents

the deflation source location during the eruption from January 2011 to February 2011 determined by GPS continuous observation stations assuming one Mogi-source [*Geospatial Information Authority of Japan*, 2011].

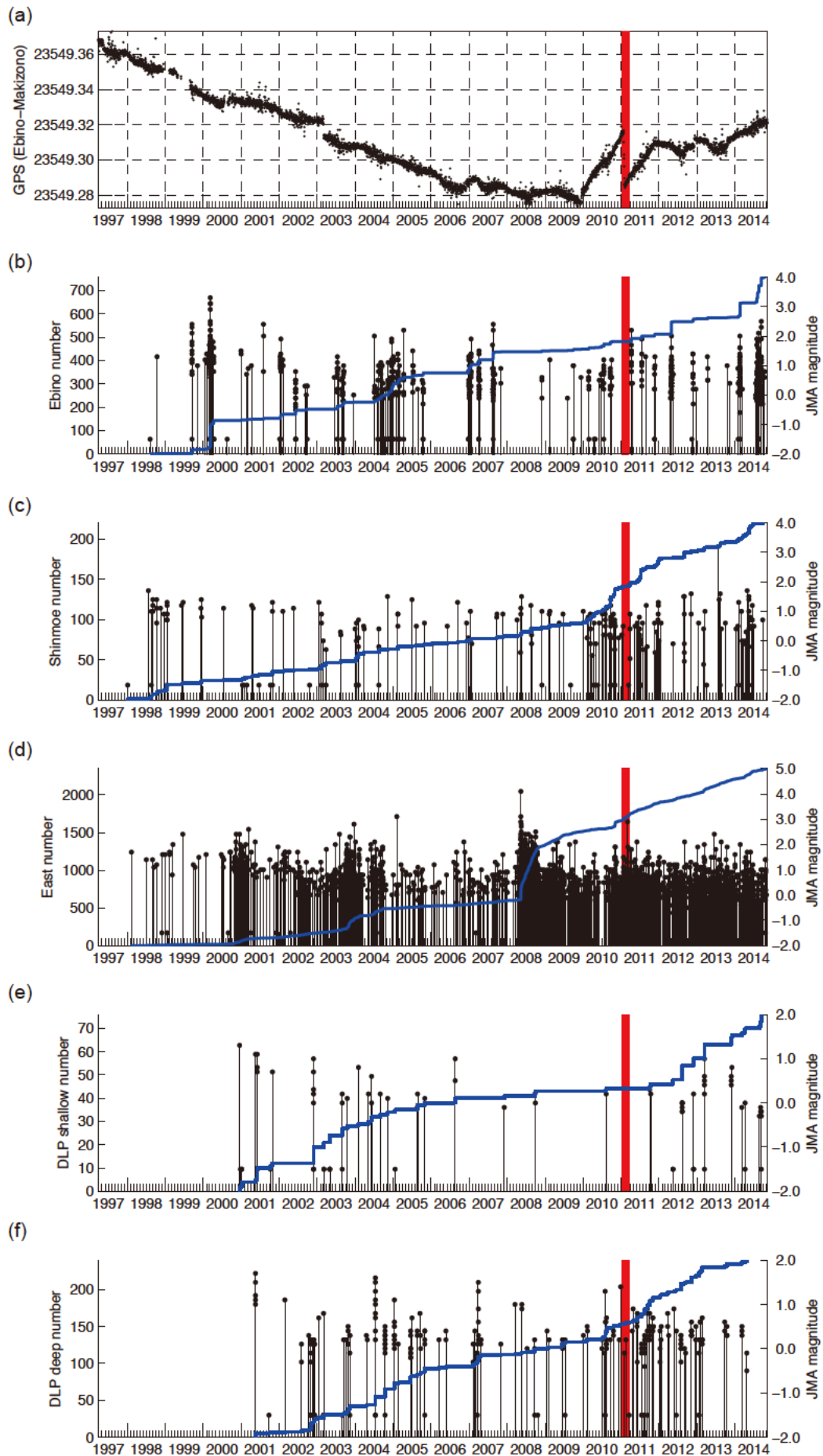


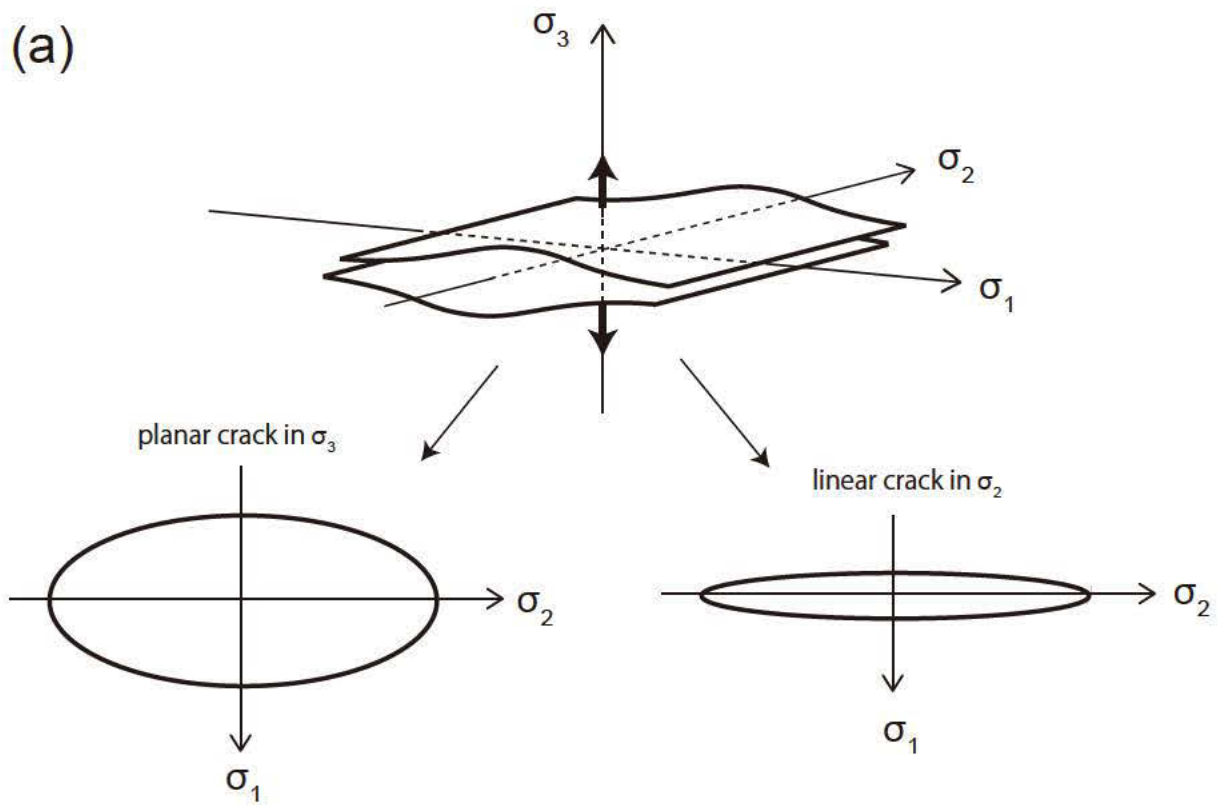
Figure 3.14 Eruption and DLPs in Kirishima

Temporal variation of GPS measurement, regular event activity, and DLP activity in Kirishima is shown with respect to the eruption sequence (red vertical lines). (a) Base-line length between two GPS stations at Ebino and Makizono. (b) Regular event activity in Ebino region (region A in Figure 3.13). (c) Regular event activity in Shinmoe region (region B in Figure 3.13). (d) Regular event activity in eastern region (region C in Figure 3.13). (e) DLP activity shallower than 16.5 km (cluster D1 in Figure 3.13). (f) DLP activity deeper than 16.5 km (cluster D2 in Figure 3.13).

The symmetric direction of the CLVD component in E. Shimane is parallel to the T-axis of the focal mechanism of the 2000 western Tottori earthquake and the minimum principal axis of a regional stress field in southwestern Japan. Although columnar magma intrusion would likely to occur in the σ_2 -axis (\sim N-axis) direction (Figure 3.15a), it is not the case if there is special geological structure. Assuming the Moho discontinuity is the preferred plane of opening crack, the pipe of magma would be parallel to the smallest stress orientation within the strata (σ_2' -axis \sim P-axis), which is consistent with this result (Figure 3.15b).

Surprisingly, there were less planar clusters than linear clusters although magma intrusion is often regarded as planar. This might be possibly because narrow part is cooled down fast during cooling process and the molten magma region may become pipe-like shape during the process even for a planar intrusion because of the fluctuation of width.

(a)



(b)

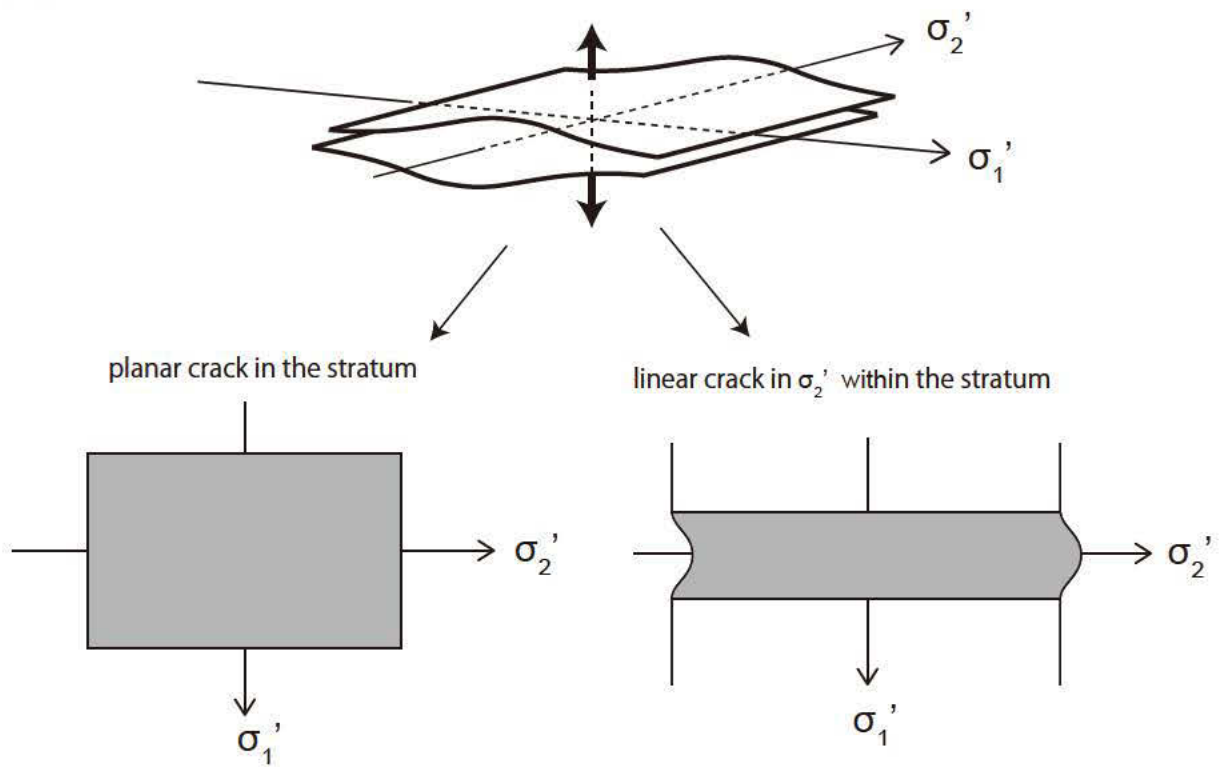


Figure 3.15 Preferred orientation of magma intrusions

Schematics of preferred orientation of tensile crack accompanied by magma intrusions. (a) When cracks in various directions are distributed, the most favorable orientation of the tensile crack is in the σ_3 direction. A planar crack in the σ_3 direction or linear crack in the σ_2 direction is produced depending on the stress conditions. (b) When there is a stratum, which is easy to open, the tensile crack is produced within the stratum. A planar crack within the stratum or linear crack in the σ'_2 direction, which is the smallest stress orientation within the plane of the stratum, is produced depending on the stress conditions.

The direction of the CLVD component in Yakedake was not so clear but at least two events have SE orientation (#03 and #26). If the orientation is regarded to be sub-parallel to the plane-normal direction of planar hypocenter distribution ($\sim S$), the cooling magma model might be applicable to these events. These orientations are close to the σ_3 -axis direction and tensile crack in the direction is easy to open. Therefore the DLPs in Yakedake can be interpreted as a tabular cooling magma whose plane-normal direction is in S-SE considering all of focal mechanism, source distribution, and local stress field.

Although some observations are consistent with cooling magma model, the polarity of the CLVD component is still unclear in any regions, which might be another key evidence or critical counter-evidence for the model. Determining the polarity is essentially important for further understanding DLPs. Although one might interpret opposite mechanism coexist in the region, we expect the real movement should have common orientation especially within such a small region.

3.4.2. Alternative Implications

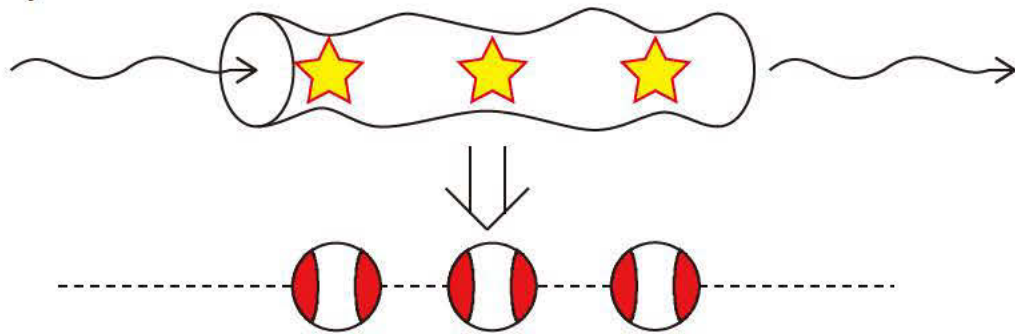
The result of source inversion itself is a realization of source process by couple forces on a point, but they are not enough to validate any model including the cooling magma model. Even if all nature could be explained by one model, we cannot conclude the model is the best without considering alternative models or implications. Considering multiple models are very important for understanding real physics by modeling. Here, we consider alternative models to have broad scope toward understanding physical process of volcanic DLPs. We note that some of these alternatives can coexist with the cooling magma model or can be just a different representation of what we have considered in the cooling magma model.

3.4.2.1. Fluid Movements

Shallow LPs or VLPs are often explained by fluid movements [e.g., *Ohminato*, 2006], and it is another possible mechanism of generating DLPs. Fluid movements can explain CLVD in the direction of flow. For a cylindrical pipe of fluids, linear hypocentral structure would appear and the direction of

+CLVD is in the direction of structure (Figure 3.16a), which is the same characteristic with what is expected from cooling magma model. This means fluid movement can be the driving force for the DLPs in E. Shimane. However we expect fluid movements are basically much slower at the Moho depth than on the surface as expected for magma movements in 3.4.1. We consider cooling magma is one of the best candidates of driving force as well as fluid movements.

(a)



(b)

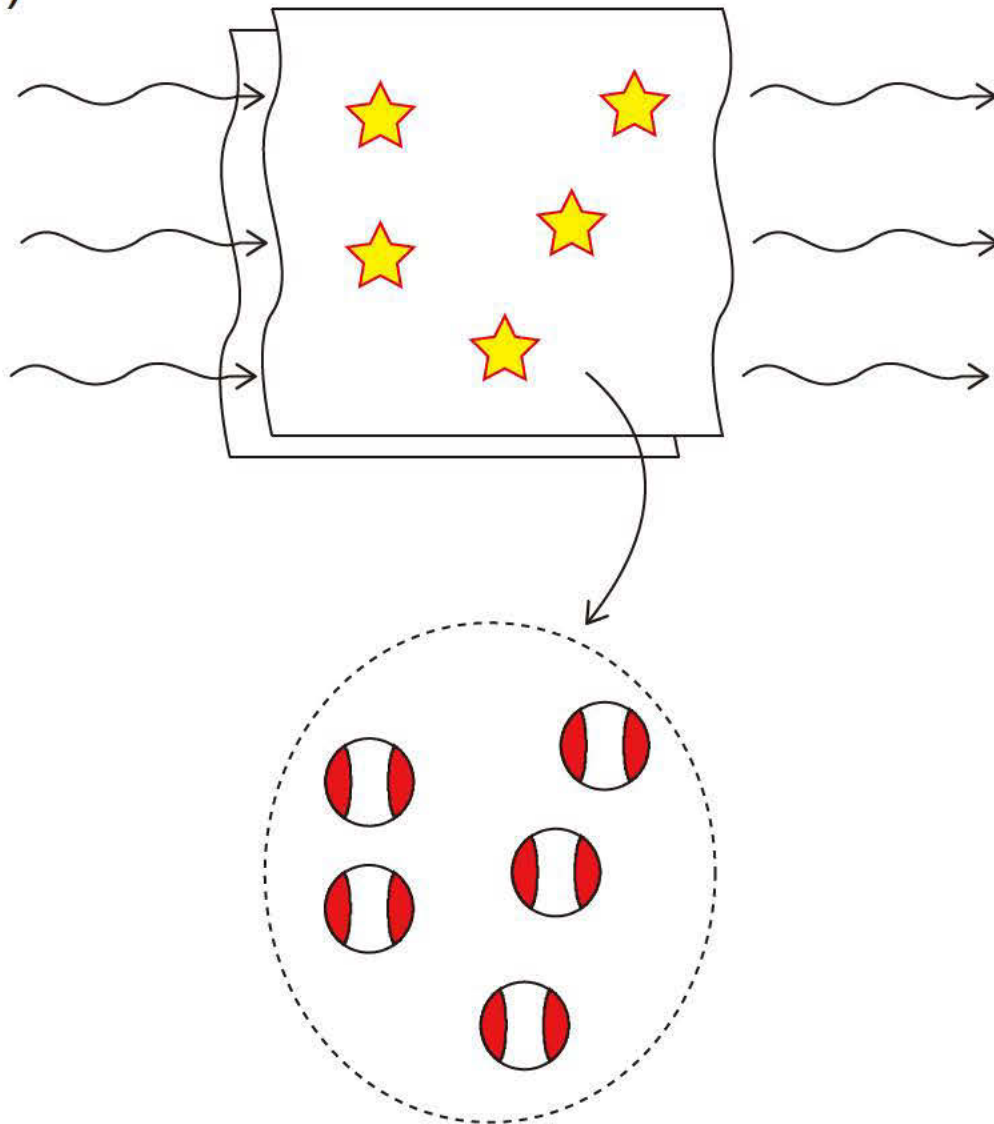


Figure 3.16 Focal mechanisms obtained by fluid movements

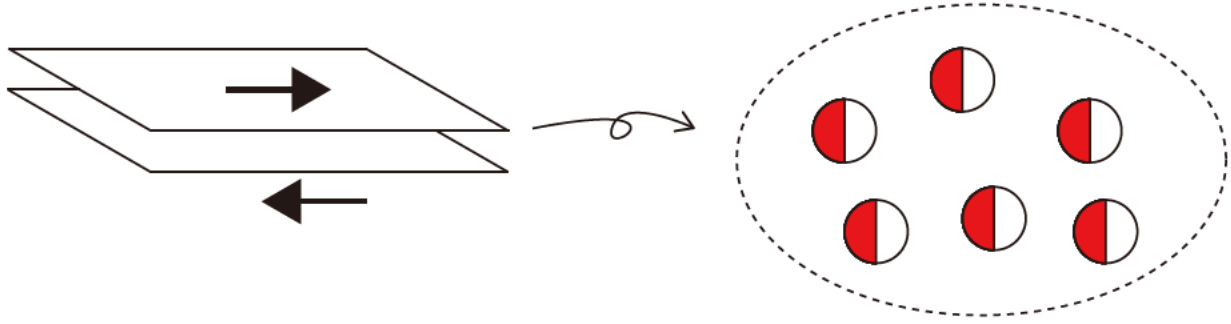
Focal mechanisms expected from fluid movements are schematically shown. (a) Linear fluid movement produces CLVD mechanism aligned in the symmetry axis of the CLVD. (b) Planar fluid movement produced CLVD mechanism distributed in the plane containing the symmetry axis of the CLVD.

For a tabular pipe of fluids, events would distribute within the plane and the direction of +CLVD would be within the plane (Figure 3.16b), which is different from the expectation from cooling magma model in terms of polarity and direction of CLVD.

3.4.2.2. Slips on Faults

Slips on faults would produce double-couple mechanisms that have nodal plane parallel to the faults, which is totally different from the expectation of CLVD from cooling magma model. Also, we expect planar distribution is easier to exist than linear distribution for slip events because they would have a mature fault. Such linear structure is observed for tectonic LFEs [*Shelly et al.*, 2007b; *Ide*, 2010], but such structure are surrounded by stable slipping regions within mature faults. Since it is difficult to assume mature faults only beneath volcanoes at depth around the Moho, we do not consider slip movements as dominant mechanisms of DLPs, which often have linear structures. However, the representative event #22 in S. Mt. Iwate are interpreted as a slip movement and it might be difficult to explain all DLPs by a single model.

(a)



(b)

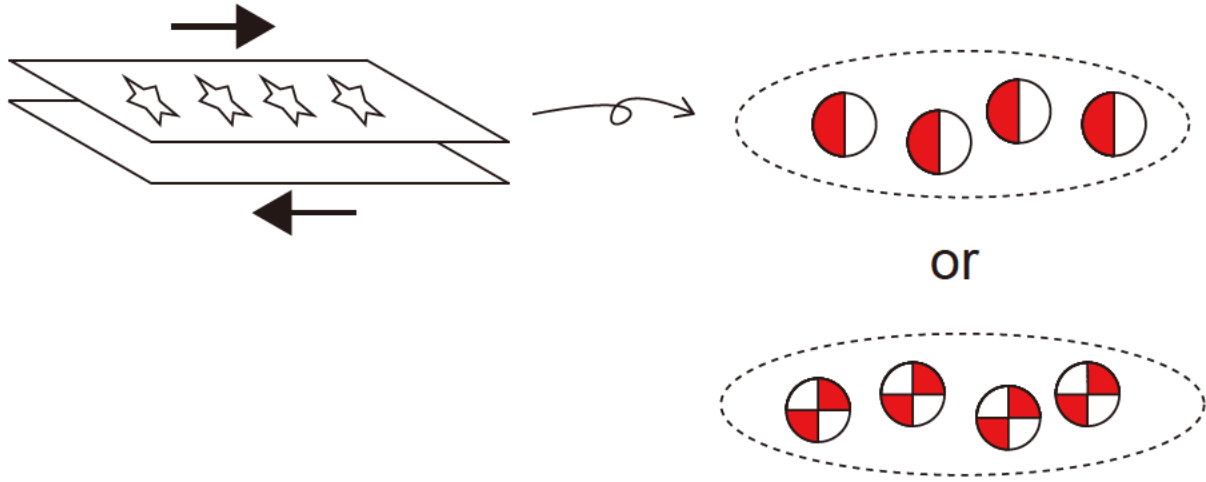


Figure 3.17 Focal mechanisms obtained by slips on faults

Focal mechanism expected from the shear movements on the fault is schematically shown.

(a) Normally, double-couple mechanisms are distributed in each of the nodal planes of the double-couple. (b) For a linear structure formed in the direction of shear, double-couple mechanisms are distributed in the direction that is perpendicular to the N-axis of the double couple and also within each of the nodal planes.

3.4.2.3. Explosion

Assuming an isotropic volumetric deformation such as an explosion or a bubble release is the seismic source, the moment tensor is expressed as

$$M = \Delta V \begin{pmatrix} \lambda + \frac{2}{3}\mu & 0 & 0 \\ 0 & \lambda + \frac{2}{3}\mu & 0 \\ 0 & 0 & \lambda + \frac{2}{3}\mu \end{pmatrix} \propto \begin{pmatrix} 1 & 0 & 0 \\ 0 & 1 & 0 \\ 0 & 0 & 1 \end{pmatrix}, \quad (3.17)$$

where λ and μ are Lamé parameters and ΔV is the expanded stress-free volume [Aki and Richards, 2002; Kawakatsu and Yamamoto, 2007; Kumagai, 2009; Kumagai et al., 2014]. Since there is no CLVD component, the estimated mechanism with CLVD component cannot be explained by an explosion alone. Moreover small explosion would have more high-frequency radiation and clear explosive P-wave with less S-waves. However, what is considered in cooling magma model is implosion that occurs slowly. Even if the driving force is isotropic displacement, such deviatoric deformation can be produced for such special structures. Considering how deviatoric part appear from pure isotropic explosion or implosion, as we did in cooling magma model, might be a key to understand the physics of DLPs.

3.4.2.4. Tensile Cracks

The intruded magma perpendicularly to the stratum is called dike, and the intruded magma parallel to the stratum is called sill. Assuming a tensile crack such as a dike or a sill is the seismic source, the moment tensor is expressed as

$$M = \Delta V \begin{pmatrix} \lambda & 0 & 0 \\ 0 & \lambda & 0 \\ 0 & 0 & \lambda + 2\mu \end{pmatrix}. \quad (3.18)$$

where ΔV is the expanded stress-free volume [Aki and Richards, 2002; Kawakatsu and Yamamoto, 2007; Kumagai, 2009]. It can be decomposed into a CLVD component and an isotropic component as

$$\begin{aligned} M &\propto \begin{pmatrix} \frac{-2\mu}{3} & 0 & 0 \\ 0 & \frac{-2\mu}{3} & 0 \\ 0 & 0 & \frac{4\mu}{3} \end{pmatrix} + \begin{pmatrix} \frac{3\lambda + 2\mu}{3} & 0 & 0 \\ 0 & \frac{3\lambda + 2\mu}{3} & 0 \\ 0 & 0 & \frac{3\lambda + 2\mu}{3} \end{pmatrix} \\ &= \frac{2\mu}{3} \begin{pmatrix} -1 & 0 & 0 \\ 0 & -1 & 0 \\ 0 & 0 & 2 \end{pmatrix} + \frac{3\lambda + 2\mu}{3} \begin{pmatrix} 1 & 0 & 0 \\ 0 & 1 & 0 \\ 0 & 0 & 1 \end{pmatrix}. \end{aligned} \quad (3.19)$$

Therefore, the isotropic polarity is same with the CLVD polarity, although it is difficult to discuss the isotropic component in the present analyses. Special distribution of tensile cracks might be possible by assuming a weak zone where tensile crack can be produced (Figure 3.18). The distribution of cracks mainly depends on the material distribution, although local stress field would affect mechanism of each crack. In volcanic regions around the Moho, such heterogeneous material would exist and can be one possible physical mechanism of volcanic DLPs. Actually the cooling magma model has same meaning with this idea. The deformation in cylindrical case of cooling magma model can be realized by tensile cracks within a cylindrical zone, and the cooling magma model would be a macroscopic representation of all the tensile cracks.

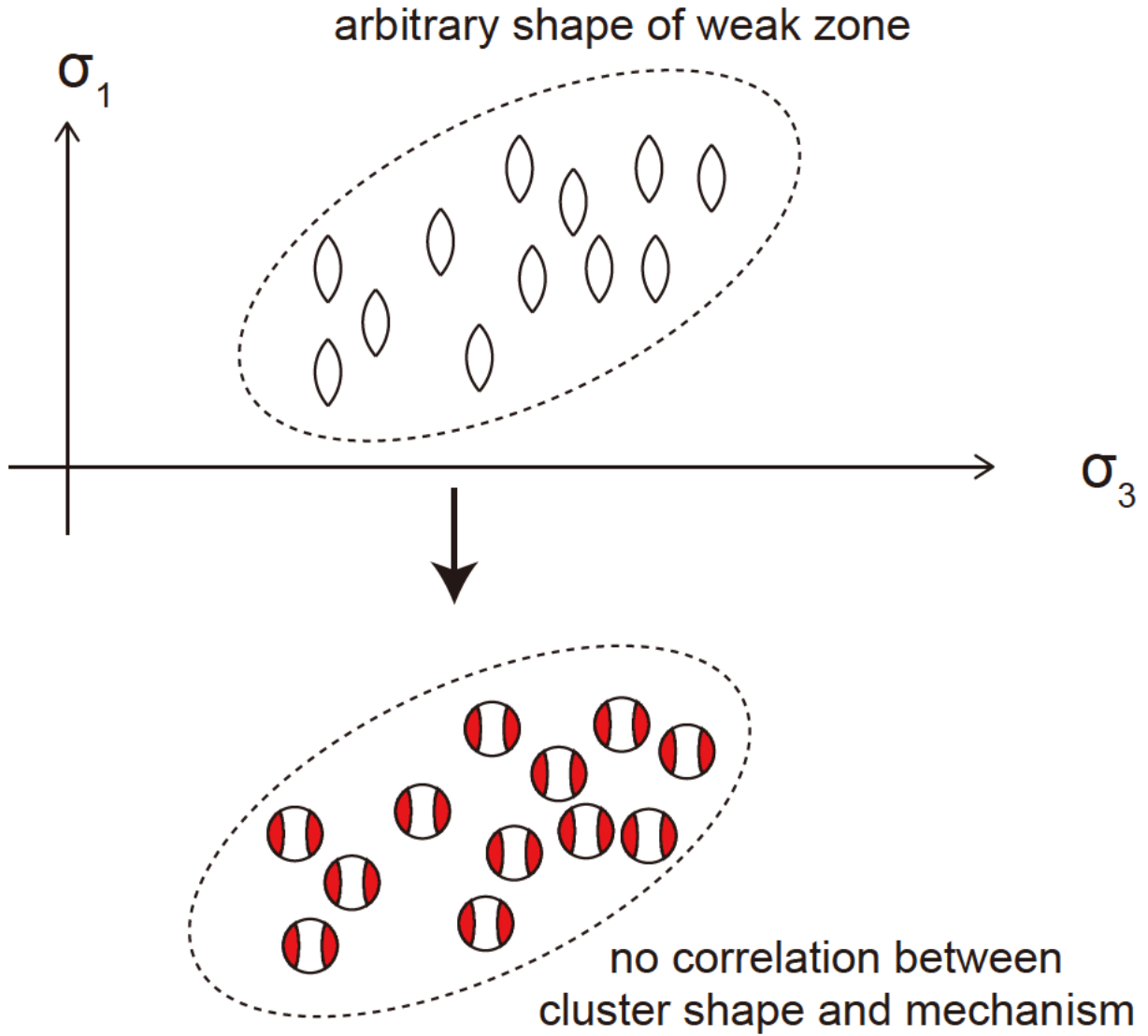


Figure 3.18 Focal mechanisms obtained by tensile cracks

Focal mechanisms expected from tensile cracks are shown. Although each tensile crack would have relationship with local stress field as discussed in Figure 3.15, their distribution is mainly controlled by the material distribution.

3.4.2.5. Compressional Cylinder

Assuming a compressional cylinder such as a magma channel is the seismic source, the moment tensor is expressed as

$$M = \Delta V \begin{pmatrix} -\lambda - \mu & 0 & 0 \\ 0 & -\lambda - \mu & 0 \\ 0 & 0 & -\lambda \end{pmatrix}, \quad (3.20)$$

where ΔV is the incremental volume change for the free surface condition [Fukuyama and Takeo, 1990; Kawakatsu and Yamamoto, 2007; Kumagai, 2009]. It can be decomposed into a CLVD component and an isotropic component as

$$\begin{aligned}
 M &\propto \begin{pmatrix} -\frac{\mu}{3} & 0 & 0 \\ 0 & -\frac{\mu}{3} & 0 \\ 0 & 0 & \frac{2\mu}{3} \end{pmatrix} + \begin{pmatrix} -\frac{3\lambda + 2\mu}{3} & 0 & 0 \\ 0 & -\frac{3\lambda + 2\mu}{3} & 0 \\ 0 & 0 & -\frac{3\lambda + 2\mu}{3} \end{pmatrix} \\
 &= \frac{\mu}{3} \begin{pmatrix} -1 & 0 & 0 \\ 0 & -1 & 0 \\ 0 & 0 & 2 \end{pmatrix} - \frac{3\lambda + 2\mu}{3} \begin{pmatrix} 1 & 0 & 0 \\ 0 & 1 & 0 \\ 0 & 0 & 1 \end{pmatrix}. \quad (3.21)
 \end{aligned}$$

In this model, we consider a cylinder filled by a fluid. Although a compressional cylinder shows a compressional isotropic component, the fluid material inside the cylinder may be pushed out to the surrounding area. The fluid will intrude to various shapes of cracks and the complex of these opening cracks in various directions may be observed as explosion. These simultaneous fluid intrusions in various directions negate the compressional isotropic component caused by a compressional cylinder and the additional tensional isotropic component appears, which is same with the CLVD polarity. After the cylinder compression and the fluid intrusion, following reversal movement of the fluid will act like oscillation.

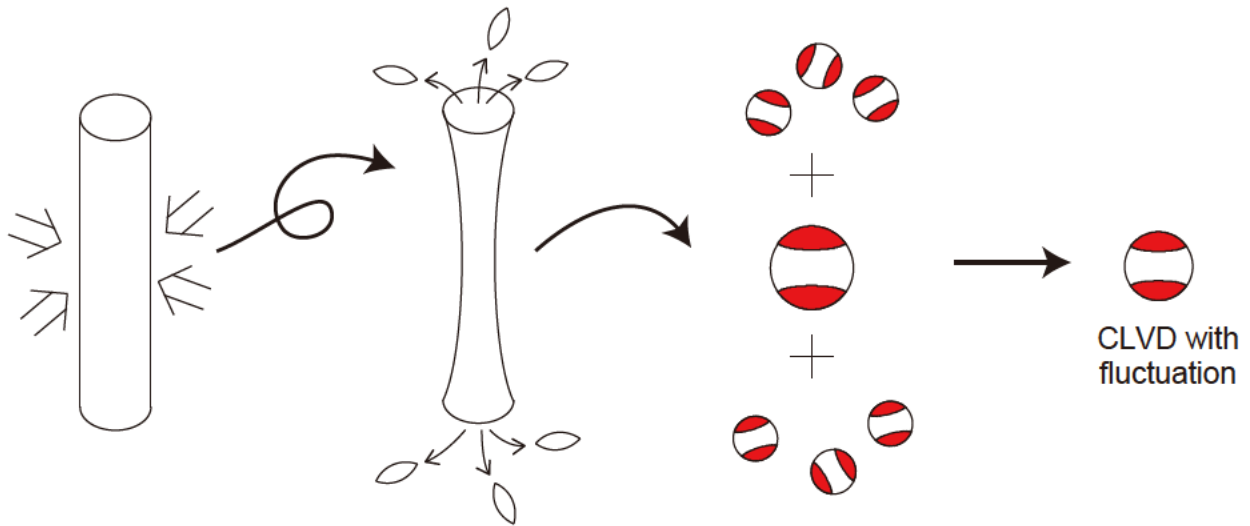


Figure 3.19 Focal mechanisms obtained by a compressional cylinder

Focal mechanism expected from compressional cylinder is shown in schematics. While the major deformation is CLVD, forwarded material inside will open tensile cracks near the edge of the cylinder. In total, the observed mechanism would be mainly CLVD but with small or large fluctuations.

4. Summary

In the present study, we studied on source inversion of DLPs and evaluated a new effect on driving force for DLPs. Each of observation and modeling gave important development of understanding DLPs as a pioneer of analyzing nationwide DLPs or considering driving force, and further several steps including data acquisition in a good quality will help understanding details of DLPs in the future.

Before working on source mechanisms, we determined fine shape of source clusters. We applied the NCC relocation method [Ohta and Ide, 2008, 2011] in 22 major regions in Japan. Among these regions, 28 clusters were extracted including seven linear clusters and four planar clusters. We also developed an inversion method specialized for volcanic DLPs that have monochromatic waveforms with unclear onsets. Using the similarities between stations for each event, we extracted source function by stacking these waveforms at first, and then applied ordinary linear inversion technique. By iterative calculations using different candidates of arrival times, we obtained the most favorable mechanism. Using this procedure, we determined source mechanisms at four linear or planar clusters. According to several stability tests, discussion on isotropic component or polarity of the initial movement is known to be still difficult and most obtained results did not satisfy statistical significance. However, some events in E. Shimane were revealed to be different from ordinary DC events and they had non-negligible CLVD component whose direction is sub-parallel to the lineation formed by a hypocenter distribution.

We considered a theoretical model of driving system for volcanic DLPs, which is the first attempt in the history of volcanic seismology. By theoretical calculation, we evaluated the strain rates produced by cooling magma in source regions of volcanic DLP events. For a tabular magma of half-width 41 m or a cylindrical magma of 74 m radius, the central temperature decreases by half at $t = 100$ years, and strain rates of $\sim 10^{-14} - 10^{-13} \text{ s}^{-1}$ are generated during the next 100 years ($t = 100-200$ years), producing a total strain of 2×10^{-4} . The thermal strain rates within the intruded magma can be equal to or larger than the tectonic strain rates driven by plate motion, but the strain rates are below the ductile relaxation level and cannot produce elastic stress in the realistic range of conditions. Even though it would be difficult for DLPs to be driven only by the thermal stress based on the quantitative evaluation, this idea of cooling magma model is consistent both with the Moho being a density discontinuity and with the seismological evidence of continuous seismicity for more than 10 years. Assuming the strains affect the DLPs under a special condition, the relationship between cluster shape and source mechanism is expected. DLP events in a linear cluster would have positive CLVD mechanisms whose directions are parallel to the orientation of the cluster, and DLP events in a planar cluster would have negative CLVD mechanisms whose directions are perpendicular

to the plane of the cluster. It will be key characteristics to verify the cooling magma model whether this relation is observed or not, while a part of this nature is observed in E. Shimane.

As a result of the present study, we contributed the approach to answer some of the big questions raised in the introduction. The cooling magma model is consistent with the concentrated occurrence of DLPs near the Moho because magma tends to stagnate near the density continuity. The cooling magma can potentially produce CLVD-like stress field. The existence of CLVD component might be accompanied by such special loading process rather than simple spring slider block model for ordinary earthquakes or slow earthquakes on plate interfaces. However, the quantitative estimate of the thermal strain is much smaller than the ductile relaxation level based on known parameters by preceding research. Although the cooling magma model is independent with the eruption activity, the relationship between DLPs and eruptions or earthquakes is observed not universally at all but sometimes. Some DLPs would possibly triggered by eruptions or magma movements near the surface because of stress state change. The frequency content or the harmonic characteristics are not explained only by cooling magma model, and slow failure process and resultant resonant oscillation can possibly explain such nature.

Following this study, the next large step of understanding DLPs in the next decade will be deeper and more collective study in data analysis, observation, and modeling. First, determining focal mechanisms in various regions under various tectonic settings such as back-arc volcanoes, hotspot volcanoes, dormant volcanoes, and the others is important to understand variety and universality of DLPs. Even in E. Shimane, where many large DLPs ($M_{JMA} \sim 1.5$) are observed with a low-level noise at a dense borehole network of seismometers, determination of polarity or isotropic component was difficult. By further developing the analysis method or technique as we did in the present study, it will be possible to extract more information from lower S/N data in more various regions. Calculation of synthetic waveforms using a 3-D structure in a good quality, if available, or considering the scattering effect in a correct way would also help better recognition of the real phenomena. More sophisticated determination of reliable mechanisms is essentially important also for comparison with the model prediction. Second, better observation or data acquisition is also an important factor in addition to the development of analysis technique. We suppose campaign observation at the place corresponding to the focalpoint of the symmetry axis of the obtained CLVD component is essential to clarify the polarity. To determine the final displacement using long-period information, deployment of broadband seismometers would be also important. Further observations and analyses at tens of regions will lead us to grasp common characteristics of volcanic DLPs. The third point is modeling. We should also start to focus on the model of DLPs although the constraint from observation is limited at this stage. Further survey on the applicable condition of the cooling magma model or study on the connection between the driving force and the possibly triggered resonance would be important. Considering other alternative models and discussion on the most probable model by comparing

expectations from each model with observations are finally important to understand the real physics of volcanic DLPs.

Appendices

A1. Cluster Shape Estimation

First we assume events are distributed in an oblique spheroid that has three characteristic lengths such as:

$$\rho = \frac{1}{\sqrt{2\pi}\sigma_{x'}} \frac{1}{\sqrt{2\pi}\sigma_{y'}} \frac{1}{\sqrt{2\pi}\sigma_{z'}} \exp \left(-\frac{(x' - x'_0)^2}{2\sigma_{x'}^2} - \frac{(y' - y'_0)^2}{2\sigma_{y'}^2} - \frac{(z' - z'_0)^2}{2\sigma_{z'}^2} \right). \quad (\text{A1.1})$$

Here let's assume coordinate rotation of

$$\begin{bmatrix} x \\ y \\ z \end{bmatrix} = R \begin{bmatrix} x' \\ y' \\ z' \end{bmatrix}, \quad \begin{bmatrix} x' \\ y' \\ z' \end{bmatrix} = R^t \begin{bmatrix} x \\ y \\ z \end{bmatrix}, \quad (\text{A1.2})$$

where R is orthogonal matrix that satisfy $R^t = R^{-1}$. Then,

$$\begin{aligned} \begin{bmatrix} x - \bar{x} \\ y - \bar{y} \\ z - \bar{z} \end{bmatrix} &= R \begin{bmatrix} x' \\ y' \\ z' \end{bmatrix} - \begin{bmatrix} \bar{x} \\ \bar{y} \\ \bar{z} \end{bmatrix} = R \left(\begin{bmatrix} x' \\ y' \\ z' \end{bmatrix} - R^t \begin{bmatrix} \bar{x} \\ \bar{y} \\ \bar{z} \end{bmatrix} \right) = R \left(\begin{bmatrix} x' \\ y' \\ z' \end{bmatrix} - \begin{bmatrix} \bar{x}' \\ \bar{y}' \\ \bar{z}' \end{bmatrix} \right) \\ &= R \begin{bmatrix} x' - \bar{x}' \\ y' - \bar{y}' \\ z' - \bar{z}' \end{bmatrix}. \end{aligned} \quad (\text{A1.3})$$

Here, covariance is calculated as

$$\begin{aligned} V &= \iiint \begin{bmatrix} x - \bar{x} \\ y - \bar{y} \\ z - \bar{z} \end{bmatrix} \rho \begin{bmatrix} x - \bar{x} \\ y - \bar{y} \\ z - \bar{z} \end{bmatrix}^t dx dy dz \\ &= \iiint R \begin{bmatrix} x' - \bar{x}' \\ y' - \bar{y}' \\ z' - \bar{z}' \end{bmatrix} \rho \begin{bmatrix} x' - \bar{x}' \\ y' - \bar{y}' \\ z' - \bar{z}' \end{bmatrix}^t R^{-1} dx' dy' dz' \\ &= R \left(\iiint \begin{bmatrix} x' - \bar{x}' \\ y' - \bar{y}' \\ z' - \bar{z}' \end{bmatrix} \rho \begin{bmatrix} x' - \bar{x}' \\ y' - \bar{y}' \\ z' - \bar{z}' \end{bmatrix}^t dx' dy' dz' \right) R^{-1} \\ &= R \left(\iiint \begin{bmatrix} x' - x'_0 \\ y' - y'_0 \\ z' - z'_0 \end{bmatrix} \begin{bmatrix} x' - x'_0 \\ y' - y'_0 \\ z' - z'_0 \end{bmatrix}^t \frac{\exp[-(x' - x'_0)^2/2\sigma_{x'}^2]}{\sqrt{2\pi}\sigma_{x'}} \right. \\ &\quad \left. \frac{\exp[-(y' - y'_0)^2/2\sigma_{y'}^2]}{\sqrt{2\pi}\sigma_{y'}} \frac{\exp[-(z' - z'_0)^2/2\sigma_{z'}^2]}{\sqrt{2\pi}\sigma_{z'}} dz' \right) R^{-1} \\ &= R \begin{bmatrix} \sigma_{x'}^2 & 0 & 0 \\ 0 & \sigma_{y'}^2 & 0 \\ 0 & 0 & \sigma_{z'}^2 \end{bmatrix} R^{-1}, \end{aligned} \quad (\text{A1.4})$$

while

$$\frac{1}{\sqrt{2\pi}\sigma_{x'}} \int \exp \left(-\frac{(x' - x'_0)^2}{2\sigma_{x'}^2} \right) dx = 1 \quad (\text{A1.5})$$

$$\int (x' - x'_0) \exp \left(-\frac{(x' - x'_0)^2}{2\sigma_{x'}^2} \right) dx = 0 \quad (\text{A1.6})$$

$$\frac{1}{\sqrt{2\pi}\sigma_{x'}} \int (x' - x'_0)^2 \exp\left(-\frac{(x' - x'_0)^2}{2\sigma_{x'}^2}\right) dx = \sigma_{x'}^2. \quad (\text{A1.7})$$

So that

$$VR = R \begin{bmatrix} \sigma_{x'}^2 & 0 & 0 \\ 0 & \sigma_y^2 & 0 \\ 0 & 0 & \sigma_z^2 \end{bmatrix} \quad (\text{A1.8})$$

and therefore we obtain

$$\sigma_{x'}^2 = \lambda_1, \quad \sigma_y^2 = \lambda_2, \quad \sigma_z^2 = \lambda_3, \quad (\text{A1.9})$$

$$R = [\mathbb{V}_1 \quad \mathbb{V}_2 \quad \mathbb{V}_3], \quad (\text{A1.10})$$

where λ_1, λ_1 , and λ_1 are eigenvalues of V and $\mathbb{V}_1, \mathbb{V}_2$, and \mathbb{V}_3 are corresponding eigenvectors. Therefore cluster shapes can be determined by solving eigenvalues and eigenvectors of the covariance matrix.

A2. Source Type Diagram

Deformation in a small volume of earth interior is expressed by a symmetric moment tensor located on a point source. The tensor contains information of characteristic directions, source amplitude, and source types such as isotropic, double-couple, or compensated-linear-vector-dipole (CLVD). Although we often assume a double couple as the source type of an earthquake, significant non-double-couple component including isotropic component is often reported for induced earthquakes and volcanic earthquakes [e.g., *Iguchi, 1994; Ross et al., 1996; Julian et al., 1997; Julian et al., 1998; Miller et al., 1998; Ross et al., 1999; Legrand et al., 2000; Kawakatsu et al., 2000; Sarao et al., 2001; Foulger et al., 2004; Shuler et al., 2013*]. Non-double-couple component also appears for regular shear slips on a bending fault [*Kikuchi et al., 1993; Adamova and Sileny, 2010*] or deep earthquakes [*Kuge and Kawakatsu, 1990; Hara et al., 1995; Kawakatsu, 1996*].

For discussions on source types including double-couple and non-double-couple components, it is helpful to display them using some visual diagrams. Since the information of source type has two degrees of freedom, it can be displayed onto a two-dimensional flat plane. Although the diagram developed by *Hudson et al. [1989]* is popular, its oblique quadrant shape makes its use difficult (Figure A2.1a). In the diagram, CLVD is not located on the corner, which is another difficulty in use. Moreover, the trace corresponding to the mechanism combined by two mechanisms is not always a smooth line.

To overcome these problems, *Chapman and Leaney [2012]* developed a new diagram (Figure A2.1b). This diagram has an advantage that a straight line passing through the center corresponds to the mechanism obtained by a combination of an arbitrary mechanism and a double-couple [*Tape and Tape, 2012a, 2012b, 2012c, 2013*], but this diagram still has some difficulties in use. First, it is slightly difficult to produce the diagram because of its curved shape. Second, it is also difficult to read out the ratios among isotropic, double-couple, and CLVD components, which we often want to know from the obtained moment tensors. Actually, isotropic component in vertical direction is exaggerated rather than deviatoric component in the horizontal directions.

Here we develop another new square diagram that overcomes the difficulties of previous diagrams (Figure A2.1c). This diagram is an orthogonal system of isotropic and deviatoric axes, so it is easy to get the ratios among isotropic, double-couple, and CLVD components.

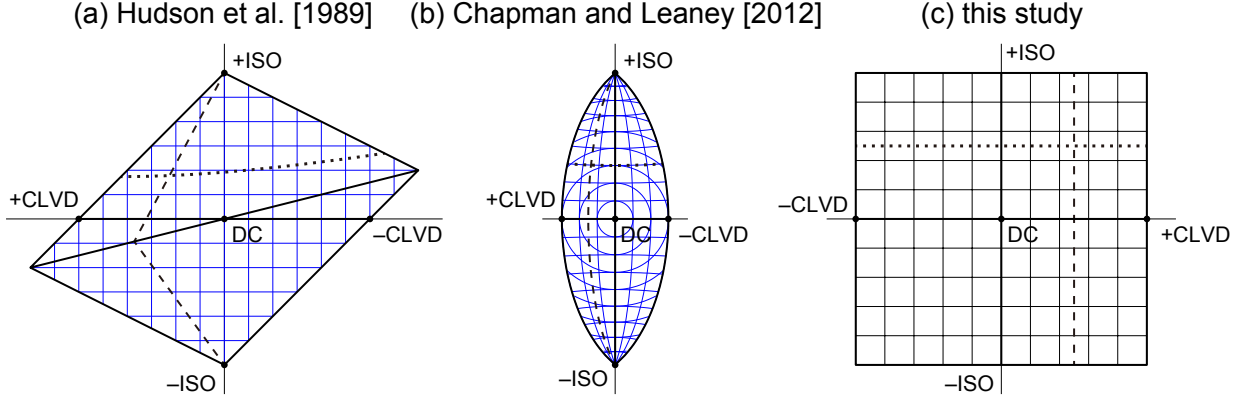


Figure A2.1 Comparison source type diagrams

(a) Traditional diagram by *Hudson et al.* [1989]. (b) Recent diagram by *Chapman and Leaney* [2012]. (c) New diagram in the present study.

The diagonalization of the moment tensor M_{ij} is expressed as follows:

$$\begin{pmatrix} v_{1x} & v_{1y} & v_{1z} \\ v_{2x} & v_{2y} & v_{2z} \\ v_{3x} & v_{3y} & v_{3z} \end{pmatrix} \begin{pmatrix} M_{xx} & M_{xy} & M_{xz} \\ M_{yx} & M_{yy} & M_{yz} \\ M_{zx} & M_{zy} & M_{zz} \end{pmatrix} \begin{pmatrix} v_{1x} & v_{2x} & v_{3x} \\ v_{1y} & v_{2y} & v_{3y} \\ v_{1z} & v_{2z} & v_{3z} \end{pmatrix} = \begin{pmatrix} \lambda_1 & & \\ & \lambda_2 & \\ & & \lambda_3 \end{pmatrix}, \quad (\text{A2.1})$$

where λ_1 , λ_2 , and λ_3 ($\lambda_1 \geq \lambda_2 \geq \lambda_3$) are eigenvalues and $\begin{pmatrix} v_{1x} \\ v_{1y} \\ v_{1z} \end{pmatrix}$, $\begin{pmatrix} v_{2x} \\ v_{2y} \\ v_{2z} \end{pmatrix}$, and $\begin{pmatrix} v_{3x} \\ v_{3y} \\ v_{3z} \end{pmatrix}$ are corresponding normalized eigenvectors. This diagonalization converts six degree of freedom of moment tensor to three parameters that define eigenvectors of three-dimensional Cartesian coordinate and three parameters of eigenvalues that define size and source type. Since the size is scalar information and the source type is two degrees of freedom, the source type can be visualized on a two-dimensional plane. There are several styles of the visualization, but these previous diagrams are difficult to apply to observed data or to read physical characteristics of the data.

Using eigenvalues of each moment tensor, a point (u, v) on the traditional source type diagram developed by *Hudson et al.* [1989], a point (p, q) on the recent source type diagram developed by *Chapman and Leaney* [2012], and a point (a, b) on a new source type diagram can be obtained as follows:

$$[u] = \begin{cases} \begin{bmatrix} \frac{2(\lambda_1 - 2\lambda_2 + \lambda_3)}{3\lambda_3} \\ \frac{\lambda_1 + \lambda_2 + \lambda_3}{3\lambda_3} \end{bmatrix} & \lambda_1 + \lambda_3 \leq 0 \\ \begin{bmatrix} \frac{2(-\lambda_1 + 2\lambda_2 - \lambda_3)}{3\lambda_1} \\ \frac{\lambda_1 + \lambda_2 + \lambda_3}{3\lambda_1} \end{bmatrix} & \lambda_1 + \lambda_3 \geq 0 \end{cases} \quad (\text{A2.2})$$

$$\begin{bmatrix} p \\ q \end{bmatrix} = \begin{bmatrix} \sqrt{1 - \frac{(\lambda_1 - \lambda_3)/\sqrt{2}}{\sqrt{\lambda_1^2 + \lambda_2^2 + \lambda_3^2}} \frac{(-\lambda_1 + 2\lambda_2 - \lambda_3)/\sqrt{3}}{\sqrt{\lambda_1^2 + 2\lambda_2^2 + \lambda_3^2 + \lambda_1\lambda_3}}} \\ \sqrt{1 - \frac{(\lambda_1 - \lambda_3)/\sqrt{2}}{\sqrt{\lambda_1^2 + \lambda_2^2 + \lambda_3^2}} \frac{\sqrt{2/3}(\lambda_1 + \lambda_2 + \lambda_3)}{\sqrt{\lambda_1^2 + 2\lambda_2^2 + \lambda_3^2 + \lambda_1\lambda_3}}} \end{bmatrix} \quad (\text{A2.3})$$

$$\begin{bmatrix} a \\ b \end{bmatrix} = \begin{bmatrix} \frac{6}{\pi} \tan^{-1} \left(\frac{\sqrt{3}(\lambda_1 - 2\lambda_2 + \lambda_3)}{\lambda_1 - \lambda_3} \right) \\ \frac{(\lambda_1 + \lambda_2 + \lambda_3)/\sqrt{3}}{\sqrt{\lambda_1^2 + \lambda_2^2 + \lambda_3^2}} \end{bmatrix} \quad (\text{A2.4})$$

A2.1. Previous Diagrams

Three-dimensional information for the diagonalized moment tensor can be expressed as a combination of two-dimensional information of source type and one-dimensional information of magnitude. This process enables the source type to be plotted in a two-dimensional plane, but there ought to be various approaches to separate the source type and the size, depending on how the size of the moment tensor is calculated. Here, we consider the three-dimensional Cartesian coordinate $(\lambda_1, \lambda_2, \lambda_3)$, where the eigenvalues of the moment tensor are λ_1, λ_2 , and λ_3 ($\lambda_1 \geq \lambda_2 \geq \lambda_3$).

The traditional source type diagram of *Hudson et al.* [1989] uses the size defined as $\max(|\lambda_1|, |\lambda_2|, |\lambda_3|)$, which means that the source type is projected onto a cube (Figure A2.2a). The area of the surface of the cube is then mapped uniformly onto a two-dimensional plane (Figure A2.2b). Therefore, the probability density function of the source type is homogeneous in a diamond-shaped domain if it is assumed that each of λ_1, λ_2 , and λ_3 has an independent and uniform distribution. This is one possible assumption of the natural distribution of the moment tensor. The projection can be written as a conversion between $(\lambda_1, \lambda_2, \lambda_3)$ and (A, u, v) , as follows:

$$\begin{bmatrix} A \\ u \\ v \end{bmatrix} = \begin{cases} \begin{bmatrix} -\lambda_3 \\ \frac{2(\lambda_1 - 2\lambda_2 + \lambda_3)}{3\lambda_3} \\ -\frac{\lambda_1 + \lambda_2 + \lambda_3}{3\lambda_3} \end{bmatrix} & \lambda_1 + \lambda_3 \leq 0 \\ \begin{bmatrix} \lambda_1 \\ \frac{2(-\lambda_1 + 2\lambda_2 - \lambda_3)}{3\lambda_1} \\ \frac{\lambda_1 + \lambda_2 + \lambda_3}{3\lambda_1} \end{bmatrix} & \lambda_1 + \lambda_3 \geq 0 \end{cases} \quad (\text{A2.5})$$

or inversely as:

$$\begin{bmatrix} \lambda_1 \\ \lambda_2 \\ \lambda_3 \end{bmatrix} = \begin{cases} \frac{A}{2} \begin{bmatrix} -u + 4v + 2 \\ u + 2v \\ -2 \end{bmatrix} & -u + 4v \leq 0 \\ \frac{A}{2} \begin{bmatrix} 2 \\ u + 2v \\ -u + 4v - 2 \end{bmatrix} & -u + 4v \geq 0 \end{cases} \quad (\text{A2.6})$$

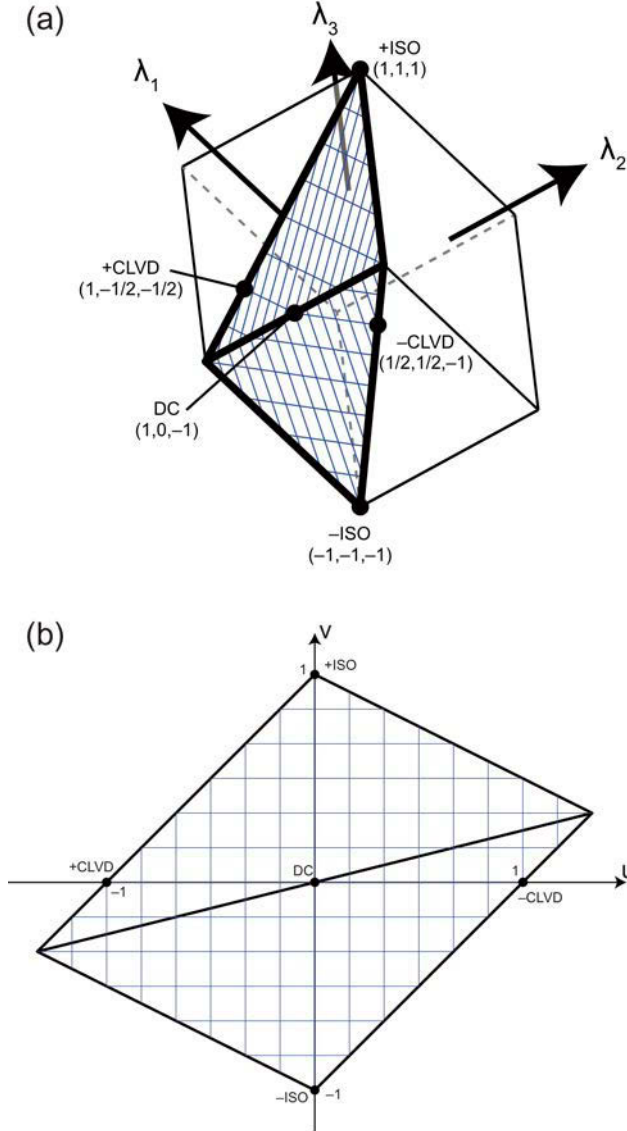


Figure A2.2 Previous source type diagram by Hudson et al. [1989]

Process followed in plotting the source type in the ordinary source type diagram. Blue lines correspond to orthogonal axes of the traditional source type diagram. End-members of double couple (DC), compensated linear vector dipole (CLVD), and isotropic deformation (ISO) are plotted. (a) Projection on the cube in three-dimensional space ($\lambda_1, \lambda_2, \lambda_3$). (b) The area on the surface of the cube uniformly mapped in two-dimensional space (u, v).

A2.2. New Diagram

We propose another type of source diagram that uses the size defined by the L2-norm as $\sqrt{(\lambda_1^2 + \lambda_2^2 + \lambda_3^2)/2}$, which means that the source type is projected onto a sphere (Figure A2.3a). This norm is the scalar moment [Shearer, 2009] and is equal to the scalar seismic moment in the case of a pure double couple source. The area of the surface of the sphere is then mapped onto a two-dimensional plane using a cylindrical projection (Figure A2.3b), which maps the area on a sphere uniformly onto a two-dimensional plane (Figure A2.3c). If we assume that each of λ_1 , λ_2 , and λ_3 has an independent normal distribution, then the probability density function of the source type is homogeneous in a square domain. This projection can be written as a conversion between $(\lambda_1, \lambda_2, \lambda_3)$ and (M_o, a, b) , as follows:

$$\begin{bmatrix} M_o \\ a \\ b \end{bmatrix} = \begin{bmatrix} \sqrt{\frac{\lambda_1^2 + \lambda_2^2 + \lambda_3^2}{2}} \\ \frac{6}{\pi} \sin^{-1} \left(\frac{\lambda_1 - 2\lambda_2 + \lambda_3}{2\sqrt{\lambda_1^2 + \lambda_2^2 + \lambda_3^2 - \lambda_1\lambda_2 - \lambda_2\lambda_3 - \lambda_1\lambda_3}} \right) \\ \frac{\lambda_1 + \lambda_2 + \lambda_3}{\sqrt{3(\lambda_1^2 + \lambda_2^2 + \lambda_3^2)}} \end{bmatrix} \quad (\text{A2.7})$$

or inversely as:

$$\begin{bmatrix} \lambda_1 \\ \lambda_2 \\ \lambda_3 \end{bmatrix} = M_o \begin{bmatrix} \sqrt{\frac{2}{3}}b + \sqrt{1-b^2} \cos\left(\frac{\pi}{6}a\right) + \sqrt{\frac{1-b^2}{3}} \sin\left(\frac{\pi}{6}a\right) \\ \sqrt{\frac{2}{3}}b - 2\sqrt{\frac{1-b^2}{3}} \sin\left(\frac{\pi}{6}a\right) \\ \sqrt{\frac{2}{3}}b - \sqrt{1-b^2} \cos\left(\frac{\pi}{6}a\right) + \sqrt{\frac{1-b^2}{3}} \sin\left(\frac{\pi}{6}a\right) \end{bmatrix} \quad (\text{A2.8})$$

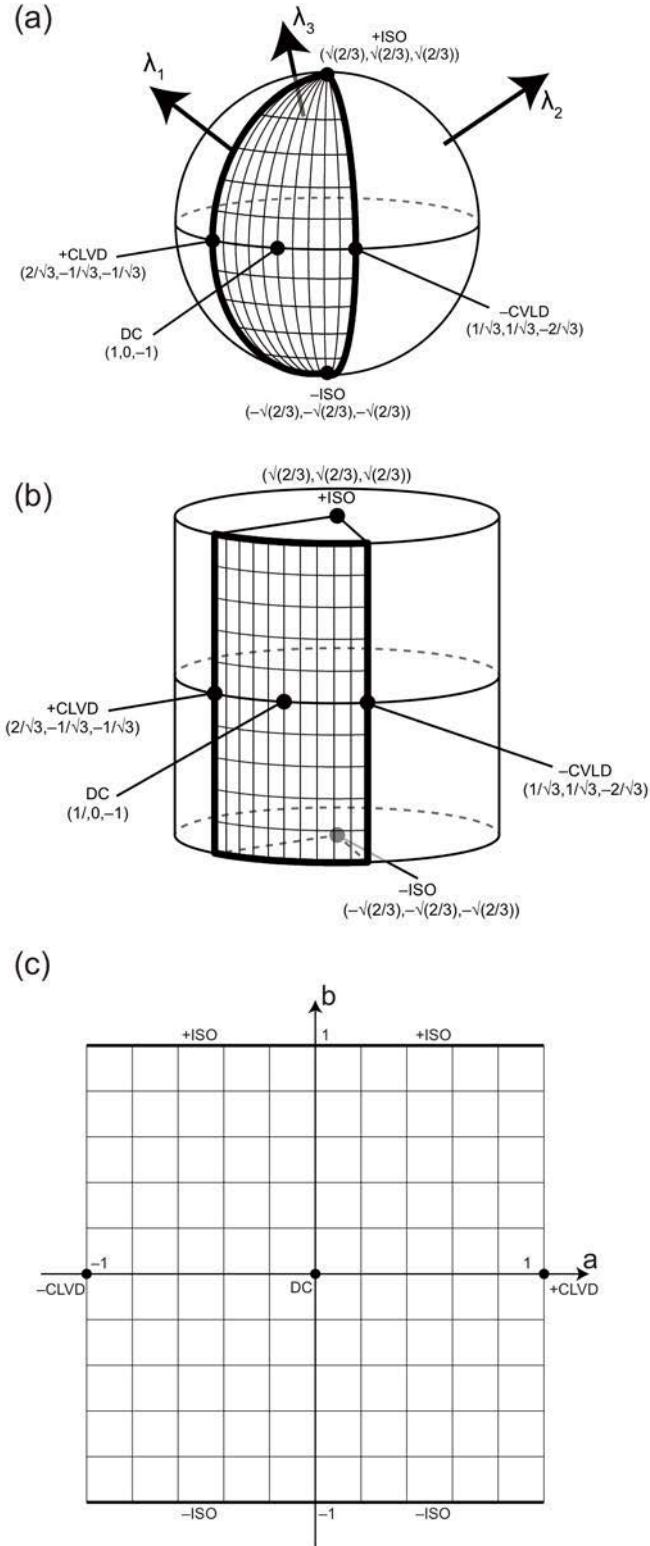


Figure A2.3 New square source type diagram

Process followed in plotting the source type in the new source type diagram. Black lines correspond to orthogonal axes of the new source type diagram. End-members of double couple (DC), compensated linear vector dipole (CLVD), and isotropic deformation (ISO) are plotted. (a) Projection on the sphere in three-dimensional space $(\lambda_1, \lambda_2, \lambda_3)$. (b) The area on

the surface of the sphere uniformly mapped on a two-dimensional curved space using a cylindrical projection. (c) The area on the cylinder uniformly mapped on a two-dimensional flat space (a, b) .

In this diagram, the deviatoric–isotropic space is readily expressed in orthogonal coordinates. A comparison between the two source type diagrams is shown in Figure A2.4.

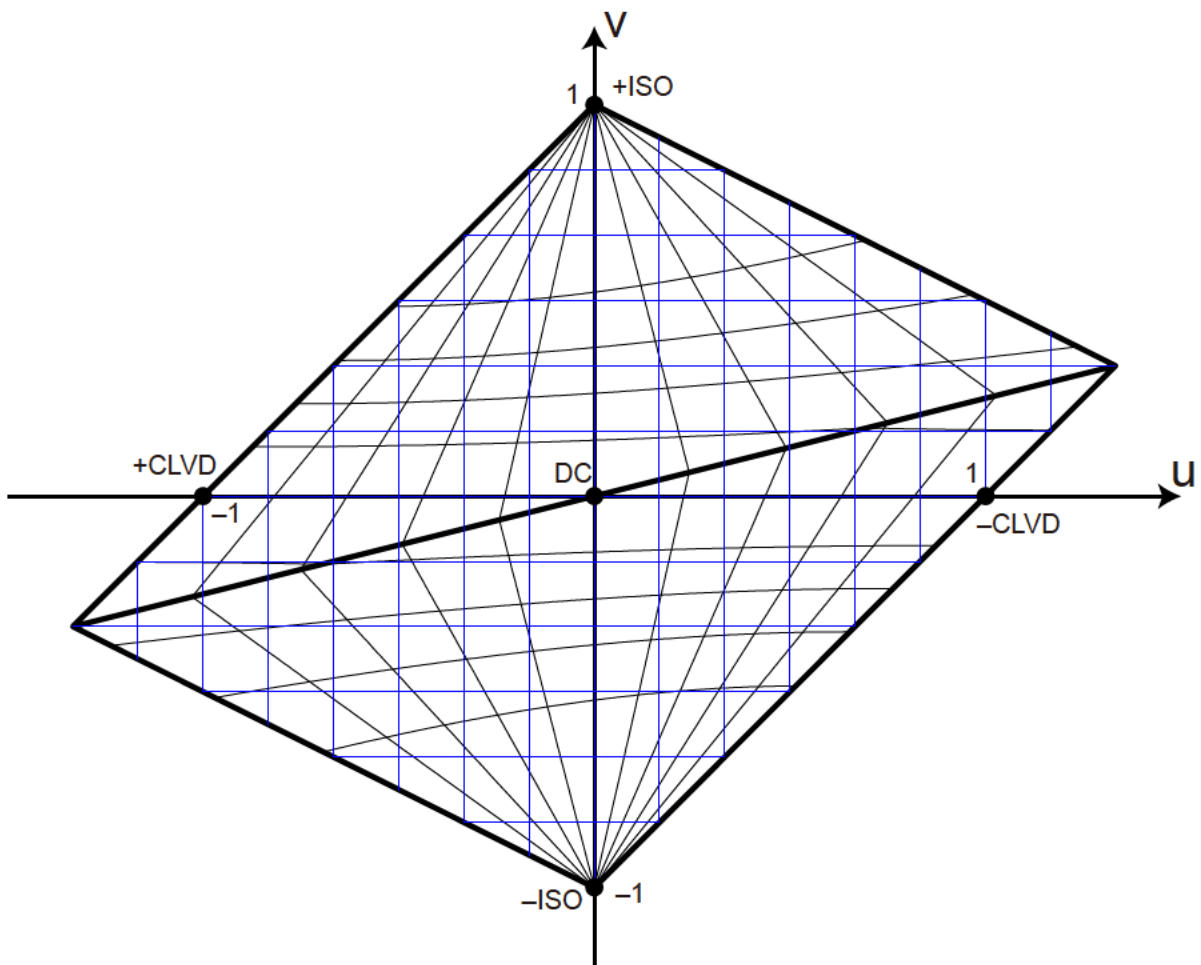


Figure A2.4 Comparison of coordinate system

Blue and black lines correspond to orthogonal axes of the traditional and new source type diagram, respectively. End-members of double couple (DC), compensated linear vector dipole (CLVD), and isotropic deformation (ISO) are plotted.

Each source type can be expressed as a combination of three components, which are DC, major CLVD ($-CLVD$ or $+CLVD$ for $a \leq 0$ or $a \geq 0$, respectively), and major isotropic deformation ($-ISO$ or $+ISO$ for $b \leq 0$ or $b \geq 0$, respectively):

$$\begin{aligned} & \begin{bmatrix} \lambda_1 \\ \lambda_2 \\ \lambda_3 \end{bmatrix} / M_0 \\ &= \begin{cases} 2\sqrt{(1-b^2)} \cos\left(\frac{\pi}{6}a - \frac{\pi}{3}\right) \begin{bmatrix} 1 \\ 0 \\ -1 \end{bmatrix} - 2\sqrt{(1-b^2)} \sin\left(\frac{\pi}{6}a\right) \begin{bmatrix} 1/\sqrt{3} \\ 1/\sqrt{3} \\ -2/\sqrt{3} \end{bmatrix} + b \begin{bmatrix} \sqrt{2/3} \\ \sqrt{2/3} \\ \sqrt{2/3} \end{bmatrix} & a \leq 0 \\ 2\sqrt{(1-b^2)} \cos\left(\frac{\pi}{6}a + \frac{\pi}{3}\right) \begin{bmatrix} 1 \\ 0 \\ -1 \end{bmatrix} + 2\sqrt{(1-b^2)} \sin\left(\frac{\pi}{6}a\right) \begin{bmatrix} 2/\sqrt{3} \\ -1/\sqrt{3} \\ -1/\sqrt{3} \end{bmatrix} + b \begin{bmatrix} \sqrt{2/3} \\ \sqrt{2/3} \\ \sqrt{2/3} \end{bmatrix} & a \geq 0 \end{cases}, \end{aligned} \quad (\text{A2.9})$$

Therefore, the magnitude of each component is as follows:

$$\begin{bmatrix} \lambda_{DC} \\ \lambda_{CLVD} \\ \lambda_{ISO} \end{bmatrix} = M_0 \begin{bmatrix} 2\sqrt{(1-b^2)} \cos\left(\frac{\pi}{6}|a| + \frac{\pi}{3}\right) \\ 2\sqrt{(1-b^2)} \sin\left(\frac{\pi}{6}|a|\right) \\ |b| \end{bmatrix}. \quad (\text{A2.10})$$

Two types of decisions in a general and specific sense are necessary to define the dominance of each component (Figure A2.5). When one component is larger than each of the other two, we note that the source type is generally dominated by the larger component. The relationship is expressed in a–b space as follows:

$$\lambda_{DC}^2 > \lambda_{CLVD}^2 \Leftrightarrow a^2 < \frac{1}{4}, \quad (\text{A2.11})$$

$$\lambda_{DC}^2 > \lambda_{ISO}^2 \Leftrightarrow \frac{1}{1-b^2} > 3 - \sqrt{3} \sin \frac{\pi}{3} |a| - \cos \frac{\pi}{3} a \quad (\text{A2.12})$$

$$\lambda_{CLVD}^2 > \lambda_{ISO}^2 \Leftrightarrow \frac{1}{1-b^2} > 3 - 2 \cos \frac{\pi}{3} a. \quad (\text{A2.13})$$

When one component is larger than the combination of the other two, we note that the source type is specifically dominated by the largest component. The relationship is expressed in a–b space as follows:

$$\lambda_{DC}^2 > \lambda_{CLVD}^2 + \lambda_{ISO}^2 \Leftrightarrow \frac{1}{1-b^2} > 1 - \sqrt{3} \sin \frac{\pi}{3} |a| + \cos \frac{\pi}{3} a. \quad (\text{A2.14})$$

$$\lambda_{CLVD}^2 > \lambda_{DC}^2 + \lambda_{ISO}^2 \Leftrightarrow \frac{1}{1-b^2} > 1 + \sqrt{3} \sin \frac{\pi}{3} |a| - \cos \frac{\pi}{3} a. \quad (\text{A2.15})$$

$$\lambda_{ISO}^2 > \frac{1}{\sqrt{2}} \Leftrightarrow b^2 < \frac{1}{2}. \quad (\text{A2.16})$$

The area dominated by each end-member is shown in Figure A2.5.

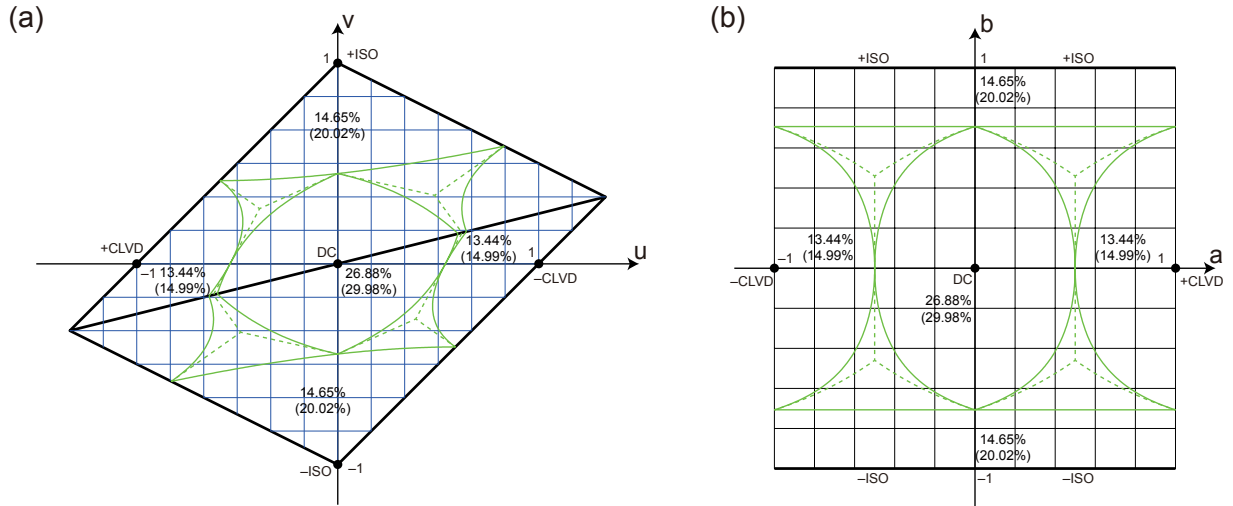


Figure A2.5 Dominated regions of ISO, DC, and CLVD

Areas dominated by each double couple (DC), compensated linear vector dipole (CLVD), and isotropic deformation (ISO) component are shown on the traditional (a) and new (b) source type diagrams. Green solid lines are the area dominated by each component in a specific sense, whereas green dashed lines indicate the area dominated by each component in a general sense. We refer to the source type as being dominated by one component in a specific sense when that component is larger than the other two combined. We refer to the source type as being dominated by one component in a general sense when that component is larger than each of the other two.

A3. Thermal Calculation for a 1D Cartesian Coordinates

For an extended tabular intrusion, the geometry can be approximated as one-dimensional and we solve the associated thermal diffusion problem

$$\frac{\partial T}{\partial t} = \alpha \frac{\partial^2 T}{\partial z^2} \quad (\text{A3.1})$$

$$\frac{\partial T}{\partial t}(t, 0) = 0 \quad (\text{A3.2})$$

$$T(0, z) = \Delta T [H(z + a) - H(z - a)], \quad (\text{A3.3})$$

where T is temperature, t is time, z is 1D coordinate, a is half thickness of the tabular intrusion, ΔT is temperature perturbation, and $H(x)$ is the Heaviside function.

Non-dimensionalization of equations (A1)–(A3) with a characteristic thermal diffusion timescale of t_c results in

$$\frac{\partial T^*}{\partial t^*} = \frac{\partial^2 T^*}{\partial z^{*2}} \quad (\text{A3.4})$$

$$\frac{\partial T^*}{\partial t^*}(t^*, 0) = 0 \quad (\text{A3.5})$$

$$T^*(0, z^*) = H(z^* + a^*) - H(z^* - a^*), \quad (\text{A3.6})$$

where $T^* \equiv T/\Delta T$, $t^* \equiv t/t_c$, $z^* \equiv z/\sqrt{\alpha t_c}$, and $a^* \equiv a/\sqrt{\alpha t_c}$.

The general solution satisfying (A4) and (A5) is

$$T^*(t^*, z^*) = \int_{-\infty}^{\infty} A(p) \exp(-p^2 t^*) \exp(ipz^*) dp \quad (\text{A3.7})$$

Using a Fourier transformation for the initial conditions,

$$T^*(0, z^*) = \int_{-\infty}^{\infty} A(p) \exp(ipz^*) dp \quad (\text{A3.8})$$

results in

$$A(p) = \frac{1}{2\pi} \int_{-\infty}^{\infty} T^*(0, z^*) \exp(-ipz^*) dz. \quad (\text{A3.9})$$

For the initial conditions of (A6),

$$A(p) = \frac{\exp(ipa^*) - \exp(-ipa^*)}{2\pi ip} \quad (\text{A3.10})$$

so that

$$\begin{aligned} T^*(t^*, z^*) &= \int_{-\infty}^{\infty} \frac{\exp[ip(z^* + a^*)] - \exp[ip(z^* - a^*)]}{2\pi ip} \exp(-p^2 t^*) dp \\ &= \int_{\infty}^{-\infty} \frac{\exp[-ip'(z^* + a^*)] - \exp[-ip'(z^* - a^*)]}{-2\pi ip'} \exp(-p'^2 t^*) (-dp') \\ &= -\frac{1}{2\pi i} \int_{-\infty}^{\infty} \frac{\exp(-p^2 t^*)}{p} \exp[-ip(z^* + a^*)] dp \\ &\quad + \frac{1}{2\pi i} \int_{-\infty}^{\infty} \frac{\exp(-p^2 t^*)}{p} \exp[-ip(z^* - a^*)] dp. \end{aligned} \quad (\text{A3.11})$$

Here, the elementary Fourier transforms are

$$\int_{-\infty}^{\infty} \exp(-p^2 t^*) \exp(-ipz^*) dp = \sqrt{\frac{\pi}{t^*}} \exp\left(-\frac{z^{*2}}{4t^*}\right) \quad (\text{A3.12})$$

$$\int_{-\infty}^{\infty} \frac{1}{p} \exp(-ipz^*) dp = -\pi i \operatorname{sgn}(z^*), \quad (\text{A3.13})$$

where $\operatorname{sgn}(x)$ is the sign function, and their convolution is calculated as

$$\begin{aligned} \int_{-\infty}^{\infty} \frac{\exp(-p^2 t^*)}{p} \exp(-ipz^*) dp &= \frac{-\sqrt{\pi} i}{2\sqrt{t^*}} \int_{-\infty}^{\infty} \exp\left(-\frac{\alpha^2}{4t^*}\right) \operatorname{sgn}(z^* - \alpha) d\alpha \\ &= \frac{-\sqrt{\pi} i}{\sqrt{t^*}} \int_0^{z^*} \exp\left(-\frac{\alpha^2}{4t^*}\right) d\alpha = -2\sqrt{\pi} i \int_0^{\frac{z^*}{2\sqrt{t^*}}} \exp(-\beta^2) d\beta = -\pi i \operatorname{erf}\left(\frac{z^*}{2\sqrt{t^*}}\right), \end{aligned} \quad (\text{A3.14})$$

where $\operatorname{erf}(x)$ is the error function. Therefore,

$$T^* = \frac{1}{2} \left[\operatorname{erf}\left(\frac{z^* + a^*}{2\sqrt{t^*}}\right) - \operatorname{erf}\left(\frac{z^* - a^*}{2\sqrt{t^*}}\right) \right] \equiv T_z^*. \quad (\text{A3.15})$$

A4. Thermal Calculation for a 1D Polar Coordinates

For an infinitely long cylindrical intrusion, the geometry can be approximated as one-dimensional in the radial direction and we solve the associated thermal diffusion problem

$$\frac{\partial T}{\partial t} = \alpha \left(\frac{\partial^2}{\partial r^2} + \frac{1}{r} \frac{\partial}{\partial r} \right) T \quad (\text{A4.1})$$

$$\frac{\partial T}{\partial r}(t, 0) = 0 \quad (\text{A4.2})$$

$$T(0, r) = \Delta T[1 - H(r - b)], \quad (\text{A4.3})$$

where r is radial coordinate, b is radius of the cylindrical intrusion, and other variables are as before.

Non-dimensionalization of equations (B1)–(B3) results in

$$\frac{\partial T^*}{\partial t^*} = \left(\frac{\partial^2}{\partial r^{*2}} + \frac{1}{r^*} \frac{\partial}{\partial r^*} \right) T^* \quad (\text{A4.4})$$

$$\frac{\partial T^*}{\partial r^*}(t^*, 0) = 0 \quad (\text{A4.5})$$

$$T^*(0, r^*) = 1 - H(r^* - b^*), \quad (\text{A4.6})$$

where $r^* \equiv r/\sqrt{\alpha t_c}$ and $b^* \equiv b/\sqrt{\alpha t_c}$.

The general solution satisfying (B4) and (B5) is

$$T_r^*(t^*, r^*) = \int_0^\infty B(q) \exp(-q^2 t^*) J_0(q r^*) dq, \quad (\text{A4.7})$$

where J_n is n -th order Bessel function. Using a Hankel transformation for the initial conditions,

$$T^*(0, r^*) = \int_0^\infty B(q) J_0(q r^*) dq \quad (\text{A4.8})$$

$$B(q) = q \int_0^\infty T^*(0, r^*) J_0(q r^*) r^* dr^*. \quad (\text{A4.9})$$

For the initial conditions of (B6),

$$B(q) = q \int_0^{b^*} J_0(q r^*) r^* dr^* = \frac{1}{q} \int_0^{q b^*} q r^* J_0(q r^*) d(q r^*) = b^* J_1(q b^*) \quad (\text{A4.10})$$

$$\begin{aligned} T^*(t^*, r^*) &= \int_0^\infty \exp(-q^2 t^*) J_0(q r^*) J_1(q b^*) b^* dq \\ &= \int_0^\infty \exp\left(-\frac{t^*}{b^{*2}} q^2\right) J_0\left(\frac{r^*}{b^*} q\right) J_1(q) dq \equiv T_r^*. \end{aligned} \quad (\text{A4.11})$$

A5. Thermal Calculation for a 2D Cylindrical Coordinates

We solve the thermal diffusion equation in a cylindrical coordinate system

$$\frac{\partial T}{\partial t} = \alpha \left(\frac{\partial^2}{\partial z^2} + \frac{\partial^2}{\partial r^2} + \frac{1}{r} \frac{\partial}{\partial r} \right) T \quad (\text{A5.1})$$

with boundary conditions

$$\frac{\partial T}{\partial z}(t, 0, r) = 0 \quad (\text{A5.2})$$

$$\frac{\partial T}{\partial r}(t, z, 0) = 0 \quad (\text{A5.3})$$

and an initial condition

$$T(0, z, r) = \Delta T [H(z + a) - H(z - a)][1 - H(r - b)]. \quad (\text{A5.4})$$

Non-dimensionalization of equations (C1)–(C4) results in

$$\frac{\partial T^*}{\partial t^*} = \left(\frac{\partial^2}{\partial z^{*2}} + \frac{\partial^2}{\partial r^{*2}} + \frac{1}{r^*} \frac{\partial}{\partial r^*} \right) T^* \quad (\text{A5.5})$$

$$\frac{\partial T^*}{\partial z^*}(t^*, 0, r^*) = 0 \quad (\text{A5.6})$$

$$\frac{\partial T^*}{\partial r^*}(t^*, z^*, 0) = 0 \quad (\text{A5.7})$$

$$T^*(0, z^*, r^*) = [H(z^* + a^*) - H(z^* - a^*)][1 - H(r^* - b^*)]. \quad (\text{A5.8})$$

The general solution satisfying (C5)–(C7) is

$$T^*(t^*, z^*, r^*) = \int_0^\infty \int_0^\infty C(p, q) \exp[-(p^2 + q^2)t^*] \exp(ipz^*) J_0(qr^*) dq dp \quad (\text{A5.9})$$

and therefore

$$T^*(0, z^*, r^*) = \int_{-\infty}^\infty \int_0^\infty C(p, q) \exp(ipz^*) J_0(qr^*) dq dp. \quad (\text{A5.10})$$

Here initial condition (C8) is

$$\begin{aligned} T^*(0, z^*, r^*) &= T_z^*(0, z^*) T_r^*(0, r^*) \\ &= \int_{-\infty}^\infty \int_0^\infty A(p) B(q) \exp(ipz^*) J_0(qr^*) dq dp \end{aligned} \quad (\text{A5.11})$$

and therefore $C(p, q) = A(p)B(q)$. So that

$$\begin{aligned} T^*(t^*, z^*, r^*) &= \int_{-\infty}^\infty A(p) \exp(-p^2 t^*) \exp(ipz^*) dp \int_0^\infty B(q) \exp(-q^2 t^*) J_0(qr^*) dq \\ &= T_z^*(t^*, z^*) \times T_r^*(t^*, r^*). \end{aligned} \quad (\text{A5.12})$$

A6. Thermal Strain and Thermal Stress

Thermal stress calculation is already summarized by *Timoshenko and Goodier* [1970], but here we verify the detailed derivation of strain rates in cylindrical coordinates. At first, we consider Cartesian coordinates. The stress-strain constitutive law is

$$\sigma_{ij} = 2\mu\epsilon_{ij} + \delta_{ij}\lambda \sum_k \epsilon_{kk} - \delta_{ij}(3\lambda + 2\mu)\frac{\kappa}{3}(T - T_0), \quad (\text{A6.1})$$

where ϵ_{ij} , σ_{ij} , λ , μ , κ , T , and T_0 are strain, stress, Lamé's first parameter, shear modulus, volumetric thermal expansion coefficient. We set λ , μ , and κ as constant parameters.

We assume that displacement is given by a scalar potential $u_i = \partial\psi/\partial x_i$, and therefore strain is given by $\epsilon_{ij} = \frac{\partial^2\psi}{\partial x_i\partial x_j}$. Solving the equations of equilibrium ($\sum_i \sigma_{ij,i} = 0$),

$$(\lambda + 2\mu)\nabla^2 \frac{\partial\psi}{\partial x_i} - \frac{(3\lambda + 2\mu)\kappa}{3} \frac{\partial}{\partial x_i}(T - T_0) = 0. \quad (\text{A6.2})$$

Taking its time derivative and replacing the time derivative of temperature with a spatial derivative for the case when temperature is driven only by thermal diffusion $\frac{\partial T}{\partial t} = \alpha\nabla^2 T$,

$$\nabla^2 \left[\frac{\partial\psi}{\partial x_i} - \frac{(3\lambda + 2\mu)\alpha\kappa}{3(\lambda + 2\mu)} \frac{\partial T}{\partial x_i} \right] = 0 \quad (\text{A6.3})$$

$$v_i = \frac{\partial\psi}{\partial x_i} = \frac{3\lambda + 2\mu\alpha\kappa}{\lambda + 2\mu} \frac{\partial T}{3\partial x_i} + F_i(x, y, z, t), \quad (\text{A6.4})$$

where F_i is a harmonic function. For the case of adiabatic ($\partial T/\partial n = 0$) and free surface ($\partial v_i/\partial n = 0$) conditions on the boundary S (therefore $\partial F_i/\partial n = 0$ on S), F_i is equal to a constant function. Even if we assume Dirichlet condition ($v_i = 0$) instead of Neumann condition, F_i is also a constant function. Since $v_i = 0$ and $\partial T/\partial x_i = 0$ at the center, $F_i = 0$ and therefore

$$v_i = \frac{3\lambda + 2\mu\alpha\kappa}{\lambda + 2\mu} \frac{\partial T}{3\partial x_i}. \quad (\text{A6.5})$$

Therefore, the strain rate in cylindrical coordinates is given by

$$\begin{aligned} \dot{\epsilon}_{rr} &= \frac{\partial v_r}{\partial r} = \left(\frac{3\lambda + 2\mu\alpha\kappa}{\lambda + 2\mu} \frac{1}{3} \right) \frac{\partial^2 T}{\partial r^2} \\ \dot{\epsilon}_{\theta\theta} &= \frac{1}{r} \frac{\partial v_\theta}{\partial \theta} + \frac{v_r}{r} = \left(\frac{3\lambda + 2\mu\alpha\kappa}{\lambda + 2\mu} \frac{1}{3} \right) \frac{1}{r} \frac{\partial T}{\partial r} \\ \dot{\epsilon}_{zz} &= \frac{\partial v_z}{\partial z} = \left(\frac{3\lambda + 2\mu\alpha\kappa}{\lambda + 2\mu} \frac{1}{3} \right) \frac{\partial^2 T}{\partial z^2} \\ \dot{\epsilon}_{r\theta} &= \frac{1}{2} \left(\frac{1}{r} \frac{\partial v_r}{\partial \theta} + \frac{\partial v_\theta}{\partial r} - \frac{v_\theta}{r} \right) = 0 \\ \dot{\epsilon}_{rz} &= \frac{1}{2} \left(\frac{\partial v_z}{\partial r} + \frac{\partial v_r}{\partial z} \right) = \left(\frac{3\lambda + 2\mu\alpha\kappa}{\lambda + 2\mu} \frac{1}{3} \right) \frac{\partial^2 T}{\partial r \partial z} \\ \dot{\epsilon}_{\theta z} &= \frac{1}{2} \left(\frac{\partial v_\theta}{\partial z} + \frac{1}{r} \frac{\partial v_z}{\partial \theta} \right) = 0. \end{aligned} \quad (\text{A6.6})$$

A7. Spatial Derivatives of the Analytic Solutions

For the calculation of thermal strain rates, we give analytic solutions for the spatial derivatives of temperature. The derivatives are

$$T_z^* = \frac{1}{2} \left[\operatorname{erf} \left(\frac{z^* + a^*}{2\sqrt{t^*}} \right) - \operatorname{erf} \left(\frac{z^* - a^*}{2\sqrt{t^*}} \right) \right] \quad (\text{A7.1})$$

$$\frac{\partial T_z^*}{\partial z^*} = \frac{1}{2\sqrt{\pi t^*}} \left[\exp \left(-\frac{(z^* + a^*)^2}{4t^*} \right) - \exp \left(-\frac{(z^* - a^*)^2}{4t^*} \right) \right] \quad (\text{A7.2})$$

$$\frac{\partial^2 T_z^*}{\partial z^{*2}} = \frac{-1}{4\sqrt{\pi t^{*1.5}}} \left[(z^* + a^*) \exp \left(-\frac{(z^* + a^*)^2}{4t^*} \right) - (z^* - a^*) \exp \left(-\frac{(z^* - a^*)^2}{4t^*} \right) \right] \quad (\text{A7.3})$$

and

$$T_r^* = \int_0^\infty \exp \left(-\frac{t^*}{b^{*2}} p^2 \right) J_0 \left(\frac{r^*}{b^*} p \right) J_1(p) dp \quad (\text{A7.4})$$

$$\frac{\partial T_r^*}{\partial r^*} = -\frac{1}{b^*} \int_0^\infty \exp \left(-\frac{t^*}{b^{*2}} p^2 \right) J_1 \left(\frac{r^*}{b^*} p \right) J_1(p) p dp \quad (\text{A7.5})$$

$$\frac{\partial^2 T_r^*}{\partial r^{*2}} = -\frac{1}{2b^{*2}} \int_0^\infty \exp \left(-\frac{t^*}{b^{*2}} p^2 \right) \left[J_0 \left(\frac{r^*}{b^*} p \right) - J_2 \left(\frac{r^*}{b^*} p \right) \right] J_1(p) p^2 dp. \quad (\text{A7.6})$$

Using the recurrence relation $J_n(x)/x = (J_{n-1}(x) + J_{n+1}(x))/2n$,

$$\begin{aligned} \frac{1}{r^*} \frac{\partial T_r^*}{\partial r^*} &= -\frac{1}{b^{*2}} \int_0^\infty \exp \left(-\frac{t^*}{b^{*2}} p^2 \right) J_1 \left(\frac{r^*}{b^*} p \right) \left(\frac{r^*}{b^*} p \right)^{-1} J_1(p) p^2 dp \\ &= -\frac{1}{2b^{*2}} \int_0^\infty \exp \left(-\frac{t^*}{b^{*2}} p^2 \right) \left[J_0 \left(\frac{r^*}{b^*} p \right) + J_2 \left(\frac{r^*}{b^*} p \right) \right] J_1(p) p^2 dp. \end{aligned} \quad (\text{A7.7})$$

Acknowledgments

I would like to express my profound gratitude to my advisor, Dr. Satoshi Ide, for helpful support, constructive discussion, and daily encouragement. I also thank Dr. Victor C. Tsai, for supporting my stay in the California Institute of Technology, discussions and encouragements during and after my internship. I also appreciate my co-workers, Dr. Kazuaki Ohta, for having lots of discussions and providing his original code to relocate hypocenters. As a member of the seismology group in the School of Science, the University of Tokyo, Dr. Ryosuke Ando, Dr. Takehito Suzuki, Dr. Koki Idehara, Dr. Julie Maury, Mr. Shintaro Tamura, Mr. Yoshiharu Kurihara, Mr. Suguru Yabe, Mr. Shimon Abe, Mr. Masamichi Ara, Mr. Tomoaki Nishikawa, and Mr. Naoto Mizuno joined our daily discussions. Ms. Agnès Chounet, Mr. Jiaxuan Li, and Ms. Hsin-Ju Tai also visited our group as internship students. I am grateful to Dr. Naoki Suda, Dr. Kazushige Obara, Dr. Minoru Takeo, Dr. Hitoshi Kawakatsu, Dr. Takao Ohminato, Dr. Mie Ichihara, Dr. Hiroyuki Kumagai, Dr. Hideo Aochi, Dr. Haruhisa Nakamichi, Dr. Hiroo Kanamori, Dr. Zhigang Peng, Dr. John E. Vidale, Dr. Haidi Huston, Dr. Kelin Wang, Dr. Gregory C. Beroza, Dr. Abhijit Ghosh, Dr. Stephen G. Holtkamp, Dr. Emily E. Brodsky, Dr. James J. Mori, Dr. Nozomu Takeuchi, Dr. Bunichiro Shibazaki, Dr. Yoshihiro Ito, Dr. Kazuhito Ozawa, Dr. Ichiko Shimizu, and Dr. Atsuko Namiki for constructive discussions. I also thank, Dr. Robert J. Geller, Dr. Satoru Honda, Dr. Nobumasa Funamori, Dr. Ataru Sakuraba, Dr. Keisuke Nishida, Dr. Kiwamu Nishida, Dr. Yosuke Aoki, and Dr. Gaku Kimura for valuable comments.

A main portion of the section 3 has been published as *Aso and Tsai* [2014]. Introduction contains previous work by us as *Aso et al.* [2011, 2013] and *Aso and Ide* [2014]. We used the earthquake catalogs by JMA, and all the waveform data were obtained from the NIED Hi-net data server. The WIN System was useful to check the hypocentral distribution and the Seismic Analysis Code (SAC) was useful to look up seismic waveforms. The figures in this thesis were created using MATLAB, Generic Mapping Tool (GMT), and Adobe Illustrator. This thesis itself was written using Microsoft Word 2011 in Mac OS 10.9. This work was mainly supported by JSPS KAKENHI (12J09135), and I was also supported by JSPS KAKENHI (20340115), and MEXT KAKENHI (21107007).

I appreciate Dr. Toshiro Tanimoto, Dr. Tsuyoshi Iizuka, Dr. Yasutaka Ikeda, Dr. Hiromitsu Mizutani, Dr. Jun Kameda, Dr. Kenji Kawai, Dr. Tomoko E. Yano, Dr. Asuka Yamaguchi, Dr. Tomoko Sato, Dr. Nobuaki Fuji, Dr. Kensuke Konishi, Ms. Chiho Kusuda, Ms. Sawako Miyabayashi Kinoshita, Dr. Yohei Hamada, Mr. Kota Okamoto, Mr. Daisuke Wakabayashi, Mr. Ryuichi Nishiyama, Mr. Hiroto Takada, Mr. Yoshiki Shirahama, Mr. Kei Hasegawa, Ms. Shoko Hina, Mr. Satoshi Fujita, Mr. Yuki Maehara, and Ms. Sunhe Yun, Mr. Kohtaro R. Araragi, Mr. Rintaro Kamata, Mr. Takeshi Akuhara, Mr. Satoshi Ogino, Mr. Mitsutsugu Igarashi, Mr. Hiroaki Koge, Ms. Mari

Hamahashi, Ms. Rina Fukuchi, Mr. Yukihiro Nakatani, Mr. Satoshi Annoura, Mr. Daisuke Haijima, and Mr. Anselme Borgeaud for daily encouragement during my graduate studies. I have successfully worked on this study owing to many other people and friends. Of course, none of this work would have been possible without the support and patience of my family including my fiancée Ms. Miki Ido.

Tokyo, Japan, December 16, 2014

Naofumi Aso

References

- Adamová, P., and J. Šílený (2010), Non-double-couple earthquake mechanism as an artifact of the point-source approach applied to a finite-extent focus, *Bull. Seismol. Soc. Am.*, *100*, 447–457, doi:10.1785/0120090097.
- Aki, K., and R. Koyanagi (1981), Deep volcanic tremor and magma ascent mechanism under Kilauea, Hawaii, *J. Geophys. Res.*, *86*, 7095–7109, doi:10.1029/JB086iB08p07095.
- Aki, K., and P. G. Richards (1980), *Qualitative Seismology*, W. H. Freeman, New York.
- Aki, K., and P. G. Richards (2002), *Quantitative Seismology, 2nd ed.*, Univ. Sci. Books, Sausalito, Calif.
- Ando, R., and S. Okuyama (2010), Deep roots of upper plate faults and earthquake generation illuminated by volcanism, *Geophys. Res. Lett.*, *37*, L10308, doi:10.1029/2010GL042956.
- Ando, R., R. Nakata, and T. Hori (2010), A slip pulse model with fault heterogeneity for low-frequency earthquakes and tremor along plate interfaces, *Geophys. Res. Lett.*, *37*, L10310, doi:10.1029/2010GL043056.
- Ando, R., N. Takeda, and T. Yamashita (2012), Propagation dynamics of seismic and aseismic slip governed by fault heterogeneity and Newtonian rheology, *J. Geophys. Res.*, *117*, B11308, doi:10.1029/2012JB009532.
- Annen, C., J. D. Blundy, and R. S. J. Sparks (2006), The genesis of intermediate and silicic magmas in deep crustal hot zones, *J. Petrol.*, *47*(3), 505–539, doi:10.1093/petrology/egi084.
- Aso, N., and S. Ide (2014), Focal mechanisms of deep low-frequency earthquakes in Eastern Shimane in Western Japan, *J. Geophys. Res.*, *119*, 364–377, doi:10.1002/2013JB010681.
- Aso, N., and V. C. Tsai (2014), Cooling magma model for deep volcanic long-period earthquakes, *J. Geophys. Res.*, *119*, doi:10.1002/2014JB011180.
- Aso, N., K. Ohta, and S. Ide (2011), Volcanic-like low-frequency earthquakes beneath Osaka Bay in the absence of a volcano, *Geophys. Res. Lett.*, *38*, L08303, doi:10.1029/2011GL046935.
- Aso, N., K. Ohta, and S. Ide (2013), Tectonic, volcanic, and semi-volcanic deep low-frequency earthquakes in western Japan, *Tectonophysics*, *600*, 27–40, doi:10.1016/j.tecto.2012.12.015.
- Aydin, A., and J. M. DeGraff (1988), Evolution of polygonal fracture patterns in lava flows, *Science*, *239*, 471–476.
- Bean, C. J., L. De Barros, I. Lokmer, J. P. Métaixian, G. O'Brien, and S. Murphy (2014), Long-period seismicity in the shallow volcanic edifice formed from slow-rupture earthquakes, *Nat. Geosci.*, *7*(1), 71–75, doi:10.1038/ngeo2027.
- Bouchon, M. (1981), A simple method to calculate Greens function for layered media, *Bull. Seismol. Soc. Am.*, *71*(4), 959–971.
- Brocher, T. M. (2005), Empirical relations between elastic wavespeeds and density in the Earth's crust,

- Bull. Seismol. Soc. Am.*, 95, 2081–2092, doi:10.1785/0120050077.
- Bürgmann, R., and G. Dresen (2008), Rheology of the lower crust and upper mantle: Evidence from rock mechanics, geodesy and field observations, *Annu. Rev. Earth Planet. Sci.*, 36, 531–567, doi:10.1146/annurev.earth.36.031207.124326.
- Burnham, C. W. (1994), Development of the Burnham model for prediction of H₂O solubility in magmas, in *Volatiles in Magmas: Reviews in Mineralogy*, vol. 30, edited by M. Carroll, and J. Holloway, pp. 123–129, Mining Soc. of Am., Washington, D. C.
- Chapman, C. H., and W. S. Leaney (2012), A new moment-tensor decomposition for seismic events in anisotropic media, *Geophys. J. Int.*, 188, 343–370, doi: 10.1111/j.1365-246X.2011.05265.x.
- Chouet, B. A. (1996), Long-period volcano seismicity: Its source and use in eruption forecasting, *Nature*, 380, 309–316, doi:10.1038/380309a0.
- Chouet, B. (2003), Volcano Seismology, *Pure Appl. Geophys.*, 160, 739–788, doi:10.1007/PL00012556.
- Chouet, B., R. A. Page, C. D. Stephens, J. C. Lahr, and J. A. Power (1994), Precursory swarms of long-period events at Redoubt Volcano (1989–1990), Alaska: Their origin and use as a forecasting tool, *J. Volcanol. Geotherm. Res.*, 62, 95–135, doi:10.1016/0377-0273(94)90030-2.
- Committee for Catalog of Quaternary Volcanoes in Japan (1999), Catalog of Quaternary volcanoes in Japan, *Bull. Volcanol. Soc. Jpn.*, 44, 285–289.
- Costa, A., L. Caricchi, and N. Bagdassarov (2009), A model for the rheology of particle-bearing suspensions and partially molten rocks, *Geochem. Geophys. Geosyst.*, 10, Q03010, doi:10.1029/2008GC002138.
- De Barros, L., I. Lokmer, C. J. Bean, G. S. O'Brien, G. Saccorotti, J.-P. Métaixian, L. Zuccarello, and D. Patanè (2011), Source mechanism of long-period events recorded by a high-density seismic network during the 2008 eruption on Mount Etna, *J. Geophys. Res.*, 116, B01304, doi:10.1029/2010JB007629.
- Dmitrieva, K., A. J. Hotovec-Ellis, S. Prejean, and E. M. Dunham (2013), Frictional-faulting model for harmonic tremor before Redoubt Volcano eruptions, *Nat. Geosci.*, 6(8), 652–656, doi:10.1038/ngeo1879.
- Ekstrom, G. (1994), Anomalous earthquakes on volcano ring-fault structures, *Earth Planet. Sci. Lett.*, 128(3–4), 707–712, doi:10.1016/0012-821X(94)90184-8.
- Eppelbaum, L., I. Kutasov, and A. Pilchin (2014), Thermal Properties of Rocks and Density of Fluids, in *Appl. Geothermics*, pp99–149, Springer, Berlin Heidelberg, doi:10.1007/978-3-642-34023-9_2.
- Eyre, T. S., C. J. Bean, L. D. Barros, G. S. O'Brien, F. Martini, I. Lokmer, M. M. Mora, J. F. Pacheco, and G. J. Soto (2013), Moment tensor inversion for the source location and mechanism of long period (LP) seismic events from 2009 at Turrialba Volcano, Costa Rica, *J. Volcanol. Geotherm.*

Res., 258, 215–223, doi:10.1016/j.jvolgeores.2013.04.016.

- Foulger, G. R., B. R. Julian, D. P. Hill, A. M. Pitt, P. E. Malin, and E. Shalev (2004), Non-double-couple microearthquakes at Long Valley caldera, California, provide evidence for hydraulic fracturing, *J. Volcanol. Geotherm. Res.*, 132, 45–71, doi:10.1016/S0377-0273(03)00420-7.
- Frank, W. B., N. M. Shapiro, V. Kostoglodov, A. L. Husker, M. Campillo, J. S. Payero, and G. A. Prieto (2013), Low-frequency earthquakes in the Mexican Sweet Spot, *Geophys. Res. Lett.*, 40, 2661–2666, doi:10.1002/grl.50561.
- Fujita, E., and Y. Ida (2003), Geometrical effects and low-attenuation resonance of volcanic fluid inclusions for the source mechanism of long-period earthquakes, *J. Geophys. Res.*, 108(B2), 2118, doi:10.1029/2002JB001806.
- Fukuyama, E., and M. Takeo (1990), Analysis of the near-field seismogram observed during the eruption of Izu-Oshima volcano on November 16, 1987, *Bull. Volcanol. Soc. Jpn.*, 35, 283–297. (in Japanese with English abstract)
- Fukuyama, E., W. L. Ellsworth, F. Waldhauser, and A. Kubo (2003), Detailed fault structure of the 2000 western Tottori, Japan, earthquake sequence, *Bull. Seismol. Soc. Am.*, 93(4), 1468–1478, doi:10.1785/0120020123.
- Geospatial Information Authority of Japan (2011), Crustal Deformations around Kirishima Volcano, *Report of Coordinating Committee for Prediction of Volcanic Eruption*, 108, 197–220.
- Gerla, J. P. (1988), Stress and fracture evolution in a cooling pluton: An example from the Diamond Joe stock, western Arizona, USA, *J. Volcanol. Geotherm. Res.*, 34, 267–282, doi:10.1016/0377-0273(88)90038-8.
- Goehring, L., and S. W. Morris (2005), Order and disorder in columnar joints, *Europhys. Lett.*, 69(5), 739–745, doi:10.1209/epl/i2004-10408-x.
- Hara, T., K. Kuge, and H. Kawakatsu (1995), Determination of the isotropic component of the 1994 Bolivia deep earthquake, *Geophys. Res. Lett.*, 22, 2265–2268, doi:10.1029/95GL01602.
- Hasegawa A., and A. Yamamoto (1994), Deep, low-frequency microearthquakes in or around seismic low-velocity zones beneath active volcanoes in northeastern Japan, *Tectonophys.*, 233, 233–252, doi:10.1016/0040-1951(94)90243-7.
- Hasegawa, A., D. Zhao, S. Hori, A. Yamamoto, and S. Horiuchi (1991), Deep structure of the northeastern Japan arc and its relationship to seismic and volcanic activity, *Nature*, 352, 683–689, doi:10.1038/352683a0.
- Hirose, H., K. Hirahara, F. Kimata, N. Fujii, and S. Miyazaki (1999), A slow thrust slip event following the two 1996 Hyuganada earthquakes beneath the Bungo Channel, southwest Japan, *Geophys. Res. Lett.*, 26, 3237–3240, doi:10.1029/1999GL010999.
- Horikawa, H., H. Sekiguchi, T. Iwata, and Y. Sugiyama (2001), A fault model of the 2000 Tottori-ken Seibu earthquake, *Active Faults Paleoearthq. Res.*, 1, 27–40. (in Japanese with English abstract)

- Hudson, J. A., R. G. Pearce, and R. M. Rogers (1989), Source type plot for inversion of the moment tensor, *J. Geophys. Res.*, *94*(B1), 765–774, doi:10.1029/JB094iB01p00765.
- Ide, S. (2010), Striations, duration, migration and tidal response in deep tremor, *Nature*, *466*, 356–359, doi:10.1038/nature09251.
- Ide, S. (2011), Variety and spatial heterogeneity of tectonic tremor worldwide, *J. Geophys. Res.*, *117*, B03302, doi:/10.1029/2011JB008840.
- Ide, S., and M. Takeo (1997), Determination of constitutive relations of fault slip based on seismic wave analysis, *J. Geophys. Res.*, *102*(B12), 27,379–27,391, doi:10.1029/97JB02675.
- Ide, S., and S. Yabe (2014), Universality of slow earthquakes in the very low frequency band, *Geophys. Res. Lett.*, *41*, 2786–2793, doi:10.1002/2014GL059712.
- Ide, S., G. C. Beroza, D. R. Shelly, and T. Uchide (2007a), A scaling law for slow earthquakes, *Nature*, *447*, doi:10.1038/nature05780.
- Ide, S., D. R. Shelly, and G. C. Beroza (2007b), Mechanism of deep low frequency earthquakes: Further evidence that deep non-volcanic tremor is generated by shear slip on the plate interface, *Geophys. Res. Lett.*, *34*, L03308, doi:10.1029/2006GL028890.
- Ide, S., K. Shiomi, K. Mochizuki, T. Tonegawa, and G. Kimura (2010), Split Philippine Sea plate beneath Japan, *Geophys. Res. Lett.*, *37*, L21304, doi:10.1029/2010GL044585.
- Idehara, K., S. Yabe, and S. Ide (2014), Regional and global variations in the temporal clustering of tectonic tremor activity, *Earth Planets Space*, *66*:66, doi:10.1186/1880-5981-66-66.
- Iguchi, M. (1994), A vertical expansion source model for mechanisms of earthquakes originating in the magma conduit of an andesitic volcano, Japan, *Bull. Volcanol. Soc. Jpn.*, *39*, 49–67.
- Ishihara, K., and M. Iguchi (1989), The relationship between micro-earthquake swarms and volcanic activity at Sakurajima Volcano, *Ann. Disast. Prev. Res. Inst., Kyoto Univ.*, 32B-1, 1–11. (in Japanese with English abstract)
- Ishihara, Y. (2003), Major existence of very low frequency earthquakes in background seismicity along subduction zone of southwestern Japan, *EOS Trans. AGU 84, Fall Meet. Supl. Abstract*, S41C-0107.
- Ito, Y., K. Obara, K. Shiomi, S. Sekine, and H. Hirose (2007), Slow earthquakes coincident with episodic tremors and slow slip events, *Science*, *315*(5811), 503–506, doi:10.1126/science.1134454.
- Japan Meteorological Agency (2003), Revision of JMA magnitude, *Newslett. Seismol. Soc. Jpn.*, *15*(3), 5–9. (in Japanese)
- Japan Meteorological Agency (2013), *National Catalog of the Active Volcanoes of Japan, 4th ed.*, http://www.data.jma.go.jp/svd/vois/data/tokyo/STOCK/souran_eng/menu.htm.
- Jellinek, A. M., and D. Bercovici (2011), Seismic tremors and magma wagging during explosive volcanism, *Nature*, *470*(7335), 522–525, doi:10.1038/nature09828.

- Julian, B. R. (1994), Volcanic tremor: Nonlinear excitation by fluid flow, *J. Geophys. Res.*, *99*, 11859–11877, doi:10.1029/93JB03129.
- Julian, B. R., A. D. Miller, and G. R. Foulger (1997), Non-double-couple earthquake mechanisms at the Hengill-Grensdalur volcanic complex, southwest Iceland, *Geophys. Res. Lett.*, *24*(7), 743–746, doi:10.1029/97GL00499.
- Julian, B. R., A. D. Miller, and G. R. Foulger (1998), Non-double-couple earthquakes 1: Theory, *Rev. Geophys.*, *36*, 525–549, doi:10.1029/98RG00716.
- Kamo, K., T. Furuzawa, and J. Akamatsu (1977), Some natures of volcanic micro-tremors at the Sakurajima volcano, *Bull. Volcanol. Soc. Jpn.*, *22*, 41–58. (in Japanese)
- Katsumata, A. (2010), Depth of the Moho discontinuity beneath the Japanese islands estimated by travelttime analysis, *J. Geophys. Res.*, *115*, B04303, doi:10.1029/2008JB005864.
- Katsumata, A., and N. Kamaya (2003), Low-frequency continuous tremor around the Moho discontinuity away from volcanoes in the southwest Japan, *Geophys. Res. Lett.*, *30*(1), 1020, doi:10.1029/2002GL015981.
- Katsumata, A., and N. Kamaya (2004), Low-frequency events away from volcanoes in the Japan islands, *J. Seismol. Soc. Jpn.*, *57*(1), 11–28. (in Japanese with English abstract)
- Kawakatsu, H. (1989), Centroid single force inversion of seismic waves generated by landslides, *J. Geophys. Res.*, *94*(B9), 12,363–12,374, doi:10.1029/JB094iB09p12363.
- Kawakatsu, H. (1996), Observability of the isotropic component of a moment tensor, *Geophys. J. Int.*, *126*, 525–544, doi: 10.1111/j.1365-246X.1996.tb05308.x.
- Kawakatsu, H., and M. Yamamoto (2007), Volcano seismology, in *Treatise on Geophysics*, vol. 4, *Earthquake Seismology*, pp. 389–420, Elsevier, New York, doi:10.1016/B978-044452748-6.00073-0.
- Kawakatsu, H., S. Kaneshima, H. Matsubayashi, T. Ohminato, Y. Sudo, T. Tsutsui, K. Uhira, H. Yamasato, H. Ito, and D. Legrand (2000), Aso94: Aso seismic observation with broadband instruments, *J. Volcanol. Geotherm. Res.*, *101*, 129–154, doi:10.1016/S0377-0273(00)00166-9.
- Kennet, B. L. N., and N. J. Kerry (1979), Seismic waves in a stratified half space, *Geophys. J. R. Astron. Soc.*, *57*, 557–583, doi:10.1111/j.1365-246X.1979.tb06779.x.
- Kikuchi, M., H. Kanamori, and K. Satake (1993), Source complexity of the 1988 Armenian Earthquake: Evidence for a slow after-slip event, *J. Geophys. Res.*, *98*(B9), 15797–15808, doi:10.1029/93JB01568.
- Kitsunezaki, S. (2009), Crack propagation speed in the drying process of paste, *J. Phys. Soc. Jpn.*, *78*(6), 064801, doi:10.1143/JPSJ.78.064801.
- Kitsunezaki, S. (2010), Crack growth in drying paste, *J. Phys. Soc. Jpn.*, *79*(12), 124802, doi:10.1143/JPSJ.79.124802.
- Kitsunezaki, S. (2013), Cracking condition of cohesionless porous materials in drying processes, *Phys.*

Rev. E, 87(5), 052805, doi:10.1103/PhysRevE.87.052805.

- Koyaguchi, T. (2008), *Modeling of Volcanic Phenomena*, Tokyo Univ. Press, Tokyo. (in Japanese)
- Kuge, K., and H. Kawakatsu (1990), Analysis of a deep non-double couple earthquake using very broadband data, *Geophys. Res. Lett.*, 17, 227–230.
- Kumagai, H. (2009), Source quantification of volcano seismic signals, in *Encyclopedia of Complexity and Systems Science*, edited by R. A. Meyers, pp. 9899–9932, Springer, New York.
- Kumagai, H., and B. A. Chouet (2000), Acoustic properties of a crack containing magmatic or hydrothermal fluids, *J. Geophys. Res.*, 105(B11), 25,493–25,512, doi:10.1029/2000JB900273.
- Kumagai, H., T. Ohminato, M. Nakano, M. Ooi, A. Kubo, H. Inoue, and J. Oikawa (2001), Very-long-period seismic signals and caldera formation at Miyake Island, Japan, *Science*, 293, 687–690.
- Kumagai, H., B. A. Chouet, and M. Nakano (2002), Waveform inversion of oscillatory signatures in long-period events beneath volcanoes, *J. Geophys. Res.*, 107(B11), 2301, doi:10.1029/2001JB001704.
- Kumagai, H., Y. Maeda, M. Ichihara, N. Kame, and T. Kusakabe (2014), Seismic moment and volume change of a spherical source, *Earth Planet. Sci.*, 66:7, doi:10.1186/1880-5981-66-7.
- Legrand, D., S. Kaneshima, and H. Kawakatsu (2000), Moment tensor analysis of near-field broadband waveforms observed at Aso Volcano, Japan, *J. Volcanol. Geotherm. Res.*, 101, 155–169, doi:10.1016/S0377-0273(00)00167-0.
- Lewicki, J. L., G. E. Hilley, D. R. Shelly, J. C. King, J. P. McGeehin, M. Mangan, and W. C. Evans (2014), Crustal migration of CO₂-rich magmatic fluids recorded by tree-ring radiocarbon and seismicity at Mammoth Mountain, CA, USA, *Earth Planet. Sci. Lett.*, 390, 52–58, doi:10.1016/j.epsl.2013.12.035.
- Lough, A. C., D. A. Wiens, C. G. Barcheck, S. Anandakrishnan, R. C. Aster, D. D. Blankenship, A. D. Huerta, A. Nyblade, D. A. Young, and T. J. Wilson (2013), Seismic detection of an active subglacial magmatic complex in Marie Byrd Land, Antarctica, *Nat. Geosci.*, 6, 1031–1035, doi:10.1038/ngeo1992.
- Mader, H. M., E. W. Llewellyn, and S. P. Mueller (2013), The rheology of two-phase magmas: A review and analysis, *J. Volcanol. Geotherm. Res.*, 257, 135–158, doi:10.1016/j.jvolgeores.2013.02.014.
- Maryanto, S., M. Iguchi, and T. Tameguri (2008), Constraints on the source mechanism of harmonic tremors based on seismological, ground deformation, and visual observations at Sakurajima volcano, Japan. *J. Volcanol. Geotherm. Res.*, 170(3), 198–217, doi:10.1016/j.jvolgeores.2007.10.004.
- Matsubara, W., K. Yomogida, J. Koyama, M. Kasahara, M. Ichianagi, H. Kawakatsu, and M. Yamamoto (2004), Distribution and characteristics in waveform and spectrum of seismic events

- associated with the 2000 eruption of Mt. Usu, *J. Volcanol. Geotherm. Res.*, *136*, 141–158, doi:10.1016/j.jvolgeores.2004.05.016.
- McNutt, S. R. (2005), Volcanic seismology, *Annu. Rev. Earth Planet. Sci.*, *32*, 461–491, doi:10.1146/annurev.earth.33.092203.122459.
- Miller, A. D., G. R. Foulger, and B. R. Julian (1998), Non-double-couple earthquakes 2: Observations, *Rev. Geophys.*, *36*, 551–568, doi:10.1029/98RG00717.
- Minakami, T. (1960), Fundamental research for predicting volcanic eruption (Part 1), *Bull. Earthq. Res. Inst.*, *38*, 497–544.
- Müller, G. (1998a), Experimental simulation of basalt columns, *J. Volcanol. Geotherm. Res.*, *86*, 93–96, doi:10.1016/S0377-0273(98)00045-6.
- Müller, G. (1998b), Starch columns: Analog model for basalt columns, *J. Geophys. Res.*, *103*(B7), 15239–15253, doi:10.1029/98JB00389.
- Nakahara, A., and Y. Matsuo (2005), Imprinting memory into paste and its visualization as crack patterns in drying process, *J. Phys. Soc. Jpn.*, *74*(5), 1362–1365.
- Nakajima, J., T. Matsuzawa, and A. Hasegawa (2002), Moho depth variation in the central part of northeastern Japan estimated from reflected and converted waves, *Phys. Earth Planet. Inter.*, *130*, 31–47.
- Nakamichi, H., H. Hamaguchi, S. Tanaka, S. Ueki, T. Nishimura, and A. Hasegawa (2003), Source mechanisms of deep and intermediate-depth low-frequency earthquakes beneath Iwate volcano, northeastern Japan, *Geophys. J. Int.*, *154*(3), 811–828, doi:10.1046/j.1365-246X.2003.01991.x.
- Nakamichi, H., M. Ukawa, and S. Sakai (2004), Precise hypocenter locations of midcrustal low-frequency earthquakes beneath Mt. Fuji, Japan, *Earth Planets Space*, *56*(11), e37–e40, doi:10.5636/eps.56.11_e37.
- Nakano, M., H. Kumagai, M. Kumazawa, K. Yamaoka, and B. Chouet (1998), The excitation and characteristic frequency of the long-period volcanic event: An approach based on an inhomogeneous autoregressive model of a linear dynamic system, *J. Geophys. Res.*, *103*, 10031–10046, doi:10.1029/98JB00387.
- Nakata, R., N. Suda, and H. Tsuruoka (2008), Non-volcanic tremor resulting from the combined effect of Earth tides and slow slip events, *Nat. Geosci.*, *1*, 676–678, doi:10.1038/ngeo288.
- Neuberg, J., R. Luckett, B. Baptie, and K. Olsen (2000), Models of tremor and low-frequency earthquake swarms on Montserrat, *J. Volcanol. Geotherm. Res.*, *101*, 83–104, doi:10.1016/S0377-0273(00)00169-4.
- Nichols, M. L., S. D. Malone, S. C. Moran, W. A. Thelen, and J. E. Vidale (2011), Deep long-period earthquakes beneath Washington and Oregon volcanoes, *J. Volcanol. Geotherm. Res.*, *200*(3–4), 116–128, doi:10.1016/j.jvolgeores.2010.12.005.
- Nishide, N., T. Hashimoto, J. Funasaki, H. Nakazawa, M. Oka, H. Ueno, N. Yamada, I. Sasakawa, K.

- Maeda, K. Sugimoto, and T. Takashima (2000), Nationwide activity of low-frequency earthquakes in the lower crust in Japan, *Abstr. Jpn. Earth and Planet. Sci. Joint Meeting*, sk-p002. (in Japanese)
- Nishidomi, I., and Takeo, M. (1996), Seismicity and a focal mechanism of low-frequency earthquakes occurring in the western part of Tochigi prefecture, Japan, *J. Volcanol. Soc. Jpn.*, *41*, 43–59. (in Japanese with English abstract)
- Nishimura, T., and M. Iguchi (2006), Volcanic Earthquakes and Tremor in Japan, *Kyoto Univ. Press*, Kyoto, Japan. (in Japanese)
- Obara, K. (2002), Nonvolcanic deep tremor associated with subduction in southwest Japan, *Science*, *296*(5573), 1679–1681, doi:10.1126/science.1070378.
- Obara, K. (2011), Characteristics and interactions between non-volcanic tremor and related slow earthquakes in the Nankai subduction zone, southwest Japan, *J. Geodyn.*, *52*, 229–248, doi:10.1016/j.jog.2011.04.002.
- Obara, K., S. Tanaka, T. Maeda, and T. Matsuzawa (2010), Depth-dependent activity of non-volcanic tremor in southwest Japan, *Geophys. Res. Lett.*, *37*, L13306, doi:10.1029/2010GL043679.
- Ohmi, S., and K. Obara (2002), Deep low-frequency earthquakes beneath the focal region of the Mw 6.7 2000 Western Tottori earthquake, *Geophys. Res. Lett.*, *29*, 1807, doi:10.1029/2001GL014469.
- Ohmi, S., K. Watanabe, T. Shibutani, N. Hirano, and S. Nakao (2002), The 2000 Western Tottori earthquake—Seismic activity revealed by the regional seismic networks—, *Earth Planets Space*, *54*, 819–830.
- Ohmi, S., I. Hirose, and J. J. Mori (2004), Deep low-frequency earthquakes near the downward extension of the seismogenic fault of the 2000 Western Tottori earthquake, *Earth Planets Space*, *56*(12), 1185–1189, doi:10.5636/eps.56.12_1185.
- Ohminato, T. (2006), Characteristics and source modeling of broadband seismic signals associated with the hydrothermal system at Satsuma–Iwo Jima volcano, Japan, *J. Volcanol. Geotherm. Res.*, *158*, 467–490, doi:10.1016/j.jvolgeores.2006.08.004.
- Ohminato, T., B. A. Chouet, P. B. Dawson, and S. Kedar (1998), Waveform inversion of very-long-period impulsive signals associated with magmatic injection beneath Kilauea volcano, Hawaii, *J. Geophys. Res.*, *103*, 23,839–23,862, doi: 10.1029/98JB01122.
- Ohminato, T., M. Takeo, H. Kumagai, T. Yamashina, J. Oikawa, E. Koyama, H. Tsuji, and T. Urabe (2006), Vulcanian eruptions with dominant single force components observed during the Asama 2004 volcanic activity in Japan, *Earth Planets Space*, *58*, 583–593.
- Ohta, K., and S. Ide (2008), A precise hypocenter determination method using network correlation coefficients and its application to deep low frequency earthquakes, *Earth Planets Space*, *60*(8), 877–882.

- Ohta, K., and S. Ide (2011), Precise hypocenter distribution of deep low-frequency earthquakes and its relationship to the local geometry of the subducting plate in the Nankai subduction zone, Japan, *J. Geophys. Res.*, *116*, B01308, doi:10.1029/2010JB007857.
- Ohzono, M., Y. Ohta, T. Iinuma, S. Miura, and J. Muto (2012), Geodetic evidence of viscoelastic relaxation after the 2008 Iwate-Miyagi Nairiku earthquake, *Earth Planets Space*, *64*, 759–764.
- Okada, T., and A. Hasegawa (2000), Activity of deep low-frequency microearthquakes and their moment tensors in northeastern Japan, *Bull. Volcanol. Soc. Jpn.*, *45*(2), 47–63. (in Japanese with English abstract)
- Okubo, P. G., and C. J. Wolfe (2008), Swarms of similar long-period earthquakes in the mantle beneath Mauna Loa Volcano. *Journal of Volcanology and Geothermal Research*, *178*, 787–94, doi:10.1016/j.jvolgeores.2008.09.007.
- Ooshida, T. (2008), Continuum theory of memory effect in crack patterns of drying pastes, *Phys. Rev. E*, *77*, 061501, doi:10.1103/PhysRevE.77.061501.
- Otsuki, M. (2005), Memory effect on the formation of drying cracks, *Phys. Rev. E*, *72*, 046115, doi:10.1103/PhysRevE.72.046115.
- Pitt, A. M., D. P. Hill, S. W. Walter, and M. J. S. Johnson (2002), Midcrustal, long-period earthquakes beneath northern California volcanic areas, *Seismol. Res. Lett.*, *73*, 144–152, doi:10.1785/gssrl.73.2.144.
- Power, J. A., A. D. Jolly, R. A. Page, and S. R. McNutt (1995), Seismicity and forecasting of the 1992 eruptions of Crater Peak vent, Mount Spurr volcano, Alaska: An overview, *USGS Bull.*, *2139*, 149–159.
- Power, J. A., A. D. Jolly, C. J. Nye, and M. L. Harbin (2002), A conceptual model of the Mount Spurr magmatic system from seismic and geochemical observations of the 1992 Crater Peak eruption sequence, *Bull. Volcanol.*, *64*, 206–218, doi: 10.1177/003231876601800104.
- Power, J. A., S. D. Stihler, R. A. White, and S. C. Moran (2004), Observations of deep long-period (DLP) seismic events beneath Aleutian arc volcanoes; 1989–2002, *J. Volcanol. Geotherm. Res.*, *138*(3), 243–266, doi:10.1016/j.jvolgeores.2004.07.005.
- Pulido, N., and L. A. Dalguer (2009), Estimation of the high-frequency radiation of the 2000 Tottori (Japan) earthquake based on a dynamic model of fault rupture: application to the strong ground motion simulation, *Bull. Seismol. Soc. Am.*, *99*(4), 2305–2322, doi: 10.1785/0120080165.
- Ramesh, D. S., H. Kawakatsu, S. Watada, and X. Yuan (2005), Receiver function images of the central Chugoku region in the Japanese islands using Hi-net data, *Earth Planets Space*, *57*, 271–280.
- Rogers, G., and H. Dragert (2003), Episodic tremor and slip on the Cascadia subduction zone: The chatter of silent slip, *Science*, *300*(5627), 1942–1943, doi:10.1126/science.1084783.
- Ross, A., G. R. Foulger, and B. R. Julian (1996), Non-double-couple earthquake mechanisms at the

- Geysers geothermal area, California, *Geophys. Res. Lett.*, 23(8), 877–880, doi:10.1029/96GL00590.
- Ross, A., G. R. Foulger, and B. R. Julian (1999), Source processes of industrially-induced earthquakes at the Geysers geothermal area, California, *Geophysics*, 64(6), 1877–1889.
- Rubinstein, J. L., D. R. Shelly, and W. L. Ellsworth (2010), Non-volcanic tremor: A window into the roots of fault zones, in *New Frontiers in Integrated Solid Earth Sciences*, edited by S. Cloetingh and J. Negendank, pp. 287–314, Springer, New York, doi:10.1007/978-90-481-2737-5_8.
- Sano, Y., and J. Nakajima (2008), Geographical distribution of $^3\text{He}/^4\text{He}$ ratios and seismic tomography in Japan, *Geochem. J.*, 42, 51–60, doi:10.2343/geochemj.42.51.
- Saraò, A., G. Panza, E. Privitera, and O. Cocina (2001), Non-double-couple mechanisms in the seismicity preceding 1991–1993 Etna volcano eruption, *Geophys. J. Int.*, 145, 319–335.
- Schmincke, H.-U. (2004), *Volcanism*, Springer, Berlin.
- Schorlemmer, D., S. Wiemer, and M. Wyss (2005), Variations in earthquake-size distribution across different stress regimes, *Nature*, 437, 539–542, doi:10.1038/nature04094.
- Shaw, H. R. (1972), Viscosities of magmatic silicate liquids: An empirical method of prediction, *Am. J. Sci.*, 272, 870–893, doi:10.2475/ajs.272.9.870.
- Shaw, H. R., and B. Chouet (1991), Fractal hierarchies of magma transport in Hawaii and critical self-organization of tremor, *J. Geophys. Res.*, 96(B6), 10191–10207, doi:10.1029/91JB00771.
- Shearer, P. M. (2009), *Introduction to Seismology, Second Edition*, Cambridge University Press, Cambridge.
- Shelly, D. R., and J. L. Hardebeck (2010), Precise tremor source locations and amplitude variations along the lower-crustal central San Andreas Fault, *Geophys. Res. Lett.*, 37, L14301, doi:10.1029/2010GL043672.
- Shelly, D. R., and D. P. Hill (2011), Migrating swarms of brittle-failure earthquakes in the lower crust beneath Mammoth Mountain, California, *Geophys. Res. Lett.*, 38, L20307, doi:10.1029/2011GL049336.
- Shelly, D. R., G. C. Beroza, S. Ide, and S. Nakamura (2006), Low-frequency earthquakes in Shikoku, Japan, and their relationship to episodic tremor and slip, *Nature*, 442, 188–191, doi:10.1038/nature04931.
- Shelly, D. R., G. C. Beroza, and S. Ide (2007a), Non-volcanic tremor and low frequency earthquake swarms, *Nature*, 446, 305–307, doi:10.1038/nature05666.
- Shelly, D. R., G. C. Beroza, and S. Ide (2007b), Complex evolution of transient slip derived from precise tremor locations in western Shikoku, Japan, *Geochem. Geophys. Geosyst.*, 8, Q10014, doi:10.1029/2007GC001640.
- Shimamoto, T. (1986), Transition between frictional slip and ductile flow for Halite shear zones at room temperature, *Science*, 231(4739), 711–714, doi:10.1126/science.231.4739.711.

- Shuler, A., M. Nettles, and G. Ekström (2013), Global observation of vertical-CLVD earthquakes at active volcanoes, *J. Geophys. Res. Solid Earth*, *118*, 138–164, doi:10.1029/2012JB009721.
- Soosalu, H., J. Key, R. S. White, C. Knox, P. Einarsson, and S. S. Jakobsdóttir (2010), Lower-crustal earthquakes caused by magma movement beneath Askja volcano on the north Iceland rift, *Bull. Volcanol.*, *72*(1), 55–62, doi:10.1007/s00445-009-0297-3.
- Sparks, R. S. J., J. Barclay, C. Jaupart, H. M. Mader, and J. C. Phillips (1994), Physical aspects of magmatic degassing I. Experimental and theoretical constraints on vesiculation, in *Volatiles in Magmas: Reviews in Mineralogy*, vol. 30, edited by M. R. Carroll, and J. R. Holloway, pp. 413–446, Mineral. Soc. Am., Washington, D. C.
- Spry, A. H. (1962), The origin of columnar jointing, particularly in basalt flows, *J. Geol. Soc. Aust.*, *8*, 191–216.
- Stehly, L., M. Campillo, and N. M. Shapiro (2006), A study of the seismic noise from its long-range correlation properties, *J. Geophys. Res.*, *111*, B10306, doi:10.1029/2005JB004237.
- Takahashi, H., and J. Miyamura (2009), Deep low-frequency earthquakes occurring in Japanese Islands, *Geophys. Bull. Hokkaido Univ.*, *72*, 177–190. (in Japanese with English abstract)
- Takei, Y., and B. K. Holtzman (2009), Viscous constitutive relations of solid-liquid composites in terms of grain boundary contiguity: 1. Grain boundary diffusion control model, *J. Geophys. Res.*, *114*, B06205, doi:10.1029/2008JB005850.
- Takei, Y., and M. Kumazawa (1994), Why have the single force and torque been excluded from seismic source models?, *Geophys. J. Int.*, *118*, 20–30, doi:10.1111/j.1365-246X.1994.tb04672.x.
- Takeo, M. (1985), Near-field synthetic seismograms taking into account the effects of anelasticity: The effects of anelastic attenuation on seismograms caused by a sedimentary layer, *Meteorol. Geophys.*, *36*, 245–257, doi:10.2467/mripapers.36.245. (in Japanese with English abstract)
- Takeo, M., H. Yamasato, I. Furaya, and M. Seino (1990), Analysis of long-period seismic waves excited by the November 1987 eruption of Izu-Oshima Volcano, *J. Geophys. Res.*, *95*(B12), 19,377–19,393, doi:10.1029/JB095iB12p19377.
- Tape, W., and C. Tape (2012a), A geometric setting for moment tensors, *Geophys. J. Int.*, *190*, 476–498, doi:10.1111/j.1365-246X.2012.05491.x.
- Tape, W., and C. Tape (2012b), A geometric comparison of source-type plots for moment tensors, *Geophys. J. Int.*, *190*, 499–510, doi:10.1111/j.1365-246X.2012.05490.x.
- Tape, W., and C. Tape (2012c), Angle between principal axis triples, *Geophys. J. Int.*, *191*, 813–831, doi:10.1111/j.1365-246X.2012.05658.x.
- Tape, W., and C. Tape (2013), The classical model for moment tensors, *Geophys. J. Int.*, *195*, 1701–1720, doi:10.1093/gji/ggt302.
- Timoshenko, S. P., and J. N. Goodier (1970), *Theory of Elasticity*, 3rd ed., McGraw-Hill, New York.
- Toramaru, A., and T. Matsumoto (2004), Columnar joint morphology and cooling rate: A starch-

- water mixture experiment, *J. Geophys. Res.*, *109*, B02205, doi:10.1029/2003JB002686.
- Ukawa, M. (2005), Deep low-frequency earthquake swarm in the mid crust beneath Mount Fuji (Japan) in 2000 and 2001, *Bull. Volcanol.*, *67*, 47–56, doi:10.1007/s00445-005-0419-5.
- Ukawa, M., and K. Obara (1993), Low frequency earthquakes around Moho beneath the volcanic front in the Kanto district, central Japan, *Bull. Volcanol. Soc. Jpn.*, *38*, 187–197. (in Japanese with English abstract)
- Ukawa, M., and M. Ohtake (1987), A monochromatic earthquake suggesting deep-seated magmatic activity beneath the Izu-Ooshima volcano, Japan, *J. Geophys. Res.*, *92*, 12,649–12,663, doi:10.1029/JB092iB12p12649.
- Varley, N., R. Arámbula-Mendoza, G. Reyes-Dávila, R. Sanderson, and J. Stevenson (2010), Generation of vulcanian activity and long-period seismicity at Volcán de Colima, Mexico, *J. Volcanol. Geotherm. Res.*, *198*, 45–56, doi:10.1016/j.jvolgeores.2010.08.009.
- Vidale, J. E., D. A. Schmidt, S. D. Malone, A. J. Hotovec-Ellis, S. C. Moran, K. C. Creager, and H. Houston (2014), Deep long-period earthquakes west of the volcanic arc in Oregon: Evidence of serpentine dehydration in the fore-arc mantle wedge, *Geophys. Res. Lett.*, *41*, 370–376, doi:10.1002/2013GL059118.
- Watanabe, H. (1971), Determination of Earthquake Magnitude at Regional Distance in and near Japan, *J. Seismol. Soc. Jpn.*, *24*, 189–200. (in Japanese with English abstract)
- Webb, S. L., and D. B. Dingwell (1990), Non-Newtonian rheology of igneous melts at high stresses and strain rates: Experimental results for rhyolite, andesite, basalt, and nephelinite, *J. Geophys. Res.*, *95*(B10), 15,695–15,701, doi:10.1029/JB095iB10p15695.
- White, R. A. (1996), Precursory deep long-period earthquakes at Mount Pinatubo: Spatio-temporal link to basaltic trigger, in *Fire and Mud: Eruptions and Lahars of Mount Pinatubo, Philippines*, edited by C. G. Newhall and R. S. Punongbayan, pp. 307–328, Univ. of Washington Press, Seattle, Wash.
- Wyllie, P. J. (1977), Crustal anatexis: An experimental review, *Tectonophysics*, *43*(1–2), 41–71, doi:10.1016/0040-1951(77)90005-1.
- Yoshioka, S., and K. Murakami (2007), Temperature distribution of the upper surface of the subducted Philippine Sea Plate along the Nankai Trough, southwest Japan, from a three-dimensional subduction model: Relation to large interplate and low-frequency earthquakes, *Geophys. J. Int.*, *171*(1), 302–315, doi:10.1111/j.1365-246X.2007.03510.x.
- Zhao, D., H. Kanamori, H. Negishi, and D. Wiens (1996), Tomography of the source area of the 1995 Kobe earthquake: Evidence for fluids at the hypocenter?, *Science*, *274*(5294), 1891–1894, doi:10.1126/science.274.5294.1891.